Development and application of a wavelet-based method for modelling of seismic wave propagation

Tae-Kyung Hong

A thesis submitted for
the degree of Doctor of Philosophy of
The Australian National University

June 2003

Statement

All the material presented in this thesis is solely based on the original work of the author, unless otherwise mentioned in the text and the acknowledgement.

Tae-Kyung Hong
Canberra, June 2003

Acknowledgments

I thank God for helping and guiding me every time in my life, and makes me finish the thesis safely. I sincerely thank Professor Brian Kennett, my supervisor, for his advice in the PhD study, encouragement and kind supports. I met him first time when I came to the Australian National University (ANU) as an exchange student from Seoul National University in 1999. He kindly accepted me as a visiting student in his group and offered a work place for the exchange study. After the exchange program and the Master study at Seoul National University, I started the PhD course at Research School of Earth Sciences, ANU under the supervision of Brian in April 2000. I was really impressed by his energetic and restless enthusiasm on science, which is not confined only in seismology. The attractive idea, developing a new numerical technique based on wavelets for modelling of seismic wave propagation, was suggested by Brian. His invaluable comments have helped me so much when I was in trouble during the PhD research. Also, I appreciate allowing the travel grants to the AGU fall meeting, 2002.

I am deeply indebted in love to my wife Yun Sun Chung, my parents, parents-in-law and my brother for enduring my PhD study and giving sincere supports. Especially, I thank my little baby, Jin-Young Hong who was born in Canberra during my PhD study for giving me refreshment and lovely smiles, and another baby in my wife who will be born in October 2003 has made me happy.

I am grateful also to Professor Chang-Eob Baag, my former supervisor at Seoul National University for his kind advice at difficult situations and broadening my basic knowledge on seismology. I appreciate kind advice and helps of my co-supervisor, Dr. Malcolm Sambridge. Also, I thank Nick Rawlinson, Kazunori Yoshizawa, Stewart Fishwick, Yoshihisa Hiyoshi, Katrina Marson-Pidgeon, Damien Bright, Todd Nicholson and Haixu Cheng for their kind helps and discussions. Other Seismology group people, Dr. Anya Reading, Dr. Alexei Gobatov, Mrs. Felicity Chivas, Armando Arcidiaco, Anthony Percival, Ms. Jennifer Badstuebner, Dr. Ted Lilley and Stefan Sirotjuk have made enjoyable enviroment during the PhD study. I thank kind helps of Dr. Herb McQueen and Ray Martin on the RSES Unix system.

I acknowledge the Australian National University Supercomputer Facility for allocation of computational time in the Alpha server, MPI-based parallel machine. Most of materials in the thesis are prepared using the parallel machine. Advises and supports of David Singleton and Stuart Midgley helped me to be familiar with the machine.

I am grateful to Drs. H. Sato, Y.-G. Li, M. Fehler, H. Igel and M. Korn for their constructive reviews on my journal papers which this thesis is partly based on. Also, I thank Dr. T. Furumura, Dr. M. Bouchon, Dr. E. Tessmer for sharing of their codes and kind comments. Discussions with Tae-Seob Kang and Dong-Hoon Shin for numerical techniques were useful. Encouragement by Drs. Ru-Shan Wu, Takashi Furumura, Liang Bao Zhu and Professor Kiyoshi Yomogida on the development of a wavelet-based method is appreciated.

I gratefully acknowledge the receipt of the ANU PhD Scholarship and the International Postgraduate Research Scholarship. Without the financial support, the PhD study may not be possible. Also, I thank people in the Korean Presbyterian Church in Canberra for their loves in Jesus.

The first journal paper on the wavelet-based method (Hong & Kennett, 2002. A wavelet-based method for simulation of two-dimensional elastic wave propagation, *Geophys. J. Int.*, **150**, 610-638) was ranked at the third place in the list of the 50 most accessed 2002 papers (3/233, 189 downloads) through the Blackwell's GJI-Synergy website.

Abstract

A wavelet-based method is developed for the numerical modelling of acoustic and elastic wave propagation. Several techniques are implemented together to develop the method. Using a displacement-velocity formulation and treating spatial derivatives with linear operators based on wavelet transform, the wave equations are rewritten as a system of equations whose evolution in time is controlled by first-order derivatives. The linear operators for the spatial derivatives are treated in wavelet bases by projection with a wavelet transform. The discretized solution in time can then be represented in an explicit recursive form using a semigroup approach. Absorbing boundary conditions are considered implicitly by including attenuation terms in the governing equations, and the traction-free boundary conditions can be implemented by augmenting the system of equations with equivalent force terms at the boundaries.

This wavelet-based method is applied to acoustic, *SH* and *P-SV* waves for several 2-D models with rigid or traction-free boundary conditions, and numerical results are compared with the analytic solutions. Also, the wavelet-based method is extended to problems with topography using a grid-mapping technique. The method is stable even in the applications to highly-varying topography problems and generates accurate responses. The wavelet-based approach is also appropriate for modelling in complex media with highly perturbed random media or with strong heterogeneities. The new technique is shown to be suitable for accurate and stable modelling of wave propagation in general complex media.

The wavelet approach is then expanded to models with localised heterogeneity, with significant contrasts with their surroundings. We consider zones with both lowered wavespeed such as a fault gouge zone and elevated wavespeeds as in a subduction zone. In each of these situations the source lies within the heterogeneity. The representation of the source has therefore been adapted to work directly in a heterogeneous environment, rather than using a locally homogeneous zone around the source. This extension also allows the wavelet method to be used with a wider variety of sources, e.g., propagating sources. For the fault zone we consider both point and propagating sources through a moment tensor representation, and reveal significant trapped waves along the gouge zone as well as permanent displacements. For subduction zones a variety of effects are produced depending on the depth and position of the source relative to the subducting slab. A variety of secondary waves, such as reflected and interface waves, can be produced in wavetrains at regional distances and tend to be more important for greater source depth.

The high stability and accuracy of the wavelet-based method in highly perturbed media allows this approach to be exploited for the investigation of seismic-wave scattering in several stochastic (Gaussian, exponential, von Karman) random media. The scattering attenuation depends on the correlation distance of the random heterogeneities, the velocity ratio of P and S waves, and the frequency content of the incident waves. Theoretical attenuation variation is derived for the comparisons with numerical results by using the first-order Born approximation. The minimum scattering angle for these stochastic media is found to be in the range 60-90 degrees, and it appears that methods such as finite-differences may overestimate scattering attenuation when the level of the heterogeneity is high.

The characteristics of scattering attenuation patterns in elastic waves are investigated using the theoretical expressions for P and S waves. S waves lose more energy in the low frequency range ($fa \leq 1$ km/s, where fa is the normalized frequency) than P waves, and the phenomenon is reversed at high frequency range. The frequency dependency of seismic scattering makes the scattering attenuation ratio increase with frequency at $0.1 < fa < 2$ km/s, and the ratio of P and S scattering is nearly constant outside these ranges of normalized frequency. The minimum ratio is determined to be about 0.4 and the maximum ratio increases with the Hurst number (ν) for von Karman random media (including exponential random media) from 1 (ν=0.05) to 1.7 (ν=0.5). Gaussian random media display a steep change in the P/S scattering ratio and may not be suitable for the representation of natural random heterogeneities in the earth. With an appropriate choice of the Hurst number, the von Karman model can reproduce the random heterogeneities of the crust.

From complementary studies on scatterings of acoustic and SH waves in stochastic random media, the effects of physical-parameter perturbation on scattering are resolved. Due to the difference in the form of the equations between acoustic and elastic waves, i.e., the differences in the placement of the density and Lamé coefficients, there are characteristic differences in scattering patterns and the attenuation rates. The perturbation in the density in elastic waves introduces additional energy loss in primary waves, and the energy loss is proportional to the magnitude of the density perturbation.

Finally, elastic waves are modelled in media with randomly distributed fluid-filled circular cavities, which is a challenging problem for numerical techniques. The energy dissipation of the primary waves is proportional to the scale of the cavities. Theoretical attenuation variations for media with circular cavities, which may be filled with any materials (e.g., vacuum, fluid, elastic materials), have been formulated and they are compared with the numerical results for the media with fluid-filled cavities. The numerically estimated attenuation rates agree well with the theoretical variation. The attenuation rates increase linearly with normalized wavenumber, unlike those in stochastic random media that display a parabolic trend for the normalized wavenumber. Also, the normalized attenuation rates are identical between those measured from media with a same normalized wavenumber (i.e., same radius of cavities) even if the number densities (number of cavities per area in a medium) are different. It appears that random heterogeneities in a specific region can be described properly with combined use of stochastic random heterogeneities and random heterogeneities with high impedance by considering the scattering attenuation patterns.

Contents

1

Introduction

1.1 Previous wavelet-based techniques and motivation of this study

The discrete wavelet transform (Daubechies, 1992) has become a powerful tool in signal analysis because wavelets are confined in both the frequency and time domains. The transformation is based on a multiresolution analysis that projects a signal onto successive wavelet subspaces representing different scales of variation.

Applications of wavelets have been made for several aspects of seismic signal processing such as the determination of the onset time of arrival of a specific phases (Anant & Dowla, 1997; Tibuleac & Herrin, 1999), measurement of an anisotropy rate in certain regions (Bear *et al.*, 1999), and the estimation of a time varying spectral density matrix (Lilly & Park, 1995). However, the applications of wavelets are not restricted to signal processing, and have been extended to numerical analysis as well exploiting the adaptivity and compactness achievable in the wavelet domain. Lewalle (1998) has exploited an explicit approach for certain classes of problem by a choice of wavelets which can be matched to the appropriate equations. He has applied Hermitian wavelets, the derivatives of a Gaussian bell-shaped curve, to a diffusion problem through a canonical transformation and showed a promising development for the numerical prediction of intermittent and nonhomogeneous phenomenon.

The adaptivity of wavelets has been one of the major motivations for the implementation of wavelets in numerical analysis (Holmström, 1999; Lippert *et al.*, 1998; Fröhlich & Schneider, 1997). Holmström (1999) has implemented a composite technique to use the Deslauriers-Dubuc interpolating wavelets (DD wavelets, see, Deslauriers & Dubuc (1989); Dubuc (1986)) as a supplementary method to a usual finite difference (FD) scheme; so that he could reduce the computational cost in FD computation by imposing a threshold on the size of wavelet coefficients. However, the composite scheme does not escape the problems inherent in FD methods, for example, accumulation of errors across the grid.

Lippert *et al.* (1998) have implemented a similar approach based on the adaptivity of DD wavelets in solving a Poisson equation. They have tried to represent physical operators (differential operators) in multilevel spaces based on DD wavelets. With the help of the adaptive scheme they could solve a problem having local nonlinear coupling in a domain with given accuracy (or, resolution) and less computational labour compared to non-adaptive full-grid based methods. Such an adaptive approach to parabolic equations may have difficulties with transient nonlinear phenomena because of the need to continually update the operators at each time step.

Fröhlich & Schneider (1997) have applied wavelets to obtain numerical solutions of a reaction-diffusion system in one- and two-dimensional spaces and they have also used the adaptivity of wavelets for space discretization. They have been able to incorporate inherently periodic boundary conditions in special cases such as an outward burning flame. However, many natural phenomena do not satisfy periodic boundary conditions (e.g., adiabatic reactions at the boundaries) and then it is difficult to use this type of wavelet-based method.

Qian & Weiss (1993) have applied the wavelet-Galerkin method to obtain numerical solution of PDEs, especially boundary value problems (e.g., Helmholtz equation) in nonseparable domains. With the introduction of an 'extensive wavelet-capacitance matrix technique' which shows fast convergence at relatively coarse levels of discretization, they have been able to handle the boundary geometry effectively. Cai & Wang (1996) have demonstrated the applicability of adaptive wavelet collocation methods using cubic splines for linear and nonlinear hyperbolic PDEs with initial boundary conditions in 1-D spatial domain. We note that Cai & Wang have introduced different shapes of wavelets and scaling functions for internal and boundary regions, and could treat the boundary effects correctly without contaminating other regions. Dahmen (1997) has reviewed basic theories of the wavelet-based scheme and adaptive techniques for numerical simulation for elliptic and parabolic problems.

Recently some numerical analysis based on wavelets has been applied in modelling of geophysical problems. In Vasilyev *et al.* (2001) the adaptive multilevel wavelet collocation method has been implemented in modelling of viscoelastic plume-lithosphere interaction by solving the partial differential equations representing viscoelastic flows with localized viscosity variations. Also, Rosa *et al.* (2001) has demonstrated that a wavelet transform could be used to model static physical quantities in elastic media (e.g., displacement and stress fields) with consideration of boundary conditions.

So far the adaptivity which leads to a reduction in computational labour and in memory use via grid adaptation or wavelet-scale adaptation, has been one of most attractive reasons for the use of wavelet-based scheme in numerical studies. However, the grid-adaptivity can only be considered in a limited way for a time-dependent PDE system due to the constraints on the spatial grid steps for stable and accurate computation, for instance, the relationship to the slowest wave speed in wave propagation modelling (see, Section 3.9). Also, such wavelet-scale adaptivity can not be applied properly when the target vector has a broad frequency content, e.g., a wavefield composed by various scattering waves.

Another important aspect is that a wavelet scheme can represent the action of operators with high accuracy and stability through a projection technique on to wavelet-based subspaces with compact support as a basis (e.g., Daubechies wavelets (Beylkin, 1992), B-spline wavelets (Jameson, 1995)). Especially for time-dependent PDEs (e.g., wave equations), high accuracy in numerical differentiation is essential since this factor is directly related to the confidence of the numerical results and also in the reduction of computational load through implementation of larger spatial grid steps and larger time steps (see, Section 3.9). For this purpose, the Fourier method (Kosloff & Baysal, 1982) which can in principle achieve high accuracy in numerical differentiation has been introduced in seismological modelling studies. However, the Fourier method often runs into difficulties in incorporating physical boundary conditions (e.g., vanishing tractions). The Chebyshev-pseudospectral method (Kosloff *et al.*, 1990; Carcione, 1994) could reduce such problems by introducing a Chebyshev method for the vertical derivatives needed in the boundary condition.

We show that a wavelet-based method can give not only high accuracy in numerical differentiation, but also a flexible implementation of physical boundary conditions in the modelling of acoustic and elastic wave propagation. We exploit the use of a non-standard form (*NS*-form) of matrix representation based on the work of Beylkin (1992, 1993), with an extension to separable multi-dimensional operators.

1.2 Methods for modelling of wave propagation

A number of different methods have been applied to the numerical simulations of wave propagation in general complex media, such as finite difference, pseudospectral and spectral element methods. The finite difference method (FDM) has a long history in numerical modelling of wave propagation, and has been steadily improved (e.g., Kelly *et al.*, 1976; Virieux, 1986; Bayliss *et al.*, 1986, Graves, 1996; Moczo *et al.*, 2000) with implementation to various studies (e.g., Frankel & Clayton, 1986; Yomogida & Etgen, 1993; Frankel, 1993) since the method is comparatively easy for code development and needs relatively small computer memory. However, the FDM has difficulty in treating a free surface with topography or internal irregular boundaries (e.g., Moczo *et al.*, 1997; Moczo, 1998); in order to treat this sort of problem, a hybrid technique implementing additional favorable method (e.g., finite element method) supplementarily has been introduced (see, Moczo *et al.*, 1997). Also, FDM has a tendency that numerical errors are accumulated across the grid during computation.

The pseudospectral method (Augenbaum, 1992; Kosloff *et al.*, 1990) based on Chebyshev expansions can provide higher accuracy spatial differentiation than simple FDM by using a series of global, infinitely differentiable basis functions. Also, this method distributes the error throughout the whole domain unlike the usual grid-based methods such as FDM. This style of computation can achieve good results with fewer grid points per wavelength than FDM, but care needs to be taken to avoid grid dispersion from the implementation of the nonuniform sampling grid system for the collocation points of the basis functions.

The spectral element method (SEM) has been introduced relatively recently for the modelling of elastic wave propagation (Faccioli *et al.*, 1996; Komatitsch & Vilotte, 1998). By including both the boundary conditions and force terms in a variational form of the governing equations and using element interaction, the SEM satisfies the free surface boundary condition implicitly and thereby avoids the complications for the implementation of boundary conditions encountered in other methods. Generally, the SEM can generate accurate modelling for most solid elastic media. However, for a fluid-solid layered medium problem, the method needs a special formulation of governing equations in terms of displacements in the solid region and velocity potential in the fluid region, and an explicit conditional time stepping should be applied (see, Komatitsch *et al.*, 2000) for stable and accurate modelling. Therefore, the SEM computational procedure becomes more complex and is difficult to use for such cases as random media, the presence of a fluid-filled cavity or an inhomogeneous fluid layer. We note that FDM also has some difficulty in treatment of liquid-solid interfaces and therefore needs special computational boundary conditions at the interfaces (see, Stephen *et al.*, 1985).

In seismological studies, the complexity of earth processes leads to the need for stable and accurate modelling of elastic wave propagation media with randomly distributed cavities (or, cracks) or in stochastic random heterogeneous media. However, existing methods have some limitations in the treatment of such media. The FDM can not generate an accurate response for a medium with highly varying physical parameters because of the limited accuracy of differentiation and strong numerical dispersion. Also, the Chebyshev-pseudospectral method has a difficulty in treatment of random heterogeneity inside a medium due to its uneven grid steps. In the same way, it is difficult to design a mesh for stochastic heterogeneous media for SEM and also difficult to implement the presence of fluid-filled cavities.

So, for the treatment of complex media, several techniques have been introduced. A boundary integral method has been implemented for modelling in media with randomly distributed cavities (Yomogida & Benites, 1995). Such boundary integral methods can deal well with heterogeneities inside a medium with irregular interfaces (e.g., cavities, cracks). The boundary conditions are satisfied by including effective sources at the boundaries at each time step. For a homogeneous background medium it is possible to get an accurate time response because the necessary Green's functions can be found analytically. However, it is difficult for the method to be applied to media with heterogeneous backgrounds (including layered media) because the Green's functions themselves need to be found numerically. Recently, the generalized screen propagators (GSP) method has been developed as a fast computational procedure for modelling of elastic wave propagation in half spaces with small-scale heterogeneities (Wu *et al.*, 2000). However, the approach used in the GSP method ignores the backscattering process and so is not suitable for full representation of scattered waves. In this circumstance, we develop a wavelet-based method for a stable and accurate computation in general complex media.

1.3 Development of a wavelet approach for wave propagation

In order to develop a wavelet-based method, some major obstacles need to be solved. The first is to find how the wave equation can be represented in a discretized time form. The second is to implement the boundary conditions such as absorbing boundary conditions and traction-free boundary conditions. The third is a way to consider topography problems.

For the discretized form, we adapt the approach introduced by Beylkin & Keiser (1997) for parabolic PDEs to the wave equation system by rewriting the governing equations in the form of a set of equations involving first-order derivatives in time. This can be achieved by working in terms of displacements and velocities with a consequent reduction in memory of about 30% compared to the more common velocity-stress formulation (e.g., Virieux, 1986; Carcione, 1994; Komatitsch & Vilotte, 1998). The time evolution of the differential equations is achieved with an explicit scheme, and a local

Taylor expansion that allows us to make an effective representation of both vector and matrix operators involving spatial derivatives in terms of scalar wavelet components.

Externally imposed boundary conditions such as the termination of a string or the free surface boundary condition of vanishing traction for elastic media need to be incorporated in the wave propagation scheme. We are able to handle such conditions with the use of equivalent force systems applied at the material boundaries. For the implementation of absorbing boundary conditions, artificial attenuation is considered at the boundaries of a domain by including attenuation terms in the governing equations.

Topography problems can be considered using a grid-mapping technique which maps a rectangular grid system to a curved grid system corresponding to the topography.

1.4 Modelling in complex media and seismic quantitative studies

High-frequency seismic waves propagating in the crust are affected by heterogeneities and anisotropy, and the seismic attenuation from the scattering and the anelastic energy dissipation is a well-known feature associated with wave propagation in the earth. However, it has been often reported that the scattering attenuation is the dominant factor in seismic attenuation in the crust (e.g., Hatzidimitriou, 1994; Del Pezzo *et al.*, 1995). Thus, understanding scattering attenuation is a way to comprehend the general seismic attenuation in the crust.

Numerical modelling allows an investigation of seismic responses under specific controlled conditions and thus has been widely implemented for scattering studies. In particular, theoretical scattering attenuation variation can be verified through comparisons with the numerical results. For this purpose, it is essential that the numerical technique should generate accurate and stable time responses in complex media. The correct measurement is particularly required for the determination of the 'minimum scattering angle' in the theoretical expressions based on the first-order Born approximation, which is used for the correction of the travel-time shift in time responses. Finite difference methods have been popularly implemented for the modelling in stochastic random media (Frankel & Clayton, 1986; Jannaud *et al.*, 1991; Roth & Korn, 1993; Frenje & Juhlin, 2000), but different scattering attenuation rates are reported with the variation of the perturbation rate of medium even among studies based on the finite difference methods. It appears that the finite difference methods can lose energy artificially when the perturbation rate is large, due to the numerical limitation based on a grid representation. An accurate and stable numerical technique is required for the studies, and so the wavelet-based method is introduced.

Although studies on scattering in 3-D spaces are desirable, it is difficult to measure energy loss accurately due to the refraction and the wavetype coupling in elastic waves. But, it has been reported that 2-D and 3-D scattering patterns are quite similar each other (Frenje & Juhlin, 2000), and also comparisons between numerical and theoretical results are relatively easy in 2-D problems. There are theoretical attenuation expressions for 2-D or 3-D scalar waves (Frankel & Clayton, 1986; Frenje & Juhlin, 2000) and those for 3-D elastic waves (Sato & Fehler, 1998). For 2-D elastic waves, Fang & Müller (1996) have introduced a hybrid technique combining the theoretical attenuation expressions for scalar (Frankel & Clayton, 1987) and acoustic waves (Roth & Korn, 1993). This hybrid technique is based on the assumption that scattering attenuation of acoustic and elastic waves are identical, but this assumption appears to be invalid at some cases. Therefore, an appropriate theoretical attenuation expression needs to formulated for 2-D elastic waves in order to compare with numerical results and this is presented in Chapter 7.

Scattering attenuation rates of elastic waves have been reported at numerous places (e.g., Hatzidimitriou, 1994; Del Pezzo *et al.*, 1995), but there are few trials to explain the results in terms of characteristic stochastic random heterogeneities. Using the theoretical attenuation expressions, the random heterogeneities at specific region can be resolved.

Limitations in current numerical modelling techniques have lead to the development of semi-analytic approaches (e.g., boundary integral method) for modelling in random media composed of heterogeneities with high impedance. Such random media are considered as an alternative representation for random heterogeneities (Benites *et al.*, 1992). However, these semi-analytic techniques have difficulty for modelling in inhomogeneous media (e.g., layered media) or in media with filled cavities due to the difficulty in the generation of the Green's function and the specifications of the boundary conditions. A general modelling technique is required for such complex media and the wavelet-based method can be applied in many circumstances. For the comparisons with numerical results, theoretical attenuation expressions are also required to be formulated. Such comparisons of scattering patterns between stochastic random media and random cavity media should allow suitable representations for the heterogeneities in the earth.

1.5 The scope of this thesis

The main emphasis of this thesis is placed on the development of a novel wavelet-based technique for the modelling of wave propagation and the display of the potential of the new technique by applying it to challenging problems. In particular, tests for complex media are extensive to ensure if the technique can be applied to more general complex-structured media.

Chapter 2 describes wavelet techniques used in numerical studies and introduces the idea of a wavelet-based method for wave propagation modelling. The basic theories for the representation of differential operators in wavelet bases and a technique to generate discrete time solutions for a simple 1-D scalar wave equation are discussed. Through modelling for this simple problem, we discuss the characteristics of the wavelet-based method and suggest a way to treat inherently periodic boundary conditions.

In Chapter 3, we extend the wavelet-based method to elastic wave modelling problems. The formulation of the elastic equation system and treatment of boundary conditions (absorbing and traction-free) are presented, and the wavelet technique is tested in simple problems where analytic solutions exist, with comparison of the numerical results and the analytic solutions. We also consider the numerical aspects (e.g., stability condition, computation time) of the implementation of the wavelet-based method.

In Chapter 4, the wavelet-based method is applied to modelling of heterogeneous media. In order to test the capacity of the method we introduce challenging problems (e.g., media with fluid-solid configuration, media with a fluid-filled crack, random heterogeneous media) where other methods encounter difficulty. Further, the technique is extended to transversely isotropic media.

In Chapter 5, the wavelet-based method is expanded to treat topography problems. Using a grid-mapping technique, the wavelet method can consider the topographic variation exactly and this approach is validated by comparisons between numerical solutions and analytic solutions for simple topography problems. The high stability of the wavelet method is tested for sinusoidal topography problems with increasing topography variation.

In Chapter 6, the wavelet-based method is applied to modelling in tectonic regions. For these applications, the wavelet method is expanded so that it can be implemented directly with heterogeneous source regions, and this new scheme is validated through comparisons of time responses. The wavelet-based method allows modelling with complicated source time function in complex media, including the investigation of trapped waves in fault gouge zones and wave-guide effects in subduction zones.

High stability and accuracy enables the wavelet-based method to be employed for quantitative studies of seismic wave propagation. In Chapter 7, we show the use of the wavelet-based method as a simulator for random heterogeneous media by comparing the accuracy in differentiation of highly varying signals corresponding to physical properties of random media and showing the stability in highly perturbed media. Scattering attenuation rates are estimated from numerical time responses and compared with theoretical attenuation curves based on the first-order Born approximation, to determine minimum scattering angles. Finally, the ratios of scattering attenuation rates for *P* and *S* waves in stochastic random media are computed, and a possible representation for random heterogeneities in the crust is discussed.

In Chapter 8, we investigate a comparison of the scattering patterns and attenuation rate variations for acoustic and *SH* waves in order to resolve effects of physical-parameter perturbation. Without consideration of the characteristics of elastic waves (e.g., wavetype coupling at a boundary), we directly compare the acoustic scattering with the *SH* scattering.

In Chapter 9, the wavelet-based method is applied to modelling of elastic waves in media with randomly distributed fluid-filled cavities. The wavelet-based method generates stable and accurate responses for such random media, which can be considered as an alternative representation of the random heterogeneities in the earth. Results for the variation of theoretical attenuation are also formulated and compared with the numerical results. We discuss the difference in the scattering patterns and attenuation variations relative to those of the stochastic random media.

Finally, in Chapter 10, we summarise the thesis, and discuss possible future avenues for research and the prospects for the wavelet-based method.

1.6 Published materials in the thesis

Materials in Chapters 2, 3, 4 and 5 have been published in two articles;
Hong & Kennett (2002), A wavelet-based method for simulation of two-dimensional elastic wave propagation, *Geophys. J. Int.*, **150**, 610-638, and
Hong & Kennett (2002), On a wavelet-based method for the numerical simulation of wave propagation, *J. Comput. Phys.*, **183**, 577-622.

Materials in Chapter 6 will be published in
Hong & Kennett (2003), Modelling of seismic waves in heterogeneous media using a wavelet-based method: application to fault and subduction zones, *Geophys. J. Int.*, (in press).

Materials in Chapter 7 have been introduced in two articles;
Hong & Kennett (2003), Scattering attenuation of 2D elastic waves: theory and numerical modeling using a wavelet-based method, *Bull. seism. Soc. Am.*, **93** (2), 922-938, and
Hong (2003), Scattering attenuation ratios of *P* and *S* waves in elastic media, *Geophys. J. Int.*, (submitted).

Materials in Chapter 9 have been introduced in an articles;
Hong & Kennett (2003), Scattering of elastic waves in media with a random distribution of fluid-filled cavities: theory and numerical modelling, *Geophys. J. Int.*, (submitted).

2

Extension of wavelets to numerical modelling: theory and test

2.1 Overview of wavelets

The use of synthetic seismograms is one of the most useful methods for estimating the seismic response of media at a given receiver. Various numerical approaches have been proposed to solve the elastic wave equations. For problems related to stratified media, the reflectivity method (Kennett, 1983) provides a useful mean of modelling the seismic response out to large distances. By taking a Fourier transform with respect to time and introducing a composite use of a Hankel transform and Fourier transform to horizontal components, Kennett (1983) recast the elastic wave equations in terms of a system of first-order differential equations for the vertical direction and then superposed the cylindrical waves in stratified media to determine the response at a receiver.

For more complex media, various methods have been introduced. The finite difference (FD) method (Kelly *et al.*, 1976; Virieux, 1986) is applicable to many problems in simple media because the FD scheme is relatively easy to implement in computer codes and does not requires too much computer time and memory. However, the FD scheme encounters difficulties when it is applied to problems such as laterally heterogeneous media with irregular nonplanar boundaries or media with free surface topography (e.g., Moczo, 1998). Therefore, special care is needed to implement the boundary conditions. Moczo *et al.* (1997) combined finite difference and finite element (FE) methods near the free surface, since it is much easier to satisfy the boundary conditions in the FE scheme. The pseudospectral method based on Chebyshev expansions can provide higher accuracy spatial differentiation than simple FD or FE methods by using a series of global, infinitely differentiable basis functions (Augenbaum, 1992; Kosloff *et al.* 1990). However, this style of pseudospectral method suffers from a nonuniform grid spacing for the collocation points of the basis functions. The nonuniform grid spacing problem requires an increase in the number of grid points to remove grid dispersion and makes it difficult to handle complicated geometries. Recently the spectral element method (SEM) has been introduced for various classes of problem (Faccioli *et al.*, 1996; Komatitsch & Vilotte, 1998; Komatitsch & Tromp, 1999). By including the boundary conditions in a variational form of the governing equations and using element interaction, Komatitsch & Vilotte (1998) satisfied the free surface boundary condition directly and so avoided one of the usual complications in numerical work.

We introduce a wavelet-based method for numerical simulation of elastic wave propagation. In this method we represent the differential operators via multiscale wavelets, and can achieve high accuracy in the spatial representation. The scheme does not require a non-uniform grid as in the Chebyshev implementation of the pseudospectral method and can be adapted to a wide range of media geometries and related phenomenon.

2.1.1 Wavelets

After Daubechies (1992) built the foundation of a discrete wavelet transform scheme, a wide range of numerical methods based on wavelets have been adopted in many areas. The ability of the wavelet transform to resolve features at various scales has made wavelet analysis one of most useful techniques in signal processing, despite its recent development. Anant & Dowla (1997) compared polarization information across a number of scales in determining *P*-phase arrival time, and used amplitude information for the transverse component compared to the radial at different scales in determining *S*-phase. Similar research was done by Tibuleac & Herrin (1999) in a study of *Lg*-phase arrivals using wavelets. Lilly & Park (1995) used multiwavelets to estimate the time-varying spectral density matrix for three-component seismic data. Multiwavelet spectral analysis seeks to minimize the spectral leakage in spectral estimates in a similar way to multitaper spectrum analysis. Another approach in signal processing using multiwavelets is to measure the anisotropy in a given area using the relative phase between components to estimate an average particle motion ellipse for the array (Bear *et al.*, 1999).

The discrete wavelet transform is based on a multiresolution analysis that decomposes a signal into components of different scales. Decomposition at a given scale is done by sampling using a scaling function $\varphi(x)$, and a companion wavelet function $\psi(x)$. The remaining part of the signal is decomposed using successively higher scales of the scaling function. Fig. 2.1 shows one pair of scaling function and wavelets (Daubechies-6 and Daubechies-20) used in discrete analysis. An example of signal decomposition onto a

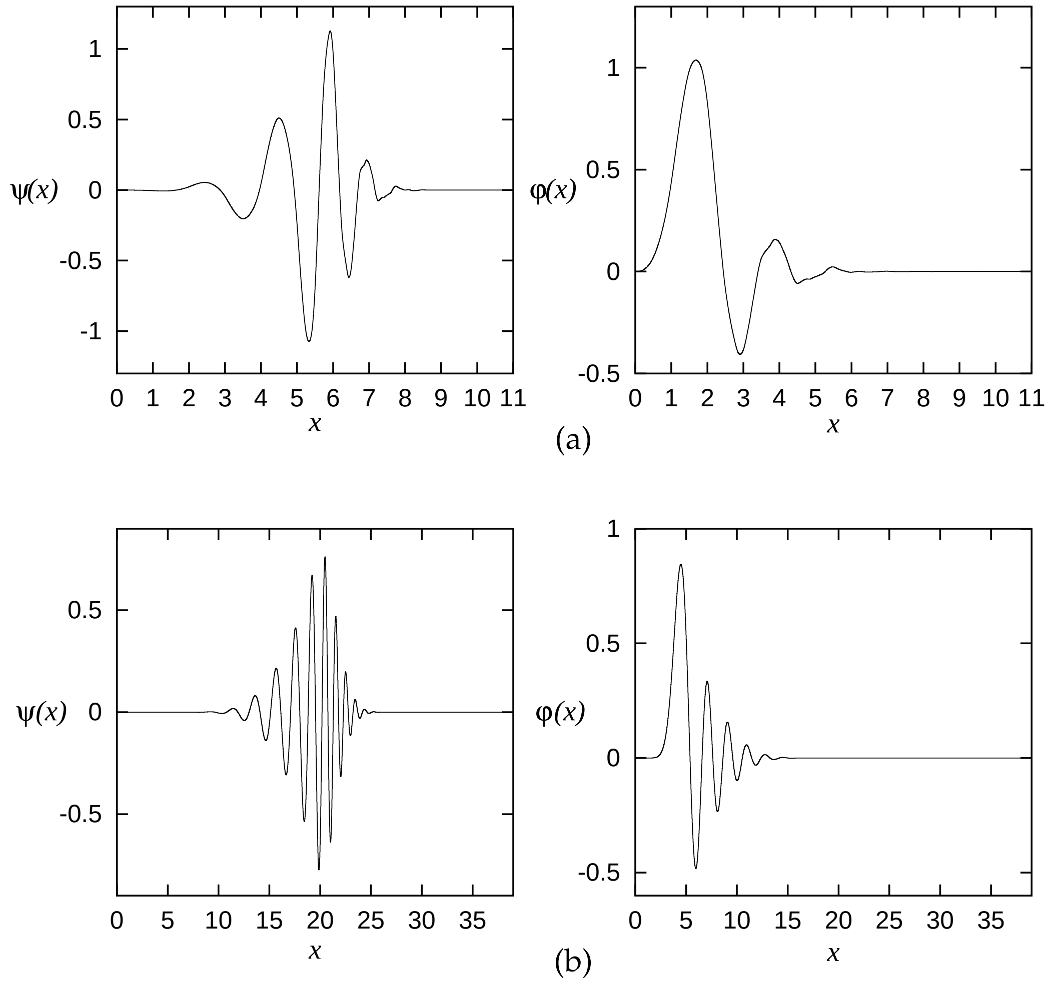

Fig. 2.1. Examples of Daubechies wavelets $\psi(x)$ and its scaling function $\varphi(x)$; (a) Daubechies-6 wavelets and (b) Daubechies-20 wavelets.

wavelet basis is presented in Fig. 2.2. The chirp signal is decomposed by projecting on a set of subspaces (Q_i, P_j) where Q_i represents the projection on the wavelet subspace with scale i and P_j the scaling subspace which the orthogonal complement of a wavelet subspace with a scale j.

The wavelet transform is similar to a Fourier transform in the sense that it maps a time function into a two dimensional function with a scale a and a translation τ that can be compared to frequency ω and a time t. When, however, we use the Fourier transform in the time-frequency analysis of a non-stationary signal in a physical problem, we have two conflicting requirements. The window width T must be long enough to give the desired frequency resolution but must also be short enough so as not to lose the localization in time. A narrow window gives a good time resolution but poor frequency resolution

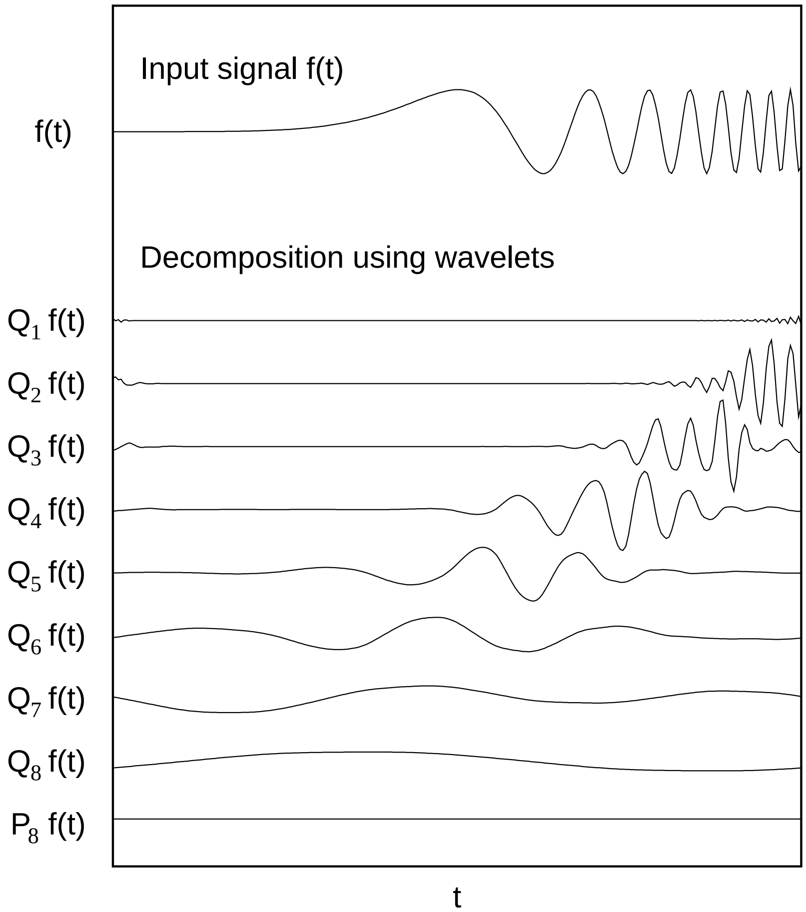

Fig. 2.2. Decomposition of chirp signals using wavelets based on a multiresolution analysis.

because it has an infinite bandwidth. On the other hand, a wide window gives a good localization in frequency but poor time localization because an impulsive response in frequency does not decay rapidly in time. The sinusoid, basis functions which are used in Fourier transform are local in frequency but global in time, and rely on cancellation to represent discontinuities in time (Chan, 1995). Therefore, sinusoids are not efficient in representing functions that have compact support in both time and frequency. However, wavelets are confined in both the frequency and time domains. When we analyze signals at a frequency ω_0 by changing the window width, we can keep the the number of cycles of a basis function constant by using wavelets. The confinement characteristics of wavelets allow an extension to the field of numerical analysis. As shown in Fig. 2.2 a wavelet transform needs only a small number of wavelet subspaces to synthesize a chirp signal, compared to a Fourier transform which would need quite large number of sinusoidal subspaces (basis functions) for such chirp signals.

2.1.2 Wavelets and PDEs

The application of wavelets in numerical analysis can be generally divided into three streams. One is to simplify the governing PDE into a lower order of PDE through a wavelet transform. Lewalle (1998) applied Hermitian wavelets, the derivatives of a Gaussian bell-shaped curve, to a diffusion problem through a canonical transformation and showed a promising development for the numerical prediction of intermittent and nonhomogeneous phenomena. However, this approach has a limitation in the sense that all equations of interest can not be treated with a certain kind of wavelets. Another approach is the composite use of a FD scheme and an interpolating wavelet transform. Holmström (1999) applied the usual techniques to do all operations in the physical representation and used interpolating wavelets to construct and update the representation. With the help of interpolating wavelets, this scheme achieves adaptability in domains by imposing a threshold on the wavelet coefficients. Moreover, the scheme is cheap in computation cost compared to other adaptive methods due to the application of FD technique in obtaining the responses of operators. However, this composite scheme suffers from defects of the usual FD scheme as well. The alternative approach is to apply a wavelet transform to the differentiation of a function. A given operator is decomposed into a wavelet basis and then the action of the operator on a function is computed using a wavelet basis which includes the operator effects (Beylkin, 1992).

Beylkin (1992) computed the non-standard form (*NS*-form) of several basic operators such as derivatives and the Hilbert transform using wavelets. The *NS*-form of operator has an advantage compared with the standard form that we can reduce the effort in applying the operator because *NS*-form of operator is a banded diagonal matrix. Using a *NS*-form of derivative operator and semi-group approach, Beylkin & Keiser (1997) developed an adaptive pseudo-wavelet method for solving nonlinear parabolic partial differential equations (PDEs) in one spatial dimension and time.

The adaptive pseudo-wavelet method is based on a semigroup approach, a well-known analytic tool for expressing the solution of PDEs in terms of nonlinear integral equations by considering a parabolic PDE as complex of linear and nonlinear parts. This wavelet approach combines the desirable features of a FD scheme, spectral methods, and adaptive grid approach. The pseudospectral method is similar to the pseudo-wavelet method in the sense that the evolution equation is split into linear and nonlinear parts and the contribution of each part is added later. We note that a pseudospectral method considers a linear contribution in the Fourier space and a nonlinear contribution in the physical space. Therefore, multiple transforms between spaces are needed to cover the full complex contribution.

We develop a wavelet-based method for wave equations. Using a displacement-velocity formulation and treating spatial derivatives with linear operators, the wave equations are rewritten as a system of equations whose evolution is rewritten as a system of equations whose time dependence is controlled by first-order derivatives. The linear operators for spatial derivatives are implemented in wavelet bases using an operator projection technique with the *NS*-form of wavelet transform. Using a semigroup approach, the discretized solution in time can be represented in an explicit recursive form, based on a Taylor expansion of exponential functions of operator matrices. The boundary conditions are implemented by augmenting the system of equations with equivalent force terms at the boundaries. The wavelet-based method is applied to acoustic wave equations with rigid boundary conditions at both ends in 1-D domain, and the nature of the method is investigated to illustrate the application of the technique.

2.2 Representation of the differential operators in wavelet bases

We have used a representation of the action of differential operators through a wavelet basis based on the work of Beylkin (1992), using Daubechies wavelets (Daubechies, 1992). In this section, we briefly review the ideas for the representation of operators in wavelet bases in non-standard form (*NS*-form; Beylkin, 1992) and set out the notation for the extension of the work. We use the terminology 'matrix operator' for the representation of an operator decomposed using wavelet bases in the form of a matrix, as distinct from an 'operator matrix' (e.g., (3.11)) with an action on a vector in physical space.

In the multiresolution analysis, each scaling subspace $\mathbf{V}_j$ ($j \in \mathbb{Z}$) is contained in spaces on lower scales such as

$$\{0\} \rightarrow \cdots \mathbf{V}_2 \subset \mathbf{V}_1 \subset \mathbf{V}_0 \subset \mathbf{V}_{-1} \subset \mathbf{V}_{-2} \cdots \rightarrow \mathbf{L}^2(\mathbf{R}), \tag{2.1}$$

where $\{0\}$ is a null space and j represents the scale (order) of space. High-frequency features can be resolved better at a space with smaller j. The scaling subspace $\mathbf{V}_j$ can be decomposed into higher wavelet and scaling subspaces ($\mathbf{W}_{j+1}, \mathbf{V}_{j+1}$) using tensor product bases (φ, ψ, e.g., Daubechies wavelets, Fig. 2.1) at scale $j+1$, and thereby the scaling subspace can be decomposed successively up to a null space. Therefore, $\mathbf{L}^2$ space can be represented with a direct sum of wavelet subspaces, and any operator defined in $\mathbf{L}^2$ space can be potentially represented via projections of the operator onto subspaces. Since data (e.g., the displacement field in a domain) have a discrete representation on a domain, the physical (numerical) space need not be an actual $\mathbf{L}^2$ space. We set the physical space to be $\mathbf{V}_0$, and an operator T defined in $\mathbf{L}^2$ space is considered as T_0 in the physical space $\mathbf{V}_0$.

When the operator T_0 is considered through its effects on subspaces up to scale J, the components of the matrix operator in standard wavelet form occur in 'finger' bands due to cross scale projections of an operator among subspaces, even from wavelet subspace to scalar subspace and vice versa (see, Beylkin, 1992). With this form of matrix operator with a dense population of components, the computation cost increases dramatically as the scale J is increased. To reduce this huge computational labour and thereby increase efficiency, Beylkin (1992) has considered an additional projection on to the set of subspaces ($\mathbf{W}_j, \mathbf{V}_j$, $j = 1, 2, \ldots, J$). With this further projection the matrix operator is reformulated as a sparse matrix where the non-zero components form submatrices arranged diagonally. We describe the details of the procedure for formulating matrix operators in *NS*-form in Appendix A.1, and for the application of the matrix operator to a vector in Appendix A.2.

Since scalar differential operators for one-dimensional spaces (Beylkin, 1992) are implemented for the representation of vector (multi-spatial) differential operator (e.g., $\partial_z \partial_x u_x$), the vectors where the operator is applied have a directional character. As shown in Fig. 2.3, by collecting a vector in a given direction (i.e., horizontal direction, pth row; vertical direction, qth row) from a target vector field (e.g., displacement field), we can implement the directionality of the partial differential operators. So, when a operator $\partial_z \partial_x$ is applied to a displacement field u in a two-dimensional space, we apply a derivative operator to a horizontally sampled displacement vector and then a derivative operator to a vertically sampled vector from a $\partial_x u$ field.

During multi-spatial differentiation through successive directed one-dimensional differentiation using wavelets, the size of each side ($x, y, z, \ldots$) of the domain is assumed to be same (namely, $0 < x, y, z, \cdots \leq 1$) regardless of number of data (i.e., grid points) employed. Therefore, a scaling process is needed to maintain the integrity of numerical modelling when there are different physical sizes of the edges of the domain. For example, when a 2-D spatial domain with size ($0 < x \leq 1$, $0 < z \leq 2$) is composed of $N \times M$ grid points and a cross partial differentiation operator $\partial_z \partial_x$ is implemented for a displacement field u, the vectors need to be multiplied by the relative size coefficient r_j (= reference length/j directional length, $j = x, z$) after each directional differentiation (e.g., $r_x = 1$, $r_z = 1/2$). Note that the actual values of N and M (or, grid spatial steps dx and dz) are not significant in this scaling procedure. However, the implementation of large enough N and M to achieve accurate (or, stable) numerical differentiation of

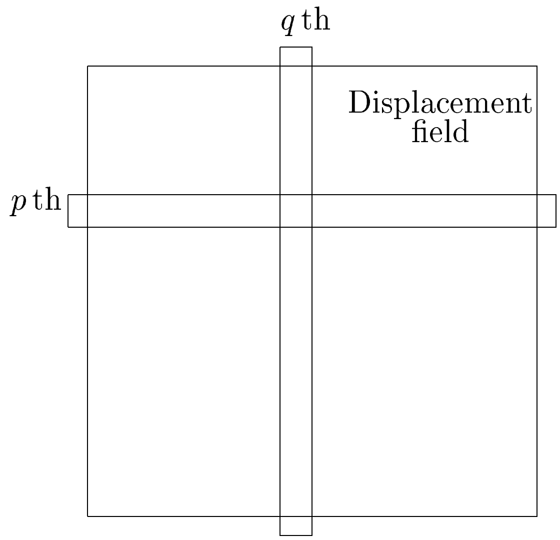

Fig. 2.3. Sampling in a displacement field

vectors is an important point to be considered for the modelling of wave propagation (see, Section 3.9).

2.3 Semigroup approach and discrete time solution

Using a displacement-velocity formulation and considering the time-independent spatial derivatives as linear operators (e.g., $\mathcal{L}$ in (2.8) or $\mathcal{L}_{ij}$ in (3.8)) which consist of an operator matrix (e.g., $\mathbf{L}$ in (2.9) or (3.11)), we can rewrite the wave equations as a first-order PDE system in time. We are then able to adapt the technique of using a semigroup approach in Beylkin & Keiser (1997) for the solution of the equation system.

Now we consider a discrete time solution of a set of first-order PDEs for evolution of a system in time using the semigroup approach. First, we consider a system of PDEs with an unknown $g(x,t)$ depending on the variables (x,t), which is composed of a linear part $\mathcal{L}g$ and a nonlinear 'forcing' term $\mathcal{N}f(g)$. Then

$$\partial_t g = \mathcal{L}g + \mathcal{N}f(g), \tag{2.2}$$

with an initial condition,

$$g(x,0) = g_0(x), \qquad 0 \le x \le 1. \tag{2.3}$$

Here $\mathcal{L}$ is a linear operator, $\mathcal{N}$ is a nonlinear operator and $f(g)$ is a nonlinear function of $g(x,t)$. Using a semigroup approach, the solution of this initial value problem (2.2) can be represented as the sum of an exponential function of the linear operator and a nonlinear integral function in time (see, Belleni-Morante, 1979):

$$g(x,t) = e^{t\mathcal{L}} g_0(x) + \int_0^t e^{(t-\tau)\mathcal{L}} \mathcal{N} f(g(x,\tau))\, d\tau. \tag{2.4}$$

This expression for $g(x,t)$ in (2.4) provides a direct dependence on the initial conditions and provides for the existence and uniqueness of solutions.

When a solution $g(x,t)$ in (2.4) is considered at a discrete time in a numerical computation, the magnitude of the nonlinear integral function in (2.4) is approximated by an estimate based on an asymptotic analysis using the exact values from the linear part. The resultant discretization formula is given by (see, Beylkin *et al.*, 1998)

$$g_{n+1} = e^{\delta t\mathcal{L}} g_n + \delta t \left(\gamma N_{n+1} + \sum_{m=0}^{R-1} \beta_m N_{n-m} \right), \tag{2.5}$$

where the coefficients γ and β_m are functions of $\delta t\mathcal{L}$, γ determines the nature of the scheme (implicit or explicit), β_m controls the order of the quadrature approximation, g_n is a function of $g(x,t)$ at the discrete times $t_n = t_0 + n\delta t$, δt is a time step and N_n is the nonlinear part at t_n. For a given R in (2.5), the order of accuracy is R for an explicit scheme and $R+1$ for an implicit scheme. Since the terms considered at the positions for nonlinear forcing terms in this study (i.e., body force terms and explicit boundary conditions) are independent of unknown variables at previous discrete times, we set $R = 1$ and consider an explicit scheme ($\gamma = 0$) throughout the study.

The operator exponential $e^{\delta t\mathcal{L}}$ in (2.5) can be represented directly by the scheme in Appendix A.1 for 1-D situation with one scalar unknown. When a vector unknown is implemented (e.g., $\mathbf{U}$ in (2.21), (3.10)) through a first-order PDE system for acoustic or elastic wave equations, the exponential is a function of an operator matrix $\mathbf{L}$ and can be represented properly using the scalar wavelet basis by augmenting a Taylor expansion. In acoustic and elastic wave situations we treat the physical boundary conditions by introducing equivalent forces which are not continuous in $\mathbf{L}^2$, due to the spatially localized nature of boundaries on the domain. We introduce both source terms (e.g., body forces) and the equivalent boundary terms by using suitable 'forcing' terms in (2.2). This enables the discrete time solution (2.5) to be used for wave propagation. When various boundary conditions and nonlinear effects are considered at every time step in a domain, the implementation via a set of forcing terms can increase the efficiency of computation and can reduce the numerical instability (e.g., Beylkin *et al.*, 1998).

We discuss detailed schemes for the acoustic and elastic wave equations in Sections 2.4.1 and 3.2.2. Also note that we consider relationships between the truncation order (i.e., the maximum order of term considered) in the Taylor expansion and the discrete time step in Section 3.9.

2.4 Acoustic wave equation

2.4.1 Numerical formulation

First, we consider an acoustic wave equation in one space dimension without any forcing term: for a uniform medium

$$\frac{\partial^2 u}{\partial t^2} = c^2 \frac{\partial^2 u}{\partial x^2}, \tag{2.6}$$

with initial conditions

$$u(x,0) = u_0(x), \quad v(x,0) = v_0(x), \tag{2.7}$$

where c is a wave velocity in a space. $u(x,t)$ and $v(x,t)$ are the components of the displacement and velocity at a point x and time t.

In order to apply the semigroup approach to the wave equation, we rewrite (2.6) as a first-order differential equation system in time

$$\frac{\partial}{\partial t}\begin{pmatrix} u \\ v \end{pmatrix} = \begin{pmatrix} 0 & I \\ \mathcal{L} & 0 \end{pmatrix}\begin{pmatrix} u \\ v \end{pmatrix}, \tag{2.8}$$

where the linear operator $\mathcal{L}$ is $c^2\partial_x^2$. We set the operator matrix $\mathbf{L}$ to be

$$\mathbf{L} = \begin{pmatrix} 0 & I \\ \mathcal{L} & 0 \end{pmatrix}. \tag{2.9}$$

Then through a semigroup approach, we can represent a solution of (2.6) as

$$\begin{pmatrix} u_{n+1} \\ v_{n+1} \end{pmatrix} = e^{\delta t \mathbf{L}}\begin{pmatrix} u_n \\ v_n \end{pmatrix}, \tag{2.10}$$

where u_n is a displacement component at discretized time t_n and v_n a velocity component. $e^{\delta t\mathbf{L}}$ is approximated using a Taylor expansion:

$$e^{\delta t\mathbf{L}} = \mathbf{I} + \delta t\mathbf{L} + \frac{\delta t^2}{2!}\mathbf{L}^2 + \frac{\delta t^3}{3!}\mathbf{L}^3 + \frac{\delta t^4}{4!}\mathbf{L}^4 + \cdots, \tag{2.11}$$

where $\mathbf{I}$ is a 2×2 unit matrix. $\mathbf{L}^n$ with an odd index n can be found from

$$\mathbf{L}^{2j-1} = \mathcal{L}^{j-1}\mathbf{L}, \quad j = 1, 2, \ldots, \tag{2.12}$$

and $\mathbf{L}^n$ with an even index n is

$$\mathbf{L}^{2j} = \mathcal{L}^{j}\mathbf{I}, \quad j = 1, 2, \ldots. \tag{2.13}$$

From (2.10) and (2.11), we can represent the discrete time solutions of (2.6) with a given accuracy in a recursive manner as

$$\begin{pmatrix} u_{n+1} \\ v_{n+1} \end{pmatrix} = \begin{pmatrix} I + \delta t^2\mathcal{L}/2 & \delta t + \delta t^3\mathcal{L}/6 \\ \delta t\mathcal{L} + \delta t^3\mathcal{L}^2/6 & I + \delta t^2\mathcal{L}/2 \end{pmatrix}\begin{pmatrix} u_n \\ v_n \end{pmatrix} + \mathcal{O}(\delta t^4), \tag{2.14}$$

or

$$\begin{pmatrix} u_{n+1} \\ v_{n+1} \end{pmatrix} = \begin{pmatrix} I + \delta t^2 \mathcal{L}/2 & \delta t \\ \delta t \mathcal{L} & I + \delta t^2 \mathcal{L}/2 \end{pmatrix} \begin{pmatrix} u_n \\ v_n \end{pmatrix} + \mathcal{O}(\delta t^3). \tag{2.15}$$

The operator matrix $\mathbf{L}$ in a system of first-order differential equations (2.8) can be represented by eigenvalues (λ_j) and eigenvectors (y_j)

$$\mathbf{L} y_j = \lambda_j y_j, \quad j = 1, 2. \tag{2.16}$$

The eigenvalues λ_j ($j = 1, 2$) of the matrix $\mathbf{L}$ are given by

$$\lambda_1 = c\partial_x, \quad \lambda_2 = -c\partial_x, \tag{2.17}$$

where c is the wave speed.

The stability and stiffness of the equation system (2.8) are related to the eigenvalues λ_j ($j = 1, 2$) of the operator matrix $\mathbf{L}$. For stability, $\lambda_j \leq 1$. Note that a system of first-order differential equations is stiff if at least one eigenvalue has a large negative real part, which causes the corresponding component of the solution to vary rapidly compared to the typical scale of variation displayed by the rest of the solution (see, Hoffman, 1992). The stiffness ratio R_s of an operator matrix $\mathbf{L}$ is given by

$$R_s = \frac{Max|\lambda_j|}{Min|\lambda_j|} = \frac{|c\partial_x|}{|-c\partial_x|} = 1, \tag{2.18}$$

where $j = 1, 2$. As the stiffness ratio is equal to 1, this system of coupled linear differential equations is not stiff. But for numerical stability during modelling, the time step size δt must satisfy the condition (see, Ferziger, 1981)

$$\delta t < \frac{K_a}{Max|\lambda_j|} = \frac{K_a}{c|\partial_x|}, \tag{2.19}$$

where K_a is a constant dependent on the method chosen. Since the operator ∂_x is represented in the form of a matrix (i.e., a matrix operator) in the physical domain, $|\partial_x|$ corresponds to the determinant of the matrix operator. The magnitude of the determinant becomes larger as the grid step (δx) becomes smaller. In other words, the more samples in space are used in the analysis, the smaller time step δt is required.

2.4.2 *Application of the numerical method*

In this section, we consider a boundary value problem for acoustic waves. Such boundary value problems are commonly met in natural problems and only a few cases can be solved analytically. We consider a string which is constrained at both ends with specified initial conditions. In this case the pulse propagates backward with a reversed phase when it meets an end of the string. The boundary conditions are given by

$$u(x_s, t) = 0, \quad u(x_e, t) = 0. \tag{2.20}$$

where x_s is set to be 0 and x_e be 1. We apply a discrete scheme to the governing equations, implementing (2.14) with fourth order accuracy. The boundary conditions at both ends of the string are considered through several different approaches. Then we compare the performance of the schemes by the level of agreement of the results with analytic solutions, expressed using a Fourier basis (see, Powers, 1972).

We introduce three different ways to implement the boundary conditions; direct application to a grid point, direct application on a band of grid points, and via equivalent forces. In principle, one can satisfy the boundary conditions at both end of string by considering those at just one end since the wavelet-based method inherently incorporates a periodic boundary condition. To implement the boundary conditions via additional equivalent force terms in a semigroup approach, we rewrite the governing equations as

$$\partial_t \mathbf{U} = \mathbf{L}\mathbf{U} + \mathbf{N}, \tag{2.21}$$

where $\mathbf{U}$ is a vector unknown composed of the displacement and velocity (u, v), $\mathbf{L}$ is the operator matrix given in (2.9), and the vector for the equivalent force terms $\mathbf{N}$ is

$$\mathbf{N} = \left\{ \sum_{i=1}^{n_b} \delta(x - x_i) \right\} \cdot \begin{pmatrix} -v \\ -\mathcal{L}u \end{pmatrix}, \tag{2.22}$$

where n_b is the number of grid points over which the boundary conditions are to be applied and x_i the corresponding positions. Using the semigroup approach, the general solution $\mathbf{U}(x, t)$ of the first-order PDE system (2.21) is given by

$$\mathbf{U}(x, t) = e^{t\mathbf{L}} \mathbf{U}(x, 0) + \int_0^t e^{\mathbf{L}(t-\tau)} \mathbf{N}(x, \tau)\, d\tau, \tag{2.23}$$

where $\mathbf{U}(x, 0)$ is an initial condition. Therefore, following (2.5), we can obtain the discrete time solution for the general solution (2.23) as

$$\mathbf{U}_{n+1} = e^{\delta t \mathbf{L}} \mathbf{U}_n + \delta t \left(\boldsymbol{\gamma} \mathbf{N}_{n+1} + \boldsymbol{\beta}_0 \mathbf{N}_n \right), \tag{2.24}$$

where $\mathbf{U}_n$ is a vector unknown and $\mathbf{N}_n$ is a vector for equivalent force terms at a discretized time t_n. When $\boldsymbol{\gamma} = 0$ (explicit case), $\boldsymbol{\beta}_0$ is determined as $(e^{\delta t \mathbf{L}} - \mathbf{I})(\delta t \mathbf{L})^{-1}$ and this can be approximated by the Taylor expansion:

$$\boldsymbol{\beta}_0 = \mathbf{I} + \frac{1}{2}\delta t \mathbf{L} + \frac{1}{6}\delta t^2 \mathbf{L}^2 + \frac{1}{24}\delta t^3 \mathbf{L}^3 + \cdots. \tag{2.25}$$

The resultant form for $\boldsymbol{\beta}_0$ is:

$$\boldsymbol{\beta}_0 = -\left\{ \sum_{i=1}^{n_b} \delta(x - x_i) \right\} \cdot \begin{pmatrix} v + \delta t\, \mathcal{L}u/2 + \delta t^2\, \mathcal{L}v/6 + \delta t^3 \mathcal{L}^2 u/24 \\ \mathcal{L}u + \delta t\, \mathcal{L}v/2 + \delta t^2\, \mathcal{L}^2 u/6 + \delta t^3\, \mathcal{L}^2 v/24 \end{pmatrix}. \tag{2.26}$$

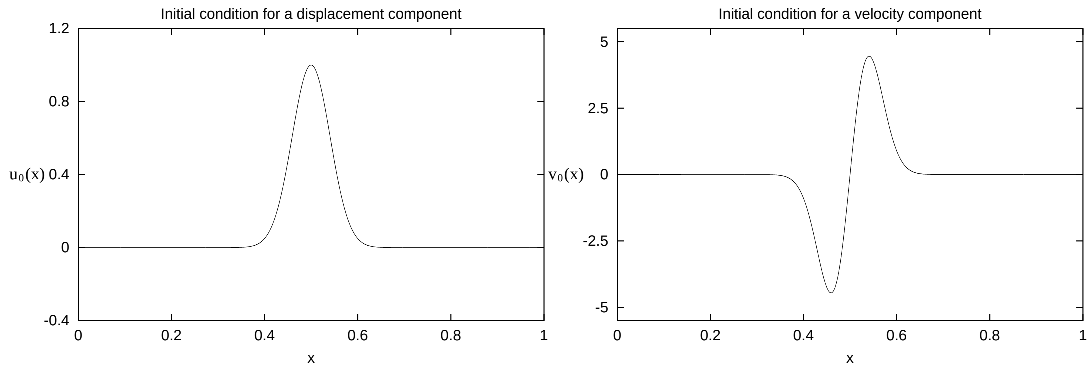

Fig. 2.4. Initial conditions for the displacement component, $u_0(x)$ and the velocity component, $v_0(x)$ for the numerical modelling of acoustic wave propagation in a 1-D space.

2.4.3 *Acoustic wave propagation*

We consider acoustic wave propagation in one space dimension using the scheme developed in Sections 2.4.1 and 2.4.2.

The domain is split into 128 grid points and the both ends of domain are considered as rigid boundaries. As a solution of the wave equation (2.6) takes the form $f(x-ct)$, we set the initial conditions as

$$f(x-ct) = e^{-300(x-0.5-ct)^2}, \quad 0 < x \leq 1, \tag{2.27}$$

and then initial conditions $u_0(x)$ and $v_0(x)$ are $f(x-ct)$ and $-cf'(x-ct)$ at $t=0$ (Fig. 2.4). In this application we set the wavespeed c to be 0.302.

We attempt to satisfy the rigid boundary condition at both ends using three different approaches and compare the results with analytic solutions. The first approach is to set displacement and velocity at one end of string to be zero (namely, $u(1) = v(1) = 0$) directly in the computation procedure. The second is to introduce the artificial extension of the boundaries of the domain (i.e., $0 < x \leq 1 + b_w$) where b_w is a band width corresponding to a rigid strip, and then displacement and velocity in these regions are set to be null (i.e., $u(x_j) = v(x_j) = 0$, $j = n, n+1, \ldots, m$ where $x_n = 1$, $x_m = 1 + b_w$). The third is to implement equivalent force terms (2.22) explicitly at the artificial boundary region while applying a semigroup approach.

The analytic solutions $u(x,t)$ ($0 \leq x \leq l$) of boundary value problem can be obtained using Fourier series as

$$u(x,t) = \sum_{n=1}^{\infty} \sin \lambda_n x \cdot (a_n \cos \lambda_n ct \ + \ b_n \sin \lambda_n ct), \tag{2.28}$$

where a_n and b_n are determined by the initial values of the displacement and velocity components ($u_0(x)$, $v_0(x)$):

$$a_n = \frac{2}{l}\int_0^l u_0(x)\sin\left(\frac{n\pi x}{l}\right)\,dx,$$
$$b_n = \frac{2}{n\pi c}\int_0^l v_0(x)\sin\left(\frac{n\pi x}{l}\right)\,dx. \tag{2.29}$$

l is the length of the domain and $\lambda_n = n\pi/l$. In this case, l is 1.

Fig. 2.5 shows comparisons between the numerical results and analytic solutions at times $t = 1, 6, 29$ s. When the boundary condition is considered at just a single grid point of the string, the energy in the waves leaks and the amplitude of reflected main phase is gradually reduced, while the spurious waves from energy leakage become larger as the number of reflections from the boundaries increases. Physically, the modelled string corresponds to successive strings having their own initial conditions, which are connected at the constraint points in a chain due to inherent periodic boundary condition of the wavelet method. Therefore, this point-wise constraint can not represent properly the physical rigid boundary. The use of a rigid strip (5 grid points in this study) in the other two cases, can reproduce the physical boundary effects well by isolating the system satisfactorily and exhibits a good agreement with the analytic solution. The technique using equivalent forces for the treatment of the boundary conditions not only produces accurate numerical results, but also fits directly into the semigroup scheme with consequent gains in the simplicity of the code by division into a main procedure and force effects. Therefore, the technique can be used efficiently for problems with complex boundary conditions to be implemented during main computational procedure. We implement this technique using equivalent forces in elastic wave problems to treat traction-free boundary conditions on a free surface.

2.5 Discussion

We have introduced a wavelet-based method for the 1-D homogeneous acoustic wave equation in order to quantify its own characteristics before extension to elastic wave equations.

Through a displacement-velocity formulation, the wave equation is recast as a first-order partial difference equation system in time, and spatial derivatives are treated as linear operators. Discrete time representations are obtained from a semigroup approach applied to a system of first-order partial differential equations in time. The numerical solution uses a recursive explicit scheme, derived from a Taylor expansion for the exponential of matrix operator.

Explicit boundary conditions (e.g., rigid boundary conditions) were implemented

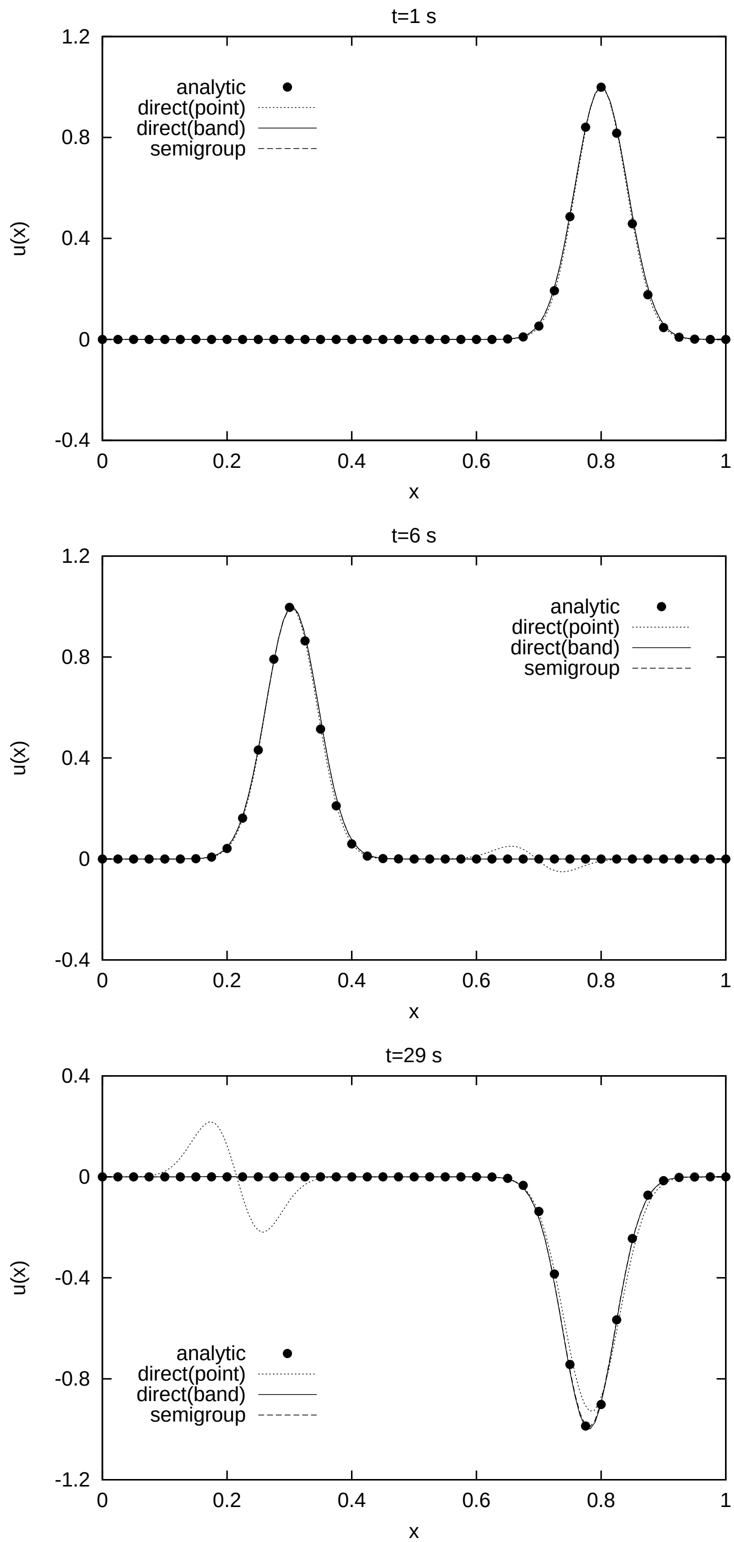

Fig. 2.5. Comparison among various numerical results with analytic solutions for the acoustic wave propagation in a 1-D space.

through equivalent force terms. As periodic boundary conditions are introduced intrinsically at the artificial boundaries in the wavelet-based method, we had to find ways to implement physical boundary conditions without producing spurious effects. When rigid boundary conditions are considered at both ends of the 1-D spatial domain, we need to apply the boundary conditions over an artificial extension of the medium with a band of grid points, considering both wave length and wave speed, to achieve sufficient accuracy. With a proper treatment of the boundary conditions, numerical results exhibit good matches to the analytic solutions.

3

A wavelet-based method for modelling of elastic wave propagation

3.1 Introduction

The wavelet-based technique developed for 1-D scalar waves in Chapter 2 is extended to 2-D elastic wave equations. We rewrite the governing equations as a system of first-order PDEs using a displacement-velocity formulation. With this transformation, we can treat elastic wave equations as a simple system of PDEs using wavelets. Also, the system of PDE using displacement-velocity formulation occupies much less memory during computation than using a velocity-stress formulation.

The implementation of the traction-free boundary condition at a free surface is one of the important issues in the numerical modelling of elastic wave propagation. One of the reasons for using a velocity-stress formulation in most numerical methods comes from the direct relation to the boundary condition.

Generally, three major approaches have been applied to express the presence of a free-surface. One way is to implement stress-free boundary condition at the free surface and satisfy the condition explicitly. Gottlieb *et al.* (1982) showed how to use one-dimensional characteristic variables to enhance the stability of the boundary treatment and Kosloff *et al.* (1990) and Bayliss *et al.* (1986) implemented a traction-free condition by maintaining the magnitude of the outgoing characteristic variables at the boundary. Although this scheme was introduced first by Bayliss *et al.* (1986) for a finite difference method, this approach has proved popular for pseudospectral methods (Carcione, 1994; Tessmer & Kosloff, 1994).

Another approach is to modify the physical parameters (a 'vacuum formalism') and set the elastic wave velocities α, β to zero with the density ρ close to zero above the free surface (Graves, 1996). Since, however, a small value of density above a free surface is considered, the time responses often show grid dispersion at the free surface or the

Rayleigh waves exhibit rather low frequency content due to progressive energy leakage of incident waves into the vacuum layer. To cure this phenomenon, some researchers have introduced a special treatment for the differentiation of the normal stress term at the free surface (Ohminato & Chouet, 1997; Zahradnik, 1995; Moczo *et al.*, 1997).

An alternative is to use an integrated form of the elastodynamic equations namely a 'weak (or, variational) form'. Faccioli *et al.* (1996) and Komatitsch & Tromp (1999) considered a composite form of equations that includes the governing equation and the boundary conditions at the same time by taking the dot product of each term with an arbitrary test function. The 'weak form' approach has advantages that one can consider the effects at the boundaries implicitly, and can overcome the drawbacks in handling nonperiodic boundary conditions when using a Fourier method.

We develop a scheme to express a traction-free condition using displacement variables, not the composite use of velocity and stress variables as in the stress-velocity formulation. Also, the condition is implemented in the system of governing equations as an equivalent force term via a semigroup approach.

We validate the scheme by comparing numerical results with analytic solutions in several simple models, and describe numerical aspects of the wavelet method.

3.2 Formulation of equations

3.2.1 SH waves

When the velocity and density are functions of x and z, the *SH* wave displacement, u_y satisfies the scalar wave equation:

$$\rho \frac{\partial^2 u_y}{\partial t^2} = \frac{\partial}{\partial x}\left(\mu \frac{\partial u_y}{\partial x}\right) + \frac{\partial}{\partial z}\left(\mu \frac{\partial u_y}{\partial z}\right) + f_y, \tag{3.1}$$

where $\rho(x, z)$ is the density, $\mu(x, z)$ is the shear modulus and $f_y(x, z)$ is the body force at a point (x, z). We can simplify and rewrite the governing equation (3.1) by introducing a linear operator $\mathcal{L}_y$ as

$$\frac{\partial^2 u_y}{\partial t^2} = \mathcal{L}_y u_y + \frac{f_y}{\rho}, \tag{3.2}$$

where

$$\mathcal{L}_y = \frac{1}{\rho}\frac{\partial}{\partial x}\left(\mu \frac{\partial}{\partial x}\right) + \frac{1}{\rho}\frac{\partial}{\partial z}\left(\mu \frac{\partial}{\partial z}\right). \tag{3.3}$$

To apply the semigroup approach to a *SH* wave equation, we rewrite (3.2) using a relationship between displacement (u_y) and velocity (v_y) of the *SH* wave as a first-order

PDE system:

$$\begin{aligned}
\frac{\partial u_y}{\partial t} &= v_y, \\
\frac{\partial v_y}{\partial t} &= \mathcal{L}_y u_y + \frac{f_y}{\rho}.
\end{aligned} \tag{3.4}$$

We consider the variables, u_y and v_y as components of a vector variable $\mathbf{U}$ and the nonlinear term f_y/ρ as a component of a force vector $\mathbf{F}$. The other component in $\mathbf{F}$ is set to zero following (3.4). The linear operator matrix $\mathbf{L}$ consists of a linear operator $\mathcal{L}_y$, the identity term I and zeros.

For stability of the numerical computation around the source, we divide the medium into a source region and the remaining main region. We assume that the source region is a homogeneous and elastic medium. As a force vector $\mathbf{F}$ is considered only in the source region, the procedures for applying the semigroup approach are different for the two regions and will be discussed in following sections.

3.2.2 *P-SV waves*

We consider the elastic wave equations for two space dimensions, which include body force terms and boundary conditions with compounds of spatial derivative terms. The partial differential equations describing *P-SV* wave propagation in 2-D media are given by

$$\begin{aligned}
\frac{\partial^2 u_x}{\partial t^2} &= \frac{1}{\rho}\left(\frac{\partial \sigma_{xx}}{\partial x} + \frac{\partial \sigma_{xz}}{\partial z} + f_x\right), \\
\frac{\partial^2 u_z}{\partial t^2} &= \frac{1}{\rho}\left(\frac{\partial \sigma_{xz}}{\partial x} + \frac{\partial \sigma_{zz}}{\partial z} + f_z\right),
\end{aligned} \tag{3.5}$$

where (u_x, u_z) is the displacement vector and $(\sigma_{xx}, \sigma_{xz}, \sigma_{zz})$ are elements of the stress tensor. The stress components σ_{xx}, σ_{xz}, σ_{zz} are expressed using compounds of spatial derivatives of displacement components as

$$\begin{aligned}
\sigma_{xx} &= (\lambda + 2\mu)\frac{\partial u_x}{\partial x} + \lambda\frac{\partial u_z}{\partial z}, \\
\sigma_{zz} &= \lambda\frac{\partial u_x}{\partial x} + (\lambda + 2\mu)\frac{\partial u_z}{\partial z}, \\
\sigma_{xz} &= \mu\left(\frac{\partial u_x}{\partial z} + \frac{\partial u_z}{\partial x}\right),
\end{aligned} \tag{3.6}$$

where $\lambda(x, z)$ and $\mu(x, z)$ are the Lamè coefficients.

The right-hand sides of equation (3.5) can be simplified by introducing linear operators $\mathcal{L}_{ij}$ ($i, j = x, z$) whose effects can be estimated in physical space by the representation of the operators on wavelet bases. The elastic wave equations in (3.5) are recast as second-order differential equations in time:

$$\begin{aligned}
\frac{\partial^2 u_x}{\partial t^2} &= \mathcal{L}_{xx} u_x + \mathcal{L}_{xz} u_z + \frac{f_x}{\rho}, \\
\frac{\partial^2 u_z}{\partial t^2} &= \mathcal{L}_{zx} u_x + \mathcal{L}_{zz} u_z + \frac{f_z}{\rho},
\end{aligned} \tag{3.7}$$

where the linear operators $\mathcal{L}_{ij}$ $(i, j = x, z)$ are:

$$\begin{aligned}
\mathcal{L}_{xx} &= \frac{1}{\rho}\frac{\partial}{\partial x}\left[(\lambda + 2\mu)\frac{\partial}{\partial x}\right] + \frac{1}{\rho}\frac{\partial}{\partial z}\left[\mu\frac{\partial}{\partial z}\right], \\
\mathcal{L}_{xz} &= \frac{1}{\rho}\frac{\partial}{\partial x}\left[\lambda\frac{\partial}{\partial z}\right] + \frac{1}{\rho}\frac{\partial}{\partial z}\left[\mu\frac{\partial}{\partial x}\right], \\
\mathcal{L}_{zx} &= \frac{1}{\rho}\frac{\partial}{\partial x}\left[\mu\frac{\partial}{\partial z}\right] + \frac{1}{\rho}\frac{\partial}{\partial z}\left[\lambda\frac{\partial}{\partial x}\right], \\
\mathcal{L}_{zz} &= \frac{1}{\rho}\frac{\partial}{\partial x}\left[\mu\frac{\partial}{\partial x}\right] + \frac{1}{\rho}\frac{\partial}{\partial z}\left[(\lambda + 2\mu)\frac{\partial}{\partial z}\right].
\end{aligned} \tag{3.8}$$

To apply the semigroup approach to the elastic wave equations and thereby obtain the discrete time solutions, we rewrite (3.7) as a system of first-order differential equations by introducing additional unknowns for the velocity components. The resultant system of first-order PDEs for the displacement-velocity formulation is:

$$\begin{aligned}
\frac{\partial u_x}{\partial t} &= v_x, \\
\frac{\partial v_x}{\partial t} &= \mathcal{L}_{xx} u_x + \mathcal{L}_{xz} u_z + \frac{f_x}{\rho}, \\
\frac{\partial u_z}{\partial t} &= v_z, \\
\frac{\partial v_z}{\partial t} &= \mathcal{L}_{zx} u_x + \mathcal{L}_{zz} u_z + \frac{f_z}{\rho},
\end{aligned} \tag{3.9}$$

where v_j $(j = x, z)$ is the velocity component in j direction. Following the acoustic wave case, the system of equations in (3.9) can be written as a first-order differential equation with a vector unknown $\mathbf{U}$:

$$\partial_t \mathbf{U} = \mathbf{L}\mathbf{U} + \mathbf{F}, \tag{3.10}$$

where $\mathbf{U}$ is $(u_x, v_x, u_z, v_z)^{\mathrm{t}}$ and $\mathbf{F}$ is composed of directional forces as $(0, f_x/\rho, 0, f_z/\rho)^{\mathrm{t}}$. The operator matrix $\mathbf{L}$ is given by

$$\mathbf{L} = \begin{pmatrix} 0 & I & 0 & 0 \\ \mathcal{L}_{xx} & 0 & \mathcal{L}_{xz} & 0 \\ 0 & 0 & 0 & I \\ \mathcal{L}_{zx} & 0 & \mathcal{L}_{zz} & 0 \end{pmatrix}. \tag{3.11}$$

3.3 Implementation technique

3.3.1 Source region

If we use the heterogeneous-media scheme for wavelets directly in the source region, we often have unstable results due to the multiple differentiation of the delta function representing a point (or, line) source. Therefore, we assume that the source region is homogeneous and apply a homogeneous-medium scheme around the source region. In this case, the linear operators $\mathcal{L}_{ij}$ $(i, j = x, z)$ in (3.8) can be rewritten by

$$\begin{aligned}
\mathcal{L}^h_{xx} &= \frac{\lambda + 2\mu}{\rho}\frac{\partial^2}{\partial x^2} + \frac{\mu}{\rho}\frac{\partial^2}{\partial z^2}, \\
\mathcal{L}^h_{xz} &= \mathcal{L}^h_{zx} = \frac{\lambda + \mu}{\rho}\frac{\partial^2}{\partial x \partial z}, \\
\mathcal{L}^h_{zz} &= \frac{\mu}{\rho}\frac{\partial^2}{\partial x^2} + \frac{\lambda + 2\mu}{\rho}\frac{\partial^2}{\partial z^2},
\end{aligned} \tag{3.12}$$

and $\mathcal{L}_y$ in (3.3) is simplified to

$$\mathcal{L}^h_y = \frac{\mu}{\rho}\frac{\partial^2}{\partial x^2} + \frac{\mu}{\rho}\frac{\partial^2}{\partial z^2}. \tag{3.13}$$

The superscript h is added to the linear operators for the homogeneous case to distinguish them from the more general ones. Equations (3.4) and (3.9) can be expressed in first order differential equation form as

$$\partial_t \mathbf{U} = \mathbf{L}_h \mathbf{U} + \mathbf{F}, \tag{3.14}$$

where $\mathbf{L}_h$ is the matrix operator for a homogeneous medium and $\mathbf{F}$ is a force term vector. For the *SH* wave case, $\mathbf{U}$, $\mathbf{L}_h$, $\mathbf{F}$ are given by

$$\mathbf{U} = \begin{pmatrix} u_y \\ v_y \end{pmatrix}, \quad \mathbf{L}_h = \begin{pmatrix} 0 & I \\ \mathcal{L}^h_y & 0 \end{pmatrix}, \quad \mathbf{F} = \frac{1}{\rho}\begin{pmatrix} 0 \\ f_y \end{pmatrix}, \tag{3.15}$$

and for the *P-SV* wave case,

$$\mathbf{U} = \begin{pmatrix} u_x \\ v_x \\ u_z \\ v_z \end{pmatrix}, \quad \mathbf{L}_h = \begin{pmatrix} 0 & I & 0 & 0 \\ \mathcal{L}^h_{xx} & 0 & \mathcal{L}^h_{xz} & 0 \\ 0 & 0 & 0 & I \\ \mathcal{L}^h_{zx} & 0 & \mathcal{L}^h_{zz} & 0 \end{pmatrix}, \quad \mathbf{F} = \frac{1}{\rho}\begin{pmatrix} 0 \\ f_x \\ 0 \\ f_z \end{pmatrix}, \tag{3.16}$$

where (v_x, v_z) is a velocity vector. Following the scheme in Section 2.3, we can write an explicit discrete time solution as

$$\mathbf{U}_{n+1} = e^{\delta t \mathbf{L}_h}\mathbf{U}_n + \delta t \boldsymbol{\beta}_0 \mathbf{F}_n, \tag{3.17}$$

where $\mathbf{F}_n$ is a force vector at a discretized time t_n and $\boldsymbol{\beta}_0$ is given by $(e^{\delta t \mathbf{L}_h} - \mathbf{I})(\delta t \mathbf{L}_h)^{-1}$ (see Beylkin *et al.*, 1998). $e^{\delta t \mathbf{L}_h}$ and $\boldsymbol{\beta}_0$ can be approximated by a Taylor expansion:

$$e^{\delta t \mathbf{L}_h} = \mathbf{I} + \delta t \mathbf{L}_h + \frac{1}{2}\delta t^2 \mathbf{L}_h^2 + \frac{1}{6}\delta t^3 \mathbf{L}_h^3 + \cdots,$$
$$\boldsymbol{\beta}_0 = \mathbf{I} + \frac{1}{2}\delta t \mathbf{L}_h + \frac{1}{6}\delta t^2 \mathbf{L}_h^2 + \frac{1}{24}\delta t^3 \mathbf{L}_h^3 + \cdots. \tag{3.18}$$

3.3.2 *The main region*

We can simulate the remainder of the medium by considering the responses at the source region via boundary conditions. As the body force only needs to be considered in the source region and its effect is transmitted to the main region via boundary conditions, we can omit the source term f_i $(i = x, y, z)$ in the governing equations (3.1) and (3.5). Therefore, the first order differential equation system can be rewritten as

$$\partial_t \mathbf{U} = \mathbf{L}\mathbf{U}, \tag{3.19}$$

where $\mathbf{L}$ is a 4-by-4 matrix operator in a *P-SV* wave problem and is 2-by-2 for a *SH* wave. The linear operators $\mathcal{L}_y$, $\mathcal{L}_{ij}$ $(i, j = x, z)$, the components of $\mathbf{L}$, are given in (3.3) and (3.8). Using a semigroup approach and the discrete representation (2.5), equation (3.19) can be discretized as

$$\mathbf{U}_{n+1} = e^{\delta t \mathbf{L}} \mathbf{U}_n, \tag{3.20}$$

where $e^{\delta t \mathbf{L}}$ is evaluated using a Taylor expansion in (3.18).

3.4 Treatment of boundary conditions

One of difficulties in the numerical simulation of elastic wave propagation is the treatment of the boundary conditions. Two kinds of boundary conditions are usually needed: absorbing boundary conditions and traction-free boundary conditions. Absorbing boundary conditions are introduced to treat the artificial boundaries which are generated due to the confinement (artificial bounds) of the numerical domain. Traction-free boundary conditions are implemented to consider the effect of a free surface. We consider the absorbing boundary conditions intrinsically in a equation system by introducing a new operator matrix including attenuation factors, and the traction-free boundary conditions are implemented via equivalent force terms.

3.4.1 *Absorbing boundary conditions*

In numerical modelling, the occurrence of artificial boundaries is an inevitable limitation. We note that many numerical studies based on wavelets have considered special cases when periodic boundary conditions are applied at those artificial boundaries (e.g., Beylkin & Keiser, 1997). However, for studies of physical transient phenomenon, especially modelling of elastic wave propagation, it is important to design good absorbing boundaries to reduce spurious phenomena. Historically, many studies have concentrated both theoretically and technically on the development of satisfactory absorbing boundary conditions (e.g., Zhang & Ballmann, 1997; Dai *et al.*, 1994; Kosloff & Kosloff, 1986; Sochacki *et al.*, 1987; Shin, 1995; Givoli, 1991; Clayton & Engquist, 1977). However, the explicit implementation of absorbing boundary conditions can sometimes evoke an instability in modelling and result in numerical dispersion (see, Mahrer, 1990) and the absorption rate of waves can be dependent on the incident angle of waves to a boundary (see, Clayton & Engquist, 1977). Moreover, the explicit implementation of absorbing boundary conditions needs additional numerical work on the boundaries with a consequent time cost.

To treat absorbing boundaries in a consistent way, we consider the boundary conditions in the equation system implicitly, by including additional attenuation terms which force the energy of incoming waves to be dissipated during propagation in the absorbing regions (see, Kosloff & Kosloff, 1986, Sochacki *et al.*, 1987). For this purpose, we make attenuation active around the artificial boundaries by assigning non-zero attenuation terms around the boundaries and zero in the main computational domain. The attenuation terms are designed to be bounded, twice differentiable (see, spatial operators $\mathcal{L}_{ij}$) and to have a sufficiently smooth derivative in order to make amplitudes of waves incident on the boundaries reduce gradually and continuously without generation of spurious waves reflected from the attenuation gradients (see, Sochacki *et al.*, 1987).

When we introduce attenuation factors (Q_x, Q_z) into the *P-SV* wave equations, we add an extra first-order time derivative term (e.g., $2Q_x\partial_t u_x$) in governing equation system (3.5) (cf., Sochacki *et al.*, 1987). The governing equation system with attenuation terms can be then written as

$$\begin{aligned} \frac{\partial^2 u_x}{\partial t^2} + 2Q_x\frac{\partial u_x}{\partial t} &= \frac{1}{\rho}\left(\frac{\partial \sigma_{xx}}{\partial x} + \frac{\partial \sigma_{xz}}{\partial z}\right), \\ \frac{\partial^2 u_z}{\partial t^2} + 2Q_z\frac{\partial u_z}{\partial t} &= \frac{1}{\rho}\left(\frac{\partial \sigma_{xz}}{\partial x} + \frac{\partial \sigma_{zz}}{\partial z}\right). \end{aligned} \tag{3.21}$$

In this case, the operator matrix $\mathbf{L}_q$ becomes:

$$\mathbf{L}_q = \begin{pmatrix} 0 & I & 0 & 0 \\ \mathcal{L}_{xx} & -2Q_x & \mathcal{L}_{xz} & 0 \\ 0 & 0 & 0 & I \\ \mathcal{L}_{zx} & 0 & \mathcal{L}_{zz} & -2Q_z \end{pmatrix}. \tag{3.22}$$

In the same way, the *SH* wave equation with $Q_y(x,z)$ is,

$$\frac{\partial^2 u_y}{\partial t^2} + 2Q_y \frac{\partial u_y}{\partial t} = \frac{1}{\rho}\frac{\partial}{\partial x}\left(\mu \frac{\partial u_y}{\partial x}\right) + \frac{1}{\rho}\frac{\partial}{\partial z}\left(\mu \frac{\partial u_y}{\partial z}\right), \tag{3.23}$$

and $\mathbf{L}_q$ is given as

$$\mathbf{L}_q = \begin{pmatrix} 0 & I \\ \mathcal{L}_y & -2Q_y \end{pmatrix}. \tag{3.24}$$

Evaluating $e^{\delta t \mathbf{L}_q}$ by a Taylor expansion, we discretize the first-order differential equation system and the discretized solution of (3.21) is given by

$$\mathbf{U}_{n+1} = \mathbf{U}_n + \delta t\, \mathbf{L}_q \mathbf{U}_n + \frac{1}{2}\delta t^2\, \mathbf{L}_q^2 \mathbf{U}_n + \cdots + \frac{1}{m!}\delta t^m\, \mathbf{L}_q^m \mathbf{U}_n + \mathcal{O}(\delta t^{m+1}). \tag{3.25}$$

The relationship between the time step (δt) and a truncation order (m) implemented in discrete time solution (3.25) is considered in Section 3.9, and the parameters for attenuation terms are considered in Section 3.5. Quantitative analysis of spurious waves generation from artificial boundaries in the implementation of these absorbing boundary conditions, is described in Section 3.6.

3.4.2 Traction-free boundary conditions

Following the explicit implementation procedure for the boundary conditions as in acoustic wave problems, the traction-free boundary conditions are considered via introduction of equivalent force terms.

For a flat free surface normal to the z-axis the traction-free boundary condition in two space dimensions requires the vanishing of both normal and tangential tractions at the free surface ($z = 0$):

$$[\sigma_{iz}]_{z=0} = 0, \qquad i = x, z. \tag{3.26}$$

Since the explicit form of condition is given to 'only' traction terms (σ_{xz}, σ_{zz}), the other variables (e.g., σ_{xx}) on the boundary need to be updated at each discrete time considering the variation of the tractions (cf., Gottlieb *et al.*, 1982; Thompson, 1990). For this purpose, finite difference methods assign values to displacement terms in an artificially extended region above the free surface boundary so that tractions on the boundary can be forced to vanish. In addition, the procedure for numerical differentiation is modified at the free surface to make the other variables balanced during implementation of the boundary conditions (Graves, 1996; Ohminato & Chouet, 1997; Zahradnik, 1995). An alternative technique uses a one-dimensional analysis scheme based on characteristic variables, and sets the outgoing characteristic variables equal to those expected from the numerical scheme when the traction-free condition is satisfied. This approach has been implemented in Chebyshev-pseudospectral methods (e.g., Kosloff *et al.*, 1990; Tessmer *et al.*, 1992; Carcione, 1994) and in the finite difference method (e.g., Bayliss *et al.*, 1986).

3.4.2.1 P-SV waves

With the introduction of the displacement-velocity formulation, which does not assign stress terms as variables explicitly during the computation, we can implement the free surface effects through consideration of the stress variations on the boundary via equivalent forces. The tractions are forced to zero, but we also need to determine the behaviour of σ_{xx}. Since there is a displacement discontinuity at the free surface, the vertical spatial differentiation in σ_{xx} (i.e., $\partial_z u_z$) is replaced through use of the boundary condition, $\sigma_{zz} = 0$. Thus using the expression for $\sigma_{zz} = 0$, the vertical derivative term can be represented by a horizontal derivative term at the free surface:

$$\frac{\partial u_z}{\partial z} = -\frac{\lambda}{\lambda + 2\mu}\frac{\partial u_x}{\partial x}. \tag{3.27}$$

From (3.27), σ_{xx} at the free surface can be expressed as

$$\sigma_{xx}|_{z=0} = \frac{4\mu(\lambda+\mu)}{(\lambda+2\mu)}\frac{\partial u_x}{\partial x}. \tag{3.28}$$

Note that the expression (3.28) is the same as that produced by the one-dimensional analysis technique (see, Carcione, 1994). Now, the governing equations including both absorbing and traction-free boundary conditions can be written as

$$\begin{aligned}
\frac{\partial^2 u_x}{\partial t^2} &= -2Q_x\frac{\partial u_x}{\partial t} + \frac{1}{\rho}\left\{\frac{\partial}{\partial x}\left(\sigma_{xx} - \sigma_{xx}^F + \sigma_{xx}^M\right) + \frac{\partial}{\partial z}\left(\sigma_{xz} - \sigma_{xz}^F\right) + f_x\right\}, \\
\frac{\partial^2 u_z}{\partial t^2} &= -2Q_z\frac{\partial u_z}{\partial t} + \frac{1}{\rho}\left\{\frac{\partial}{\partial x}\left(\sigma_{xz} - \sigma_{xz}^F\right) + \frac{\partial}{\partial z}\left(\sigma_{zz} - \sigma_{zz}^F\right) + f_z\right\},
\end{aligned} \tag{3.29}$$

where,

$$\begin{aligned}
\sigma_{ij}^F &= \delta(z)\sigma_{ij}, \quad i,j = x,z, \\
\sigma_{xx}^M &= \delta(z)\left\{\frac{4\mu(\lambda+\mu)}{(\lambda+2\mu)}\frac{\partial u_x}{\partial x}\right\}.
\end{aligned} \tag{3.30}$$

The equivalent force terms for traction-free conditions can be considered via forcing terms, and thereby the equation system with a displacement-velocity formulation can be expressed by

$$\partial_t \mathbf{U} = \mathbf{L}_q\mathbf{U} + \mathbf{N}, \tag{3.31}$$

where $\mathbf{N}$ is a vector for body forces and equivalent force terms expressing traction-free boundary conditions and the operator matrix $\mathbf{L}_q$ includes the absorbing boundary conditions. The vector $\mathbf{N}$ is composed of four equivalent force terms $(\mathcal{N}(v_j), \mathcal{N}(u_j)$,

$j = x, z$):

$$
\begin{aligned}
\mathcal{N}(u_x) &= \mathcal{N}(u_z) = 0, \\
\mathcal{N}(v_x) &= \frac{1}{\rho}\left\{ f_x - \frac{\partial \sigma_{xx}^F}{\partial x} - \frac{\partial \sigma_{xz}^F}{\partial z} + \frac{\partial \sigma_{xx}^M}{\partial x} \right\}, \\
\mathcal{N}(v_z) &= \frac{1}{\rho}\left\{ f_z - \frac{\partial \sigma_{xz}^F}{\partial x} - \frac{\partial \sigma_{zz}^F}{\partial z} \right\}.
\end{aligned} \tag{3.32}
$$

In a similar approach for the implementation of boundary conditions to that employed in the acoustic wave problems in Section 2.4.3, we introduce a zero-velocity artificial layer ($\lambda = \mu = 0$) above the free surface. This has the effect of confining the elastic wave in the domain to which equivalent forces are applied on the boundary, and significantly improves the accuracy.

Finally, considering (2.11) and (3.25), we can express the discrete time solution for the elastic wave equation including implicitly absorbing and traction-free conditions as

$$
\begin{aligned}
\mathbf{U}_{n+1} = &\ \mathbf{U}_n + \delta t\, \mathbf{L}_q \mathbf{U}_n + \frac{\delta t^2}{2} \mathbf{L}_q^2 \mathbf{U}_n + \cdots + \frac{\delta t^m}{m!} \mathbf{L}_q^m \mathbf{U}_n \\
&+ \delta t\, \mathbf{N}_n + \frac{\delta t^2}{2} \mathbf{L}_q \mathbf{N}_n + \frac{\delta t^3}{6} \mathbf{L}_q^2 \mathbf{N}_n + \cdots + \frac{\delta t^{m+1}}{(m+1)!} \mathbf{L}_q^m \mathbf{N}_n,
\end{aligned} \tag{3.33}
$$

where $\mathbf{U}_n$ is a variable vector at discrete time t_n and $\mathbf{N}_n$ is a vector for forcing terms.

3.4.2.2 *SH waves*

Since we set *SH* waves to be polarized along the y-axis in a cartesian coordinate, $u_x = u_z = 0$. Therefore, $\sigma_{xz} = \sigma_{zz} = 0$ by definition and only σ_{yz} has to satisfy the condition at the free surface. Since σ_{yz} vanishes at a free surface, we can include this condition in the governing equation system by writing

$$
\frac{\partial}{\partial t}\begin{pmatrix} u_y \\ v_y \end{pmatrix} = \begin{pmatrix} 0 & I \\ \mathcal{L}_y & 0 \end{pmatrix} \begin{pmatrix} u_y \\ v_y \end{pmatrix} + \frac{1}{\rho}\begin{pmatrix} 0 \\ f_y - \partial_z\left(\sigma_{yz}^F\right) \end{pmatrix}, \tag{3.34}
$$

where $\delta(z)$ is a Dirac delta and σ_{yz}^F is a free-surface tangential stress vector which is set to be zero except at the free surface:

$$
\sigma_{yz}^F = \delta(z)\left(\mu \frac{\partial u_y}{\partial z}\right). \tag{3.35}
$$

The remaining procedure follows the scheme described in the previous section.

3.5 Sources and initial conditions

The sources are either a compressional line force or a vertically directed line force with a source time function $h(t)$ given by

$$
h(t) = C_s (t - t_0) e^{-w(t-t_0)^2}, \tag{3.36}
$$

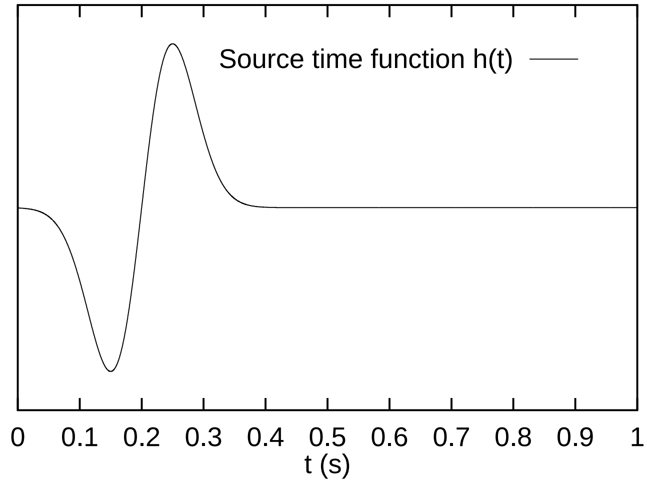

Fig. 3.1. Source time function $h(t)$ for the numerical modelling of elastic wave propagation.

where C_s is a constant value, t_0 is time shift and w controls the wavelength content of the excitation. We set $t_0 = 0.2$ seconds and $w = 200$ (Fig. 3.1). The initial condition is that the material is undistorted and at rest at time $t = 0$.

3.6 Test of absorbing boundary conditions

To test the efficiency of the attenuation terms in (3.21) for the waves approaching the artificial boundaries, we check the absorption of the displacement fields at the artificial boundaries in a 2-D homogeneous medium (Fig. 3.2) with compressional velocity 3.15 km/s, shear velocity 1.8 km/s and density 2.2 $\mathrm{g/cm^3}$.

The attenuation factors (Q_x & Q_z for *P-SV* wave case, Q_y for *SH* wave case) are designed following conditions suggested by Sochachi *et al.* (1987) so that these attenuation factors are bounded, twice continuously differentiable and their derivatives are sufficiently smooth on a domain. In this study, we distribute attenuation factors on a domain by

$$Q_j(i_x, i_z) = \mathcal{A}_x \left[e^{\mathcal{B}_x i_x^2} + e^{\mathcal{B}_x (i_x - N_x)^2} \right] + \mathcal{A}_z \left[e^{\mathcal{B}_z i_z^2} + e^{\mathcal{B}_z (i_z - N_z)^2} \right],$$
$$j = x, y, z, \qquad i_x = 1, 2, \ldots, N_x, \qquad i_z = 1, 2, \ldots, N_z, \tag{3.37}$$

where $\mathcal{A}_k$ and $\mathcal{B}_k$ ($k = x, z$) are constants determined by considering the wave speeds in the media, N_x is the number of grid points in the x direction, N_z the total number of grid points in the z direction and (i_x, i_z) is a discretized grid position. $\mathcal{A}_j$ controls the magnitude of attenuation and $\mathcal{B}_j$ modulates the width of the attenuation area. In this experiment, we set $\mathcal{A}_j$ ($j = x, z$) is to be 8 and $\mathcal{B}_j$ to -0.015 (Fig. 3.3).

We apply a line source in the *SH* wave case and compressional and vertically-directed

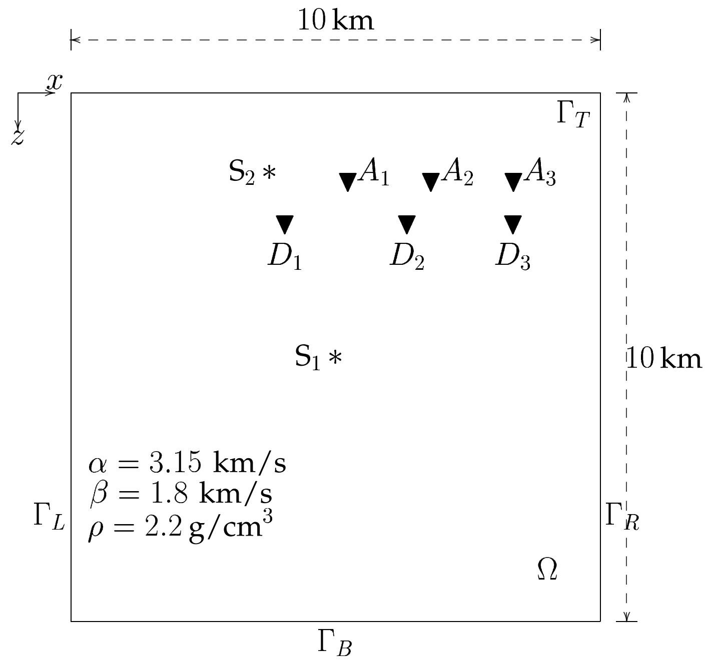

Fig. 3.2. Description of 2-D homogeneous elastic media used for a test of absorbing boundaries and for a modelling of elastic wave propagation in in the presence of a free surface (Lamb's problem). Source S_1 is a source position for a test of absorbing boundaries and S_2 for a validation test for *SH*-wave problem. Also, receivers A_j and D_j) are placed horizontally at each depth (h =1719 and 2500 m) in the medium to obtain time responses for numerical comparisons.

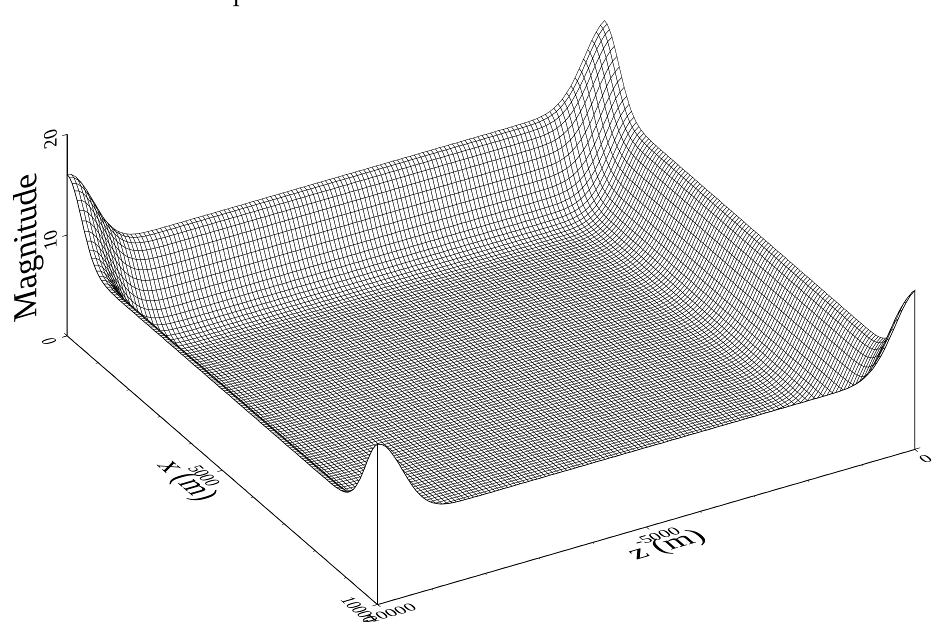

Fig. 3.3. Distribution of attenuation factors (Q_j, $j = x, y, z$) on a 2-D medium with four absorbing boundaries when $\mathcal{A}_x = \mathcal{A}_z = 8$ and $\mathcal{B}_x = \mathcal{B}_z = -0.015$ in (3.37).

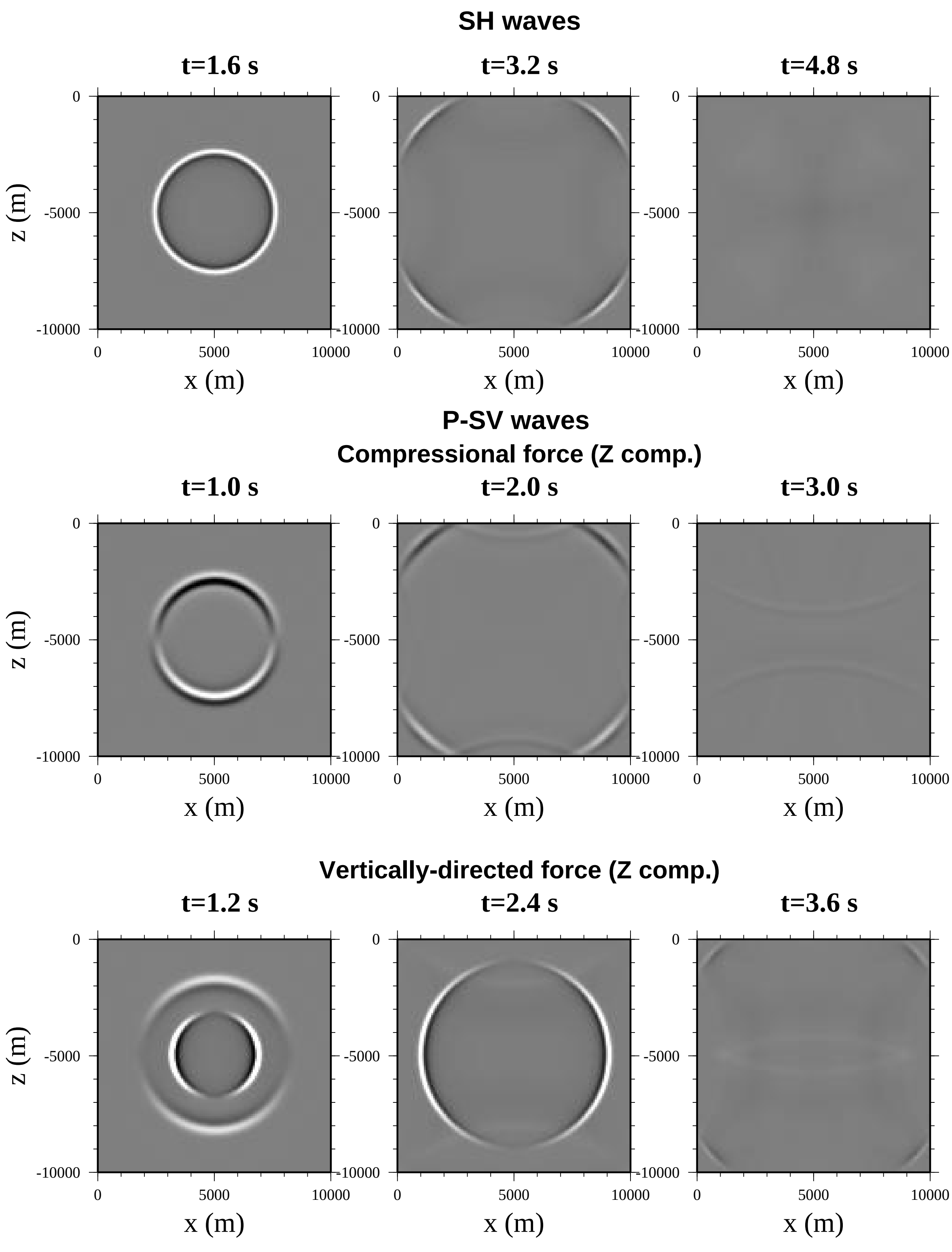

Fig. 3.4. Successive forms of *SH* and *P-SV* wave propagation in a homogeneous elastic medium where four artificial boundaries are treated by absorbing boundary conditions. For a test of the *P-SV* wave case, both a compressional source and a vertically-directed force are considered.

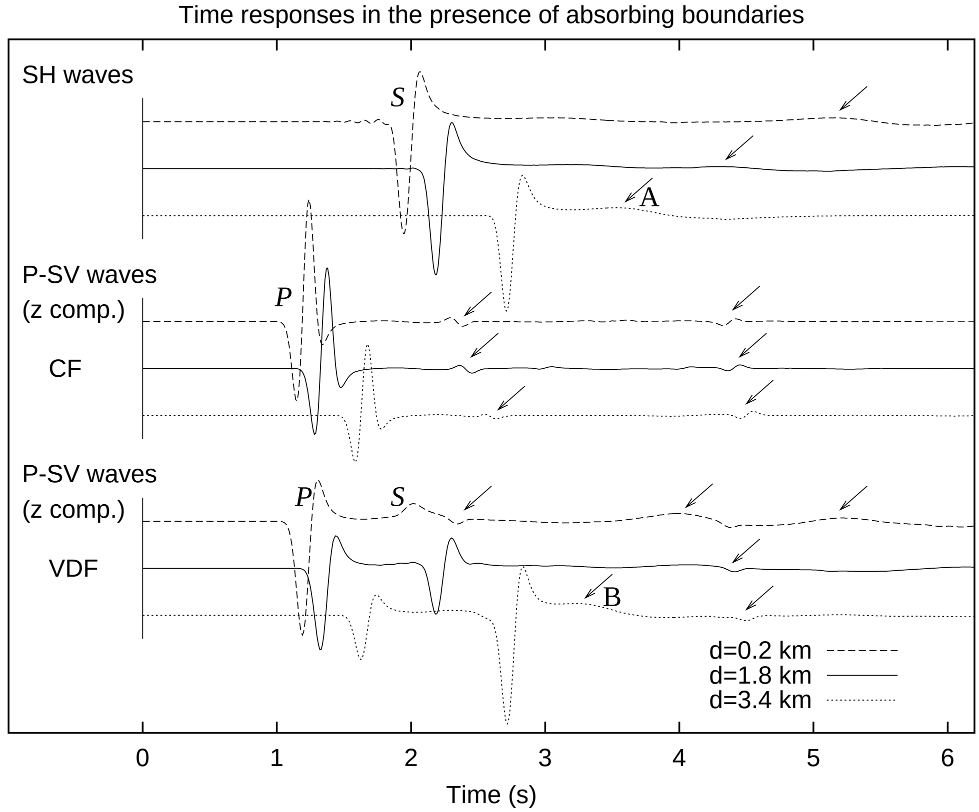

Fig. 3.5. Time responses of *SH* and *P-SV* waves (vertical component) at three receivers (A_j, $j = 1, 2, 3$ in Fig. 3.2) in homogeneous media with four absorbing boundaries. For a test in *P-SV* waves, both compressional force (CF) and vertically-directed force (VDF) are considered. Some major spurious waves are indicated by arrows.

line forces for the *P-SV* wave case. Fig. 3.4 shows the absorption of the displacement fields at four absorbing boundaries with time. The direct phases are absorbed effectively at the boundaries, spurious waves reflected from the boundaries are weak enough not to spoil the wavefields. To provide a quantitative check on the time responses in the presence of absorbing boundaries, we consider three receivers placed horizontally at the 21th grid point below the top absorbing boundary (A_j, $j = 1, 2, 3$ in Fig. 3.2) where free surface receivers are placed in later experiments (Fig. 3.5). The major spurious waves are indicated by arrows to compare with the main phases (*P, S*). We note that generally *P* phases are absorbed well at the boundaries, but small amounts of *S* phases are reflected from the absorbing boundaries and spurious waves develop following the *S* waves because the wavelength is comparable to the size of the attenuation zones. As shown in A, B in Fig. 3.5, this effect is more marked at the four corners of domain where the gradients in the attenuation factors are augmented (see, Fig. 3.3).

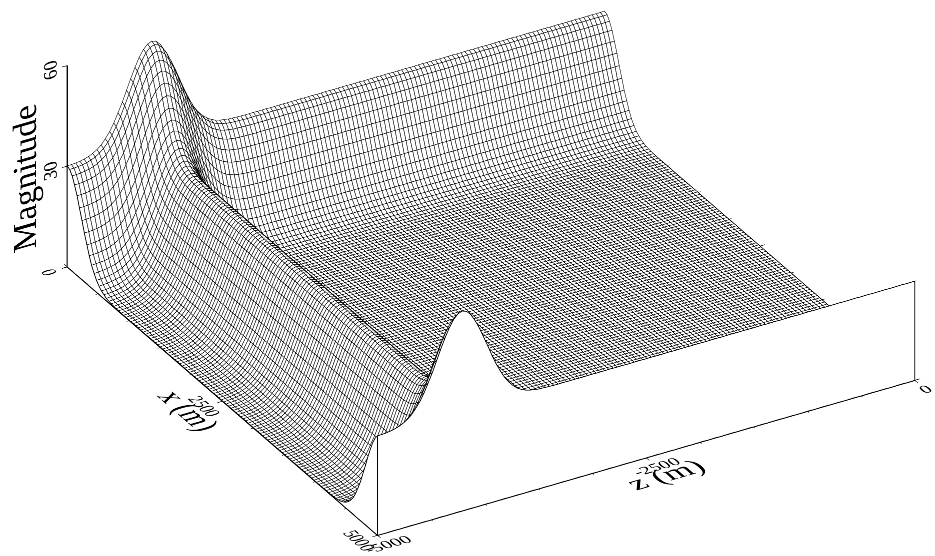

Fig. 3.6. The attenuation factors (Q_j, $j = x, z$) distribution on the 2-D media. To consider a top boundary as a free surface, the distribution of attenuation factors is shifted vertically by 20 rows of grids.

3.7 Validation tests of the scheme: I. *SH* waves

3.7.1 Medium with a free surface

Since the *SH* wave equation is relatively simple and does not generate additional phases at the free surface, a *SH* wavefront can be simulated easily by introducing virtual image sources (Virieux, 1984). But, in this study, we introduce a way of implementing a traction-free condition in *SH* wave equation without use of a virtual image scheme. We introduce a line source just beneath a free surface and then model the response of *SH* wave.

The numerical model has a width of 10000 m and a height of 10000 m, with a superimposed 128-by-128 grid. Here the top boundary is treated as a free surface. The shear wave velocity β is 1.8 km/s and the density in the medium is 2.2 g/cm^3. The source is located at 1.5 km below the free surface (Fig. 3.2).

As the top boundary of a domain is considered as a free surface, we design the distribution of the attenuation terms in (3.21) so as not to disturb the effects from the presence of a free surface. We shift the attenuation layers from top and bottom artificial boundaries by 20 material points to give

$$Q_j(i_x, i_z) = A_x \left[e^{B_x i_x^2} + e^{B_x (i_x - N_x)^2} \right] + A_z \left[e^{B_z (i_z + 20)^2} + e^{B_z (i_z - N_z + 20)^2} \right],$$
$$j = x, z, \quad i_x = 1, 2, \ldots, N_x, \quad i_z = 1, 2, \ldots, N_z, \tag{3.38}$$

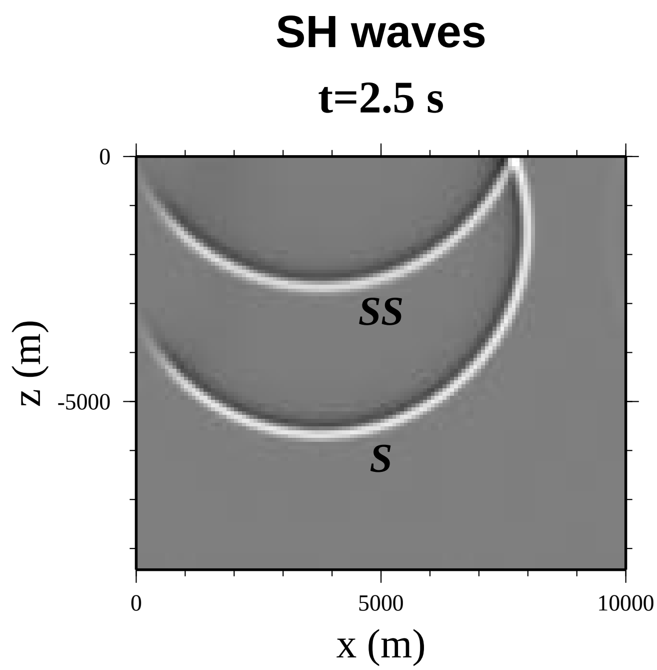

Fig. 3.7. Snapshot of *SH* wave propagation in a homogeneous medium with a free surface at $t = 2.5$ s. The entire wavefield is composed of direct (*S*) and reflected (*SS*) phases.

where we use $A_x = A_z = 30$, $B_x = B_z = -0.015$, N_x is the number of grid points in the x direction, N_z the total number of grid points in the z direction and (i_x, i_z) is position in the discrete grid (Fig. 3.6).

We compare the numerical time responses with analytic solutions for three receivers with horizontal distances d=0.3, 2.6, 4.5 km at depth 2500 m (D_j, $j = 1, 2, 3$ in Fig. 3.2). The entire wavefields are composed of a direct phase (*S*) and a reflected phase (*SS*) from a free surface (Fig. 3.7) and they exhibit a good match with the analytic solutions (Fig. 3.8).

3.7.2 Two-layered media

The formulation of the wavelet method is based on a fully heterogeneous medium and so we can introduce particular cases by simply specifying the material parameters. We therefore consider a further case where an analytic solution can be obtained for 2-D propagation of *SH* waves in a two layer medium where the velocity in bottom layer is twice of that in top layer and the density in bottom layer is 1.5 times of that in top layer (Fig. 3.9). The displacement in *SH* waves lies along y-axis (i.e., normal to the x-z plane where *SH* waves are propagating), and reflection and transmission without conversion of wavetype occurs at the interface.

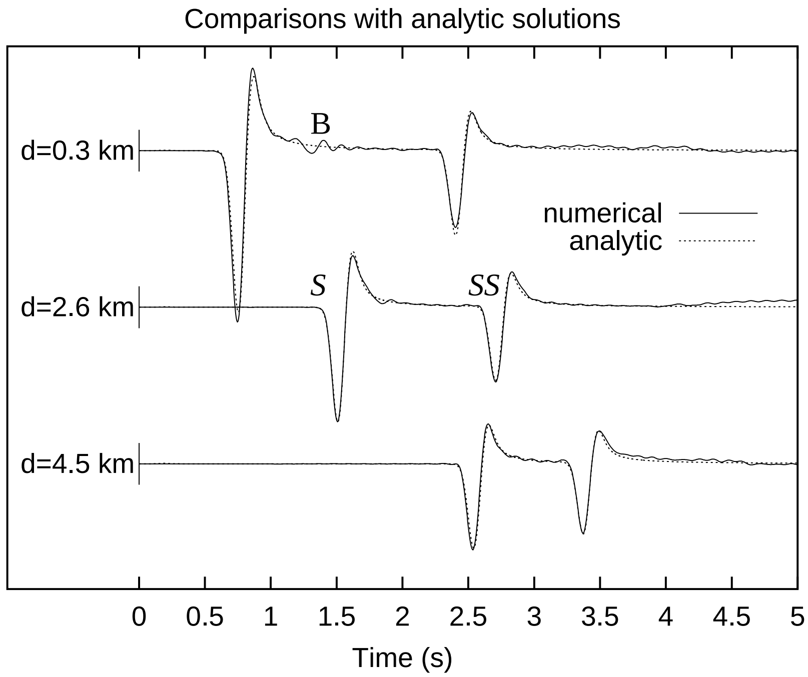

Fig. 3.8. Comparisons of numerical time responses of *SH* waves with analytic solutions for three receivers (D_j, $j = 1, 2, 3$ in Fig. 3.2) in a homogeneous medium with a free surface. The receivers are placed horizontally at depth 2.5 km with distances d=0.3, 2.6 and 4.5 km.

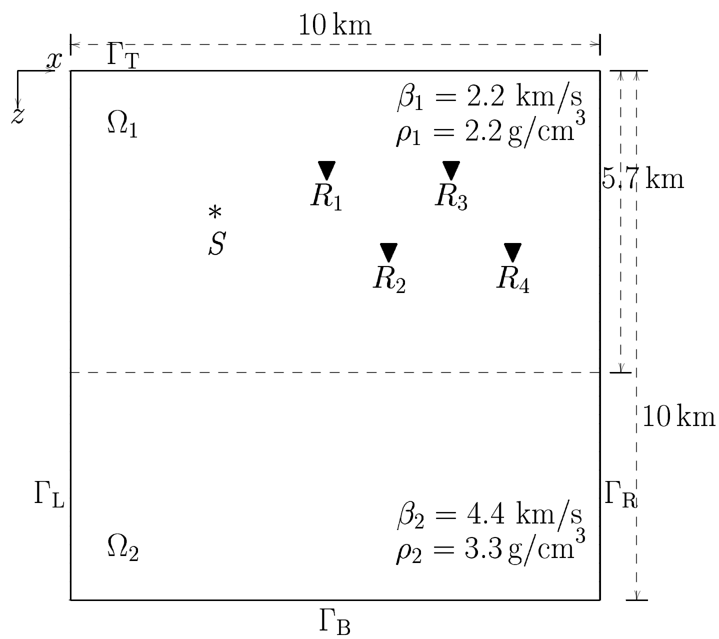

Fig. 3.9. Description of a two-layered medium for modelling of *SH* wave propagation. The bottom layer has the twice the velocity and 1.5 times the density compared to the top layer. Four receivers (R_j, $j = 1, 2, 3, 4$) are placed inside the top layer and the numerical responses from the receivers are compared with analytic solutions.

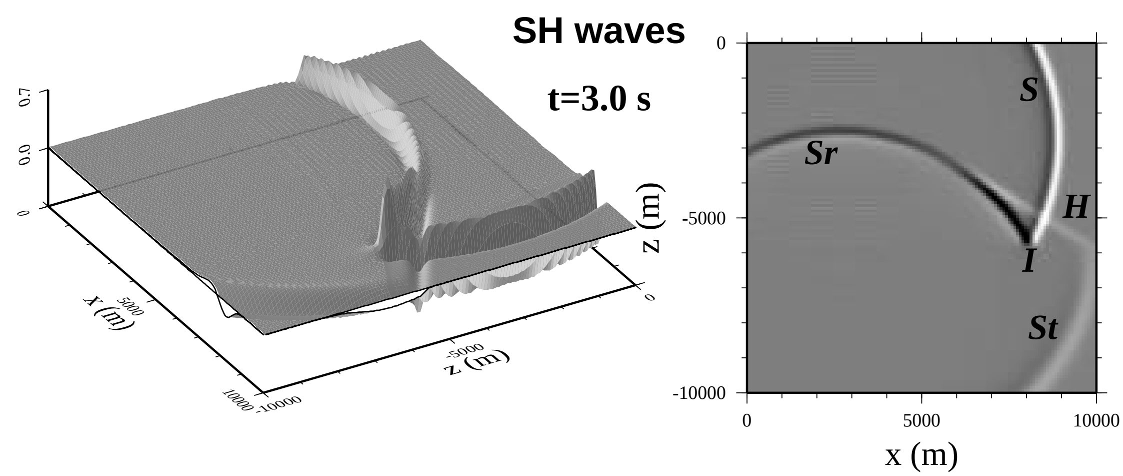

Fig. 3.10. Snapshot of *SH* wave propagation in a two-layered medium at *t*=3.0 s. Direct wave (S), reflected wave (S_r), transmitted wave (S_t), interface wave (I) developing on a boundary, and head waves (H) connecting the transmitted wave and reflected wave are displayed.

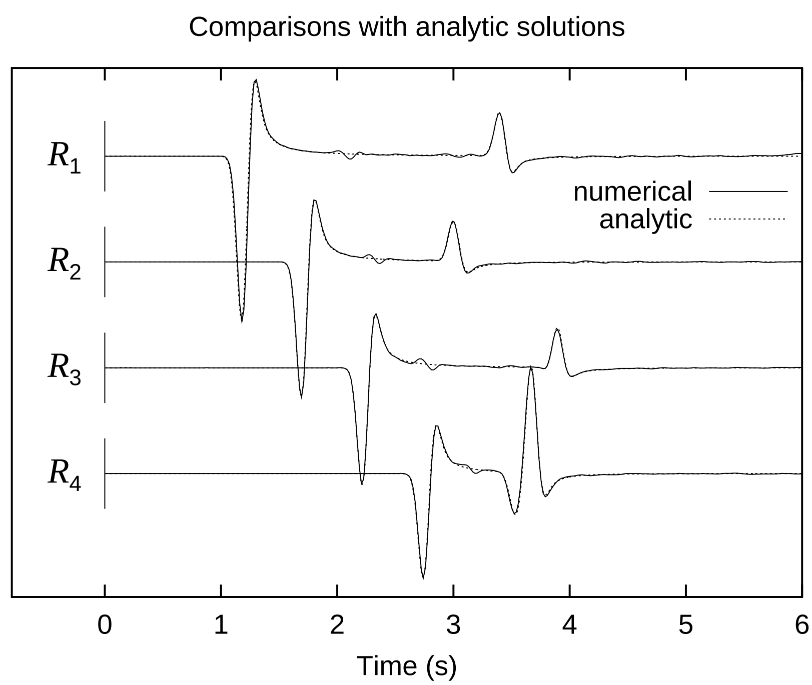

Fig. 3.11. Comparison between numerical results and analytic solutions for *SH* waves in a two-layered medium. The numerical responses are collected by four receivers (R_j, $j = 1, 2, 3, 4$) in Figure 3.9.

A line force is applied at (2734 m, 2656 m) (S in Fig. 3.9) and the internal boundary is located at depth 5703 m with four artificial but absorbing boundaries (Γ_T, Γ_B, Γ_R, Γ_L). The *SH* displacements at four receivers (R_j, $j = 1, 2, 3, 4$) collecting numerical responses placed at (4844m, 1875 m), (6016 m, 3438 m), (7188 m, 1875 m), (8359 m, 3438 m), are compared with analytic solutions (Aki & Richards, 1980) based on the Cagniard

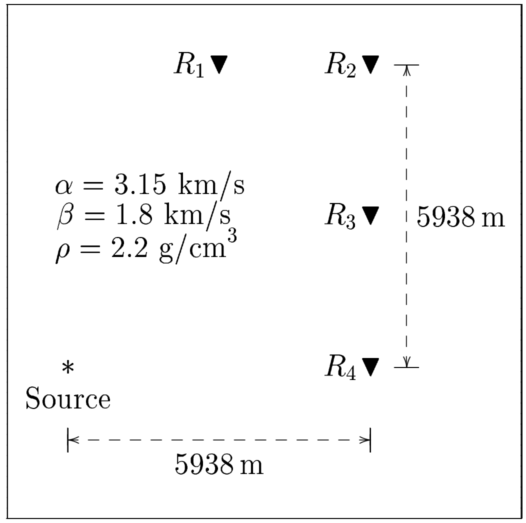

Fig. 3.12. Description of a 2-D homogeneous unbounded medium and deployment of receivers (R_j, $j = 1, \ldots, 4$) with hypocentral distances from 5938 m to 8397 m.

technique (see, Fig. 3.11). There is very good agreement between the numerical and analytic results for both the direct waves and those interacting with the interface between the two layers. The pattern of the wavefield can be seen in the snapshot at 3.0 s (Fig. 3.10) with a direct wave (S), reflected wave (SS_r), transmitted wave (SS_t), interface wave on the internal boundary (I) and head wave (H) connecting transmitted wave and reflected wave.

The comparisons with the analytic solutions in the homogeneous half-space and layered medium case indicate the successful implementation of the wavelet representation for both the main propagation and the boundary conditions.

3.8 Validation tests of the scheme: II. *P-SV* waves

3.8.1 Unbounded homogeneous media

In Figs. 3.12 and 3.13 we consider a numerical test of wave excitation by a delta function source using the wavelet approach with comparison with analytic solutions (Pilant, 1979) for four receivers (R_j, $j = 1, \ldots, 4$ in Fig. 3.12) at 5938 to 8397 m from the source (Fig. 3.13).

Because the wavelet transform can provide a full description of the effects of a delta function, we get an excellent representation of the wavefield excited by a vertically-directed force at each location. The slight discrepancies at later times come from the absorbing boundary conditions. We also note that the high frequency waves before the S waves (A in Fig. 3.13, B in Fig. 3.8) are related to the fact that the

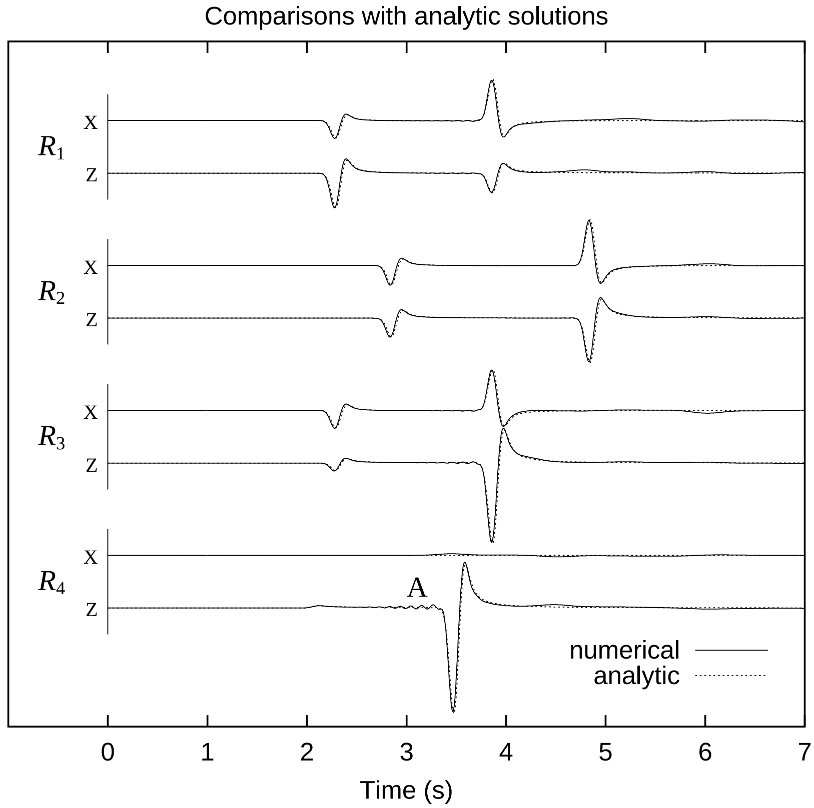

Fig. 3.13. Comparisons between numerical time responses of *P-SV* waves and analytic solutions for four receivers in in a homogeneous unbounded medium.

differentiation of delta function (in a source region) using wavelets with a limited band of frequency produces small amplitude high frequency waves before and after the exact solutions. This phenomenon also can be found in a Fourier method (Kosloff *et al.*, 1984).

3.8.2 *Medium with a free surface (Lamb's problem)*

First, we consider the excitation of elastic waves by a surface source in a homogeneous medium with a planar free surface (Lamb's problem). We check the stability and accuracy of the method with an explicit traction-free boundary condition by considering media with two different values of Poisson ratio (ν=0.26, 0.4). Since Earth materials generally have Poisson ratios between 0.22 and 0.35 (see, Lay & Wallace, 1995; Kennett *et al.*, 1995; Kennett, 2001), the tests with two different Poisson ratios can justify the stability of the method for a general case. We note when $\nu = 0.5$, the medium would be fluid and then the governing equation can be written as an acoustic wave equation.

For the first experiment for Lamb's problem with $\nu = 0.26$, we consider the compressional wave speed α to be 3.5 km/s, the shear wave speed β to be 2.0 km/s

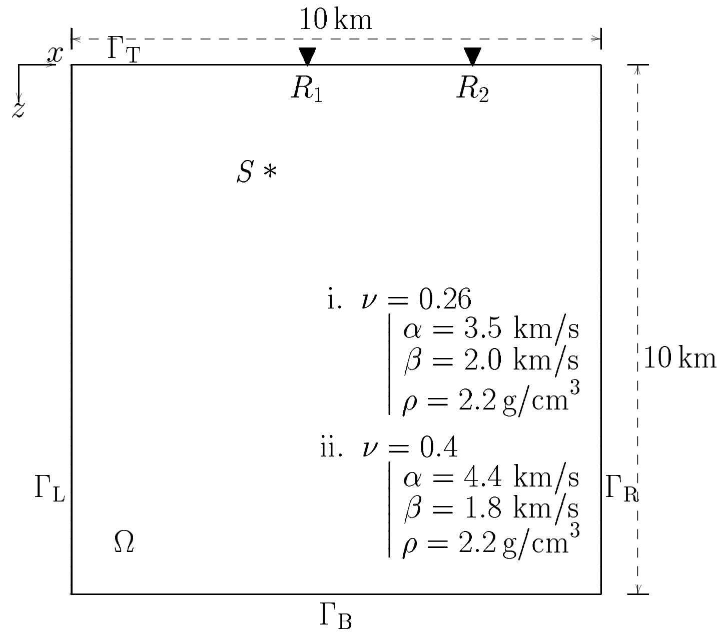

Fig. 3.14. Description of a homogeneous elastic medium with a planar free surface. Two different Poisson ratios ($\nu = 0.26, 0.4$) are considered for the accuracy tests. S indicates a line source position and two receivers (R_1, R_2) are placed on the free surface at distances x= 4453, 7578 m.

and the density ρ to be 2.2 $\mathrm{g/cm^3}$ (see, Fig. 3.14). Whereas for the second experiment with $\nu = 0.4$, the physical parameters of a medium are $\alpha = 4.4$ km/s, $\beta = 1.8$ km/s and $\rho = 2.2\,\mathrm{g/cm^3}$. The 10×10 $\mathrm{km^2}$ domain is represented through a 128×128 grid points.

The top boundary (Γ_T) is treated as a free surface where the traction vanishes, and the other three artificial boundaries (Γ_R, Γ_L, Γ_B) with absorbing boundary conditions following the technique in Sections 3.4.1 and 3.5. A vertically directed line force is applied at (3750 m, 2000 m). Fig. 3.15 shows snapshots of elastic wave propagation for the two Poisson ratios. In both cases, the wavefields are stable and clear reflected phases from the free surface are generated (*PP, PS, SP, SS* in Fig. 3.15).

In Fig. 3.16 we display the calculated displacement seismograms at two receivers (R_1,R_2 in Fig. 3.14) located at x=4453, 7578 m on the free surface. The numerical responses for the wavelet method are compared with analytic solutions based on Cagniard's technique (Pilant, 1979; Burridge, 1976). For each of the values of Poisson ratios there is a good match with the analytic solutions up to the time when there is a small wave reflection from the artificial boundary (about 3.5 s), indicating the successful implementation of the free-surface boundary condition. For the larger Poisson ratio a very slight time shift can be seen between the numerical and analytic solutions for the

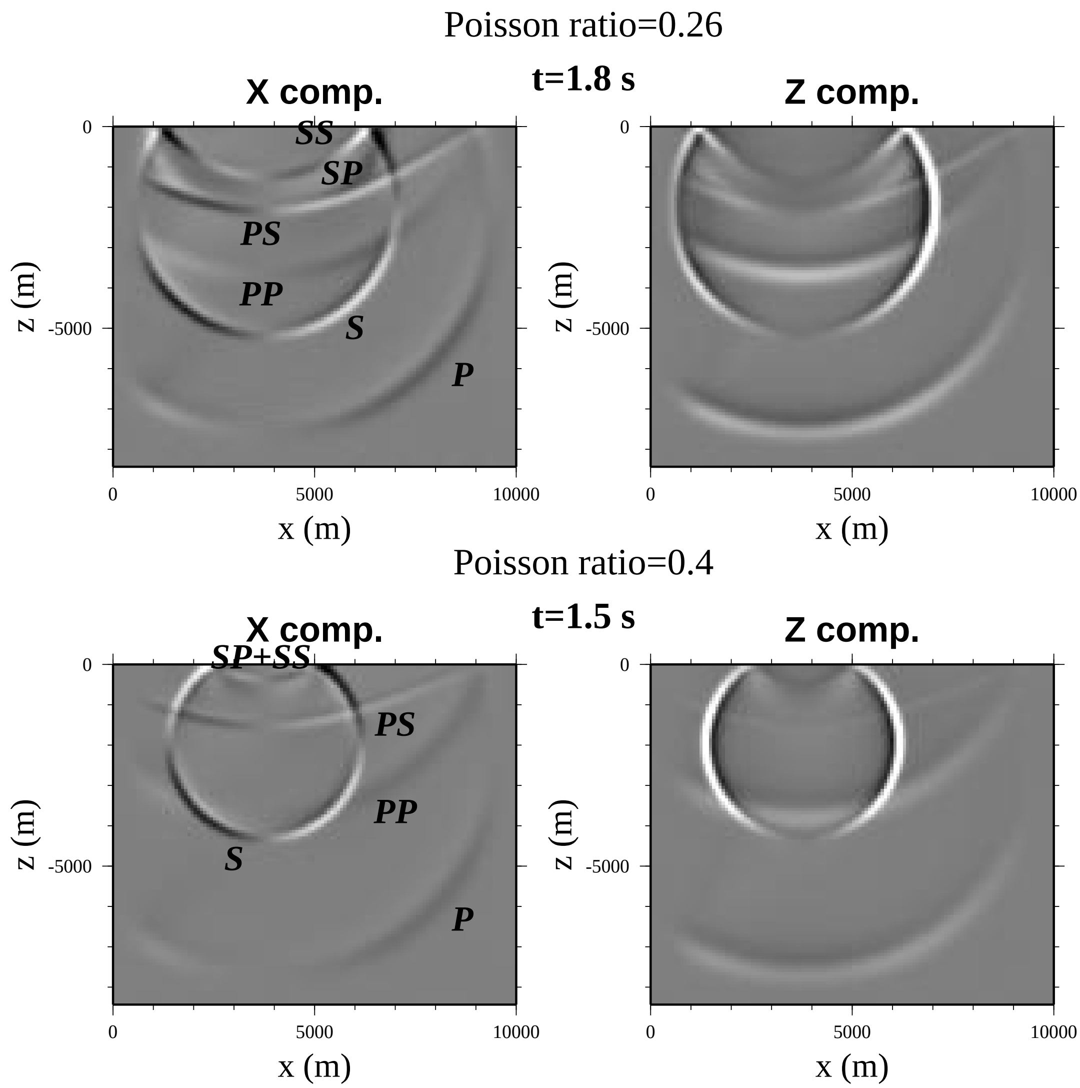

Fig. 3.15. Snapshots of elastic wave propagation in a homogeneous media with a planar free surface (Lamb's problem). The wavefields are computed for two different Poisson's ratios (ν =0.26, 0.4).

large amplitude Rayleigh wave at 2.5 s but the amplitude and pulse shape are well represented.

We note that adjustment of the absorbing boundary conditions may be needed to avoid spoiling the main wavefield by the effect of spurious waves from absorbing boundaries. In particular, spurious waves from surface waves (e.g., Rayleigh waves) tend to become dominant, since surface waves experience lower order geometrical spreading effect compared to body waves (i.e., in 2-D elastic medium with a line source, surface waves do not decay with propagation distance (r), while body waves decay as $\sqrt{1/r}$). Therefore, the absorbing region should be designed to give sufficient attenuation of the surface waves by suitable modulation of the attenuation factors (Q_x, Q_z in (3.38)). We can

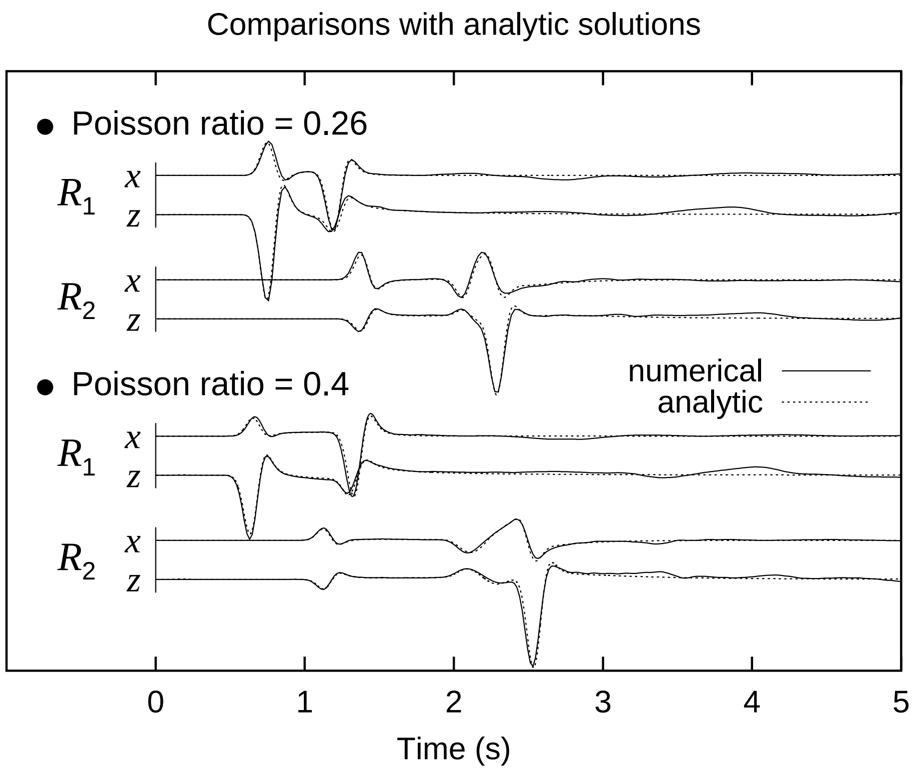

Fig. 3.16. Comparison between numerical results and analytic solutions for Lamb's problem at two receivers (R_1, R_2 in Fig. 3.14) placed on a free surface for two different Poisson ratios ($\nu = 0.26, 04$).

use, for instance, an extension of the effective absorbing region by adjusting B_x and B_z in Q_x and Q_z, or enhancement of attenuation rate in the region by modulating A_x and A_z.

3.9 Stability and numerical analysis

For stable computation in numerical modelling, one has to consider two kinds of conditions; the time step condition and the grid dispersion condition. The usual time step (δt) condition for grid steps (δx, δz) in grid-based methods for 2-D elastic waves, is independent of the S wave velocity or of the Poisson's ratio ν, but related with largest wave speed (usually P wave velocity, α) of a domain. We set δx to be equal to δz in this study. Then an empirical stability condition for the relationship between the time step and the grid step (cf., Virieux, 1986) can be expressed as

$$K_e \, \alpha_{max} \, \frac{\delta t}{\delta z} < 1, \tag{3.39}$$

where α_{max} is the highest wave velocity in the domain and K_e is a constant depending on the maximum order (m) of term (i.e., truncation order) considered in a discrete time solution (3.33) based on Taylor expansion. Empirically, the K_e value linearly decreases with increase in the truncation order; when $m = 2$, $K_e = 10$, when $m = 10$ $K_e = 2$, and when $m = 20$, $K_e = 1$. Since K_e is in inverse proportion to m, the total computational time is almost constant regardless of the value m used. Also, since m (or, K_e) is related only to the time step (δt), not to the grid sizes ($\delta x, \delta z$), the numerical accuracy of the wavelet-based method is held constant during computation. However, we have found that effects from boundary forcing terms (e.g., traction-free boundary conditions) can be implemented more accurately with larger time step (i.e., larger values of m). Taking into account the representation of the physical medium, the frequency content of the source time function for suitable excitation and the accuracy of modelling, we implement $m = 20$ for the maximum order of term considered (i.e., $K_e = 1$) in this study.

In numerical modelling of wave propagation, every numerical method needs to satisfy a minimum grid occupancy per wavelength not to evoke numerical grid dispersion. The grid dispersion condition is related to the slowest velocity (i.e., smallest wavelength) of elastic waves in a given medium (e.g., Rayleigh waves in a homogeneous medium with a free surface). Generally, the minimum number of grid points per wavelength varies with the type of wavelets implemented. From numerical experiments using Daubechies wavelets, a high order wavelet (i.e., wavelets with large vanishing moments) needs a much smaller number of grid points per wavelength for stable computation than a low order wavelet (i.e., wavelets with small vanishing moments); as the order of wavelets increases by a factor of two, only half as many grid points are needed. Empirically, Daubechies-3 wavelets need 32 grid points, Daubechies-6 wavelets 16 grid points, and Daubechies-20 wavelets 3 grid points. However it is rather difficult to obtain accurate Daubechies wavelet coefficients with high order using known numerical schemes (e.g., Shensa, 1992; Strang & Nguyen, 1996) due to instability and round-off error in the numerical computation, so the relationship between an order of wavelets and the minimum grid number can not be carried indefinitely. In this study, Daubechies-6 wavelets (Fig. 2.1(a)) have been implemented for a modelling of acoustic wave propagation and Daubechies-20 wavelets (Fig. 2.1(b)) are used for modelling of elastic wave propagation.

To provide a reasonable comparison with other numerical techniques (e.g., finite difference method), we consider the computational resources needed for a specific situation. We consider a medium with size 10-by-10 km, where the *P* wave velocity is 3.5 km/s, the *S* wave velocity 2.0 km/s and the density 2.2 $\mathrm{g/cm^3}$, with a line source which generates waves with dominant frequency 4.5 Hz. The fourth-order finite difference method (FDM) then needs 250-by-250 grid points and the wavelet-based method (WBM) based on Daubechies-20 wavelets needs 64-by-64 grid points. The discrete time step

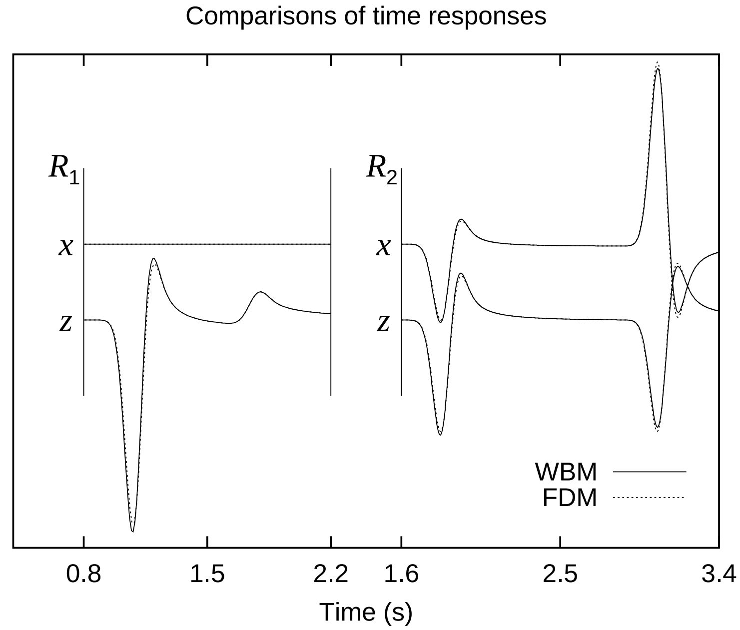

Fig. 3.17. Comparisons of time responses with a fourth-order finite difference method (FDM) and a wavelet-based method (WBM) in a homogeneous medium (α=3.5 km/s, β=2.0 km/s, ρ=2.2 $\mathrm{g/cm^3}$). The receiver R_1 is located at (0 km, 3.125 km) from the source and R_2 is at (3.125 km, 3.125 km).

(δt) is 0.006 s for the fourth-order FDM and 0.0446 s for the WBM when $m = 20$. The memory occupation is 3.8 megabyte for the FDM and 2.5 megabyte for the WBM when variables are held with double-precision accuracy. The CPU time for computation of the time response for a 1 s interval is 126 s in FDM and 252 s in WBM on an Ultra Sparc III (360 MHz). The most time consuming procedure in the WBM is differentiation (i.e., application of differential operator to velocity or displacement field, see, Beylkin (1992)), which will need further improvement to achieve fast implementation. A comparison of seismograms using the WBM and the FDM is presented in Fig. 3.17 and exhibits good matches between the very different methods.

In order to convey an idea of the accuracy of proposed method, the number of grid points per wavelength needed for stable and accurate modelling has been often considered (e.g., Komatitsch & Vilotte, 1998). The fourth-order FDM needs at least 5 grid points per wavelength in simple media (Levander, 1988). However, it has been reported that more grid points are needed in a model with strong impedance contrast between layers (Shapiro *et al.*, 2000) such as the contact of liquid and solid layers. On the other hand, the WBM needs a constant number of grid points in any media. For media with topography, the difference between the methods becomes larger and the WBM is more economical than the FDM. A FDM based on an unstructured grid system, which is suitable for topography problems, needs a dense grid system (about 20 grid points per wavelength, see, Käser & Igel, 2001), for media with sinusoidal topography, while the WBM is still invariant (see, Section 5.4).

This advantage of the WBM is particularly important for accurate modelling in random heterogeneous media or complex media, which have been considered for representation of heterogeneities in the crust, since quantitative estimates of wavefield properties are based on time responses from numerical modelling. Also, WBM generates accurate time responses in a random medium with very strong variation of physical parameters, while a fourth-order FDM displays artificially attenuated seismograms (see, Chapter 7). Thus, the WBM can also be effective in Earth models where wave velocities and physical parameters are strongly dependent on depth, without the need for the introduction of a dense grid system.

For the stability test for the explicit implementation of traction-free boundary condition, we consider both high and low Poisson's ratio cases ($\nu = 0.26, 0.4$) and compare numerical results with analytic solutions in Section 3.8.2.

3.10 Discussion

The wavelet-based method has been introduced for numerical modelling of elastic wave propagation in two-dimensional media problems. The scheme represents spatial differentiation operators through wavelet bases and the resulting second-order differential equations for time are treated by a displacement-velocity formalism and a semigroup approach.

The wavelet-based method for a spatial differentiation is not grid-based scheme in the physical domain like a Fourier method although sampling is needed at given points. Therefore, we can maintain the accuracy of computation of spatial derivatives uniformly throughout a whole domain in contrast to usual grid methods such as the finite-difference scheme that cumulates numerical errors during the computation of derivative terms from grid point to grid point.

The displacement-velocity formulation recasts the elastic wave equations in a form where the semigroup approach previously developed for a parabolic partial difference equation can be employed. Using a Taylor expansion, a recursive discrete solution can be computed by approximating an exponential function with a linear operator matrix in the exponent. The traction-free boundary is treated by an equivalent force term in the semigroup approach, leading to a stable implementation of the boundary conditions.

The use of equivalent force terms to represent boundary conditions may readily be adapted to other classes of problems and we expect that we can include different types of boundary conditions or singular features in the media (e.g., azimuthal anomalies, scattering) which are hard to describe by just controlling the physical parameters. The inclusion of attenuation factors for treating artificial boundaries in elastic wave equations reduces the cost of computation by allowing the use of smaller domains.

For classical 2-D problems, we have compared the numerical results with analytic solutions and we studied the accuracy of the method. The method is not only stable during numerical computation, but also has achieved accurate results in the comparisons.

We have not made use of the other commonly exploited aspect of wavelets, i.e., their adaptivity. The difficulty of taking an adaptive approach, especially with elastic waves, arises from the multiplicity of possible waves, which becomes most severe for highly heterogeneous media. For some simple problems it may well be possible to make some adaptive grid refinement. But, for the complex problems needed for seismological applications, it is difficult to see how adaptivity can be introduced in a systematic way.

4

Modelling in heterogeneous and transversely isotropic media

4.1 Introduction

We have developed a wavelet-based technique for modelling of elastic wave propagation and the technique has been validated through comparisons between numerical results and analytic solutions for simple media. In order to be effective as a general purpose wave simulator, the wavelet-based method needs to be tested for problems with with challenging heterogeneous media.

We model wavefields in two-layered media with sharp transition of physical properties in solid-solid or fluid-solid configurations. In particular, many numerical methods have difficulty in treating problems with fluid-solid contact without increase of the number of grid points around the interface. As a more complex problem, we introduce a medium with a linear gradient in physical properties and a stochastic heterogeneous medium. For a test of stability of the method in media with extremely strong impedance contrast, we consider a stochastic heterogeneous medium with a fluid-filled crack which is treated with a line of grid points.

The wavelet-based method is also applied to modelling in transversely isotropic media. As an extreme case we consider a solid-fluid contact problem where the solid layer is transversely isotropic while the fluid layer is isotropic.

The wavelet technique will be extended to modelling in heavily perturbed media in Section 7.2 and the accuracy and stability of the method will be tested.

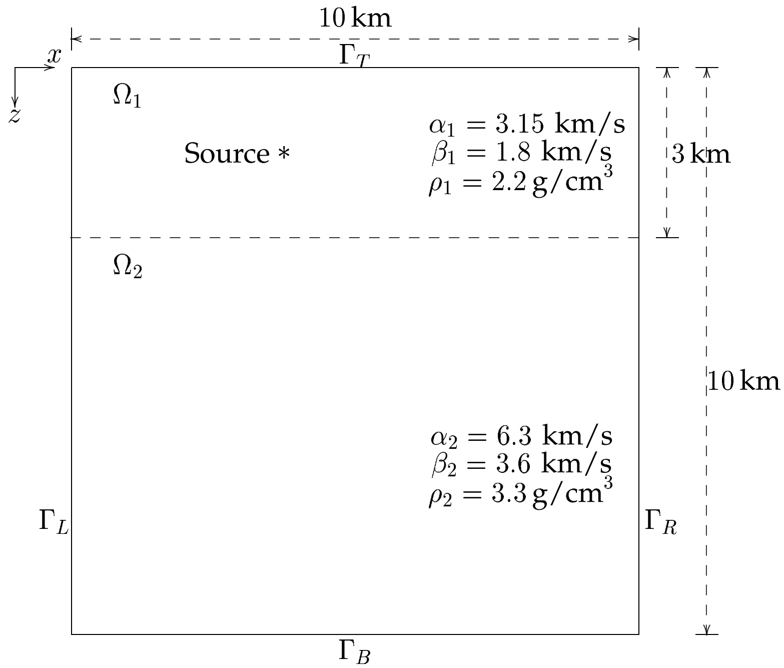

Fig. 4.1. Description of two-layered heterogeneous elastic media with a planar internal boundary at depth 3000 m. The elastic wave velocities in a bottom layer are twice of those in a top layer. An explosive source is applied at (3.57 km, 1.5 km).

4.2 Two-layered media

4.2.1 Solid-solid configuration

The first model we consider for heterogeneous media cases is a two-layered media problem which has often been considered in the modelling of elastic wave propagation (Virieux, 1986; Kelly *et al.* 1976). Since, however, it is difficult to obtain an exact analytic solution for the *P-SV* wave case due to wavetype coupling at boundaries, we consider numerical modelling and features of elastic wave propagation in a medium with a free surface. The medium has a horizontal internal boundary that divides it into two layers. The compressional wave velocity in the top layer (α_1) is 3.15 km/s, the shear wave velocity (β_1) is 1.8 km/s and the density is 2.2 g/cm^3. The velocities in the bottom layer are twice those in the top layer (α_2=6.3 km/s, β_2=3.6 km/s) and the density is 3.3 g/cm^3 (Fig. 4.1). The width and height of the model are both 10000 m and an internal boundary is placed at a depth of 3000 m. An explosive source is applied at x=3.75 km, z=1.5 km. The top artificial boundary (Γ_T) is considered as a free surface and the other boundaries ($\Gamma_B, \Gamma_R, \Gamma_L$) are treated by absorbing boundary conditions.

The explosive source which generates only *P* waves makes it easier to identify phases in the two layered media. As a result of wavetype coupling at the boundaries, the wavefields are complicated and the entire wavefields are composed of direct *P* waves,

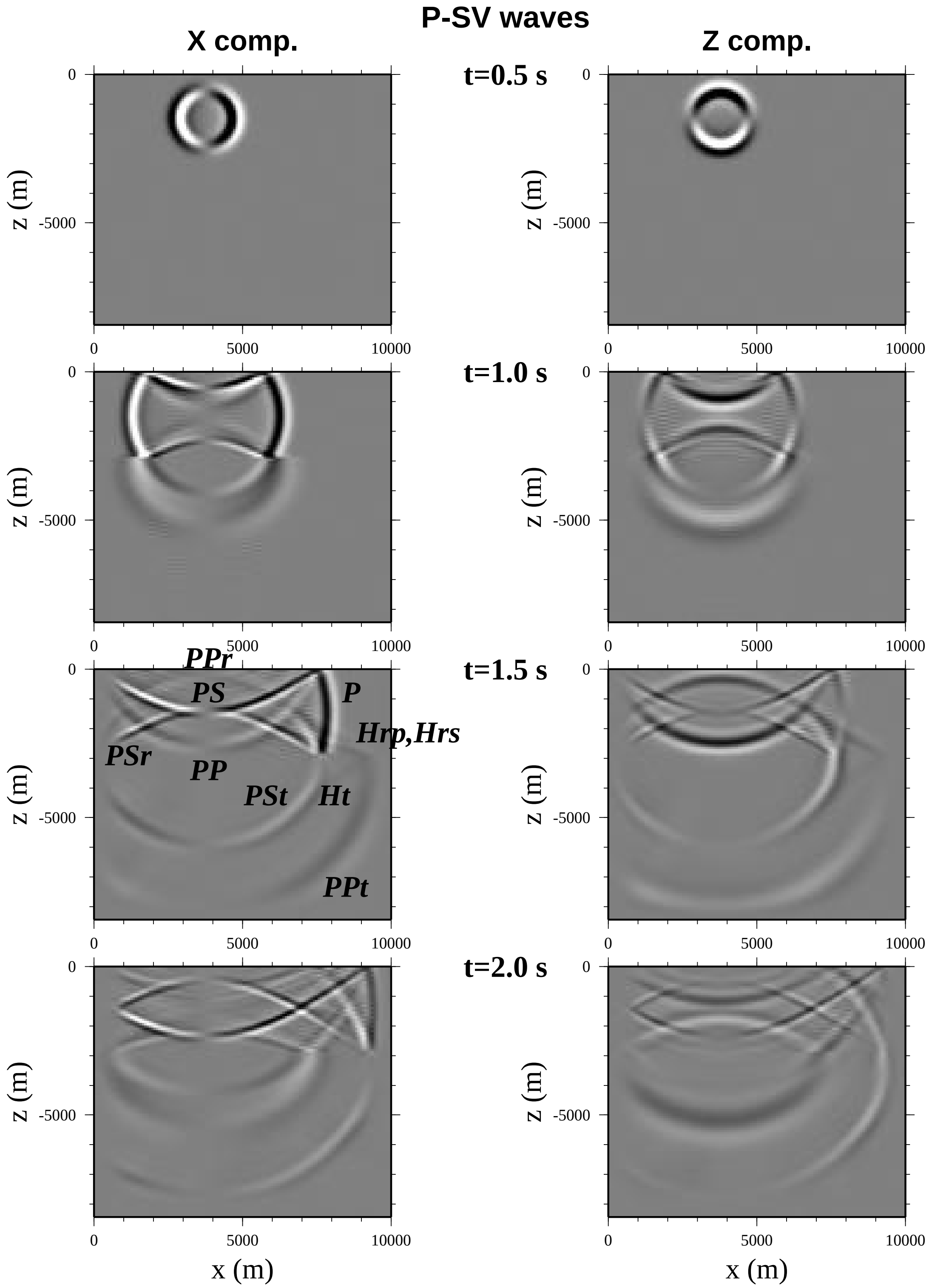

Fig. 4.2. Snapshots of *P-SV* wave propagation in two-layered media with compressional line force inside a top layer at t =0.5, 1.0, 1.5 and 2.0 s. The entire wavefields are composed of direct phases (*P, S*), reflected waves from the internal boundary (*PPr, PSr*) or the free surface (*PP, PS*), various head waves (e.g., *Hrp, Hrs, Ht*) and interface waves.

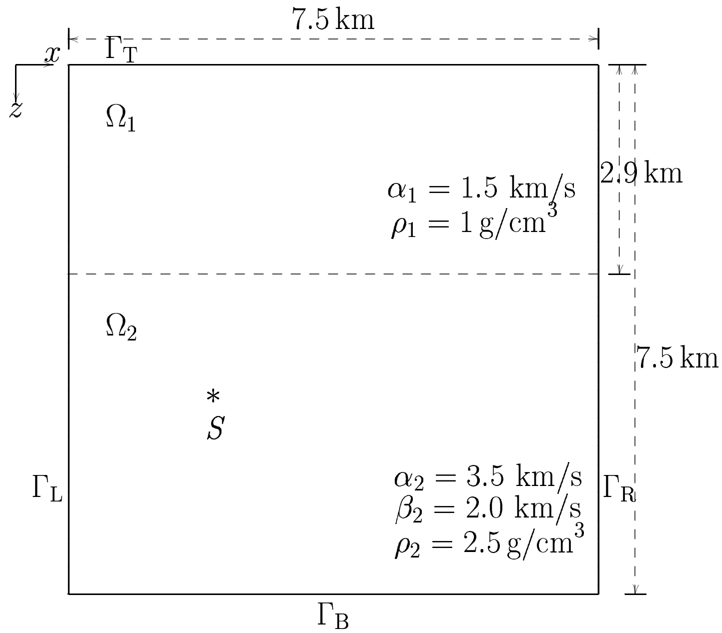

Fig. 4.3. Description of a fluid-solid configurational medium. An explosive source is applied inside the solid layer (S).

reflected *P* and *S* waves from the internal boundary (represented as *PPr* and *PSr* in Fig. 4.2) and the free surface (*PP, PS*), transmitted *P* and *S* waves at the internal boundary (*PPt*, *PSt*), head waves (*Ht*, *Hrp*, *Hrs*) and interface waves. Note that various head waves are generated at the free surface and the internal boundary. At the internal boundary, the head waves connect the reflected phases with transmitted phases (e.g., *Hrp, Hrs*) or transmitted phases to conversions (e.g., *Ht*), and they propagate to upper or lower layer with a body wave velocity from the internal boundary.

4.2.2 Liquid-solid configuration

As an alternative two layer case we undertake a stability test of the method for two-layered medium where a fluid layer $\nu = 0.5$ overlies a solid layer (Fig. 4.3). Many numerical methods have difficulty in treating this problem with a large contrast in Poisson ratio due to the large discrepancy between the elastic wave speeds (α, β). The incident *P* wave from an explosive source inside the solid layer gives rise to both *P* and *S* reflected waves (PPr, PSr) from the interface, but only a *P* wave (PPt) is transmitted to the fluid layer (see, Fig. 4.4). This behaviour is correctly reproduced with the wavelet treatment using an elastic representation for the whole medium.

For more general problems we need to be able to handle the case of non-planar boundaries, Boore (1972) has suggested two approaches to represent an internal

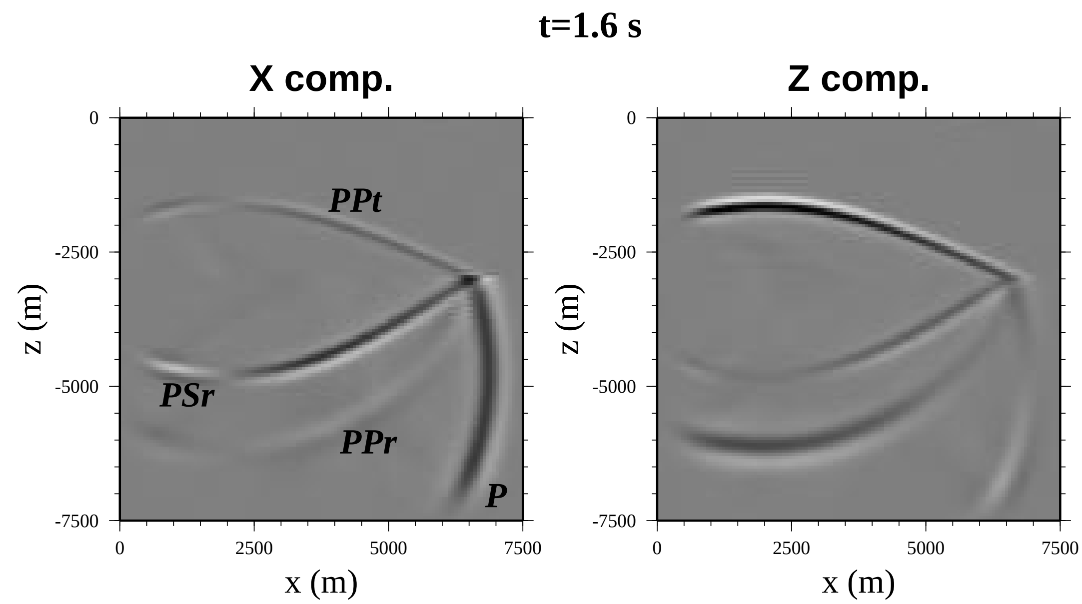

Fig. 4.4. Snapshots of elastic wave propagation in a fluid-solid configurational medium at *t*=1.6 s. Incident *P* wave is reflected as *P* and *S* waves (PP_r, PS_r) due to wavetype coupling on the boundary, and only a *P* wave (PP_t) propagates into the fluid layer.

boundary which passes between grid points in finite difference modelling for *SH* waves. These are firstly, the modification of the physical parameters at grid points near the boundary, and secondly, the implementation of explicit boundary condition (i.e., continuity of stress over the boundary). However, as noted by Boore, both approaches need additional computation and also may lead to instability. For a stable treatment with the wavelet-based method, a grid generation technique (Section 5.2) can be implemented by adjusting the grid system so as to be locally parallel to the boundaries (e.g., Komatitsch *et al.*, 1996). In the next chapter, we consider some topography problems using the grid generation technique.

4.3 Medium with a general linear gradient in seismic properties

As a further more complex example we consider a model with a slanted linear gradient in seismic properties (Fig. 4.5). We construct the model by setting the velocities and the density to increase linearly in both the vertical and horizontal coordinates. This linear gradient model provides a good test of the wavelet-based scheme in a model without symmetries in the expected wavefront behavior.

The top layer is set to be homogeneous and the artificial boundary over the top layer is considered as a free surface (Fig. 4.5). The compressional wave velocity (α) ranges from 3.15 to 7.88 km/s, the shear wave velocity (β) from 1.8 to 4.5 km/s, the density (ρ) from

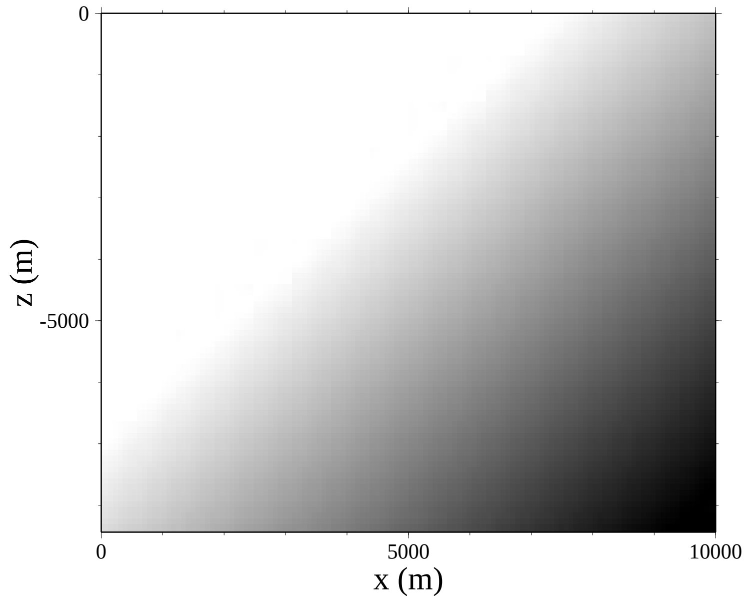

Fig. 4.5. Distribution of compressional and shear wave velocities (α, β) and density (ρ) in a heterogeneous medium. The velocity structure is slanted by 38.7° and the elastic wave velocity and the density increase linearly with depth and distance. The compressional wave velocity ranges from 3.15 to 7.88 km/s, the shear wave velocity from 1.8 to 4.5 km/s and the density from 2.2 to 3.85 g/cm^3.

2.2 to 3.85 g/cm^3, and the angle of the slanted velocity structure is 38.7° (Fig. 4.5). We consider *P-SV* wave propagation in this model with a vertically-directed force applied at (3750 m, 1500 m).

As the velocities increase with both depth and distance, the shape of wavefields becomes elliptic towards the bottom right in Fig. 4.6. Since the velocity in media increase gradually, there are no significant reflected phases or head waves at the internal boundary. Therefore, entire wavefields are composed of direct phases (*P*, *S*) and reflected phases from a free surface (*PP*, *PS*, *SP*, *SS*), surface head waves (*H*) and Rayleigh wave (*R* in Fig. 4.7), as in a case of homogeneous medium (α=3.15 km/s, β=1.8 km/s,ρ=2.2 g/cm^3). The time responses at receivers on a free surface and at depth 2500 m in Fig. 4.7 show that the phases arrive faster than those in the homogeneous medium (Fig. 4.8).

We also note that the composite waves of *S* and Rayleigh waves in Fig. 4.7 (a) exhibit larger amplitude of waves compared to those in homogeneous medium in Fig. 4.8 (a) because the wave velocities of media in Fig. 4.5 are increased gradually from $x = 7500$ m at the free surface and the phases are not attenuated with distance much compared to a homogeneous medium case.

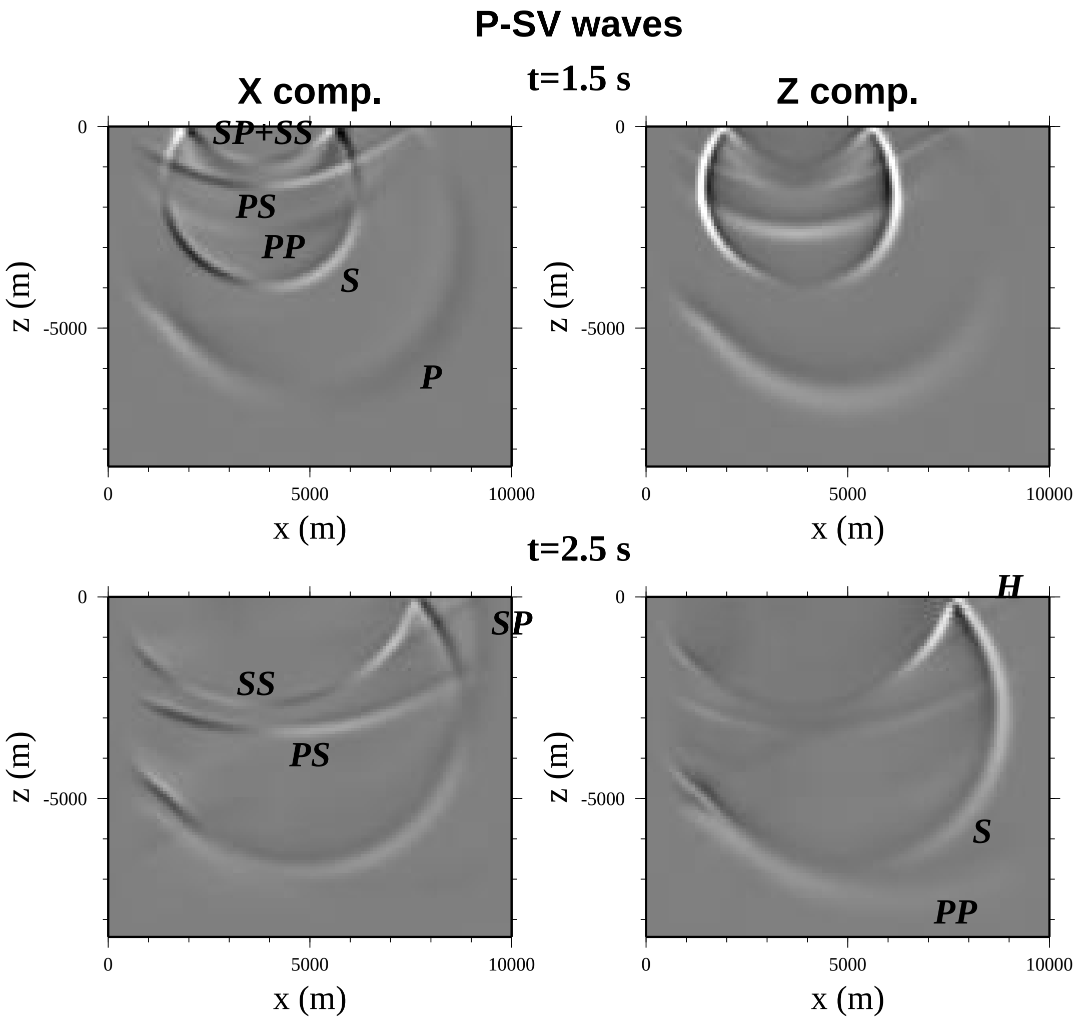

Fig. 4.6. Snapshot of *P-SV* wave propagation in the linear gradient velocity media at *t*=1.5 and 2.5 s. The wavefields respond to the gradients in structure.

4.4 Random heterogeneous media

Up to now, we have tested the wavelet-based method in simple models and shown that the method could generate good numerical responses. However, the 'real' earth has a significant variation in its mineral composition and grain size distribution due to chemical activity with depth or tectonic processes, e.g., folding, faulting (Sato & Fehler, 1998). As a result, these variations form strongly heterogeneous media in the lithosphere with significant spatial variation of physical properties such as velocities and density. These wide spatial variations of elastic properties in the lithosphere have been revealed by various geophysical and seismic studies. Also, irregular heterogeneity in a region about 200 km thick above the core-mantle boundary was revealed through seismic records (Kennett, 1983).

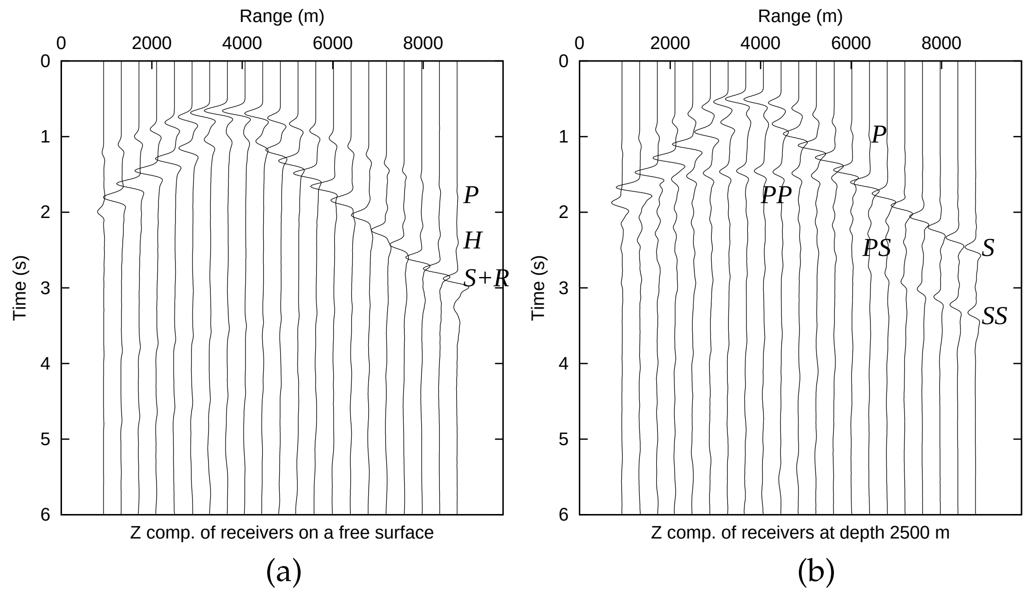

Fig. 4.7. Numerical time responses of *P-SV* waves (vertical components) in linear gradient velocity media recorded at 21 receivers placed horizontally (a) on a free surface and (b) at depth 2500 m.

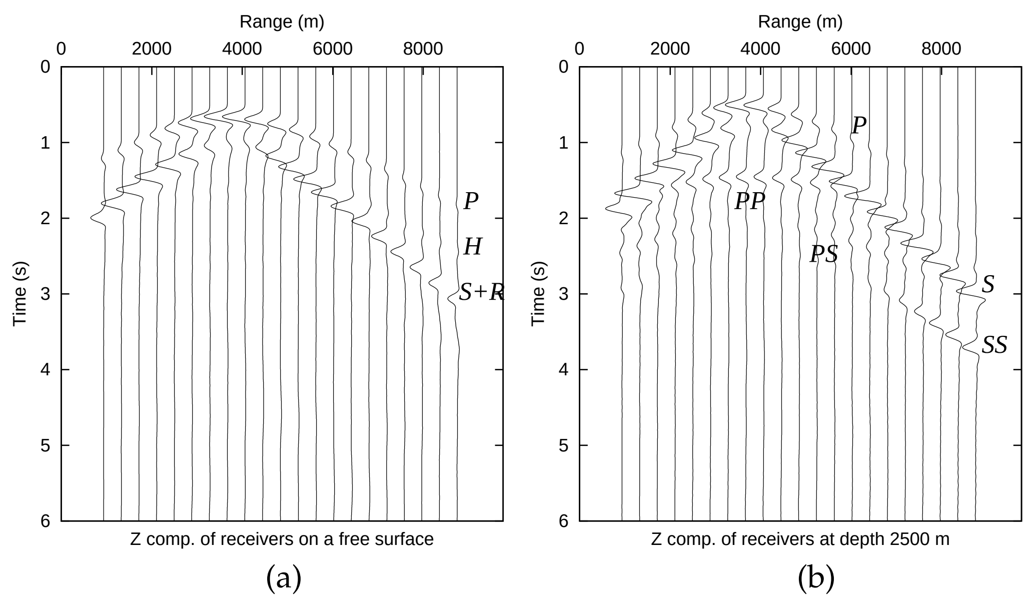

Fig. 4.8. Numerical time responses (vertical components) of elastic wave propagation in a homogeneous medium recorded at 21 receivers placed horizontally (a) on a free surface and (b) at depth 2500 m.

Even if the numerical results exhibit good agreements with analytic solutions in simple models, one can't guarantee that methods can generate the reliable numerical responses in a 'real' earth with often large variations of physical parameters just because numerical methods based on discretized grid points, such as finite difference and finite element methods, are not affected much in accuracy in simple heterogeneous media

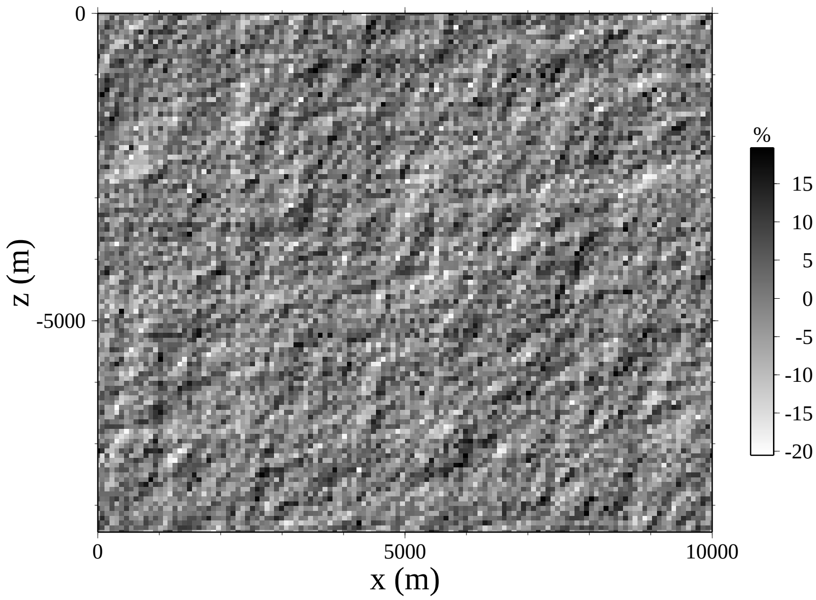

Fig. 4.9. A representation of a random perturbation of velocities using a von Karman autocorrelation function.

(e.g., two-layered media). Sato & Fehler (1998) indicated that the grid-based schemes approximate the responses of the waves through averages over many grid points in calculating spatial derivatives. Therefore, the methods become unstable in highly perturbed media. Also, Sato & Fehler provided the fact as an evidence that the numerical responses using the finite difference method show the correct arrival times but the amplitudes of waves are large compared to the expected ones.

We therefore introduce a highly perturbed medium with maximum 20 % perturbation on physical parameters which can be expected to represent an extreme for the 'real' earth for which usual grid-based methods often fail to compute accurate responses. By testing the stability of the wavelet-based method, which can compute spatial derivative exactly and stably, we show the possibility of the application of the method as a tool for the 'real' earth. For the construction of a perturbed medium, we follow the scheme of Roth & Korn (1993), see also Sato & Fehler (1998).

Fig. 4.9 shows the stochastic perturbation of P and S wave velocities added to background homogeneous medium with α=3.15 km/s, β=1.8 km/s and ρ=2.2 $\mathrm{g/cm}^3$. The systematic spatial perturbation in medium is considered by implementing a von Karman autocorrelation function with a correlation distance a =10 km. We place a compressional source inside a medium at (3750 m, 5500 m). The entire wavefields are composed of direct phase (*P*), reflected waves (*PP, PS*) from a free surface and various complex back-scattered waves (Fig. 4.10). Also, due to the generation of

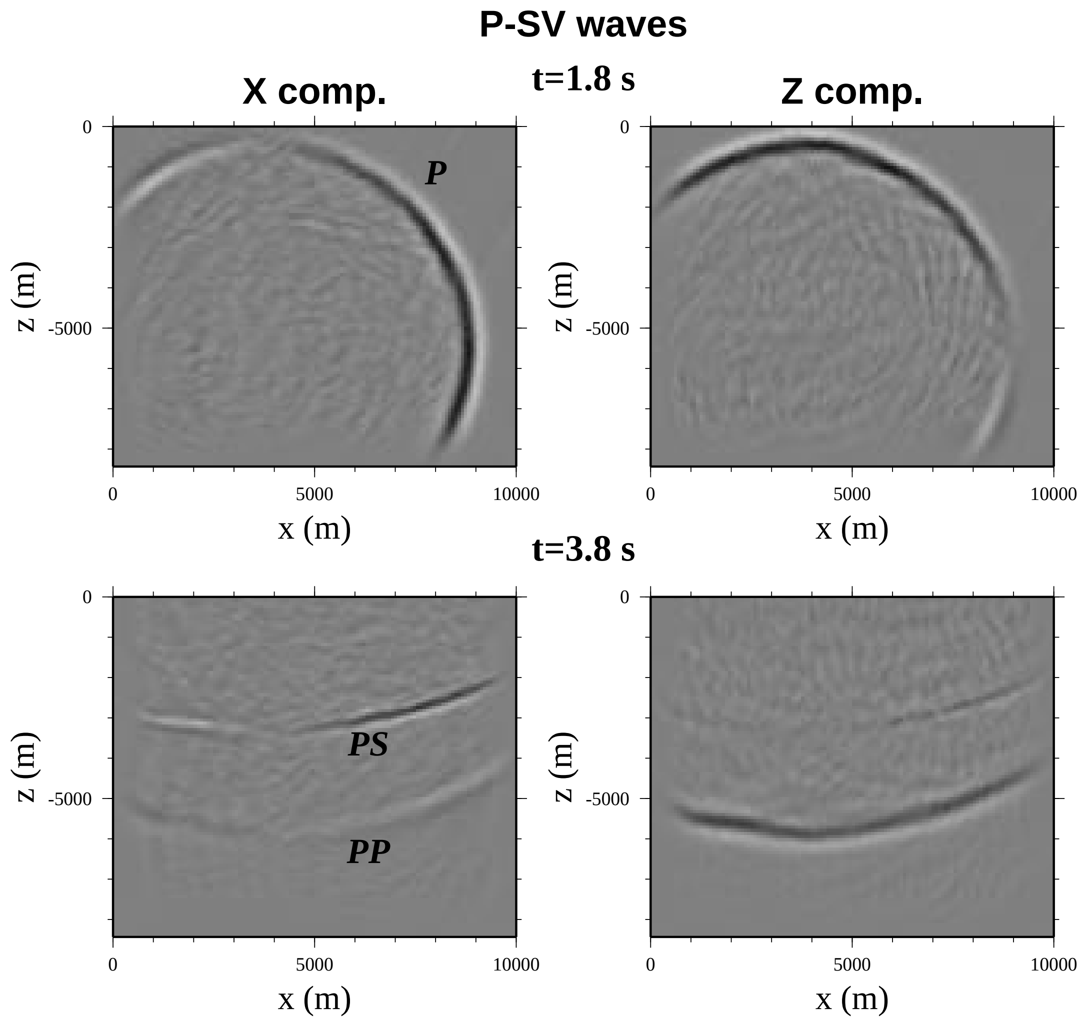

Fig. 4.10. Snapshot of *P-SV* wave propagation for a compressional source in the stochastic heterogeneous medium in Fig. 4.9 at t =1.8 and 3.8 s. The back-scattered phases develop after the direct phase *P* and the reflected phases (*PP, PS*) from a free surface exhibit distorted wavefronts.

back-scattered waves, the main phases exhibit apparent attenuation during propagation in the media. The numerical responses in the random medium are compared with those in the homogeneous medium in Fig. 4.11. The numerical responses with large amplitudes of back-scattered waves are stable throughout the time interval (Fig. 4.11).

These numerical calculations using the wavelet scheme illustrate the resilience of both P and S wavefronts in the presence of strong heterogeneity. Significant coda waves are shed and there are local perturbations of the wavefronts, but the dents are soon infilled by 'wavefront healing' (see, Igel & Gudmundsson, 1997). There is some redistribution of amplitude, but the major phases are recognizable in Figs. 4.10, 4.11 despite the substantial variations in medium properties (Fig. 4.9).

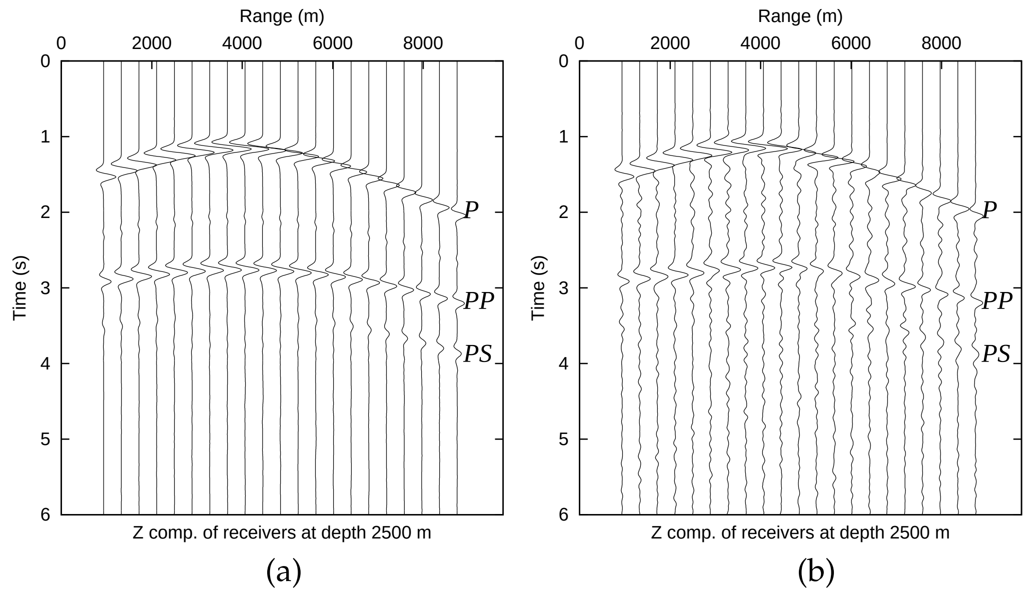

Fig. 4.11. Comparison between numerical time responses of *P-SV* waves (vertical components) (a) in a homogeneous medium and (b) in a stochastic heterogeneous medium. The 21 receivers are placed horizontally at depth 2500 m.

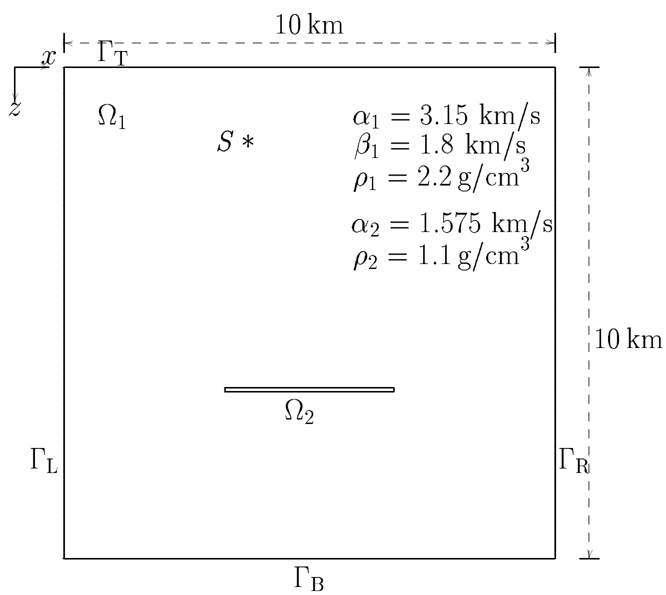

Fig. 4.12. Description of a medium with a fluid-filled crack. The compressional wave velocity and density in the crack are half of those in reference medium. The reference medium is considered as homogeneous or stochastic heterogeneous with a standard deviation by 10 %. Four artificial boundaries (Γ_T, Γ_B, Γ_R, Γ_L) are treated as absorbing boundaries.

4.5 Medium with a fluid-filled crack

Our next example is more complex, with elastic wave propagation in a medium containing a fluid-filled crack (Fig. 4.12). Such a feature with a high contrast over a

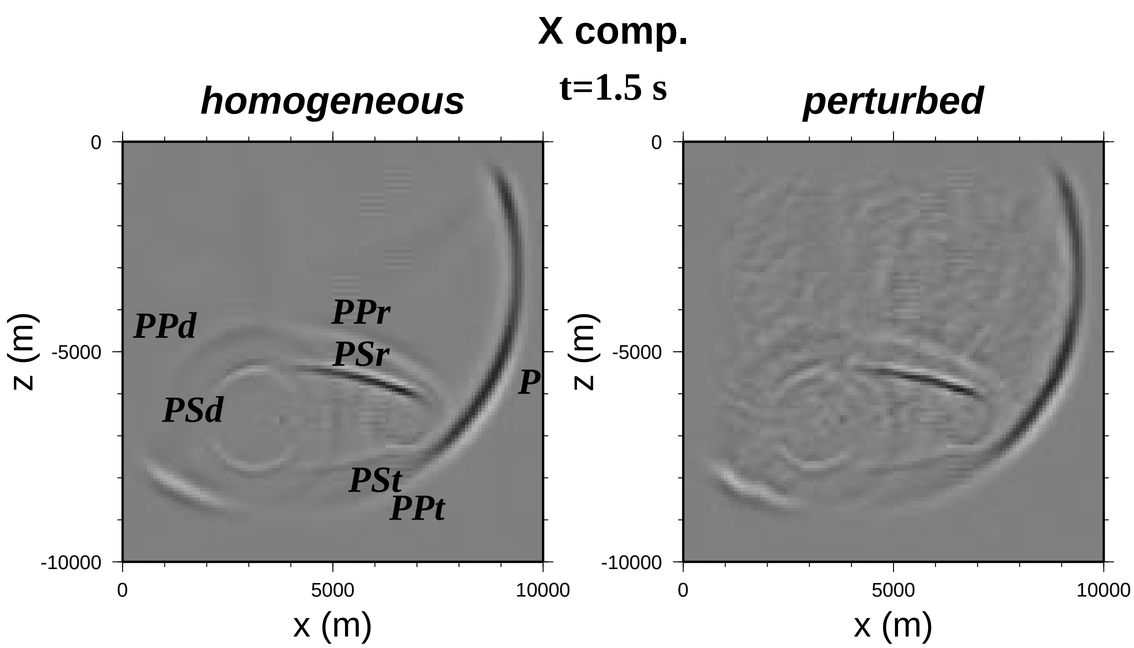

Fig. 4.13. Snapshots of elastic wave propagation in a complex medium with a fluid-filled crack for two cases; the background medium is considered either homogeneous or stochastic heterogeneous.

narrow interval presents a major challenge to traditional grid based methods because of the rapid variations in the medium. We note that the wavelet-based method can give accurate responses in a medium with highly and abruptly varying physical parameters, as demonstrated by comparison of numerical differentiation by the wavelet-based method with that achieved with a fourth-order finite difference method. The wavelet method can achieve accurate differentiation even when the higher order finite difference method is having difficulties (see, Section 7.2).

In applications to seismology we need to take account of the complex nature of the 'real' Earth with both mixtures of materials and strong local variations in seismic wave speeds. Scattered waves are a major feature of observed seismograms and the most effective quantitative way of simulating such effects is to introduce some form of stochastic representation of wave speed superimposed on a long wavelength structure (e.g., Frankel & Clayton, 1986).

We therefore compare the results for the fluid-filled crack problem with a homogeneous background medium and a heterogeneous medium where the variations in wave speed are based on the Von Karman autocorrelation function (see, Sato & Fehler, 1998) with 10 % standard deviation. A detailed description of the generation of a stochastic heterogeneous medium is given in Chapter 7.

A compressional force (S in Fig. 4.12) is applied at (3750 m, 1500 m) and the four artificial boundaries are treated as absorbing boundaries. The compressional wave velocity in main medium is 3.15 km/s, the shear wave velocity is 1.8 km/s and the density is 2.2 $\mathrm{g/cm}^3$. The crack is filled with fluid for which the compressional wave velocity and density are half of those of main medium.

Fig. 4.13 shows snapshots of the elastic wave propagation for this crack problem at $t = 1.5$ s. Reflected phases (PP_r, PS_r) from the surface of crack, transmitted phases (PP_t, PS_t) through the crack and diffracted phases (PP_d, PS_d) from both ends of the crack can be seen clearly in the results for the homogeneous background in the left panel of Fig. 4.13. For the perturbed medium in the right panel, the generated phases are mixed with scattered waves arising from the whole domain through which the P wavefront has passed, and the wavefield displays a more complex character. Such a combination of a clear initial phase and a complex coda fits well with the nature of observed seismograms.

4.6 Transversely isotropic media

The earth is generally stratified in elastic properties and transversely isotropic media can represent earth structures well. The 2-D P-SV wave equations in a transversely isotropic medium have the same form of those in isotropic media (3.5) but the stress terms are expressed by (e.g., Carcione *et al.*, 1988)

$$\begin{aligned} &\sigma_{xx} = c_{11}\frac{\partial u_x}{\partial x} + c_{13}\frac{\partial u_z}{\partial z}, \quad \sigma_{zz} = c_{13}\frac{\partial u_x}{\partial x} + c_{33}\frac{\partial u_z}{\partial z}, \\ &\sigma_{xz} = \sigma_{zx} = c_{44}\left(\frac{\partial u_x}{\partial z} + \frac{\partial u_z}{\partial x}\right), \end{aligned} \tag{4.1}$$

where c_{ij} (i, j=1,3) represents an elastic modulus written in a compressed matrix notation (e.g., Kennett, 2001, ch.8). The physical properties of medium are symmetric about the z axis, and the compressional and shear wave speeds are given by

$$\alpha_h = \sqrt{\frac{c_{11}}{\rho}}, \quad \alpha_v = \sqrt{\frac{c_{33}}{\rho}}, \quad \beta_v = \sqrt{\frac{c_{44}}{\rho}}, \quad \gamma = \sqrt{\frac{c_{13}}{\rho}}, \tag{4.2}$$

where subscripts v and h represent for vertical and horizontal propagation (e.g., Kennett, 2001) and γ, a supplementary velocity term, is introduced for the complementary description of physical properties.

The equation system for transversely isotropic media can be readily recast into a suitable form for the wavelet method following the procedure in Chapter 3. We first consider a homogeneous transversely isotropic medium with α_v=3.6 km/s, α_h=4.0 km/s, β_v=2.16 km/s, γ=1.1 km/s, and ρ=3.0 g/cm^3. The domain is composed of 128-by-128 grid points, corresponding to a 10-by-10 km medium. The top artificial boundary is

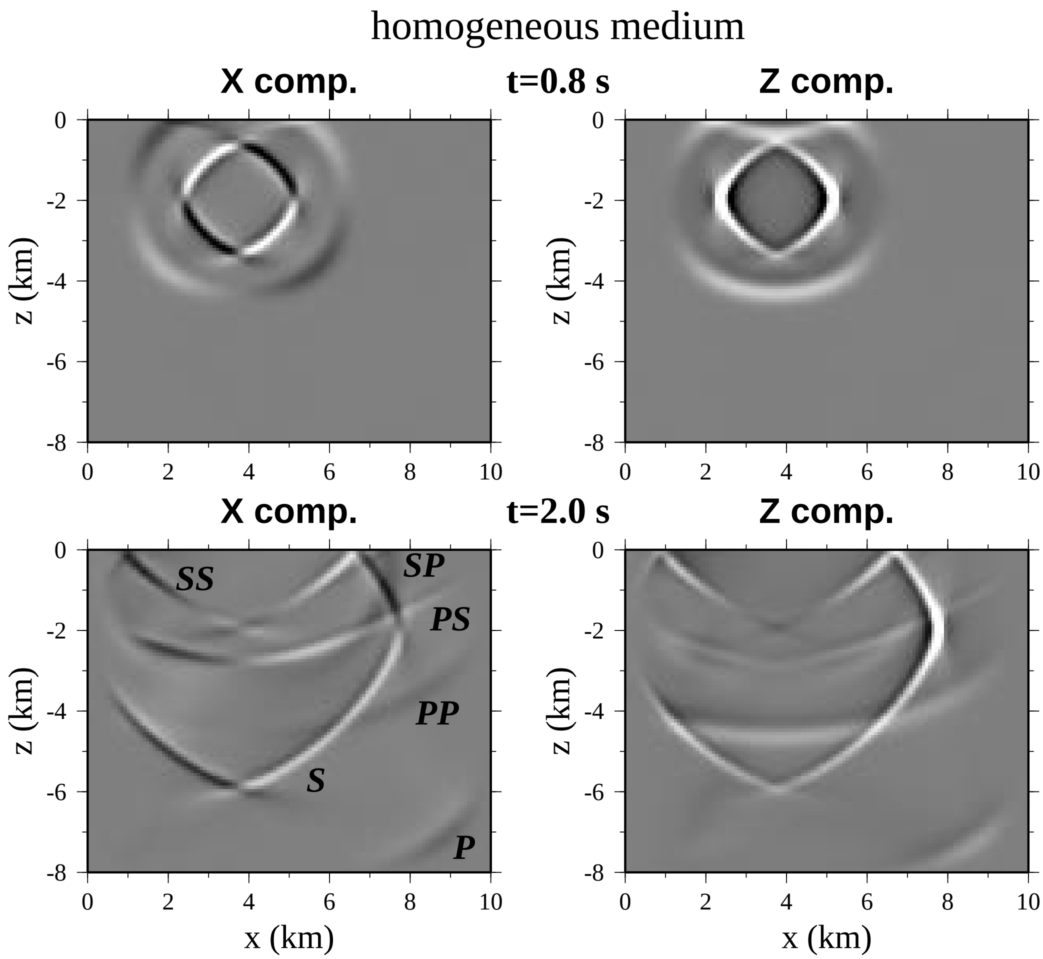

Fig. 4.14. Snapshots of *P-SV* wave propagation at t=0.8 and 2.0 s in a homogeneous transversely isotropic medium. The horizontal and vertical *P* wave velocities (α_h, α_v) are 4.0 km/s and 3.6 km/s, *S* wave velocity (β_v) is 2.16 km/s, γ (=$\sqrt{c_{13}/\rho}$) is 1.1 km/s, and the density is 3.0 g/cm^3. A vertically directed force is applied at (3.75 km, 2.0 km).

considered as a free surface and the other boundaries are treated by absorbing boundary conditions. A vertically directed point force is applied at x=3.75 km and z=2.0 km.

Fig. 4.14 displays the characteristic wavefront pattern in transversely isotropic medium. Since the horizontal *P*-wave velocity (α_h) is larger than the vertical velocity (α_v), the *P* wavefronts become flatter on the vertical axis. A similar pattern is found in the *S* wavefronts, and the reflected waves from the free surface display the wavetype coupling effect clearly.

As a challenging experiment, we consider a two-layered medium where a transversely isotropic solid layer overlies on an isotropic fluid layer. The physical properties in the upper layer are same as those of the homogeneous medium, and the compressional wave

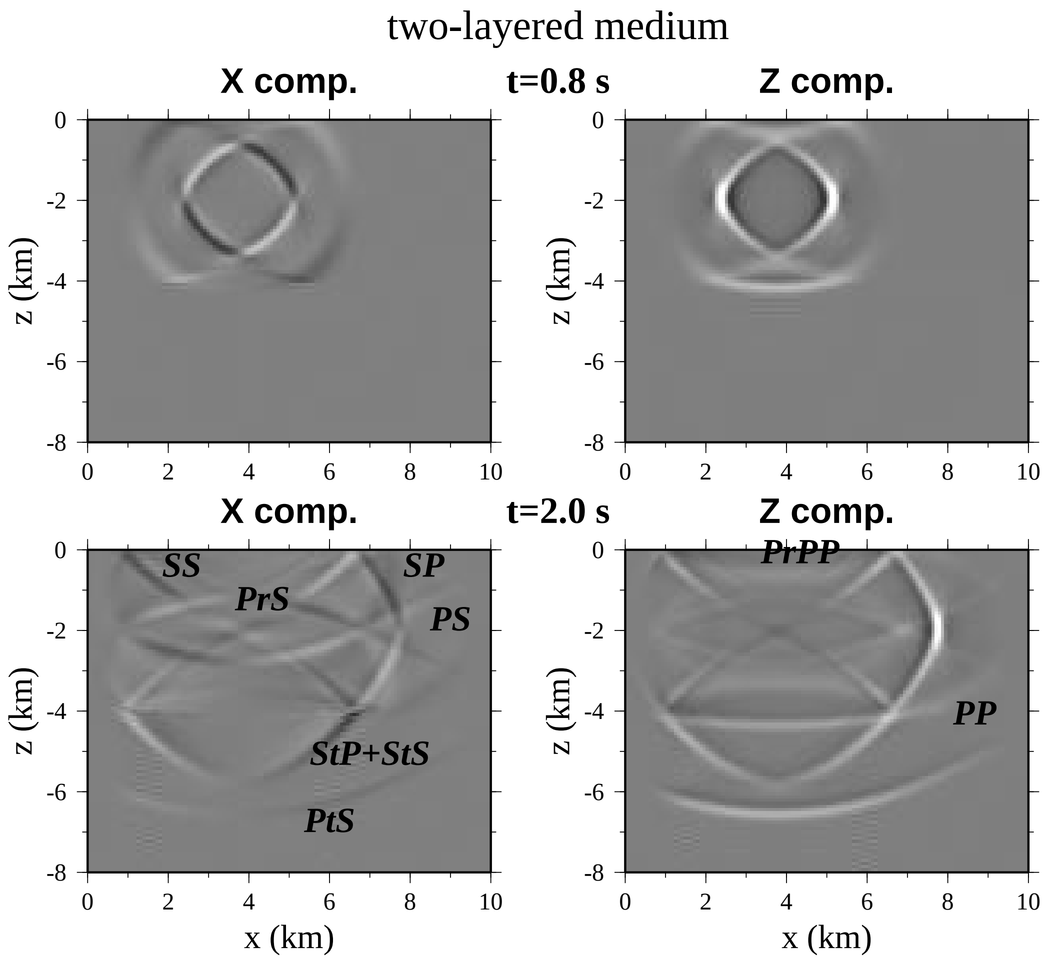

Fig. 4.15. Snapshots of *P-SV* wave propagation at t=0.8 and 2.0 s in a two-layered heterogeneous medium where a transversely isotropic solid layer overlies on isotropic fluid layer. The parameters in the upper layer are the same as those in Fig. 4.14, and the compressional velocity in the fluid layer is 2.0 km/s and the density is 1.2 g/cm^3. The planar internal boundary is placed at a depth of 4.0 km.

velocity in the fluid layer is 2.0 km/s and the density is 1.2 g/cm^3. The layer boundary is placed at depth 4 km below the free surface.

There is wavetype coupling at both boundaries (free surface, internal layer boundary), various reflected and head waves develop and propagate in the upper layer (Fig. 4.15). On the other hand, only compressional waves are present and propagate in the lower layer. The wavelet-based method generates stable wavefields in heterogeneous anisotropic medium with sharp transition of physical properties.

4.7 Discussion

We have demonstrated the way in which the wavelet projection can provide a means of coping with physical variations on small scales. For this purpose, we introduced several heterogeneous models and randomly perturbed media to test the capability of the method. The wavelet-based method works well not only in the case of a sudden variation of physical parameters at a boundary, but also for linear gradients where physical parameters are changing continuously. In particular, the strength of the approach lies in applications to complex media, e.g., a medium with a fluid-filled crack, due to compact support of the representation of differential operators with wavelets. Thus, the wavelet-based method allows a correct representation of seismic wave behavior in the crack problem with a sharp variation of physical parameters over a narrow region (defined by one row of grid points) in random media.

Also, it was shown that method provide stable time responses in a highly perturbed medium and in anisotropic media with a sharp transition in physical parameters. We expect that the method can be extended to complex media problems, including random heterogeneities and anisotropic structures, where accurate treatments of spatial derivatives are essential for stable modelling.

5

Modelling in media with surface topography

5.1 Introduction

For accurate measurement of amplification or deamplification of seismic waves in the crust, it is important to take account of surface-topography in seismic modelling. The consideration of surface topography in seismic modelling has been a challenging issue for most numerical techniques, and numerous studies have considered the problem.

Although finite difference techniques may treat a simple geometry for topography with accuracy, it is not a trivial problem to consider a complex surface topography. Generally, as the geometry becomes more complicated, the scheme displays lower accuracy of results and has restriction in consideration of perturbation in media. Of course, for the consideration of arbitrary complex topography, there were trials in finite-difference community (e.g., Jih *et al.*, 1988, Ohminato & Chouet, 1997).

Jih *et al.* (1988) approximated surface topography with various sizes of triangle grids, and satisfied the free-surface conditions in a rotated coordinate system parallel to the surface topography. This approach appears promising, but has limitation for larger Poisson ratios and also heterogeneities can not be considered around the surface.

Ohminato & Chouet (1997) introduced a simple scheme for arbitrary surface topography. They manipulate the value of the vertically differentiated normal stress field at the free surface (i.e., $\partial_z \sigma_{zz}|_{z=0}$) by a factor of two, so that the normal stress at the free surface is equivalent to that above free surface. The stresses above free surface are determined to be vanished since the Lamé coefficients are set to zero in the scheme. However, the scheme does not satisfy the traction-free boundary condition exactly (i.e., vanishing of normal stress), but rather fulfills the required condition in an approximate way by setting very fine grid steps in the domain. Therefore, they needed 25 grids per wavelength for stable computation. As a result, this method needs huge computational labour and memory, and thus the method may not be suitable for large scale seismic modelling.

The finite element method has an attractive strong point since it can satisfy naturally the traction-free boundary conditions including surface topography. However, finite element methods exhibit numerical dispersion in low-order schemes and can generate spurious waves with higher-order schemes (Komatitsch & Vilotte, 1998).

Combining the strong points of finite difference and finite element methods, Moczo *et al.* (1997) introduced a hybrid modelling technique that applies the finite element method for the computation in near surface structures and the finite difference method to the other media. However, this technique needs a restricted condition in generation of grid system for the finite difference method and mesh for finite element method.

Another hybrid method based on the boundary-integral method and the discrete wavenumber method has been introduced for modelling in media with topography (Bouchon *et al.*, 1996). This semi-analytic technique can model topographic effects, e.g., diffraction, on elastic waves accurately. However, this technique still has difficulty in the treatment of arbitrary non-layered heterogeneities inside a medium.

The Chebyshev-spectral method can incorporate the traction-free conditions easily unlike spectral (or, Fourier) method. In particular, Tessmer *et al.* (1992) presented a technique based on a grid generation (or, grid mapping) scheme for the implementation of the free surface conditions for surface topography in the Chebyshev-spectral modelling.

We apply the grid generation scheme to the wavelet-based method and see the applicability in topographic structures. In order to validate the scheme, we compare numerical results with analytic solutions in an inclined medium, and show the stability of the method in media for highly varying topography by reducing the number of grid points describing the topography.

5.2 Grid generation scheme

To treat a medium with topography in the wavelet-based method, we introduce a grid generation technique (or, grid-mapping technique; Tessmer *et al.*, 1992); a rectangular grid system can be mapped into a curved grid system considering physical topography by using an one dimensional linear stretch in the vertical direction. For convenience, we set the topography of the bottom artificial boundary to be same as that of the free surface and stretch the grids from the free surface to the lower artificial boundary. So, the function of grid mapping from a ξ-η coordinate system to a x-z coordinate system is given by

$$
\begin{aligned}
x(\xi, \eta) &= \xi, \\
z(\xi, \eta) &= z_0(\xi) + \eta,
\end{aligned} \tag{5.1}
$$

where $z_0(\xi)$ is a topography of a free surface which depends on only ξ, and the rectangular domain size is considered to be normalized so as to satisfy $0 < \xi, \eta \leq 1$.

The spatial derivatives of any variable g in a physical grid system can be represented using a chain rule by

$$
\begin{aligned}
\frac{\partial g}{\partial x} &= \frac{\partial \xi}{\partial x}\frac{\partial g}{\partial \xi} + \frac{\partial \eta}{\partial x}\frac{\partial g}{\partial \eta}, \\
\frac{\partial g}{\partial z} &= \frac{\partial \xi}{\partial z}\frac{\partial g}{\partial \xi} + \frac{\partial \eta}{\partial z}\frac{\partial g}{\partial \eta},
\end{aligned} \tag{5.2}
$$

where the matrices of the transformation is given by

$$
\begin{aligned}
\frac{\partial \xi}{\partial x} &= J\frac{\partial z}{\partial \eta}, \quad \frac{\partial \xi}{\partial z} = -J\frac{\partial x}{\partial \eta}, \\
\frac{\partial \eta}{\partial x} &= -J\frac{\partial z}{\partial \xi}, \quad \frac{\partial \eta}{\partial z} = J\frac{\partial x}{\partial \xi},
\end{aligned} \tag{5.3}
$$

and the Jacobian J is

$$
J = 1 \Bigg/ \left(\frac{\partial x}{\partial \xi}\frac{\partial z}{\partial \eta} - \frac{\partial x}{\partial \eta}\frac{\partial z}{\partial \xi} \right) = 1. \tag{5.4}
$$

Therefore, from (5.3) and (5.4), equation (5.2) can be rewritten as

$$
\begin{aligned}
\frac{\partial g}{\partial x} &= \frac{\partial g}{\partial \xi} - \frac{\partial z_0}{\partial \xi}\frac{\partial g}{\partial \eta}, \\
\frac{\partial g}{\partial z} &= \frac{\partial g}{\partial \eta}.
\end{aligned} \tag{5.5}
$$

Using (5.5), we can rewrite the linear operator ($\mathcal{L}_{ij},\ i, j = x, z$) for elastic wave equations in (3.8) with the remapped coordinate scheme:

$$
\begin{aligned}
\mathcal{L}_{xx} &= \frac{1}{\rho}\left[\frac{\partial}{\partial \xi} - \frac{\partial z_0}{\partial \xi}\frac{\partial}{\partial \eta}\right]\left[(\lambda+2\mu)\frac{\partial}{\partial \xi} - (\lambda+2\mu)\frac{\partial z_0}{\partial \xi}\frac{\partial}{\partial \eta}\right] + \frac{1}{\rho}\frac{\partial}{\partial \eta}\left[\mu\frac{\partial}{\partial \eta}\right], \\
\mathcal{L}_{xz} &= \frac{1}{\rho}\frac{\partial}{\partial \eta}\left[\mu\frac{\partial}{\partial \xi} - \mu\frac{\partial z_0}{\partial \xi}\frac{\partial}{\partial \eta}\right] + \frac{1}{\rho}\left[\frac{\partial}{\partial \xi} - \frac{\partial z_0}{\partial \xi}\frac{\partial}{\partial \eta}\right]\left[\lambda\frac{\partial}{\partial \eta}\right], \\
\mathcal{L}_{zx} &= \frac{1}{\rho}\frac{\partial}{\partial \eta}\left[\lambda\frac{\partial}{\partial \xi} - \lambda\frac{\partial z_0}{\partial \xi}\frac{\partial}{\partial \eta}\right] + \frac{1}{\rho}\left[\frac{\partial}{\partial \xi} - \frac{\partial z_0}{\partial \xi}\frac{\partial}{\partial \eta}\right]\left[\mu\frac{\partial}{\partial \eta}\right], \\
\mathcal{L}_{zz} &= \frac{1}{\rho}\left[\frac{\partial}{\partial \xi} - \frac{\partial z_0}{\partial \xi}\frac{\partial}{\partial \eta}\right]\left[\mu\frac{\partial}{\partial \xi} - \mu\frac{\partial z_0}{\partial \xi}\frac{\partial}{\partial \eta}\right] + \frac{1}{\rho}\frac{\partial}{\partial \eta}\left[(\lambda+2\mu)\frac{\partial}{\partial \eta}\right].
\end{aligned} \tag{5.6}
$$

For numerical stability, we continue to use a locally homogeneous medium around the source. Following the scheme in Chapter 3, we assume physical parameters (λ, μ, ρ) are constant in the source region and therefore the linear operators $\mathcal{L}^h_{ij}$ $(i, j = x, z)$ for the source region can be written as

$$
\begin{aligned}
\mathcal{L}^h_{xx} &= \frac{\lambda+2\mu}{\rho}\frac{\partial^2}{\partial\xi^2} - \frac{\lambda+2\mu}{\rho}\frac{\partial^2 z_0}{\partial\xi^2}\frac{\partial}{\partial\eta} - \frac{2(\lambda+2\mu)}{\rho}\frac{\partial z_0}{\partial\xi}\frac{\partial^2}{\partial\xi\partial\eta} \\
&\quad + \left[\frac{\lambda+2\mu}{\rho}\left(\frac{\partial z_0}{\partial\xi}\right)^2 + \frac{\mu}{\rho}\right]\frac{\partial^2}{\partial\eta^2}, \\
\mathcal{L}^h_{xz} &= \mathcal{L}^h_{zx} = \frac{\lambda+\mu}{\rho}\frac{\partial^2}{\partial\xi\partial\eta} - \frac{\lambda+\mu}{\rho}\frac{\partial z_0}{\partial\xi}\frac{\partial^2}{\partial\eta^2}, \\
\mathcal{L}^h_{zz} &= \frac{\mu}{\rho}\frac{\partial^2}{\partial\xi^2} - \frac{\mu}{\rho}\frac{\partial^2 z_0}{\partial\xi^2}\frac{\partial}{\partial\eta} - \frac{2\mu}{\rho}\frac{\partial z_0}{\partial\xi}\frac{\partial^2}{\partial\xi\partial\eta} + \left[\frac{\mu}{\rho}\left(\frac{\partial z_0}{\partial\xi}\right)^2 + \frac{\lambda+2\mu}{\rho}\right]\frac{\partial^2}{\partial\eta^2}.
\end{aligned}
\tag{5.7}
$$

To satisfy the traction-free boundary conditions on a free surface in a medium with topography, we consider stress terms on a rotated local coordinate system (x', z') where the z' axis is perpendicular and the x' axis is parallel to the tangent to the free surface. The angle of rotation (θ) is determined by the rate of variation of local topography compared to the horizontal distance (ξ) in the rectangular grid system:

$$
\theta = \tan^{-1}\left(\frac{\partial z_0(\xi)}{\partial\xi}\right), \tag{5.8}
$$

where $z_0(\xi)$ is the topography of the surface as a function of horizontal position (ξ).

The relationships among the stress components in the physical coordinate system and a rotated local coordinate system are given by (see, Tessmer *et al.*, 1992)

$$
\sigma_{ij} = \sum_m \sum_n a_{mi} a_{nj} \sigma'_{mn}, \tag{5.9}
$$

and

$$
\sigma'_{ij} = \sum_m \sum_n a_{im} a_{jn} \sigma_{mn}, \tag{5.10}
$$

where $i, j, m, n = x, z$ and the directional cosines are

$$
\begin{pmatrix} a_{xx} & a_{xz} \\ a_{zx} & a_{zz} \end{pmatrix} = \begin{pmatrix} \cos\theta & \sin\theta \\ -\sin\theta & \cos\theta \end{pmatrix}. \tag{5.11}
$$

From (5.9), we can estimate σ'_{mn} using σ_{ij}. As σ'_{xz} and σ'_{zz} are zero on the free surface, we can write equivalent force terms for a free surface boundary using σ_{jz} ($j = x, z$) in the form:

$$
\begin{aligned}
\mathcal{N}(u_x) &= \mathcal{N}(u_z) = 0, \\
\mathcal{N}(v_x) &= \frac{1}{\rho}\left\{f_x - \frac{\partial}{\partial x}\Sigma^F_{xx} - \frac{\partial}{\partial z}\Sigma^F_{xz}\right\}, \\
\mathcal{N}(v_z) &= \frac{1}{\rho}\left\{f_z - \frac{\partial}{\partial x}\Sigma^F_{xz} - \frac{\partial}{\partial z}\Sigma^F_{zz}\right\},
\end{aligned}
\tag{5.12}
$$

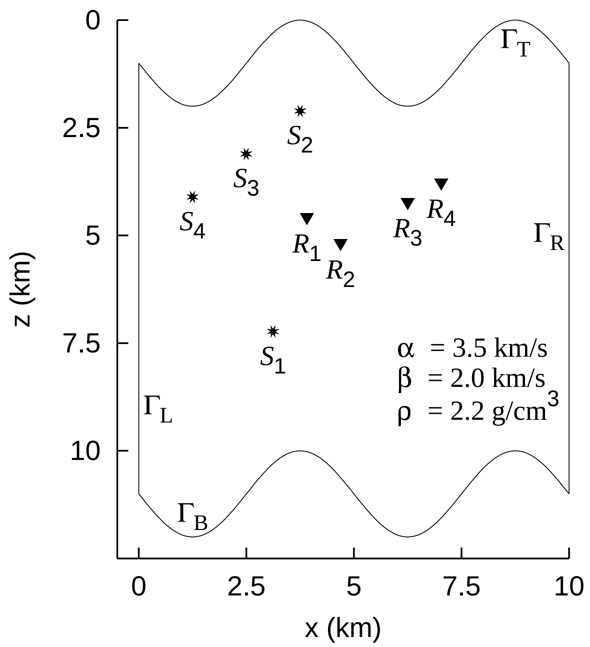

Fig. 5.1. Description of a 2-D homogeneous elastic medium with topography. For an accuracy test in an unbounded medium with a vertically directed force at S_1, four artificial boundaries (Γ_T, Γ_B, Γ_L, Γ_R) are treated as absorbing boundaries and numerical results from four receivers (R_1, R_2, R_3, R_4) are compared with analytic solutions (Section 5.3). In numerical modelling of seismic wave propagation in the medium for three different source positions (S_2, S_3, S_4), the top boundary (Γ_T) is considered as a free surface (Section 5.4).

where Σ_{ij}^F $(i, j = x, z)$ is the composite effects of the stress components at the free surface which can be computed from (3.32) and (5.9) by

$$\begin{aligned}
\Sigma_{xx}^F &= \delta(z)\left(\sigma_{xx} - \cos^2\theta\ {\sigma'}_{xx}^M\right), \\
\Sigma_{xz}^F &= \delta(z)\left(\sigma_{xz} - \sin\theta\cos\theta\ {\sigma'}_{xx}^M\right), \\
\Sigma_{zz}^F &= \delta(z)\left(\sigma_{zz} - \sin^2\theta\ {\sigma'}_{xx}^M\right).
\end{aligned} \tag{5.13}$$

Here, ${\sigma'}_{xx}^M$ is a corrected stress term (see, Section 3.4.2) for σ'_{xx} at a free surface in a rotated local coordinate system including the effect of topography

$${\sigma'}_{xx}^M = \frac{(\lambda + 2\mu)\sigma'_{xx} - \lambda\sigma'_{zz}}{\lambda + 2\mu}, \tag{5.14}$$

where the stress components σ'_{jz} $(j = x, z)$ on the free surface can be computed from (5.10).

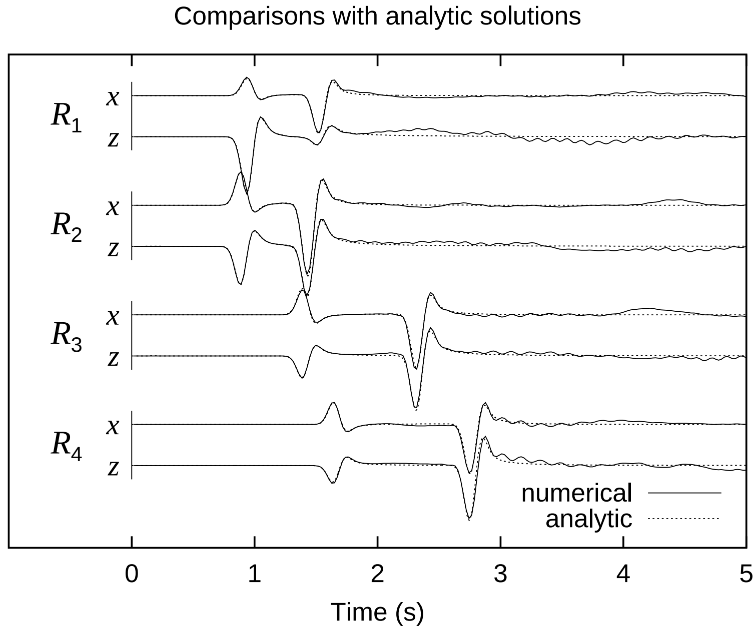

Fig. 5.2. Comparisons with analytic solutions in a homogeneous unbounded medium represented by a grid system with sinusoidal topography.

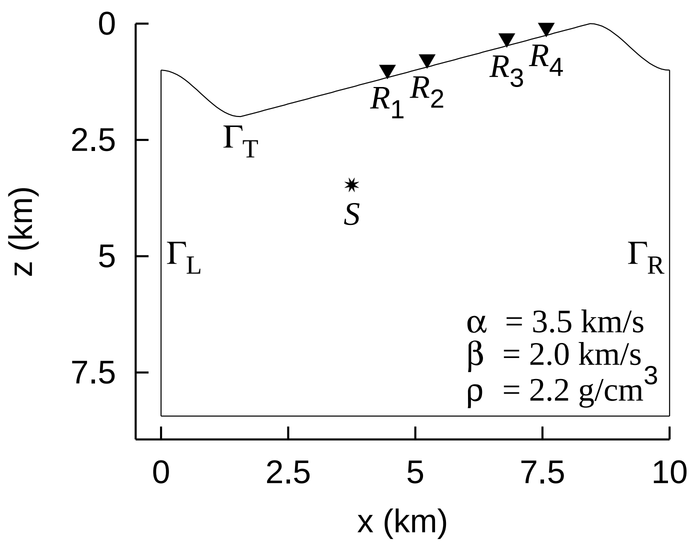

Fig. 5.3. Description of a homogeneous elastic medium with a inclined free surface. A line force (S) normal to the free surface is applied at a depth of 2 km and four receivers (R_1, R_2, R_3, R_4) on a free surface record numerical responses to be compared with analytic solutions.

5.3 Validation tests for surface topography

We introduce an unbounded elastic medium with a sinusoidal internal topography (see, Fig. 5.1); i.e., the internal horizontal grids are set to be sinusoidal. For this purpose, we consider four artificial boundaries ($\Gamma_{\mathrm{T}}, \Gamma_{\mathrm{B}}, \Gamma_{\mathrm{L}}, \Gamma_{\mathrm{R}}$) with absorbing boundary conditions.

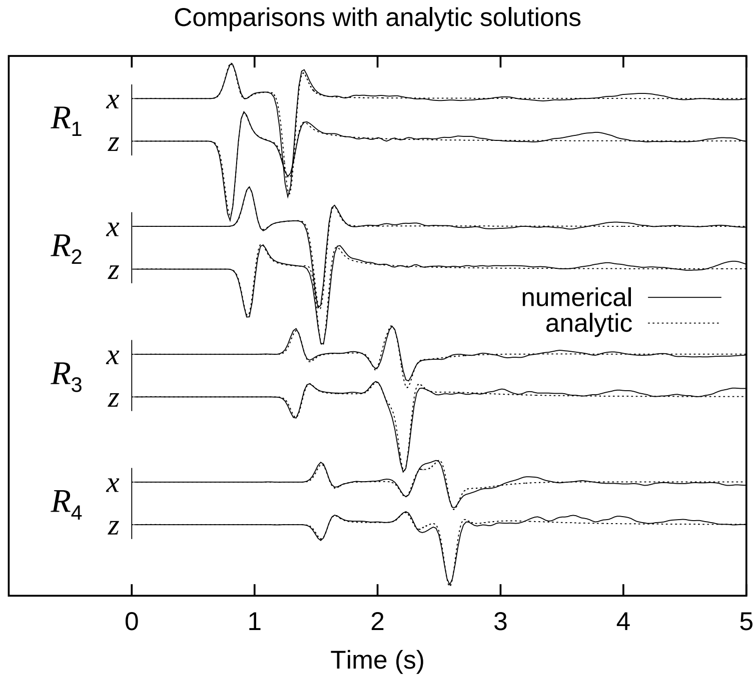

Fig. 5.4. Comparisons of numerical responses with analytic solutions at four receivers (R_j, $j = 1, 2, 3, 4$, in Figure 5.3) in a homogeneous medium with an inclined free surface.

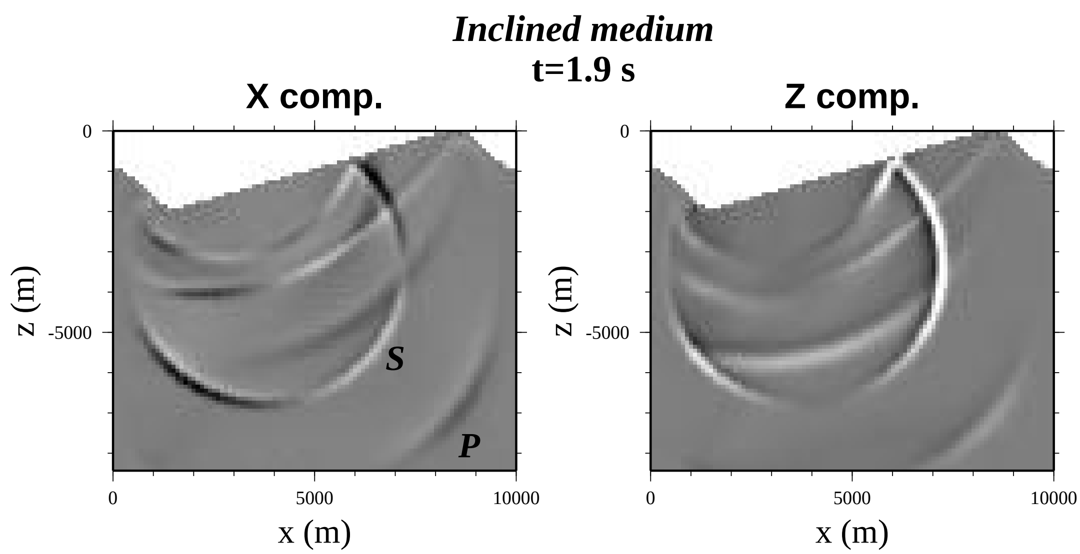

Fig. 5.5. Snapshots of elastic wave propagation in a homogeneous media with a inclined free surface at *t*=1.9 s.

The material properties are as in Section 3.8.2 with a Poisson ratio of 0.26. The period of sinusoidal topography is 5 km and the amplitude is 1 km. A vertically directed force (S_1 in Fig. 5.1) is applied at (3125 m, 3125 m) from the left and bottom boundaries and four receivers (R_j, $j = 1, 2, 3, 4$) at (3906 m, 5469 m), (4688m, 5469 m), (6250 m, 7813 m), (7031m, 7813 m) from the left and bottom boundaries record the numerical response. As we see in Fig. 5.2 a good match is achieved between the numerical seismograms using the grid-remapping and the analytic solutions (Pilant, 1979) for an unbounded domain. The ripples in the numerical solution at later time in the shear wave portion of the response arise from the discretization of the sinusoidal grids and could be reduced by finer discretization of the medium.

Next, we consider the more difficult problem of an elastic medium with topography at the free surface. We introduce a model where analytic solutions can be obtained; a homogeneous medium with an inclined free surface and a line force which is normal to the topography. The analytic solutions can be computed from those of Lamb's problem for a planar surface as in Section 3.8.2 via suitable rotation of a coordinate system.

The line force normal to the surface is introduced at (3750 m, 2000 m) from the left and top boundaries and four receivers (R_j, $j = 1, 2, 3, 4$) are placed on the free surface at distance $x =$ 4453, 5234, 6797, 7578 m from left boundary (see, Fig. 5.3). In the numerical model we need to have periodicity and so the slanted boundary has to be connected at each end with a hill and valley structure. The comparisons between the numerical and analytic results at the four receivers in Fig. 5.4, exhibit a good match for the time window before any interaction occurs with the edges of the topography. The more distant receivers (R_3, R_4) display some amplitude discrepancy in the S waves due to effects of reflected waves from the hill near right boundary Γ_{R} (see, Fig. 5.5) which are not included in the analytic results.

5.4 Elastic wave propagation in media with a sinusoidal surface topography

The results of our validation tests of the wavelet-based method for the topographic-media scheme, indicate that the method can be expected to generate accurate responses in complex-topography problems with sufficiently fine discretization. However, it is also important to check the stability of the method with regard to the discrete representation of the topography, we therefore consider two cases of sinusoidal topography: with low frequency and high frequency variations.

First we consider the case with long wavelength surface topography, with the same form and material properties as in Section 5.3, and implement line forces at three different positions; sources beneath the crest (S_2 in Fig. 5.1), on the side of the hill (S_3) and in a trough (S_4). All forces are applied at (3750 m, 2000 m) from the left and top boundaries (i.e., the sinusoidal topography is shifted relative to the line-force positions). The top boundary (Γ_{T}) is considered as a free surface in these examples. We see from Fig. 5.6, that the position of source has a very strong influence on the character of the elastic wavefield.

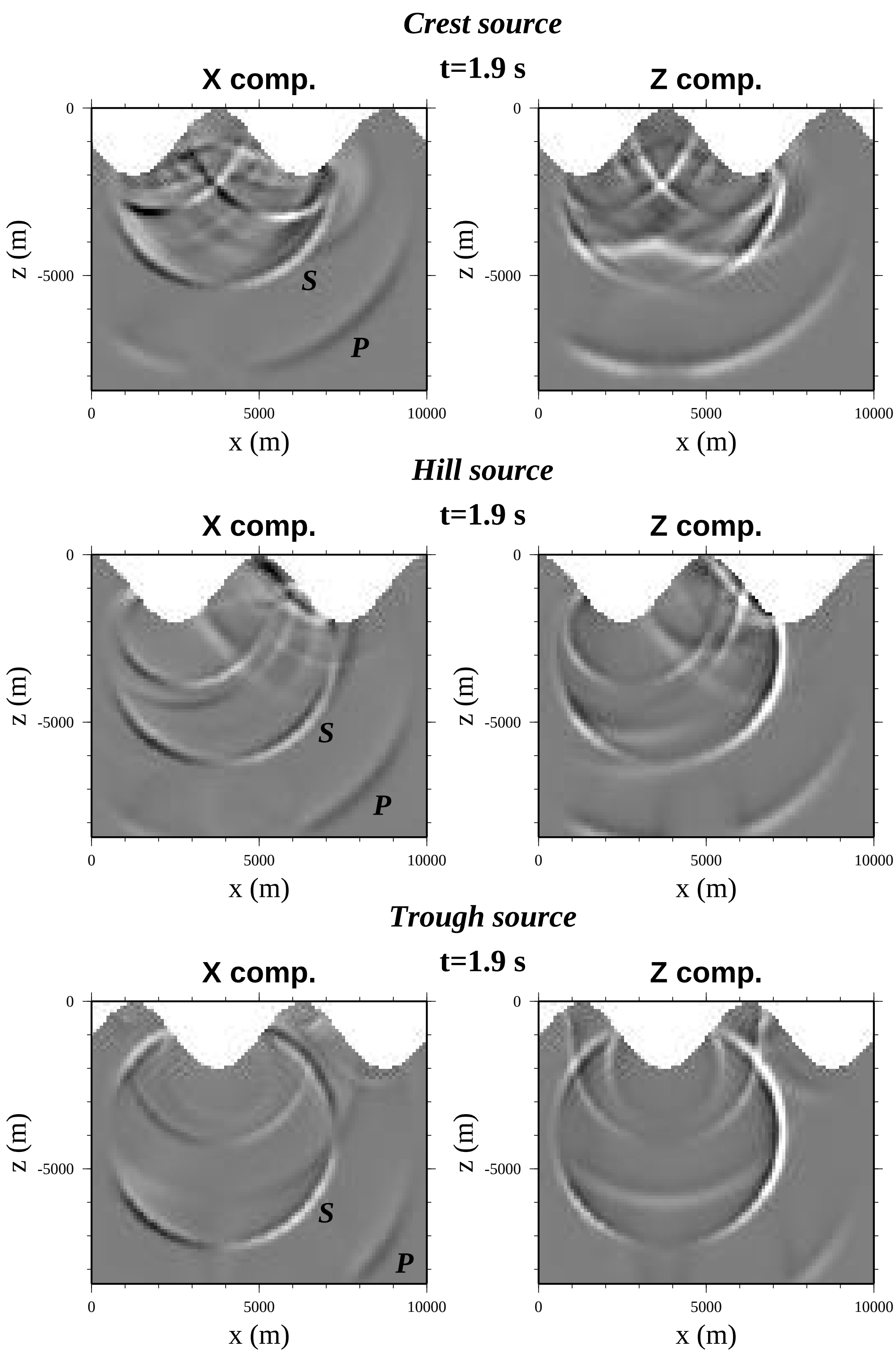

Fig. 5.6. Snapshots of elastic wave propagation in a medium with a 4π sinusoidal topographic surface at t=1.9 s. Vertically directed forces are applied at three characteristic positions; beneath the crest, on the flank of the hill and at the trough.

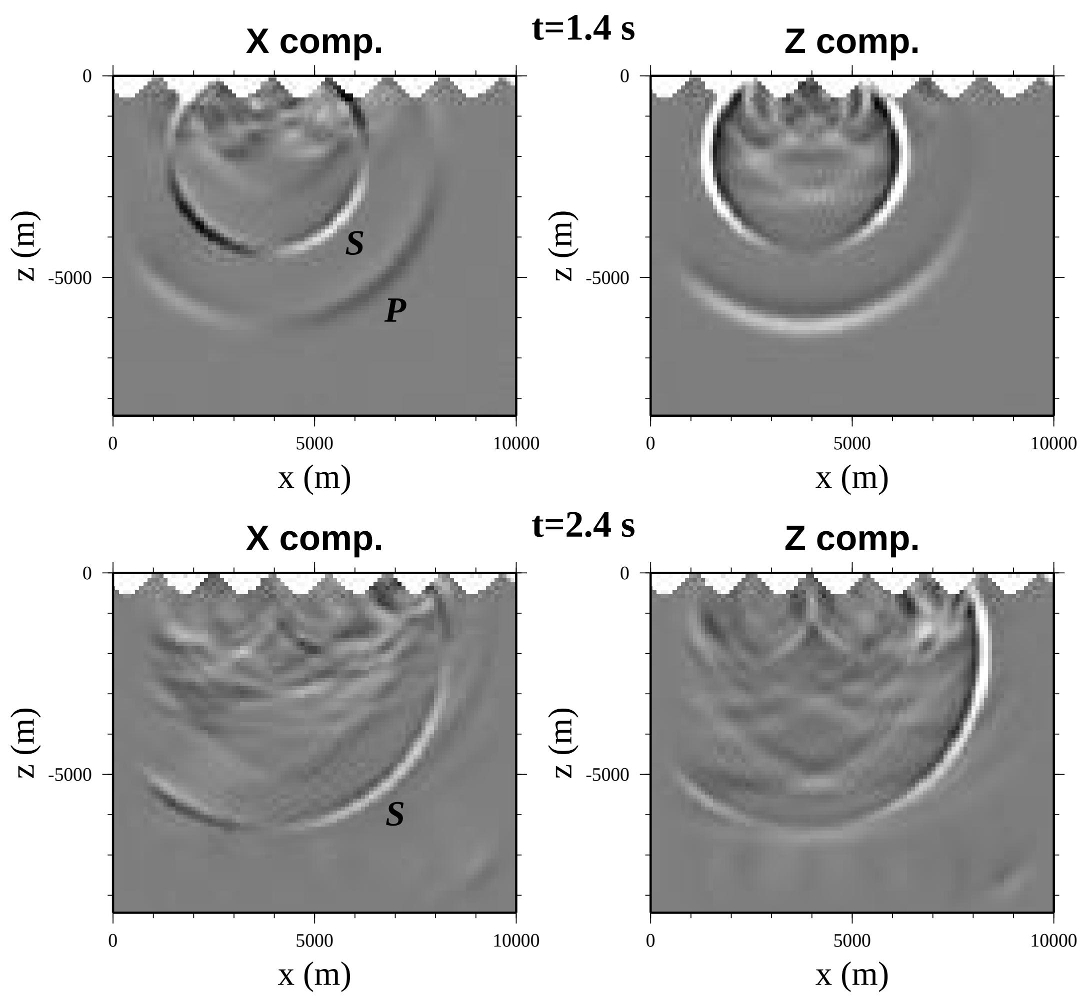

Fig. 5.7. Snapshots of elastic wave propagation in a medium with a highly varying sinusoidal topography (14π) at t=1.4, 2.4 s.

The main P and S phases are well developed in all cases but the secondary phases are rather different. Internal reflected waves can be generated inside the "hills", and there is also the possibility of body waves produced by conversion from the Rayleigh waves propagating along the sinusoidal free-boundary. The influence of the discretization is minor at this scale.

For the case with high frequency surface topography we consider a sinusoidal surface with 1428 m wavelength and an amplitude of 250 m. This leads to 9.1 grid points each period of the topography for the 128×128 grid system. Fig. 5.7 shows snapshots of elastic wave propagation in the medium at $t = 1.4, 2.4$ s, and the wavefields generated are stable throughout domain as would be expected from the analysis in Section 3.9. The effect of the topography is to produce a complex pattern of scattered phases following the S wave.

There is now some influence from the coarse discretization of the surface, the small stair steps lead to irregularities in the coda.

5.5 Discussion

We introduced a grid generation scheme for the wavelet-based method In order to treat topography of media, the wavelet-based method was augmented with a grid generation scheme which maps a rectangular grid system to one fitting to the nature of the medium. The free surface condition could be satisfied by rotating appropriately the condition for planar media.

The technique was validated through comparisons between numerical results and analytic solutions in unbounded medium represented by sinusoidal grid lines and a medium with a slanted free surface. The comparisons with analytic results show that the numerical scheme is accurate. Through experiments in modelling in media with sinusoidal topography, we have shown that the stability of the wavelet-based method allows a sparse grid step in the representation of topography. In the experiment, the surface waves are found to convert progressively to body waves during propagation following the topography. By considering the spatial derivatives which are required in the grid mapping scheme, with the wavelet technique it is possible to incorporate complicated rough topography. Thus, the wavelet method can be implemented for the understanding of seismic waves in complex media and for the extraction of quantitative physical information.

6

Modelling including dynamic sources in tectonic regions

6.1 Introduction

Tectonic regions are associated with complex and faulted structures which can bring material with considerable contrast in properties into close proximity. Earthquakes are initiated in regions of considerable heterogeneity which needs to be taken into account in the description of the generation of seismic waves by the source. Small distortions in the wavefield associated with systematic structure can lead to substantial differences on further propagation (e.g. Li & Vidale, 1996).

It is therefore necessary to develop techniques which can consider sources in a heterogeneous environment and which do not depend on the commonly used assumption of local homogeneity near the source (e.g., Alterman & Karal, 1968; Kelly *et al.*, 1976; Levander, 1988). In many circumstances such an approximation can work well when waves propagate from a simple into a more complex zone (e.g., Yomogida & Etgen, 1993), but may be misleading where the source region itself is complex.

Two representative regions in the earth where tectonic processes develop strongly heterogeneous structures in which earthquakes initiate are fault and subduction zones. Many different styles of numerical techniques have been used to simulate the propagation of seismic waves in such regions. Finite difference methods have been used in investigating trapped waves in fault zones (Li & Vidale, 1996; Igel *et al.*, 2002) and guided waves in a subduction zone with an accretionary prism (Shapiro *et al.*, 2000). To study waveform and amplitude variations associated with subduction zones, Vidale (1987) applied a coupled finite-difference and Kirchhoff method, Furumura & Kennett (1998) implemented a pseudospectral method, and Cormier (1989) and Sekiguchi (1992) used Gaussian-beam methods.

Classical finite difference techniques (e.g., Alterman & Karal, 1968) generally need more grid points per wavelength than other methods implementing a high-accuracy differentiation scheme (e.g., the pseudospectral method). Since a large region needs to be considered for subduction zone modelling memory requirements are high. If strong heterogeneity needs to be modelled, numerical dispersion is likely. Higher-order finite difference techniques (Igel *et al.*, 1995; Falk *et al.*, 1998), cure most of the limitations in classical finite difference methods, but require the source time functions to be smooth enough to be differentiated many times. This requirement makes it difficult to handle dislocation sources whose displacement time functions are complicated and may well not be differentiable.

The Gaussian-beam method is attractive because of its low computational cost for simple situations because it is built on the framework of ray theory, with the superposition of all Gaussian beams passing through the neighbourhood of a point. However, in zones of high heterogeneity the ray tracing itself becomes a daunting task. Further, it is difficult to include all necessary secondary phases which may affect the waveforms, such as interface waves along a zone of contrast such as the boundary of a subducting slab.

As we have discussed in the previous sections, the pseudospectral method (or Fourier method, Kosloff, *et al.*, 1984) has a difficulty in implementing the traction-free condition on a free surface effectively, and the Chebyshev spectral method (Kosloff *et al.*, 1990) suffers from a nonuniform spatial grid spacing in the vertical direction imposed from the character of the Chebyshev polynomials.

The wavelet-based method (WBM) has been introduced for modelling of elastic wave propagation in Chapters 2, 3. Because the representation of differential operators is carried to high accuracy, the WBM approach is very effective for describing propagation through highly heterogeneous random media retaining both accuracy and stability (see, Chapter 7). In this chapter, we consider the extension of the WBM to a general source representation (such as dislocation sources) embedded in heterogeneous zones. The treatment of heterogeneity is based on splitting the second order differential operators in the zone around the source into two parts, so that a simple first order operator is all that is left at the source location itself.

The extended WBM scheme is applied to two representative problems with heterogeneous source regions: fault and subduction zones. Fault zones are composed of physically perturbed materials created during prior rupturing processes, and resultantly behave as low-velocity structures. In contrast, a subduction zone has a dynamically subducting cool slab which displays high-velocity anomaly to surrounding media.

In the application to fault-zone problems, we probe the effects of trapped waves in the low-velocity fault zone and the permanent displacements around sources. We include dislocation sources (including a propagating rupture) in the fault zone and are able to include an arbitrarily complex time history of slip to handle the complexities of real events.

In modelling for subduction zones, we investigate waveform and amplitude variation of *SH* waves propagating through a subducting slab. The size of the subduction zone means that we need to take account of the sphericity of the Earth and we make the approximation of working in a cylindrical coordinate system for *SH* waves. Previous studies (e.g., Sekiguchi, 1992) on waveform variation in subduction zones did not pay attention to effects of interface waves and post critically reflected waves sufficiently in regional distances, we investigate those effects by varying the relative position of the source and the slab boundaries. In particular, since earthquakes are, in general, close to the boundaries of the subducting slabs (e.g., Pankow & Lay, 2002), there are possibilities for the development of interface waves which can travel considerable distances along the slab.

6.2 Modified technique

6.2.1 Theory

We modify the source representation by using a linear combination of operators to cope with heterogeneity whilst retaining numerical stability. We require that the operators both inside and outside the source zone should be equivalent to the linear operators $\mathcal{L}_{ij}$ in (3.8) for a general medium. We extract the $\mathcal{L}^s_{ij}$ contribution in the source region, and write the new form of the linear operators $\mathcal{L}^r_{ij}$ as

$$\begin{aligned}
\mathcal{L}^r_{xz} = \mathcal{L}_{xz}, \quad \mathcal{L}^r_{xx} &= \begin{cases} \mathcal{L}_{xx}, & z > z_s + l, \ \ z < z_s - l, \\ \mathcal{L}^s_{xx} + \mathcal{L}^d_{xx}, & z_s - l \le z \le z_s + l, \end{cases} \\
\mathcal{L}^r_{zx} = \mathcal{L}_{zx}, \quad \mathcal{L}^r_{zz} &= \begin{cases} \mathcal{L}_{zz}, & x > x_s + l, \ \ x < x_s - l, \\ \mathcal{L}^s_{zz} + \mathcal{L}^d_{zz}, & x_s - l \le x \le x_s + l, \end{cases}
\end{aligned} \tag{6.1}$$

where (x_s, z_s) is the source position and l defines the size of the immediate source zone. The additional operators $\mathcal{L}^d_{jj}$ ($j = x, z$) in a heterogeneous source zone take the form

$$\begin{aligned}
\mathcal{L}^d_{xx} &= \frac{1}{\rho}\frac{\partial}{\partial x}\left[(\Delta\lambda + 2\Delta\mu)\frac{\partial}{\partial x}\right] + \frac{1}{\rho}\frac{\partial}{\partial z}\left[\Delta\mu\frac{\partial}{\partial z}\right], \\
\mathcal{L}^d_{zz} &= \frac{1}{\rho}\frac{\partial}{\partial x}\left[\Delta\mu\frac{\partial}{\partial x}\right] + \frac{1}{\rho}\frac{\partial}{\partial z}\left[(\Delta\lambda + 2\Delta\mu)\frac{\partial}{\partial z}\right],
\end{aligned} \tag{6.2}$$

where $\Delta\lambda(x,z) = \lambda(x,z) - \lambda_s$ and $\Delta\mu(x,z) = \mu(x,z) - \mu_s$.

It can be readily proved that $\mathcal{L}^s_{jj} + \mathcal{L}^d_{jj}$ is mathematically equivalent to $\mathcal{L}_{jj}$. Also, note that the terms $\mathcal{L}_{ij}$ ($i \neq j$) do not need to be recast in the new form since only multiple differentiations in the same direction (e.g., $\partial_x \partial_x$ or $\partial_z \partial_z$) develop numerical instability and they are not included in these operators. Therefore, the original form of $\mathcal{L}_{ij}$ can be implemented directly when $i \neq j$.

In addition, we can find that only the linear operators $\mathcal{L}^s_{ij}$ are needed at the source position since the Lamé coefficient difference terms ($\Delta\lambda$, $\Delta\mu$) vanish at this point. So, with this modified linear operators $\mathcal{L}^r_{ij}$, one can treat any variation in the properties of source regions without numerical dispersion.

6.2.2 Validation test

In order to test if the modified procedure is equivalent to the previous technique in Sections 2.4.1 and 3.2.2, which has been validated by comparison with analytical solutions and other numerical methods, we compare the time responses of both techniques in a heterogeneous situation. We implement several values of l and compare the results to determine a suitable value for accurate and stable modelling and also to investigate whether any numerical anisotropy arises from the implementation of a combination of linear operators (see e.g., Käser & Igel, 2001).

We consider a two-layered medium (Fig. 6.1) in a 10×10 km domain, represented by 128×128 grid points. The elastic wave velocities in the lower layer are twice those in the upper layer and the density ratio is a factor of 1.5. The four artificial boundaries ($\Gamma_T, \Gamma_B, \Gamma_R, \Gamma_L$) are treated via absorbing boundary conditions. A vertically directed force is applied at (2.34 km, 2.97 km) inside the upper layer and 8 receivers (R_j, D_j, j=1,…,4) are deployed with a spacing of 1.875 km starting from x=2.5 km at depths z=3.75 km and z=6.88 km. A Ricker wavelet with dominant frequency 4.5 Hz is introduced as the source time function.

When direct *P* and *S* waves are incident on an internal boundary, reflected (*PPr, PSr, SPr, SSr*) and transmitted (*PPt, PSt, SPt, SSt*) waves with wavetype coupling, interface waves and head waves develop and propagate from the boundary as indicated in Fig. 6.2.

We consider 3 different implementations of the modified approach with different values of l, and compare the resulting seismograms with those for the previous scheme. In case A we consider use the sum of the two operators $\mathcal{L}^s_{jj}$ and $\mathcal{L}^d_{jj}$ across the whole domain. In the other two cases we consider a more localized application of the split operator. In case B we use 3 grid steps for l, and in case C we take the extreme position where the modified technique is just the row and column of grid points in which the source are placed.

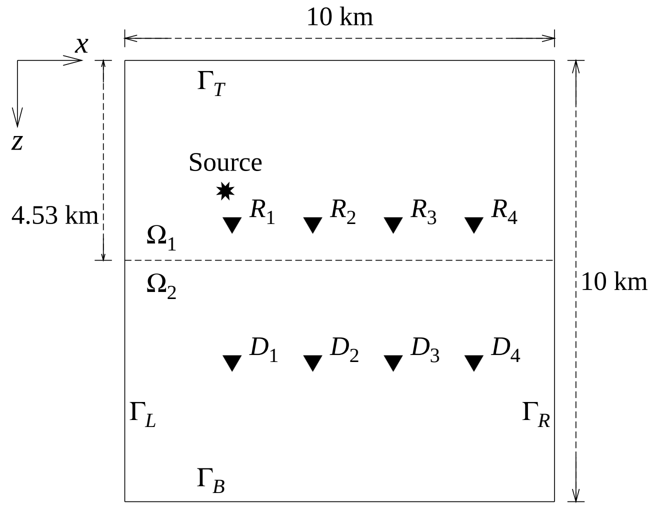

Fig. 6.1. Representation of the two-layered medium used for the validation test of the modified WBM. The domain is 10$\times$10 km and a planar internal boundary is placed at depth z=4.53 km. The compressional wave velocity (α_1) in the top layer (Ω_1) is 3.5 km/s, the shear wave velocity (β_1) 2.0 km/s, and the density (ρ_1) 2.2 $\mathrm{Mg/m^3}$. The velocities in the bottom layer (Ω_2) are twice of those in the top layer (i.e., α_2=7.0 km/s, β_2=4.0 km/s) and the density (ρ_2) is 3.3 $\mathrm{Mg/m^3}$. A vertically directed force is applied at (2.34 km, 2.97 km), and four artificial boundaries ($\Gamma_T, \Gamma_B, \Gamma_R, \Gamma_L$) are treated by absorbing boundary conditions. In order to record time responses, 8 receivers are deployed at depths z =3.75 km (R_j, j=1,. . .,4) and 6.88 km (D_j) from x = 2.5 km with constant spacing 1.875 km.

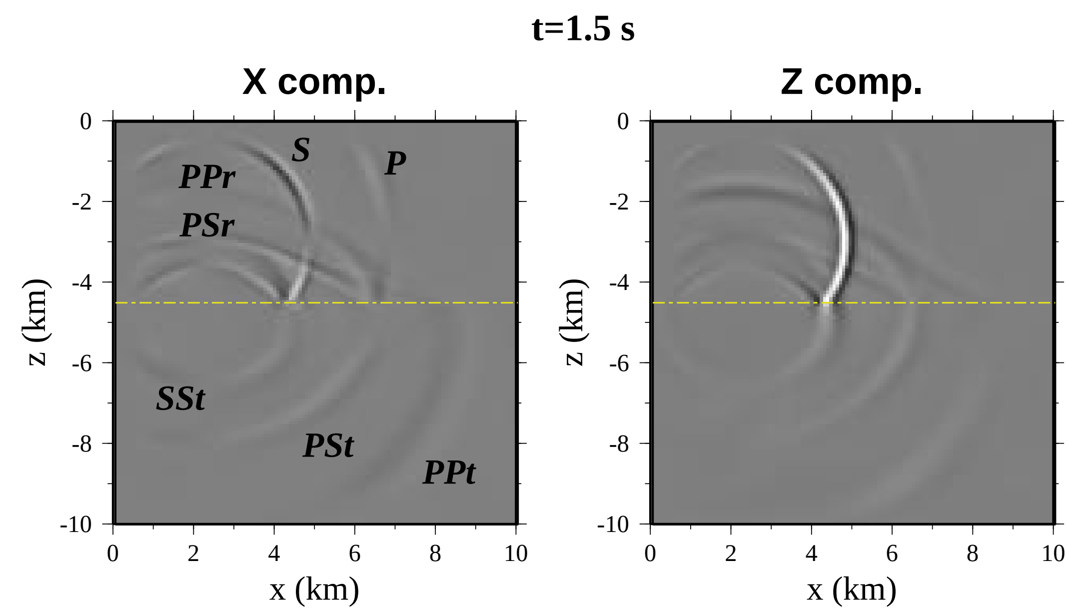

Fig. 6.2. Snapshots of elastic wave propagation in the two-layered medium of Fig. 6.1 at t=1.5 s. Incident P and S waves are reflected (*PPr, PSr, SPr, SSr*) and transmitted (*PPt, PSt, SPt, SSt*) with wavetype coupling on the boundary.

Fig. 6.3 displays a comparison of the numerical results for the three cases with a reference solutions calculated with the previous approach. In general, the numerical results for the cases A and B agree well with reference solutions for the whole wave trains except for a couple of slight misfits (indicated by the solid arrows in Fig. 6.3). These effects may arise from numerical anisotropy (e.g., Käser & Igel, 2001) whereby the successive action of operators can have different effects depending on the order of application and analytically equivalent operators can have different numerical properties.

Although case C needs much less computational effort, the quality of the time response is not satisfactory. There are numerically dispersed phases arriving before the first-arrival phases and some slight misfits among the main phases (marked by broken arrows). The problem is that the operator is acting on too small a region to achieve accurate results. The quality of the time response can be assured by applying the modified technique in a 'sufficiently-broad localized' area, i.e., a band of rows and columns including a source position. Case B satisfies the number of grid points per wavelength needed for the WBM based on Daubechies-20 wavelets, i.e., 3 grid points, and generates time responses that match well with the reference solutions.

Also, it is worthy to mention that except for case A the solutions display slight oscillations after main phases (see, a in the figure). This phenomenon is also related with the numerical anisotropy which is developed by the transition of numerical schemes in a limited area. Note that the reference solutions are computed by the previous technique in Chapter 3 which needs both source-region and main-region schemes. On the contrary, the case A displays good results. However, the maximum amplitude of the oscillations is less than 2 % of that of main phases and reduces with time, and thus the oscillations do not affect wavefields. In the following modellings, we implement the scheme for case A.

6.3 Modelling seismic waves in fault zones

The implementation of a realistic fault source in numerical modelling has been a challenging issue, and many studies have confined their scope to cases using simple single body forces (e.g., Igel *et al.*, 2002; Huang *et al.*, 1995). Although some *SH* studies based on finite-difference techniques (Vidale *et al.*,1985; Li & Vidale, 1996) have managed to incorporate dislocation sources by considering near-field displacement fields with approximate analytic representations, such dislocation modelling is still difficult for *P-SV* waves. An attempt to incorporate dislocation sources in a *P-SV* wave system by controlling stress values around a source position has been made by Coutant *et al.*, (1995), but the proposed scheme is unsatisfactory for accurate modelling. Moreover, since a real

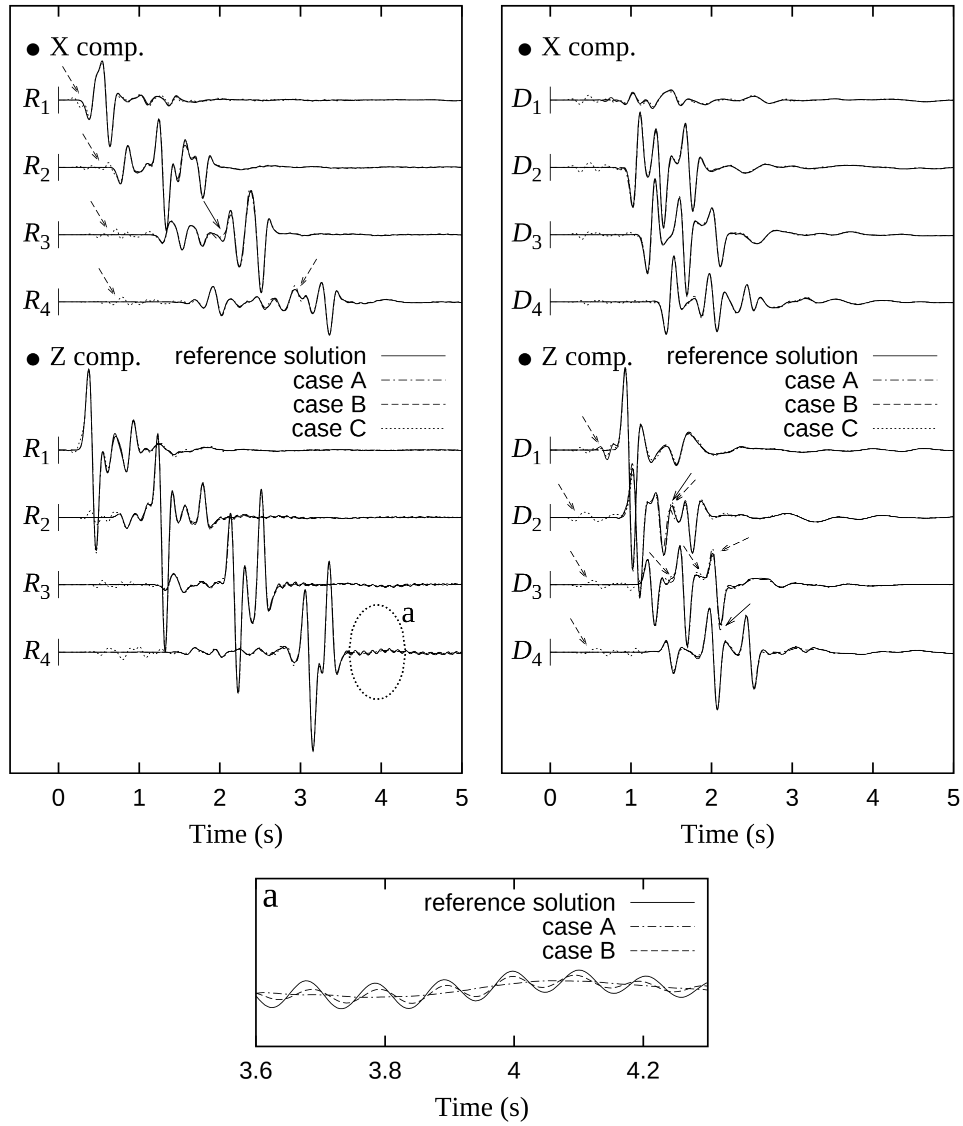

Fig. 6.3. Comparisons of time responses, for several different versions of the modified WBM with a reference solution by the previous method described in Chapter 3. The seismograms are recorded at 8 receivers (R_j, D_j, $j = 1, \ldots, 4$) in Fig. 6.1. Amplified seismograms are provided for the vertical component in R_4 (marked a). Case A applies the modified WBM technique to whole domain, case B to a region three grid points across around the source point, and case C to a row and a column of grid points including a source position. Major misfits in the waveforms for case C are indicated by broken arrows, with solid arrows for other cases. The discrepancies for case C mainly arise from numerical dispersion. Records of D_j are amplified by 6 for the display.

fault zone is highly heterogeneous it is desirable to be able to implement dislocation sources, including rupture in realistic modelling.

The fault gouge zone has lowered velocities relative to its surroundings and so is able to support trapped waves. Such trapping phenomena have been investigated for fault zones by using 2-D (Li & Vidale, 1996) and 3-D (Graves, 1996) finite-difference codes or using analytic expressions (Ben-Zion, 1998). The analytic expression for *SH*-type fault-zone trapped waves with a unit source have been established by several studies (e.g., Li, 1988; Li *et al.*, 1990; Li & Leary, 1990; Ben-Zion & Aki, 1990). They demonstrated shear-waveform variations for 2-D fault zones as a function of the parameters of the fault zone and the observation pattern, e.g., fault-zone width, velocity structures, relative source and receiver positions, and attenuation factors; they were able to show clear development of trapped waves and head waves as features of time responses in fault zones. The analytical approach demonstrates the presence of the phenomenon but is not able to handle heterogeneity or more complex geometry. Such effects can however be examined with numerical methods such as higher-order finite difference technique (e.g., Jahnke *et al.*, 2002), which could treat a problem with seismic-wave initiation on material boundary in a fault zone. However, the finite difference scheme may generate artificially attenuated seismic waves in media with complex strong heterogeneities (Chapter 7) and has a difficult in treatment of complicated (non-smooth) source time function. The WBM is particularly effective in this context because of its capacity to handle strong heterogeneity, and, as we shall see, is able to include a propagating rupture with non-smooth source time function within the heterogeneous zone. Note that the WBM has been shown to preserve energy of seismic waves correctly even in strongly perturbed media (Chapter 7).

6.3.1 Implementation of dislocation sources

Dislocation sources can be implemented in the WBM through the double-couple force system based on a moment-tensor ($\mathbf{M}$) representation, and the equivalent body force $\mathbf{f}(t)$ for the dislocation sources can be expressed as (e.g., Komatitsch & Tromp, 2002; Ben-Menahem & Singh, 1981)

$$\mathbf{f}(t) = -\mathbf{M} \cdot \nabla \delta(\mathbf{r} - \mathbf{r}_s) D(t), \tag{6.3}$$

where $D(t)$ is the displacement history of a particle on the fault, $\mathbf{r}$ the location vector, and $\mathbf{r}_s$ the location of the source, (x_s, z_s). Note that $\dot{D}(t)$ corresponds to the far-field source time function and the area under $\dot{D}(t)$ is unity (Vidale *et al.*, 1985; Lay & Wallace, 1995).

For an arbitrary fault the moment tensor can be expressed in terms of strike angle (ϕ), dip angle (ξ) and rake angle (η) of a fault geometry (e.g., Lay & Wallace, 1995; Kennett, 2001). Six independent components of the moment tensor are given by

$$M_{xx} = -M_0(\sin\xi\cos\eta\sin 2\phi + \sin 2\xi\sin\eta\sin^2\phi),$$

$$
\begin{aligned}
M_{yy} &= M_0(\sin\xi\cos\eta\sin 2\phi - \sin 2\xi\sin\eta\cos^2\phi),\\
M_{zz} &= M_0\sin 2\xi\sin\eta,\\
M_{xy} &= M_{yx} = M_0(\sin\xi\cos\eta\cos 2\phi + \sin 2\xi\sin\eta\sin\phi\cos\phi),\\
M_{xz} &= M_{zx} = -M_0(\cos\xi\cos\eta\cos\phi + \cos 2\xi\sin\eta\sin\phi),\\
M_{yz} &= M_{zy} = -M_0(\cos\xi\cos\eta\sin\phi - \cos 2\xi\sin\eta\cos\phi),
\end{aligned} \tag{6.4}
$$

where the scalar factor M_0 corresponds to $\mu_s A\bar{D}$, μ_s is the shear modulus in the source position, A the fault area, and $\bar{D}$ the average displacement of fault (fault offset). The strike angle (ϕ) is measured from the north, the dip angle (ξ) from the horizontal plane normal to z direction, and the rake angle (η) from the strike direction on the fault plane.

We consider a thrust fault (i.e., η=$\pi/2$) with a dip angle ξ, which is placed parallel to E-W direction (i.e., ϕ=$\pi/2$). Therefore, the moment tensor is given by

$$
\begin{aligned}
&M_{xx} = -M_0\sin 2\xi, \quad M_{zz} = M_0\sin 2\xi, \quad M_{xz} = -M_0\cos 2\xi,\\
&M_{yy} = M_{xy} = M_{yz} = 0.
\end{aligned} \tag{6.5}
$$

where, x corresponds to east and z is the downward vertical direction. From (6.3) and (6.5), the equivalent body force for a thrust faulting can be represented as

$$
\begin{aligned}
f_x &= -\Big\{M_{xx}\partial_x\delta(\mathbf{r}-\mathbf{r}_s) + M_{xz}\partial_z\delta(\mathbf{r}-\mathbf{r}_s)\Big\}D(t), \quad f_y = 0,\\
f_z &= -\Big\{M_{xz}\partial_x\delta(\mathbf{r}-\mathbf{r}_s) + M_{zz}\partial_z\delta(\mathbf{r}-\mathbf{r}_s)\Big\}D(t).
\end{aligned} \tag{6.6}
$$

With the assumption that there is no structural variation in the y direction, the fault source (6.6) can be implemented in 2-D as a 90° dip-slip fault activated on a vertical plane (x-z plane). The results for this line source in 2-D can be adjusted to match the geometrical spreading in 3-D for a point source by convolving seismograms with $1/\sqrt{t}$ and differentiating in time (Vidale *et al.*, 1985; Igel *et al.*, 2002).

Fig. 6.4 displays snapshots of elastic wave propagation in a homogeneous medium (α=3.15 km/s, β=1.8 km/s, ρ=2.2 $\mathrm{Mg/m^3}$) with 90° dip-slip on a fault plane. Here a ramp excitation model (Fig. 6.5) with t_r=0.1 s is implemented for the displacement time function $D(t)$. Permanent displacements induced by the dislocation are found in a four-lobed pattern around the source position (*N* in Fig. 6.4), and diminish with distance as r^{-1}. On the other hand, transient displacement activated by propagating elastic waves falls off with distance as $1/\sqrt{r}$ (Vidale *et al.*, 1985). Therefore, in the far field, only the transient displacements are discernible in wavefields.

We are able to simulate the effect of rupture propagation by combining several dislocation sources with their own source time histories, and model a simple rupture problem with ramp source time function in Section 6.3.3.

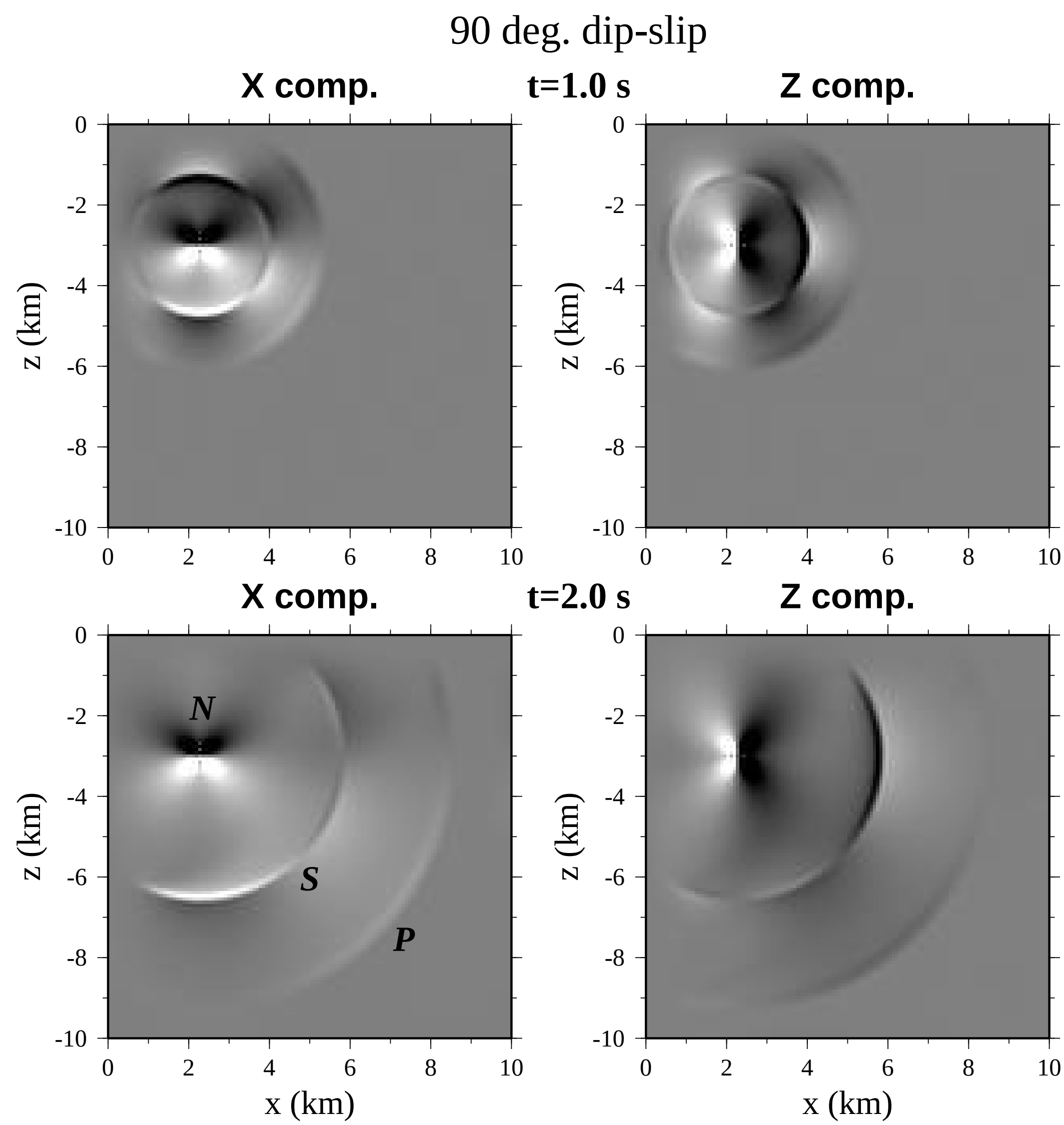

Fig. 6.4. Snapshots of elastic wave propagation from a 90° dip-slip fault in a homogeneous medium. Both permanent displacements (*N*) and and transient wavefields (*P*,*S*) are clearly shown.

6.3.2 Modelling with a point dislocation in a fault zone

We consider a model of a fault gouge zone with significant heterogeneity in a material with lower wavespeeds than its surroundings and simulate the response from a dislocation source in the fault zone. A horizontal fault zone (Ω_1 in Fig. 6.6) with random perturbation in physical properties (wave velocities, density) is set in a homogeneous background medium (Ω_2) where the P wave velocity (α_2) is 3.5 km/s, the S wave velocity (β_2) 2.0 km/s, and the density (ρ_2) 2.2 $\mathrm{Mg/m^3}$. The average wave velocities in the fault zone are 2.63 km/s for P waves (α_1) and 1.5 km/s for S waves (β_1), and the average density (ρ_1) is 1.83 $\mathrm{Mg/m^3}$. A 90° dip-slip dislocation source is located in the middle

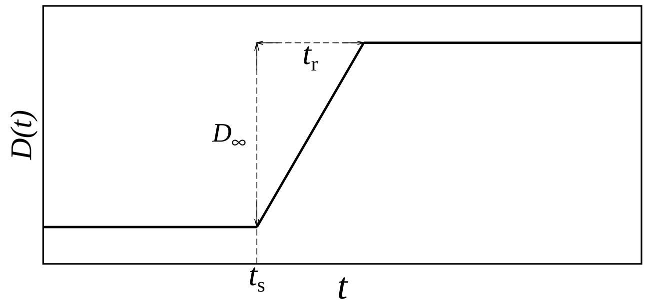

Fig. 6.5. A ramp model for displacement time history of a fault. t_s is the starting time of fault slip, t_r the slip duration time, and D_∞ the final dislocation amount. The average dislocation amount in entire fault plane $\bar{D}$ is set equal to D_∞.

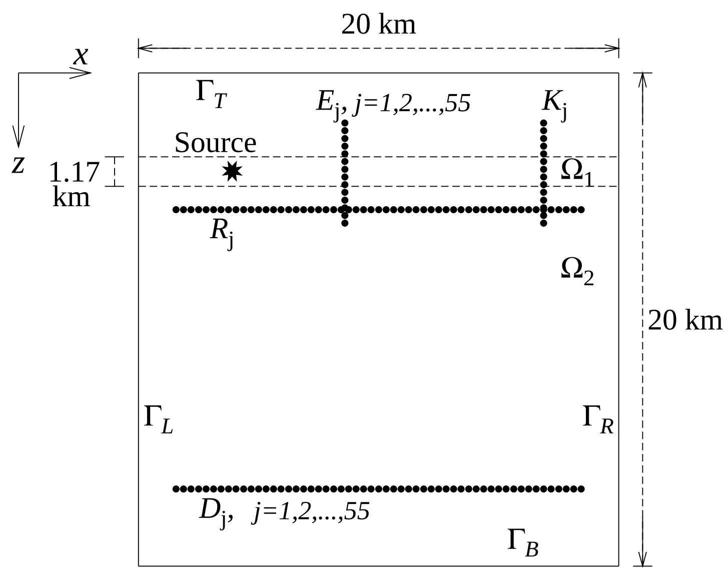

Fig. 6.6. Representation of a domain (20×20 km) with a perturbed fault zone. The average compressional wave velocity (α_1) in the fault zone (Ω_1) is 2.63 km/s, the shear wave velocity (β_1) 1.5 km/s, and the density (ρ_1) 1.83 $\mathrm{Mg/m^3}$. The velocities in the background medium (Ω_2) are 3.15 km/s for P (α_2), 1.8 km/s for S waves (β_2), and the density (ρ_2) is 2.2 $\mathrm{Mg/m^3}$. The perturbation of the fault zone is represented through a stochastic process such that physical parameters are randomly perturbed with standard deviations of 10 % for the wave velocities and 8 % for the density. A 90° dip-slip dislocation source is applied at (3.9 km, 4.0 km), and four artificial boundaries ($\Gamma_T, \Gamma_B, \Gamma_R, \Gamma_L$) are treated by absorbing boundary conditions. 220 receivers are deployed at z=5.5 km (R_j, $j = 1, 2, \cdots, 55$), z =16.9 km (D_j), x =8.59 km (E_j) and x=16.9 km (K_j) with a constant spacing.

of the fault zone at x=3.9 km, z=4.0 km. The thickness of the fault zone is 1.17 km and the perturbations in the zone are generated from a stochastic representation using a von Karman autocorrelation function (cf., Sato & Fehler, 1998) with Hurst number 0.25 and correlation distance 56 m. The wave velocities in the zone have a 10 % standard deviation

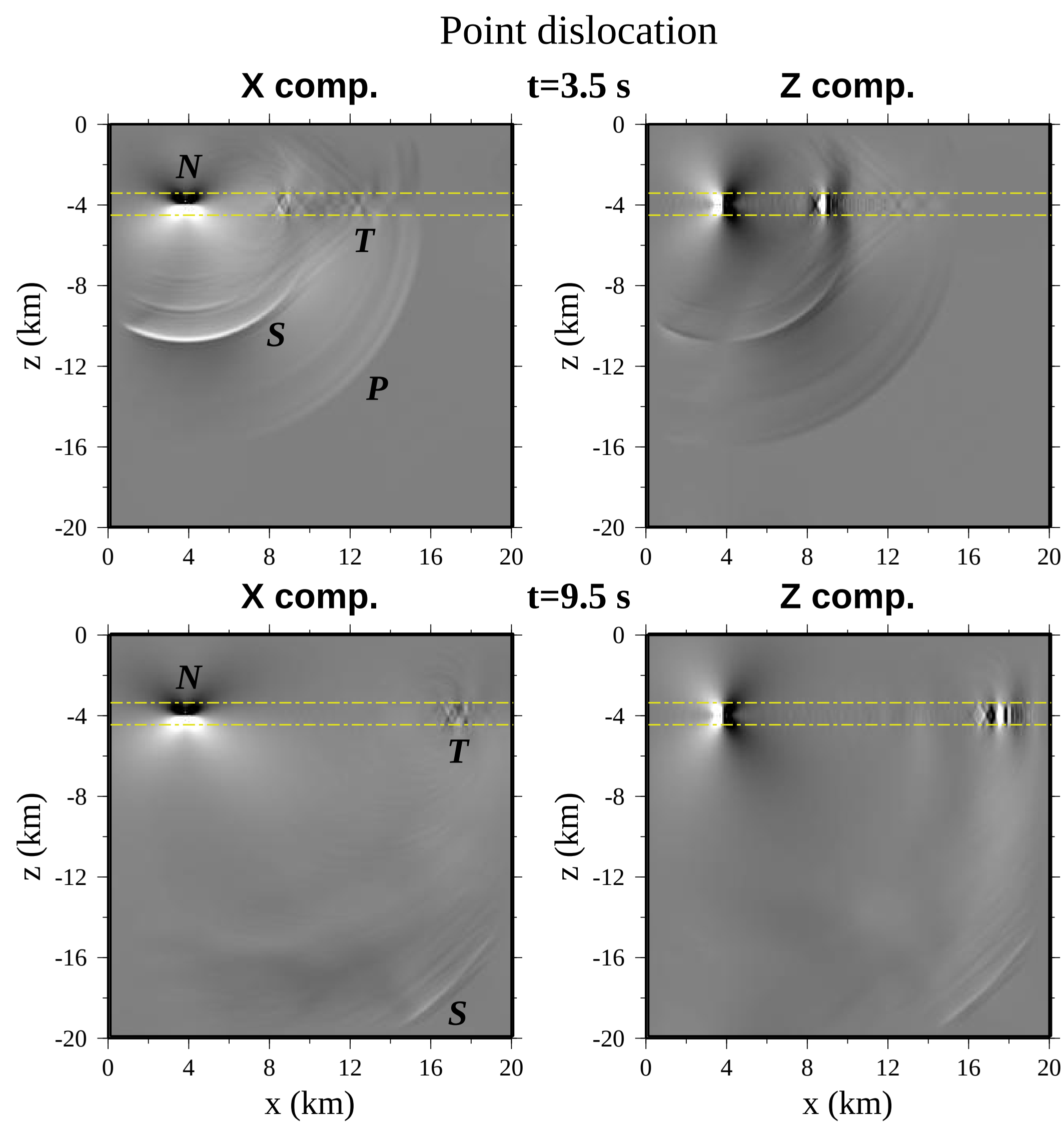

Fig. 6.7. Snapshots of elastic wave propagation in the medium with a horizontal fault zone (see, Fig. 6.6) with a 90° dip-slip dislocation source. Multi-reflected phases follow after direct phases (P and S in the figure) from the source. Also considerable trapped waves (T) develop inside the fault zone.

and the density 8 %. More detailed information on the construction of suitable stochastic media has been discussed in Chapter 7.

Fig. 6.7 displays snapshots of elastic wave propagation in the medium with the fault zone, at t=3.5 and 9.5 s. Various reflected waves develop inside the fault zone, and parts of the multi-reflected wavetrain drain continuously into the homogeneous background medium following after direct phases (P, S in the figure). In particular the P waves generated inside the fault zone give rise to a multiplicity of SV head waves. Meanwhile, most of the S waves are trapped in the low-velocity layer in form of over-critically

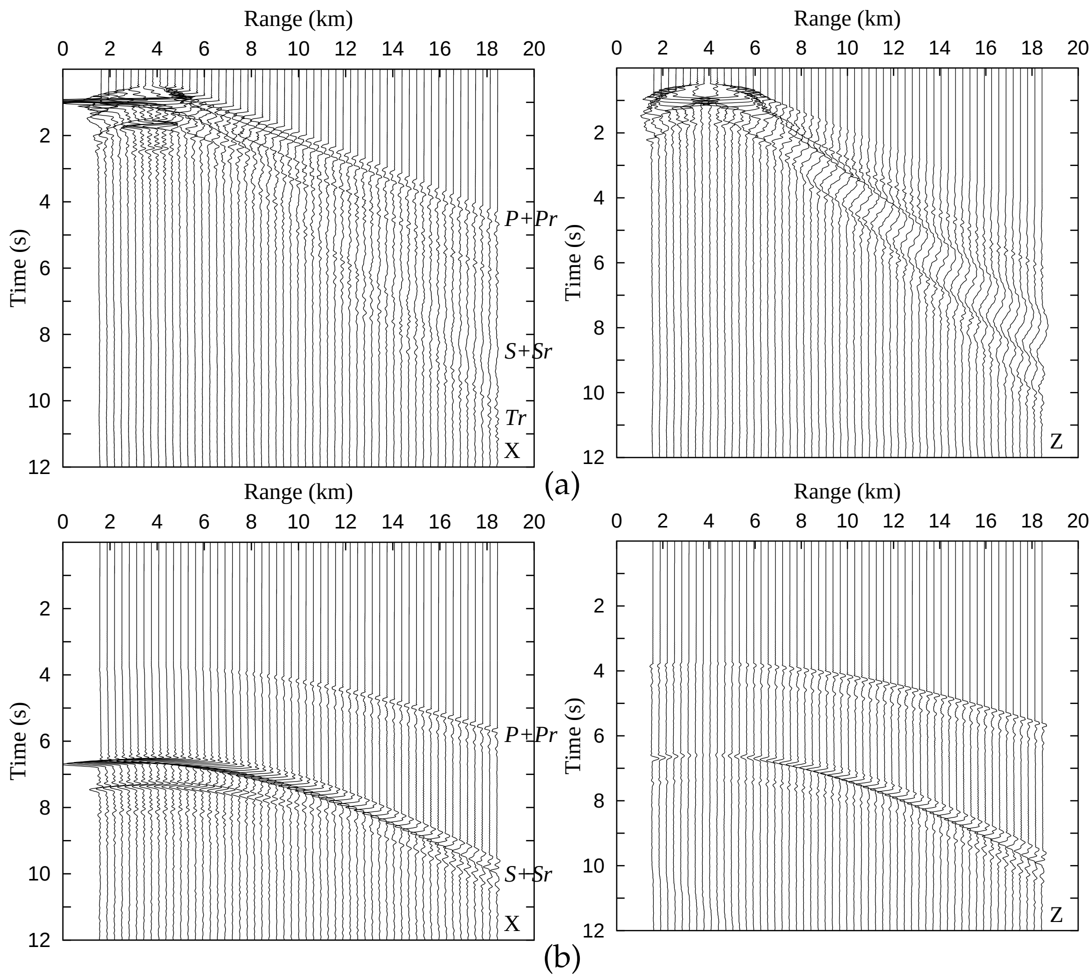

Fig. 6.8. Time responses, with conversion to 3-D response, at 110 receivers placed at (a) depth z=5.5 (R_j in Fig. 6.6) and (b) 16.9 km (D_j) with an appropriate spreading conversion procedure to the case of a point source. Multi-reflected phases (*Pr,Sr*) in the fault zone follow direct waves (*P,S*). Trapped waves interfere with random heterogeneities in the fault zone, and leak into the background medium in a form of scattered waves (*Tr*).

reflected waves, and so significant energy is transported along the layer (T in the figure) at a fairly slow group speed. The trapped waves on the vertical component are much larger than those on the horizontal component; this arises from the combination of the fault zone geometry (i.e., horizontal extension) and slip direction of the fault (i.e., 90° dip-slip).

The equivalent 3-D time response for two sets of 110 receivers at 313m spacing, placed at depths z=5.5 and 16.9 km, are shown in Fig. 6.8. The upper set of receivers is set close to the fault zone and so emphasises near-field effects, whilst the lower set is dominantly influenced by the far-field radiation. The onsets of the P arrivals are relatively simple because they come in ahead of any of the scattered arrivals, but the influence of the

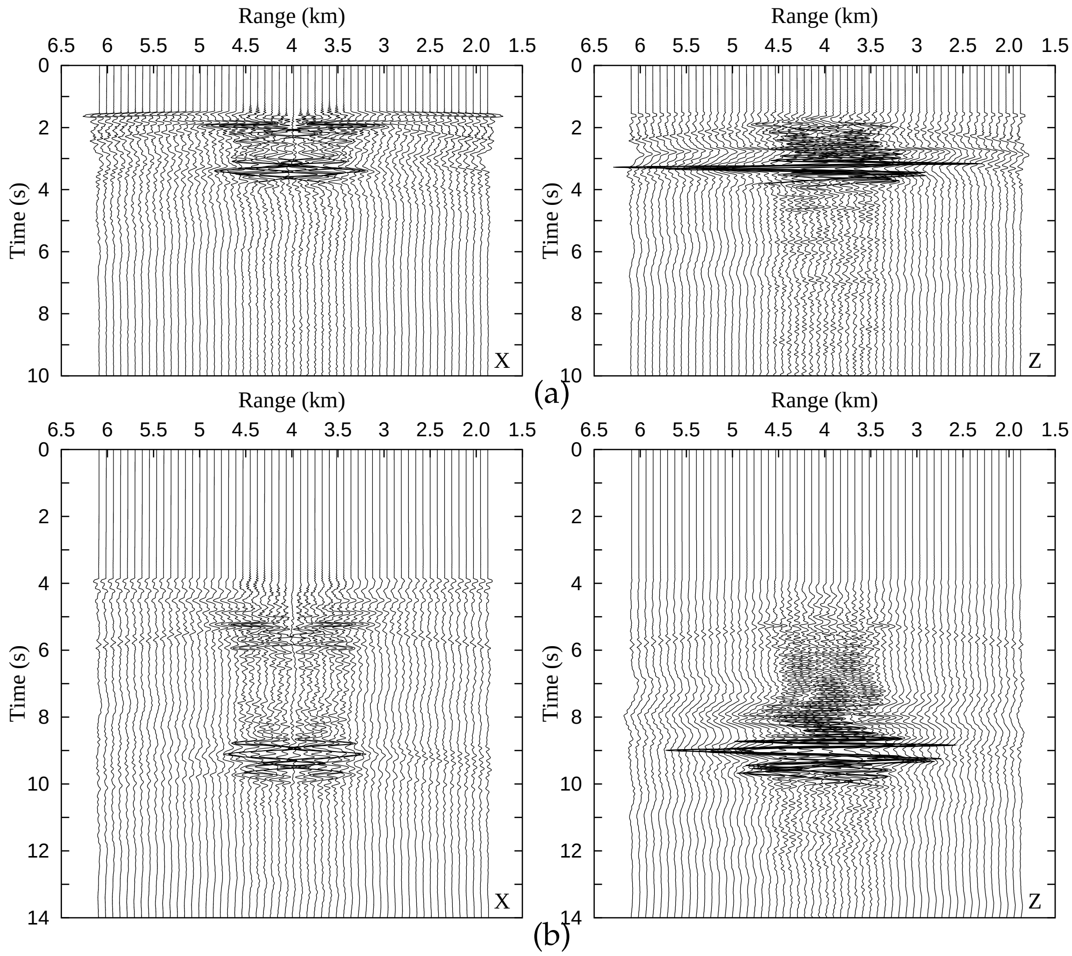

Fig. 6.9. Time responses, with conversion to 3-D response, for lines of receivers crossing the fault zone illustrating the nature of the trapped wave system in the heterogeneous gouge zone (a) at x=8.59 km (E_j in Fig. 6.6) and (b) at 16.88 km (K_j) from the source.

heterogeneity is seen in the significant S arrivals for the x component on the upper line of receivers. The main trapped wave is relatively low frequency, reflecting evanescent decay outside the fault-zone waveguide, but is accompanied by a higher frequency coda with complex waveforms from multiple scattering in the fault zone (*Tr* in the figure). A distinct complex of scattered energy is seen on the x component seismograms for small offsets from the source location. At larger distances a more coherent set of arrivals follows S and becomes more distinct for larger offsets.

The nature of the trapped wave phenomena can be most clearly seen in a receiver profile across the fault zone as illustrated in Fig. 6.9. The lines are set at 4.7 km and 13.0 km from the source. On the closer profile, Fig. 6.9(a), there is still a significant influence from near-field effects and the main part of the trapped wave train tends to merge with the direct phases. The heterogeneity in the gouge zone leads to an extended coda of back scattered waves on the z component. On the further line, Fig. 6.9(b), the nature of the trapping phenomena becomes more evident. On the x component the fast *P* waves in the surrounding material link into the slower *P* waves in the gouge from which a significant *SV* head wave is being shed. The main amplitude on the z component lies as expected on the *S* wave and decays exponentially away from the fault zone so that relatively low frequency energy dominates at the receivers furthest from the fault zone. A similar pattern was reported in Li & Leary (1990, Figs. 7 and 8). Part of the trapped waves consists of conversions between *P* and *S* and these are again prominent on the z component. The patterns of arrivals including long dispersed wavetrains behind *S* are similar to those recorded from aftershocks of the Hector Mine earthquake in California (Li *et al.*, 2002) in a similar profile across the fault zone. In this case the concentration of high frequency arrivals was used as a means of mapping out the location of the fault zone.

6.3.3 Modelling with rupture propagation

In studies of ground motion in the vicinity of earthquakes it is normally not adequate to approximate fault sources by a point dislocation source since the radiation patterns and frequency content of the transient waves are strongly dependent not only on fault geometry but also on dynamic source process. For instance, Kasahara (1981) showed that radiation patterns vary with the ratio of rupture velocity to shear wave velocity in background medium and they are shown to be elongated with increase of rupture velocity.

For realistic modelling, the source process needs to be considered and a direct representation of the faulting process is desired. In this section, we introduce a simple rupture-propagation problem in a fault zone by the superposition of multiple dislocation sources each of which may have their own displacement time functions along the rupture-propagation direction in the fault zone. We consider once again the fault gouge zone model problem of Fig. 6.6 and consider a bilateral propagating rupture initiated at the same point as the line force location in Section 6.3.2. The rupture velocity is taken as 0.9 times the shear wave velocity (β_1) in the fault zone, and the rupture terminates at a distance 0.43 km (corresponding to 5 grid points) from the origin. We here consider a simple case in which each segment of the fault has the same particle displacement time history (the ramp model in Fig. 6.5) and the same amount of energy release (i.e., the same permanent dislocation at steady state). However, the same approach can readily be extended to much more complex problems where every segment of fault has own displacement time history and energy release rate.

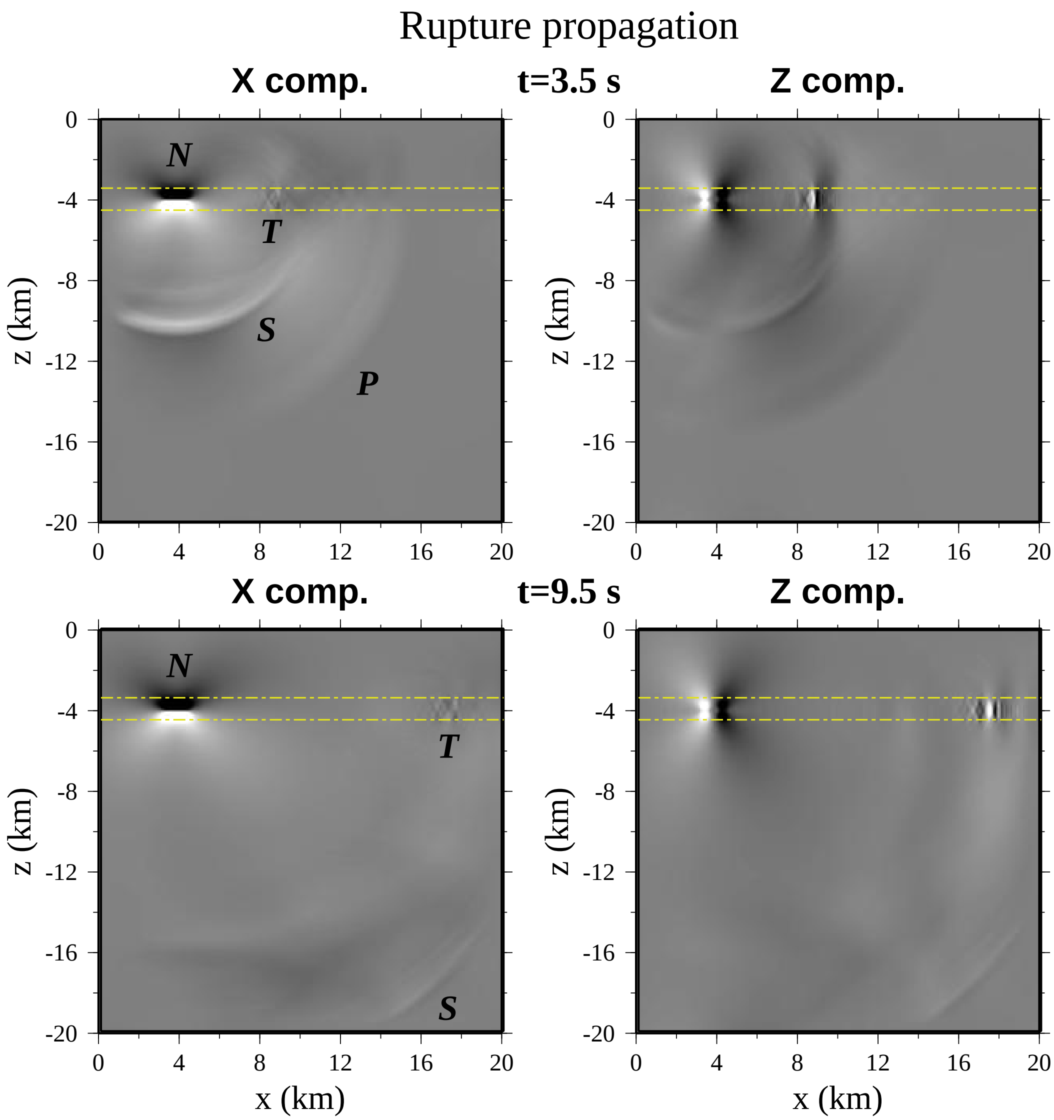

Fig. 6.10. Snapshots of elastic wave propagation in a medium with a horizontal fault zone (Fig. 6.6) with a propagating 90° dip-slip rupture. The same magnitude of scalar moment M_0 as in Fig. 6.7 is considered, and subsequent dislocations are considered in an area with horizontal extent 0.86 km. The permanent displacement pattern on the x component displays a horizontally extended shape following the rupture direction, but that on the z component is concentrated at the ends of the rupture.

For comparison with the results of the point-dislocation case (Section 6.3.2), we consider the same magnitude of seismic moment M_0 by distributing the magnitude evenly along the fault plane over the total rupture distance. The general character of the wavefields seen in the snapshots (Fig. 6.10) are similar to the point-dislocation case (Fig. 6.7). However, since the energy is released over a time interval at each segment of the fault, the transient waves exhibit smaller amplitudes and lower frequencies (see also, Fig. 6.11). Also, we note that there is now a much weaker P disturbance in the fault

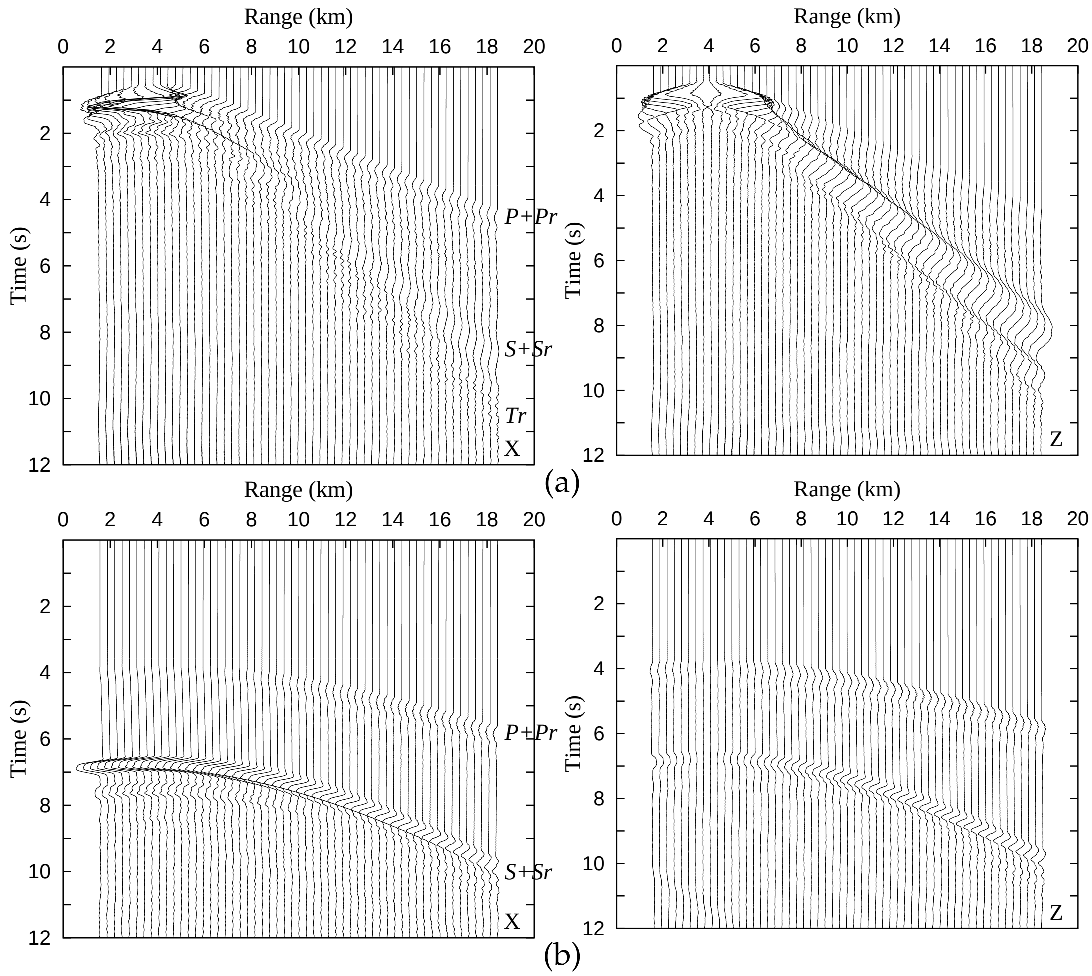

Fig. 6.11. Time responses, with conversion to 3-D response, for the propagating fault problem with 110 receivers placed at depth z=5.5 (a) and 16.9 km (b). The traces are amplified by a factor of two compared with Fig. 6.8. The main phases (*P,S,Pr,Sr,Tr*) are similar to those for a point dislocation but the frequency contents of phases are lower than those in Fig. 6.8, since the rupture velocity is lower than the elastic wave velocities.

zone and consequently much less in the way of *S* head waves in the surroundings. The permanent displacement patterns (*N* in Fig. 6.10) around the fault display horizontal extension along the fault propagation direction in the x components. In contrast the permanent displacements are concentrated at the end of the rupture on the z component and are not discernible along the plane of rupture.

The time responses in Fig. 6.11 for the propagating rupture source are displayed with twice the amplification used in Fig. 6.8. The multiple reflected waves following the *S* waves for receivers at short offset on the x components for the point dislocation case (Fig. 6.8) do not appear in the profiles for propagating rupture.

Time responses for lines of receivers crossing the fault zone (Fig. 6.12) display

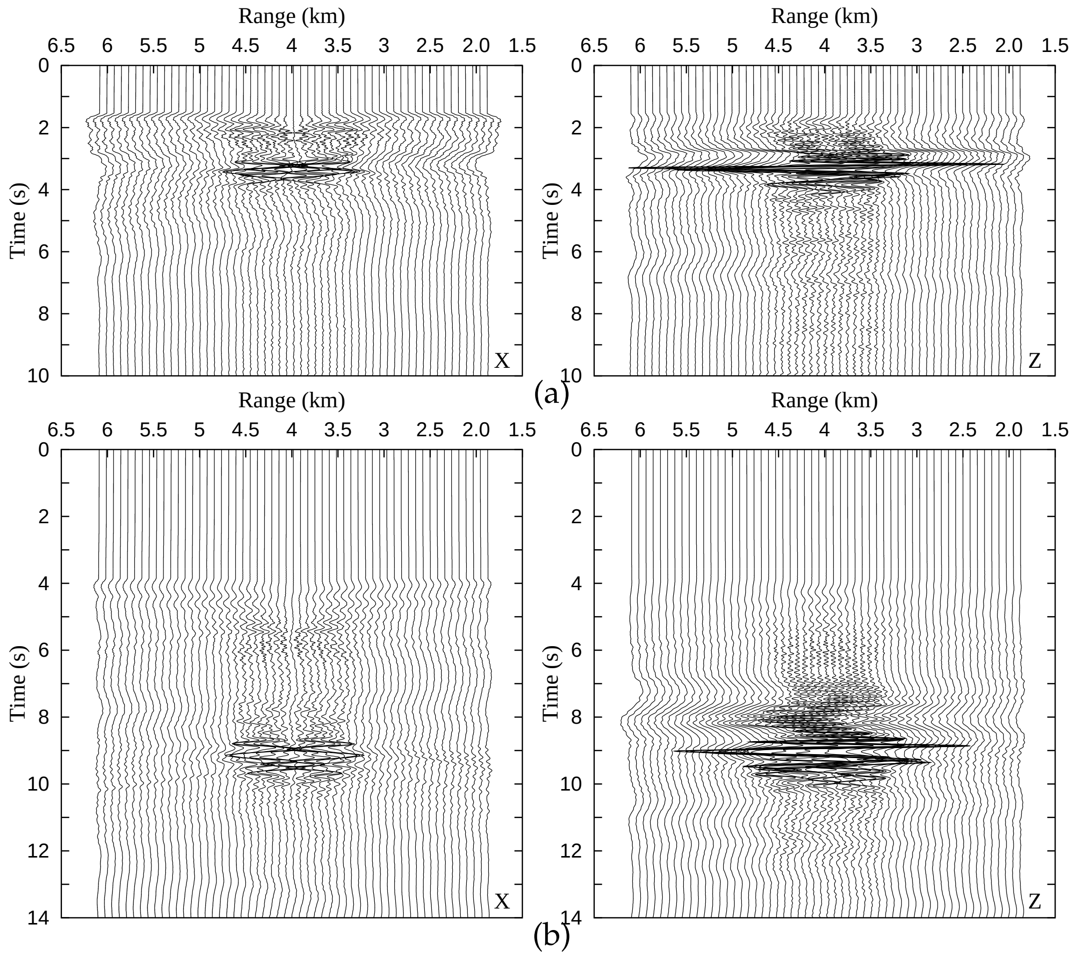

Fig. 6.12. Time responses, with conversion to 3-D response, for the propagating fault problem at receivers crossing the fault zone, (a) x=8.59 km (E_j in Fig. 6.6) and (b) x=16.88 km (K_j) from the source.

long-period wavetrains compared to those of the point dislocation case (Fig. 6.8) since dislocation energy is distributed on finite segments of fault with time intervals. Trapped P waves are affected considerably and thus the amplitudes are reduced compared to those of S waves.

6.4 Modelling in subduction zones

A further region in which sources occur within a zone of heterogeneity is in the coherent and systematic high velocity zone of the subducting slab. The majority of earthquakes associated with the subduction zone lie within the slab but relatively close to its upper surface. Seismic waves generated from such sources within the slab have the potential of strong interaction with the slab boundaries with reflections and conversions. There is also the possibility of interface waves associated with the contrasts in properties at the edge of the slab. The combination of the effects introduced by the slab can have significant effects on the local wavefield and also have the potential to modify the high frequency characteristics for teleseismic propagation.

Waveform and amplitude variations of incident waves propagating through a slab have been studied at regional distance with both numerical modelling (e.g., Vidale, 1987; Cormier, 1989; Sekiguchi, 1992) and observational analysis (Lay & Young, 1989). Recently, wave-guide effects in the accretionary prism above the slab have been investigated by Shapiro *et al.* (2000). However, the generation of secondary waves in subduction zones (such as reflected waves, interface waves) have not received much attention. Moreover, when waves interfere with a fast-velocity layer placed between low-velocity layers, it is possible to get tunneling effects (Fuchs & Schulz, 1976; Drijkoningen, 1991), which depend on the frequency content of the wavefield and the thickness of the layer, which can contribute to waveform complexity. Thus, low frequency waves with large wavelength are hardly affected by the presence of the subducting slab but the impact increases at higher frequencies.

We consider the *SH* wave case at a regional scale, and show how the WBM method can be used to handle the presence of a simplified subduction zone embedded in a radially stratified background model, including secondary wave effects.

The subduction zone structure extends to such a depth that we cannot ignore the influence of the sphericity of the Earth and so need to adapt the WBM to a non-cartesian coordinate system. Spherical finite-difference methods have been introduced for the simulation of *SH* waves in the mantle (Igel & Weber, 1995; Chaljub & Tarantola, 1997) and *P-SV* (Igel & Weber, 1996) wave propagation in the sphere. An alternative approach which remains in 2-D was adopted by Furumura *et al.* (1998) with a cylindrical-coordinate representation for *P-SV* wave equations in modelling using a pseudospectral method. For a 2-D structure such as a subducting plate, modelling with a spherical coordinate system, requires the pole axis to be treated by a symmetry condition, with a vanishing displacement vector on the axis, and thus an additional boundary condition is needed. To preserve the simplicity of the situation we use cylindrical coordinates for *SH* waves with the background radially stratified model based on *ak135* (Kennett *et al.*, 1995).

6.4.1 Numerical implementation

The SH wave equation in a cylindrical coordinate (r,θ,y) system (cf., Aki & Richards, 1980) takes the form:

$$\frac{\partial^2 u_y}{\partial t^2} = \frac{1}{\rho}\left(\frac{\sigma_r}{r} + \frac{\partial \sigma_r}{\partial r} + \frac{1}{r}\frac{\partial \sigma_\theta}{\partial \theta} + f_y\right), \tag{6.7}$$

where the stress terms σ_r and σ_θ are given by

$$\sigma_r = \mu \frac{\partial u_y}{\partial r}, \quad \sigma_\theta = \frac{\mu}{r}\frac{\partial u_y}{\partial \theta}. \tag{6.8}$$

This set of equations for SH can be recast in the wavelet representation in a similar way to that in Section 6.2, working with normalised radius.

The traction-free condition at the free surface and the core-mantle boundary (if applicable) is $\sigma_r = 0$, and this can be implemented as via equivalent forces in $\mathbf{N}$ (3.10).

6.4.2 Validation tests

The accuracy of the wavelet-based method in cylindrical coordinates has been tested with a variety of models where analytic solutions are available. We illustrate these tests for a cylinder with small radius where the influence of curvature is strong.

We consider a portion of a uniform cylinder with radius 22 km (Fig. 6.13). Four artificial boundaries ($\Gamma_R, \Gamma_L, \Gamma_T, \Gamma_B$) are treated by absorbing boundary conditions. Four receivers (R_j, j=1,2,3,4) are placed at depth 3.04 km in a row with interval 1.61 km, and a line force is applied at a depth of 6.3 km. The numerical model is represented with 128$\times$128 grid points, the shear wave velocity is set to be 2.0 km/s, and the density 2.2 $\mathrm{Mg/m^3}$. A Ricker wavelet with dominant frequency 4.5 Hz is implemented for the source time function.

As shown in Fig. 6.14, the wavelet-based method generates time responses with correct travel times and amplitudes for this uniform cylinder case. A barely noticeable high frequency jitter distinguishes the numerical simulation from the analytical results.

Similar comparison have been made for both the effects of the free surface and layering for model segments placed at the surface of the Earth so that curvature effects are minimised. The replication of the analytic results matches that of Fig. 6.14 and so confirms the accuracy of the cylindrical WBM method. For more complex stratified models analytic solutions are not available but a strong check on the validity of the WBM method is provided by the precise match of the wavefront patterns for both shallow and deep sources.

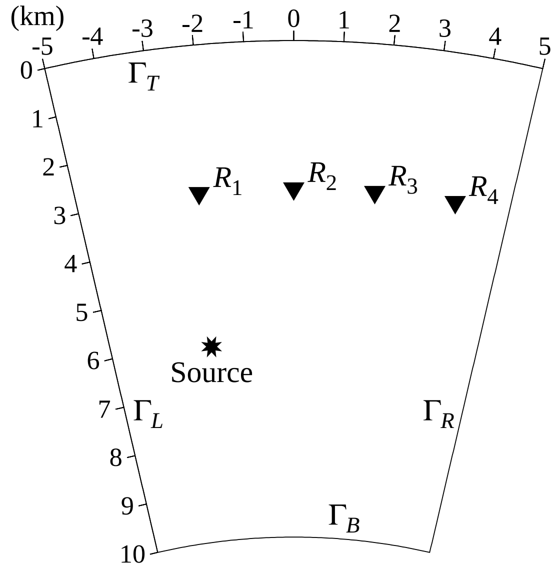

Fig. 6.13. Description of a homogeneous medium, a part of the circle with radius 22 km, for a validation test of the wavelet-based method in circular media. Four receivers (R_j, j=1,2,3,4) are placed at depth 3.04 km and the source at depth 6.3 km. The four artificial boundaries ($\Gamma_R, \Gamma_L, \Gamma_T, \Gamma_B$) are treated as absorbing boundaries.

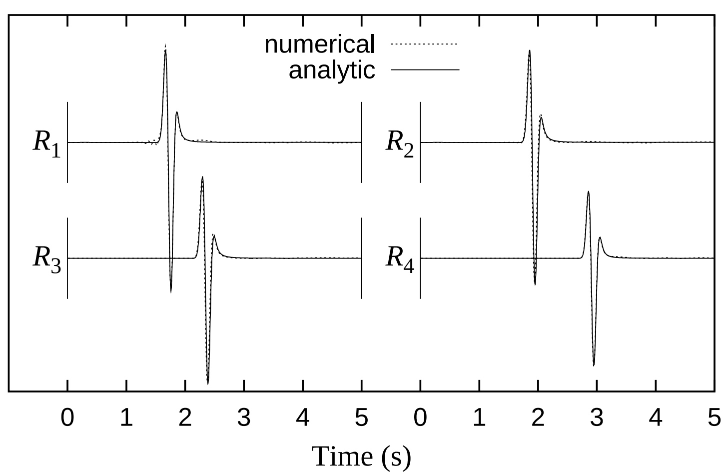

Fig. 6.14. Comparisons between analytic solutions and numerical results recorded at four receivers (R_j in Fig. 6.13) in a homogeneous circular medium.

6.4.3 SH waves in subduction zones

6.4.3.1 Wavefronts

The geometry of subducting slabs is approximately two-dimensional, but the velocity anomalies revealed by seismic tomography indicate that there can be significant variations along a single subduction zone (e.g., Pankow & Lay, 2002; Kennett, 2002; Widiyantoro *et al.*, 1999; Ding & Grand, 1994).

Here we implement a simplified slab model based on a recent study (Pankow & Lay,

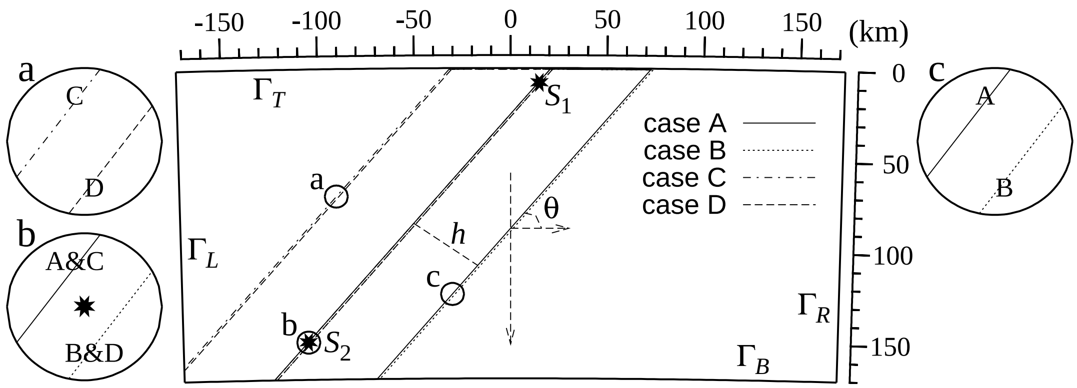

Fig. 6.15. Simplified model of a subduction zone with a dip (θ) of 50° and thickness (h) 40 km. The uniform slab has a wavespeed set 5% higher than the wavespeed just above the upper boundary and is embedded in the radially stratified model *ak135* (Kennett *et al.*, 1995). Sources are placed at two representative depths: shallow (S_1, z=11.88 km) and intermediate-depth (S_2, z=149.15 km). Point sources with dominant frequency 1 Hz are introduced near the boundaries of the slab. The four sources lie just below the upper boundary of the slab (case A), or just above the slab boundary (case B), and in a similar configuration just below the lower boundary (case C), or just above the boundary (case D).

2002) of shear wave velocity structure in the Kurile subduction zone. We consider a slab with a dip (θ) of 50° and a velocity anomaly raised by 5 % compared to its surroundings (Fig. 6.15); the properties of the slab are constant across its thickness. The slab is embedded in the radially stratified model *ak135* (Kennett *et al.*, 1995). The thickness (h) of the slab is taken as 40 km and the velocity anomaly of the slab starts at 0.68 km depth. Four different positions of the source relative to the slab are considered for both a shallow source (S_1 in the figure, z=11.88 km) and an intermediate depth source (S_2, z=149.15 km) depths. The four sources lie just below the upper boundary of the slab (case A), or just above the slab boundary (case B), and in a similar configuration just below the lower boundary (case C), or just above the boundary (case D).

The different source configurations are achieved by slight rotations of the basic model. The slab in case B is generated by a rotation of case A clockwise about the center of the earth by 1.35 km, the slab for case C by rotating counterclockwise by 52.22 km, and finally the slab for case D by counterclockwise by 50.87 km. The source location is kept fixed so that direct comparison of the seismograms can be made for free surface receivers. The source time function is taken as a Ricker wavelet with dominant frequency of 1 Hz. The domain is represented with 512×256 grid points; three domain boundaries ($\Gamma_R, \Gamma_L, \Gamma_B$) are treated by absorbing boundary conditions, and the top domain boundary (Γ_T) is considered as a free surface. We consider a slab with a constant relative velocity anomaly as a means of understanding the effects of slab boundaries on the waveforms and the systematic deformation of wavefronts due to subduction zones.

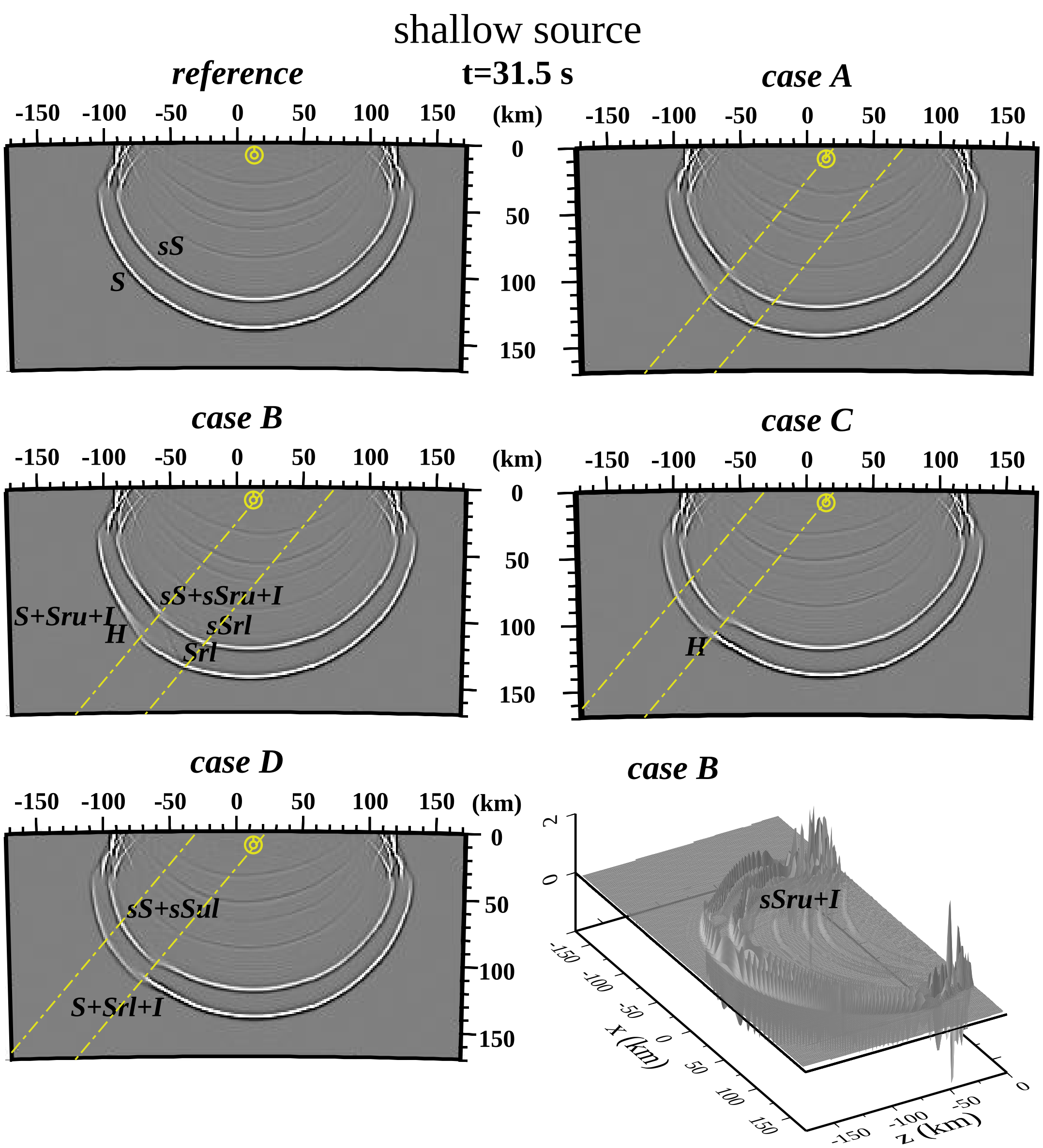

Fig. 6.16. Snapshots of *SH* wave propagation in the simplified subduction zone model with a shallow source at t=31.5 s. Major phases in the reference model are direct waves (*S*), free-surface reflected waves (*sS*), and Love waves. The patterns of reflected waves at the upper boundary of slab (*Sru*, *sSru*) and at the lower boundary (*Srl*,*sSrl*), depend on the source positions relative to the slab. Interface waves (*I*) and head waves (*H*) develop strongly along the slab boundary closest to the source.

Figs. 6.16 and 6.17 compare snapshots for the four source positions at t=31.5 s for both shallow source depths and intermediate depth of source. The reference snapshot in the figure is computed in the radially stratified earth model *ak135*. The outlines of the perturbed slab are superimposed on the snapshots to aid in identification of the different classes of arrivals.

The relative position of the source compared with the upper or lower boundary of the

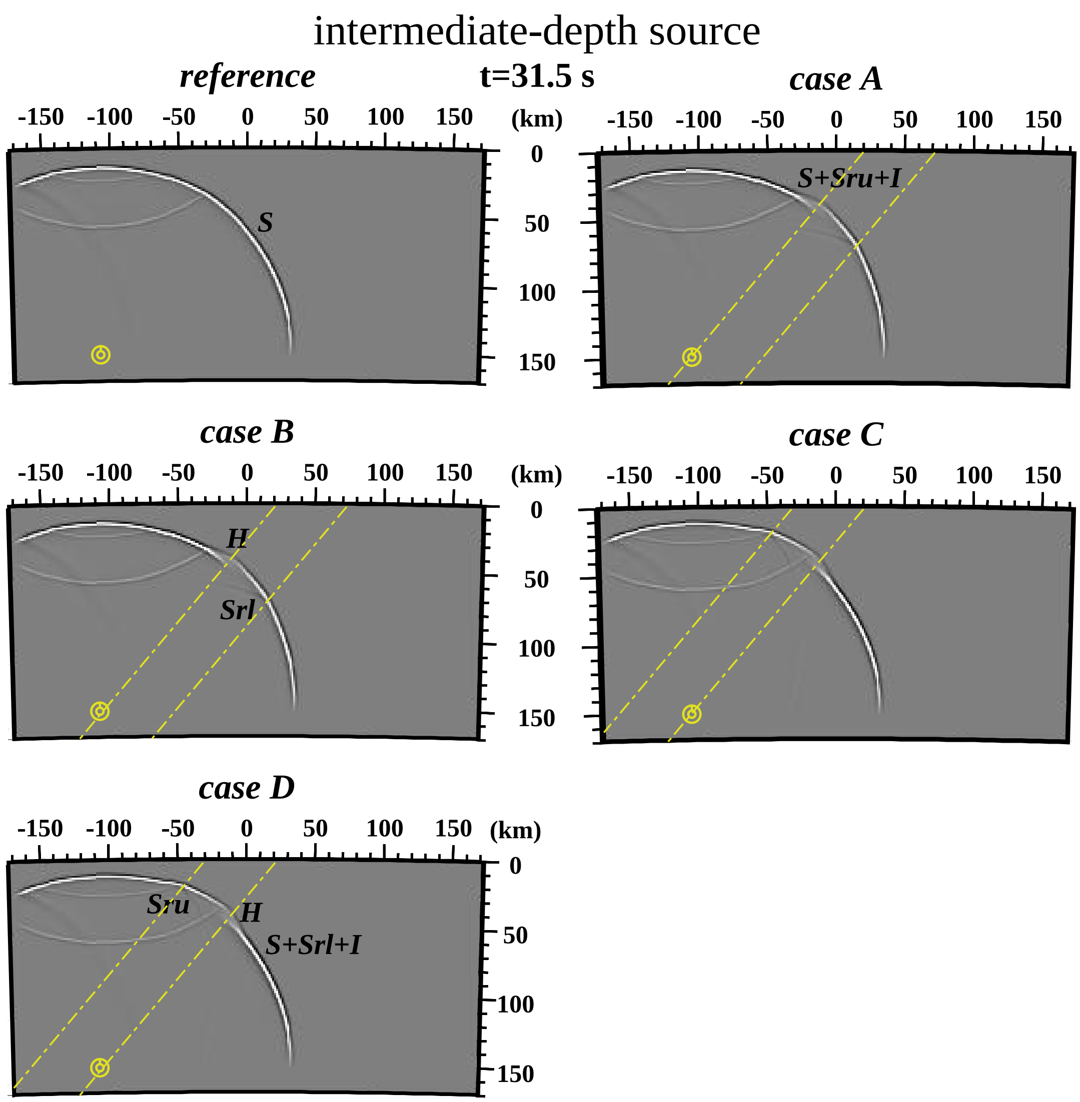

Fig. 6.17. Snapshots of *SH* wave propagation in subduction zones with an intermediate-depth of source at t=31.5 s. The wavefields are simpler than those in Fig. 6.17, but the phases developing on boundaries are clearly shown to travel into the free surface. The main reflected waves (*Sru*, *Srl*), interface waves (*I*), and head waves (*H*) are indicated.

slab does not make significant differences in the wavefields (compare cases A and B, cases C and D in the figure). However, there are noticeable difference between the snapshots for sources near the upper boundary (cases A and B) and the lower boundary (cases C and D), with characteristic patterns of interaction with the boundaries. Even though the contrast at the slab edge is not large, significant modifications to the wavefield can be introduced.

For shallow sources (S_1) near the upper boundary of the slab (cases A and B in Fig.

6.16), significant interface waves (*I*) and reflected waves (*Sru*, *sSru*) propagate along the upper boundary mixed in with or following both the *S* and *sS* phases. Weak reflected waves (*Srl, sSrl*) can be recognised from their hook shape. The interface waves (*I*) and reflected waves (*sSru*) following *sS* waves are shown clearly in the 3-D perspective view, the last snapshot, in the figure.

On the other hand, for shallow sources (S_1) near the lower boundary of slab (cases C and D), reflected waves and interface waves from the lower boundary develop after the *S* waves, but there is little interaction with the *sS* waves which have passed through the slab on their way to the free surface. Nevertheless, weak reflected waves (*sSru*) can be still found after *sS* waves from the upper boundary (see, case D).

Head wave effects outside the slab (*H*) are more apparent for cases A and B since they become detached from reflected waves with both distance and time (see, *H* in case B). However, head waves in cases C and D have a less distinct identity (see, *H* in case C), because the contrast with the background velocity is less.

For the group of intermediate-depth sources (Fig. 6.17) the wavefront patterns are relatively simple and the effects of the slab can be transferred updip towards the surface. Noticeable reflected waves and interface waves develop along the boundary near the source, and weak reflected waves are generated at the other boundary of the slab. Head waves surrounding the slab appear in each case.

6.4.3.2 *Waveforms recorded at the surface*

The influence of the high velocity slab can be clearly seen in the seismograms recorded at the surface. We use a set of 60 receivers with a spacing of 5.4 km, and enhance the range of arrivals associated with the presence of the slab by using difference seismograms between the various cases.

In Fig. 6.18 we show the seismograms for a shallow source for the reference model and the difference seismograms between the cases A,B,C,D and the reference model. The general pattern of the wave trains for the reference case is preserved in all cases but the introduction of a slab leads to travel-time anomalies which depend on the relative positions of receivers to the source and the slab. The main variations occur on the far side of the slab from the source position as can be seen in the difference seismograms Fig 6.18(b),(c), the strong contributions arise from the phase shifts induced by the passage through the slab.

Reflected waves from the upper boundary of slab also play an important role in the waveform variation in the later part of the wave trains recorded above the slab in a narrow interval x=-60 to -140 km, Fig. 6.18(b), corresponding to ranges of 80 to 160 km

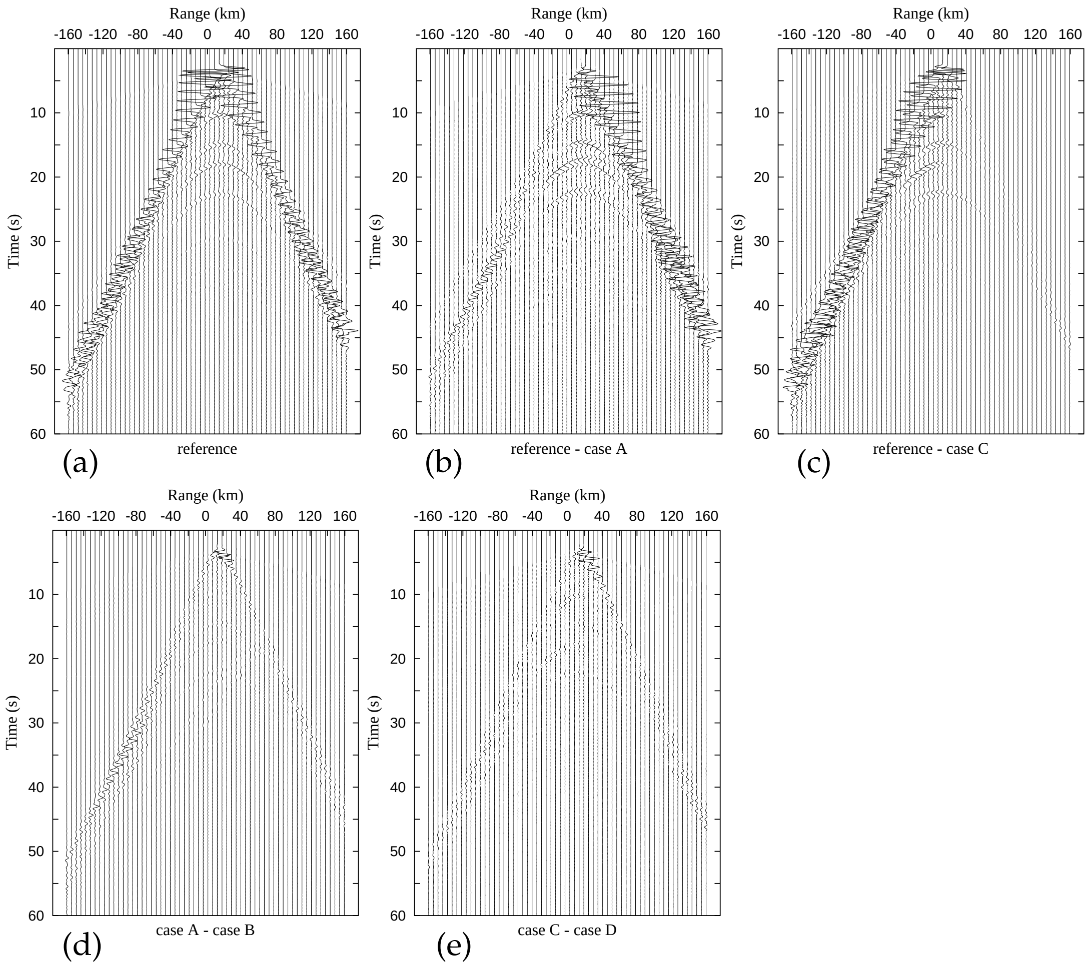

Fig. 6.18. Seismograms at the surface for shallow sources in the simplified subduction model. (a) The main features of the seismograms are well represented by the reference model. The features associated with the presence of the slab are enhanced by considering difference seismograms. The main features of source positions at the upper and lower slab boundaries can be seen from (b) reference - case A (upper), (c) reference - case C (lower). The more subtle differences arising from the position of the source, inside or outside the slab, are apparent from the difference seismograms (d) case A - case B, and (e) case C - case D. The main differences arise from the time advance of the waves in the slab models when they pass through the slab. Reflected arrivals from the upper boundary of the slab are important for sources near the upper boundary, and are more pronounced for case B where the source lies outside the slab.

from the epicenter. For the source inside the slab (case A) the reflected waves are mainly generated by *sS* waves, but for an external source (case B) both *S* and *sS* waves contribute and the amplitude is enhanced (see, Fig. 6.18(b) and (d) for x=-100.0 km). For shallow sources near the lower boundary of slab (cases C,D), the main effect is just the travel time anomaly caused by introduction of the high-velocity zone (see, Fig. 6.18(c) and (e)).

The waveforms for two locations on either side of the slab are compared in Fig. 6.19. At x=-100 km, the influence of the reflected waves for the upper boundary of the slab

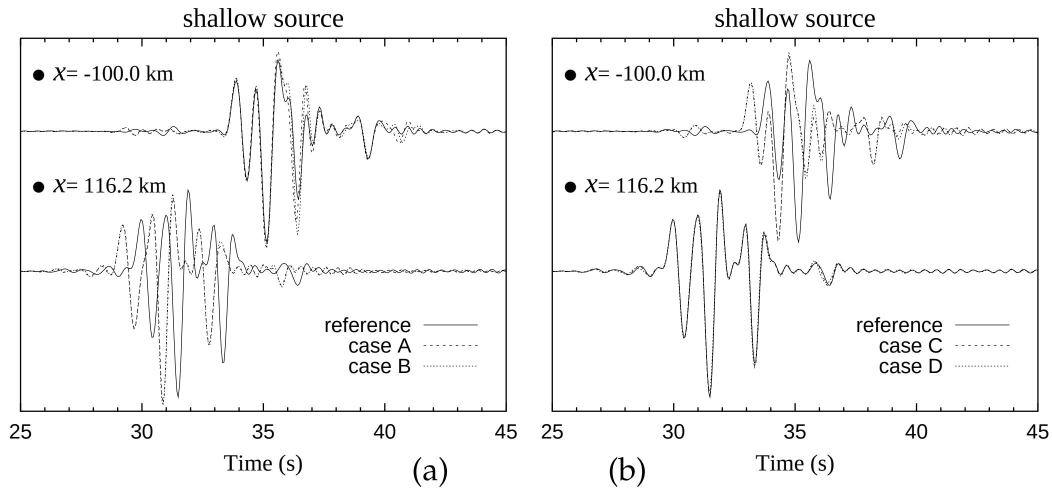

Fig. 6.19. Comparisons among time responses of models for shallow sources at two representative places (x=-100, 116.2 km): among (a) reference model, cases A and B and (b) reference model, cases C and D. The strong influence of passage through the slab is apparent in each case.

can be seen in the modification of the later part of the main pulse, whereas the dominant influence for the cases C,D is the time shift due to passage through the slab. With the observation point on the other side of the slab at x=116.2 km, there is little difference from the reference for the sources near the lower boundary (cases C,D) and a bulk shift of the waveforms for the cases A,B with sources at the upper boundary of the slab.

For an intermediate depth source a rather different pattern of arrivals is produced. Although the slab offers a fast propagation path, energy is continuously shed from the high velocity slab into the lower velocity surroundings (note the weakened wavefronts in the slab in Fig. 6.17). As a result the waves emerging at the surface in the slab zone are advanced in time but show rather small amplitudes compared with the reference case (Fig. 6.21 at x =18.9 km).

Intermediate-depth sources implemented around a slab make distinctive variation in the waveforms (Fig. 6.20) and, in particular, a wave dissipation pattern is observed at receivers placed above boundaries of slab, depending on the relative position of the source and the slab boundaries. When the source is close to the upper boundary of the slab, significant energy as the sum of reflected (case B), refracted (case A) and interface waves arrives at the side of the upper boundary (Fig. 6.20(b),(d)). That is, a portion of incident waves are reflected from the upper boundary in the case B, and successive energy drains from the high-velocity region to low-velocity background media occur in case A. So, as a result, the wave dissipation appears around both boundaries of slab. The effect is present in broad ranges around the upper boundary, but only in a narrow

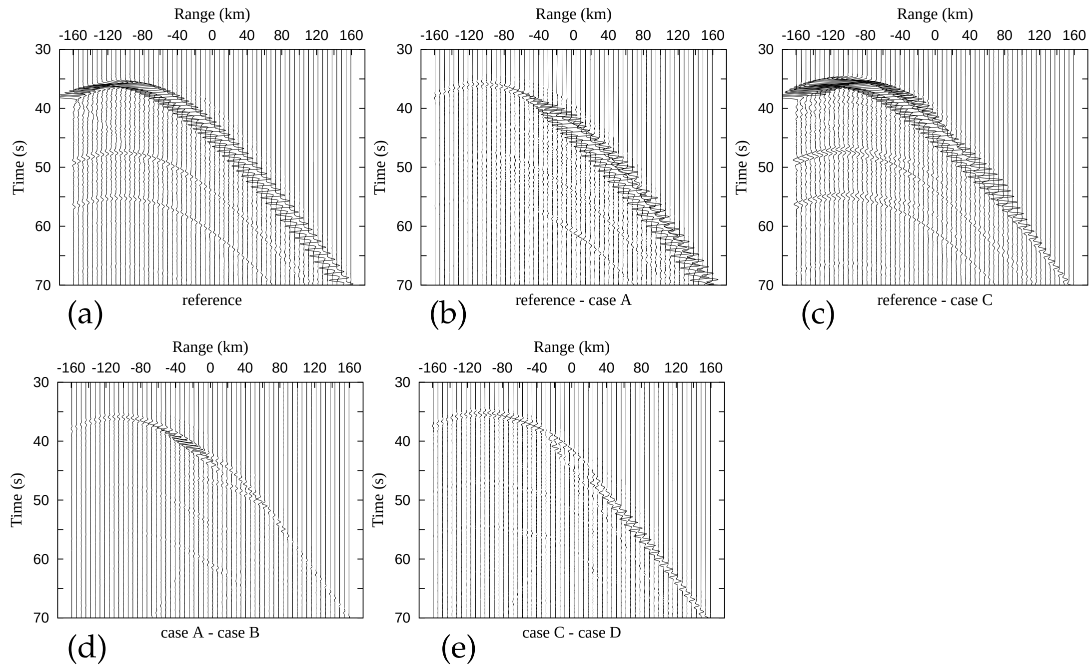

Fig. 6.20. Seismograms at the surface for intermediate-depth sources in the simplified subduction model. (a) The main features of the seismograms are well represented by the reference model. The features associated with the presence of the slab are enhanced by considering difference seismograms. The main features of source positions at the upper and lower slab boundaries can be seen from (b) reference - case A (upper), (c) reference - case C (lower). The more subtle differences arising from the position of the source, inside or outside the slab, are apparent from the difference seismograms (d) case A - case B, and (e) case C - case D.

zone at the lower-boundary region. Also, waves which are transmitted through the slab and recorded at far distances, display reduced amplitudes. Reflected (or refracted) waves combined with interface waves are recorded on the side of the lower boundary at regional distances.

A travel time anomaly due to transmission through the slab is found on the opposite side of slab to the source position (Fig. 6.20(b),(c)). An amplitude anomaly from the arrivals of reflected (or refracted) waves and interface waves is observed at a narrow region at x=0 to -40 km with implementation of a source around the upper boundary. Direct transmission through the slab also induces some loss in amplitude due to the contrasts at the slab boundaries (cases A,B at x = 78.3, 116.2 km and cases C,D at x = -29.7, -137.8 km). Reflected waves can contribute to local enhancement of the amplitude just outside the slab zone (cases A,B at x =-29.7 km and cases C,D at x = 78.3 km).

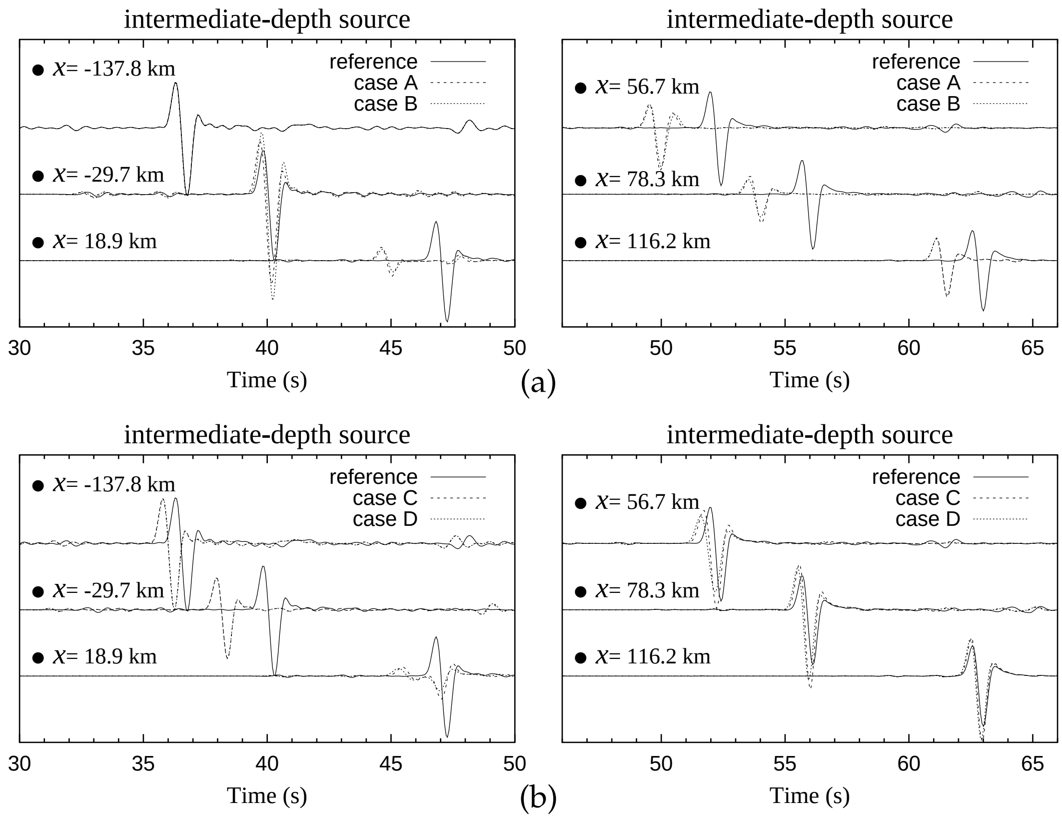

Fig. 6.21. Comparisons of seismograms for intermediate-depth sources at six representative locations (x=-137.8, -29.7, 18.9, 56.7, 78.3, 116.2 km): (a) reference model, cases A and B; (b) reference model, cases C and D. Both amplitude differences and travel time anomalies are displayed in traces with characteristic patterns depending on the configuration of the source relative to the slab.

6.4.4 Modelling in realistic slab models

We introduce slab models with realistic geometry and investigate variations of waveforms and wavefields in the models. The models are designed such that the portions of slabs at near surface bend smoothly and then are extended parallel to the surface. Also, transitional layers with 2 % velocity contrast to the background media are added around both boundaries of slabs with 5 % velocity increase. The thickness of the inner portion of slabs is set to be 40 km as in the simplified slab models, and the thickness of the transitional layers is 10 km. For comparisons with wavefields in the simplified slab models, we implement sources with the same position. Note that sources in cases B and C are placed inside the transitional layers.

In general, wavefronts in the realistic slab models (Fig. 6.22) are similar to those in the simplified slab models (Fig. 6.17). However, head waves are less discernible and various reflected waves develop at the boundaries of slabs due to the introduction of transitional

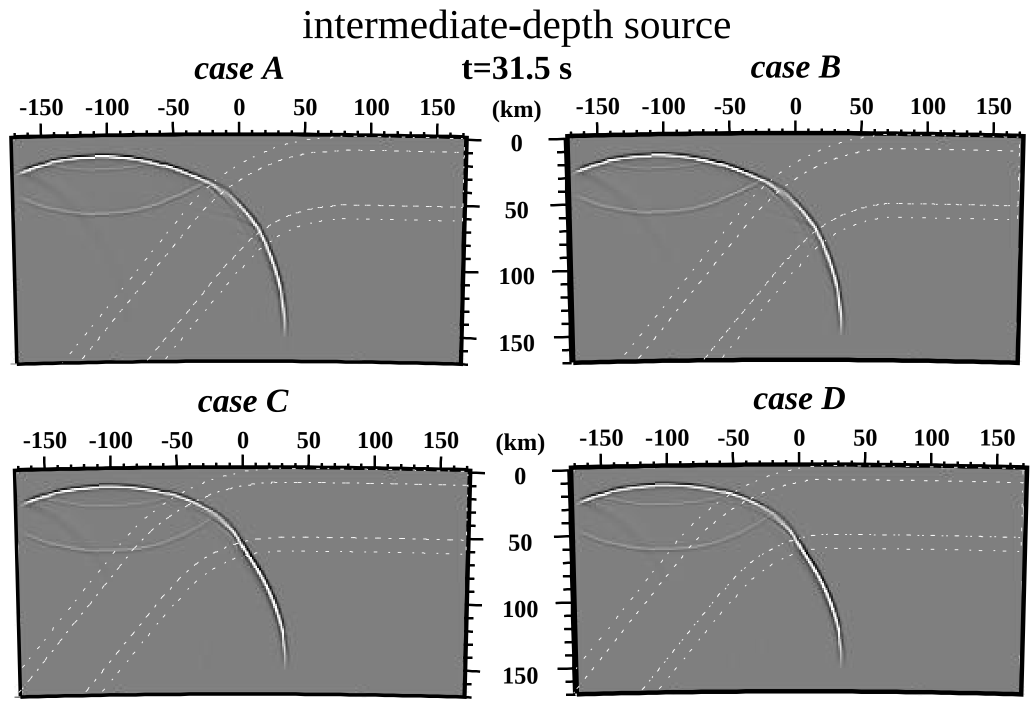

Fig. 6.22. Snapshots of *SH* wave propagation in subduction zones with realistic geometrical structures for an intermediate-depth of source at t=31.5 s. Head waves are not discernible in every case since the velocity contrasts at the slab boundaries are not large. But, instead, various reflected waves develop at the boundaries and also the wavefronts are affected by the curvature of the slabs.

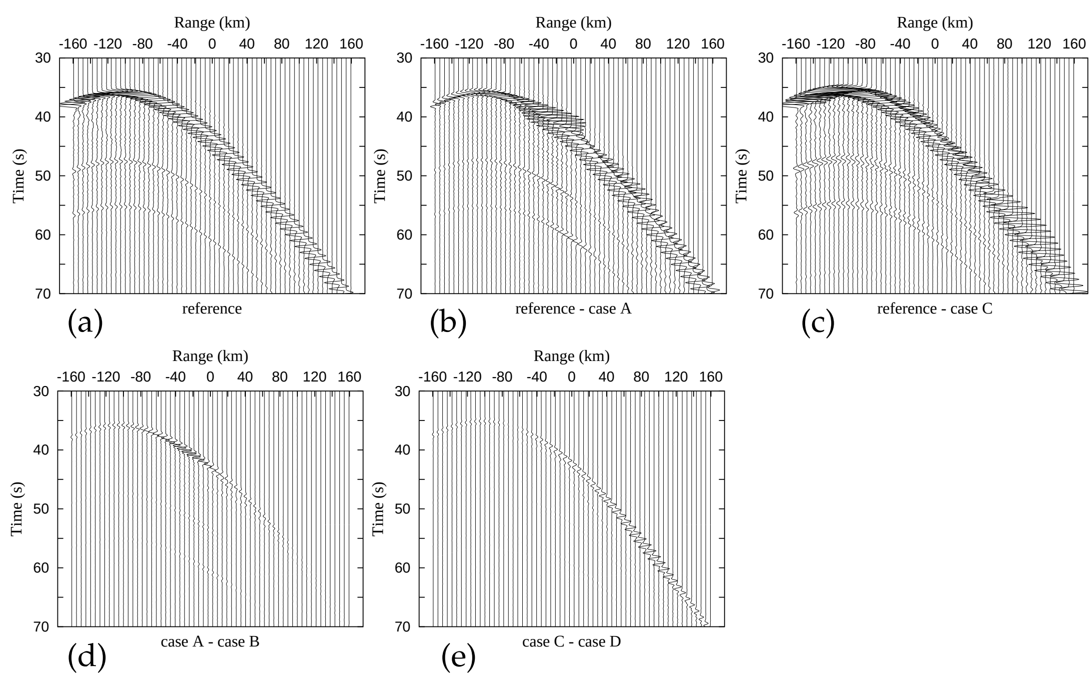

Fig. 6.23. Seismograms at the surface for intermediate-depth sources in realistic subduction models. (a) reference model, (b) reference - case A, (c) reference - case C, (d) case A - case B, and (e) case C - case D.

layers with weak velocity contrast. With the curvature of slabs, the wavefronts are affected by the focusing and defocusing effect.

Significant guided waves in the upper transitional layer in cases A and B which depart from the slab at the turn are recorded at receivers around x=0 km in Fig. 6.23(b), and the guided energy is larger than that for simple transmission in the simplified slab models (see, Fig. 6.20(b)). The horizontal layering of the slab at the surface generates a travel time anomaly in time responses of cases C and D, while the effect is not severe in cases A and B at regional distances. The differences between cases A & B and cases C & D are similar to those in the simplified slab models, but the particular patterns recorded at receivers placed on slab boundaries in Fig. 6.20(d) and (e), are not displayed in Fig. 6.23(d) and (e) due to the bending in the slab.

6.5 Discussion

The wavelet-based method (WBM) provides an effective means of simulating elastic wave propagation in heterogeneous media, since it can cope with rapid variations in physical properties without loss of accuracy. With the improved scheme for source representation introduced in this paper it is possible to place moment-tensor or dislocation sources directly in regions of heterogeneity. This enables the WBM to be used effectively in a variety of problems where significant contrasts in physical properties occur in the neighbourhood of the source.

In the case of sources within a highly heterogeneous fault gouge zone, we get strong waveguide effects for *P-SV* waves, which are modified somewhat when we introduce a propagating rupture. The fault-trapped waves decay outside the fault zone and the presence of high frequency energy provides a good guide to the location of the fault zone itself.

In subduction zones, the slab represents a region of elevated wavespeed compared to its surroundings. Although propagation along the slab is fast, substantial energy is shed in an anti-waveguide effect. The contrasts at the boundaries of the slab have the potential to generate reflected and interface phases that can add to the complexity of the seismograms for stations in the vicinity of the slab.

7

Scattering of elastic waves in stochastic random media

7.1 Introduction and overview of seismic scattering

7.1.1 Numerical modelling and scattering attenuation

One of the most important topics in regional seismic studies is the influence of scattering due to material inhomogeneities and anisotropy in the crust and the upper mantle (e.g., Wu *et al.*, 1994; Nolet *et al.*, 1994). Scattering processes modify both the travel times and amplitudes of seismic waves. A full representation of scattering phenomena requires consideration of multiple scattering effects which are difficult to handle. In consequence attention has focused on single scattering implemented via a first-order Born approximation for weakly heterogeneous regions (e.g., Wu, 1982; Frankel & Clayton, 1986)

The single scattering theory is applied mainly to back-scattered and side-scattered energy and the more complex effects in forward scattering are taken care of by including a correction for the induced travel-time shift inside a certain angular range around the propagation direction. The separation between the two different approximation regimes is made at the 'minimum (or, cutoff) scattering angle' (e.g., Roth & Korn, 1993; Sato & Fehler, 1998; Kawahara, 2002). Estimates of this minimum scattering angle have been made using numerical modelling of stochastic media in an acoustic approximation or with a full elastic treatment (e.g., Frankel & Clayton, 1986; Roth & Korn, 1993; Jannaud *et al.*, 1991; Frenje & Juhlin, 2000). Alternatively estimates of the minimum scattering angle have been made theoretically for random acoustic media (e.g., Sato, 1984; Kawahara, 2002).

However, there is still some uncertainty as to the appropriate minimum scattering angle for elastic waves because much of the work has been undertaken in the acoustic approximation (e.g., Roth & Korn, 1993) or with a scalar wave approach, even for elastic wave studies (e.g., Frankel & Clayton, 1986). The scattering pattern of elastic waves is complex and is significantly different from that of scalar waves (Wu & Aki, 1985) due to the inherent characteristics of elastic waves such as wave type coupling, the radiation patterns in scattering, and complex interferences between the waves. As a result numerical modelling for elastic waves needs to be compared with theoretical results for a full understanding of the influence of elastic wave scattering. The minimum scattering angle, as one of the key factors in single scattering theory, thus needs to be determined properly and the relation to the acoustic theory explored.

Single scattering theory for 3-D elastic waves has been developed in several studies. Wu & Aki (1985) compared theoretical scattering coefficients based on the Born approximation with results derived from observations, and tried to reveal the characteristics of heterogeneities in the lithosphere. Wu (1989) introduced the 'perturbation method' for the scattering of elastic waves in random media, which considers the scattering waves as the response of the perturbations to the incident waves in a sense of a radiation problem. Sato & Fehler (1998) followed a similar approach, but considered an additional important factor, a travel-time correction applied to the Born approximation in order to determine the correct energy loss during scattering. They associate the travel-time shift by the fractional-velocity fluctuation due to the long wavelength component of scattered waves, i.e., waves with wavelength more than twice that of the dominant frequency. This approach has been used to determine the minimum scattering angle to be employed in the estimation of scattering attenuation of elastic waves in 3-D.

It is therefore important to check the theoretical estimates of the minimum scattering angle match those determined empirically. Although Sato & Fehler's minimum scattering angle is supported by some numerical studies (e.g., Roth & Korn, 1993) for the scalar-wave cases, it has not been fully checked for elastic waves. The numerical studies of elastic waves (e.g., Frankel & Clayton, 1986) used the theoretical attenuation curve for scalar waves as the reference curve for determination of the minimum scattering angle. However, since numerical modelling for 3-D elastic wave propagation is still requires considerable computational expense to achieve an adequate domain for the assessment of the scattered energy, we confine our study to 2-D elastic waves.

For 2-D elastic waves, hybrid methods have been used. Fang & Müller (1996) attempted to formulate the governing equation in a rational form by incorporating two formulae for scalar waves with both velocity perturbation (e.g., Frankel & Clayton, 1986) and density perturbation (e.g., Roth & Korn, 1993). The coefficients of each term in the rational form need to be determined for each stochastic medium by curve fitting to the results from numerical experiments. This approach of Fang & Müller is based on the fundamental assumption that the scattering attenuation pattern of elastic waves is similar to that of scalar waves for the given stochastic medium (e.g., exponential media for Fang & Müller's study) and that the minimum scattering angle ($\theta_{\min}$) would be the same for (20°) for both acoustic and elastic waves.

To avoid such assumptions it is important to develop a fully elastic 2-D theory for the variation of scattering attenuation as a function of normalized wavenumber for 2-D elastic waves to compare with numerical results, and thereby determine the minimum scattering angle.

It is very important that we not only have a correct correct derivation and implementation of scattering theory for comparisons with numerical results, but also that high accuracy numerical modelling is available for the assessment of the value of the minimum scattering angle. The finite difference method (FDM) with 4th-order accuracy in spatial differentiation has been used widely for the modelling in random heterogeneous media due to the convenience in treatment of numerical models and simplicity in implementation (e.g., Frankel & Clayton, 1986; Jannaud *et al.*, 1991; Roth & Korn, 1993; Fang & Müller, 1996; Frenje & Juhlin, 2000; Fehler *et al.*, 2000). However, Sato & Fehler (1998) have pointed out that derivatives in a FDM scheme are computed in the sense of an average over some grid points in a domain. It is still therefore an open question as to whether the 4th-order accuracy in spatial differentiation is sufficient for stable and accurate modelling in random heterogeneous media.

High accuracy in spatial differentiation can be achieved with the pseudospectral method, and this approach has been applied in seismic wavefield computation for laterally heterogeneous models on upper mantle and global scales (Furumura *et al.*, 1999). However, it is difficult to achieve a comparable level of accuracy in the representation of the free-surface condition of vanishing traction. Yomogida & Benites (1995) have applied the boundary integral method for modelling media with randomly distributed cavities. Such boundary integral methods can deal well with heterogeneities inside a medium with irregular interfaces (e.g., cavities, cracks. The boundary conditions are satisfied by including effective sources at the boundaries at each time step. For a homogeneous medium it is possible to get an accurate time response because the necessary Green's functions can be found analytically. However, it is difficult for the method to be applied to media with heterogeneous backgrounds (including layered media) because the Green's functions themselves need to be found numerically. Recently, the generalized screen propagators (GSP) method has been developed as a fast computational procedure for modelling of elastic wave propagation in half spaces with small-scale heterogeneities

(Wu *et al.*, 2000). However, the approach used in the GSP method ignores the backscattering process and so is not suitable for full representation of scattered waves.

We use the wavelet-based method (WBM) as an accurate and stable simulator of elastic wave propagation in random media. The accuracy and the stability of the method is addressed through comparisons with the FDM. The WBM is then applied to calculate synthetic seismograms for several styles of stochastic media, from which the scattering attenuation is measured. The nature of the scattering needs to be taken into account to get accurate estimates of the attenuation, since in large-scale heterogeneity significant deviations in the primary wave field mean that both components of motion need to be considered for a 2-D medium. With accurate modelling we are able to place constraints on the minimum scattering angle for 2-D elastic waves to the span 60-90°.

7.1.2 Scattering attenuation of elastic waves

Seismic attenuation is a well-known feature associated with wave propagation in the earth, and many studies of field data have tried to resolve the magnitude of apparent attenuation rates in various regions (e.g., Tselentis, 1998; Chung & Sato, 2001; Yoshimoto *et al.*, 1998; Adams & Abercrombie, 1998; Hatzidimitriou, 1995).

The total attenuation rates are determined by the contributions from scattering (Q_s^{-1}) and intrinsic attenuations (Q_i^{-1}). The intrinsic attenuation is related to the physical and chemical nature of the media, for example, the rock type (Assefa *et al.*, 1999), the material state (Del Pezzo *et al.*, 1995), and temperature (Roth *et al.*, 2000). Also, the thermoelastic effect, the irreversible conversion of kinetic energy to heat flow, causes anelasticity in the earth (Frankel *et al.*, 1990; Aki, 1980). Such effects may lead to variation of attenuation in the earth with depth (e.g., Menke *et al.*, 1995; Tselentis, 1993; Der, 1998; Flanagan & Wiens, 1998). Tectonic activity is responsible for large attenuation in tectonic regions (Sarker & Abers, 1998; Frankel *et al.*, 1990).

However, it has been reported that the scattering attenuation is usually the dominant factor in seismic attenuation in the crust (e.g., Hatzidimitriou, 1994; Del Pezzo *et al.*, 1995). Even when the intrinsic attenuation is comparable to the scattering attenuation, the intrinsic attenuation appears to vary with the scattering attenuation in many regions (e.g., Mayeda *et al.*, 1992). Thus, a precise estimation of scattering attenuation variation allows an understanding of seismic attenuation patterns in the crust.

Field-data analysis has usually been focused on obtaining apparent attenuation factors, but there are few studies characterizing the heterogeneities in terms of stochastic random processes. Thus, it is still uncertain which type of stochastic random model can adequately represent the nature of the real crust and which level of variation can reproduce the heterogeneities of the crust. Through comparisons of scattering effects between field data and synthetic data, it may be possible to provide reference stochastic random models for specific areas. In which case, the models can be used for fundamental studies on the seismic signatures in the areas, such as the duration of coda waves and their spectral composition, through numerical modelling. Such synthetic studies on scattering attenuation may also allow the understanding of effects of anisotropic materials (e.g., Adam & Abercrombie, 1998). For this purpose, we need to be able to characterise the scattering attenuation and the properties of stochastic random model, which can be achieved by considering the theoretical scattering behavior validated by seismic responses.

Although the ultimate goal is to understand scattering in 3-D, we are able to use 2-D simulations to good advantage because 3-D scattering effects are quite similar to 2-D (Frenje & Juhlin, 2000). Further we can make a more effective investigation of coupling between phases and energy partition. The theoretical expressions for attenuation in 3-D (Sato & Fehler, 1998) require 3-D integrations, resulting in multiple 2-D integrations, over propagation angles to describe the dependency of coupled phases such as *SP, PS* on scattering angle due to geometrical complexity of heterogeneities. The corresponding expressions are simpler in 2-D and may be more readily compared to numerical results. Although the absolute magnitude of energy losses due to scattering may be different between 2-D and 3-D cases, the scattering attenuation ratios are expected to be consistent in both cases.

In order to make the theoretical scattering attenuation forms based on a single scattering theory (first-order Born approximation) comparable to the results from seismic data which associate a travel-time shift with the perturbation of physical parameters, it is required to eliminate the contribution of forward scattering within a minimum scattering angle when computing theoretical attenuation rates. Therefore, it is so important to determine the minimum scattering angle correctly for the implementation of the theoretical expressions to seismic quantitative studies.

We formulate the theoretical 2-D scattering attenuation variation for P and S waves, and compare them with numerical results. Artificial attenuation may be incorporated from the modelling technique due to limitation of the accuracy in spatial differentiations of perturbed wavefields, and thus we implement a wavelet-based method, which retains high accuracy and stability even in highly heterogeneous media, for the numerical modelling in this study.

The theoretical attenuation curves for S waves are compared with four different types of stochastic random models: von Karman with Hurst number ν=0.05, 0.25, exponential and Gaussian random media. We display the scattering attenuation patterns of elastic waves by comparing the theoretical curves for *P* and *S* waves in terms of wavenumber or frequency. The estimated attenuation ratios are compared with the reported results from field-data analysis, and we present the properties of stochastic random media in terms of scattering attenuation rates.

7.2 WBM as a tool for obtaining synthetic data in seismic quantitative studies

We now consider some aspects of numerical modelling to display the efficiency of the WBM as a simulator of elastic wave propagation in random media. In every numerical method, to achieve accurate and stable results without numerical dispersion requires the size of the grid steps to depend on the frequency content of source time function and the wave velocities in the medium. In particular, the number of grid points needed for the smallest expected wavelength expected in the media will determine the size of the required grid and the consequent computational effort. Hence the number of grid points per wavelength is often used to present the efficiency of given method as a numerical simulator (e.g., Komatitsch & Vilotte, 1998). The 4th-order FDM requires at least 10 grid points per wavelength in models with strong impedance contrast between layers (Shapiro *et al.*, 2000), while WBM using Daubechies-20 wavelets needs 3 grid points per wavelength (see, Section 3.9). These grid steps are sufficient to produce stable and accurate results in simple media. However, it is necessary to check if such methods can generate accurate responses in complex media such as random media. In complex media we expect sharp changes in physical parameters between grid points and so resolution of physical changes is an important issue, as well as the accuracy of differentiation.

We first consider the process of differentiation in a random medium and then present examples of WBM modelling in the presence of very strong heterogeneity. In a random medium we can expect strong variations in properties and we can simulate the effects by taking discrete samples of a rapidly varying function $f(x)$ on 1-D domain x. Where, e.g., $f(x)$ can be considered as a displacement field combined with highly perturbed Lamé coefficients (e.g., λu_x) in the media. We use the functional form (Fig. 7.1(a)):

$$f(x) = x^3 \sin(x\sqrt{x}) \exp\left(-\frac{x}{2}\right), \tag{7.1}$$

and the analytic derivative $f'(x)$ is (Fig. 7.1(b))

$$f'(x) = \frac{3}{2}x^{\frac{7}{2}} \cos(x\sqrt{x}) \exp\left(-\frac{x}{2}\right) + (3x^2 - \frac{1}{2}x^3) \sin(x\sqrt{x}) \exp\left(-\frac{x}{2}\right), \tag{7.2}$$

where $0 < x \leq 20$ and x corresponds to the dimensionless distance in the domain. For the numerical differentiation, we implement both the 4th-order FDM and the WBM. When

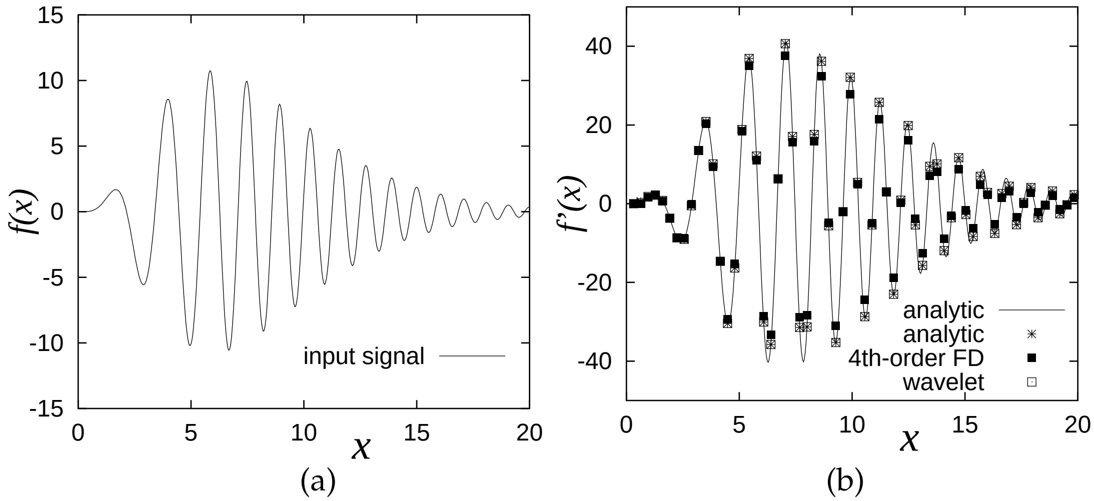

Fig. 7.1. Comparison of the accuracy of differentiation between the 4th-order finite difference method (FDM) and the wavelet-based method (WBM): (a) highly varying input signal which corresponds to the variation of physical parameters in random media and (b) numerical results which show that the 4th-order FDM exhibits the attenuated results for the derivative but WBM generates the very accurate results even when the number of discretization points for the input signal is decreased to 64.

the signal $f(x)$ is considered on a sufficiently dense grid system (e.g., number of grid points N_x=256, grid step δx=0.0781), both numerical estimates of the derivative ($f'(x)$) are apparently coincident with the analytical solution. However, for a sparser grid system with N_x=64 (δx=0.3125), the derivative estimates from the FDM exhibit attenuated amplitudes while WBM generates correct responses. This example of the differentiation of $f(x)$ on the sparse grid system would correspond physically to the situation of a medium with high fractional fluctuation or where diverse strong heterogeneities are present in a given area. Thus, FDM may generate attenuated results for fine-scale heterogeneities or when a high fractional fluctuation is considered in the random media.

This phenomenon has previously been reported in a study based on FDM for modelling in random media; Jannaud *et al.* (1991) have shown that the measured scattering attenuation rates exhibit high attenuation relative to the theoretically expected rates when a high fractional fluctuation is considered in the random media (ϵ=10, 20 % in their study). However, there was good agreement between numerical and theoretical results for the case of a weakly perturbed medium (ϵ=4 %). In the presence of high levels of fluctuations the smoothness assumptions underlying the FDM forms of the numerical operators for differentiation break down, with the result that artificially attenuated wavefields are produced. The WBM, on the other hand, considers the differentiation of the whole data at all grid points through wavelet decomposition on a set of spaces (i.e., the variations of high frequency content and low frequency content are handled

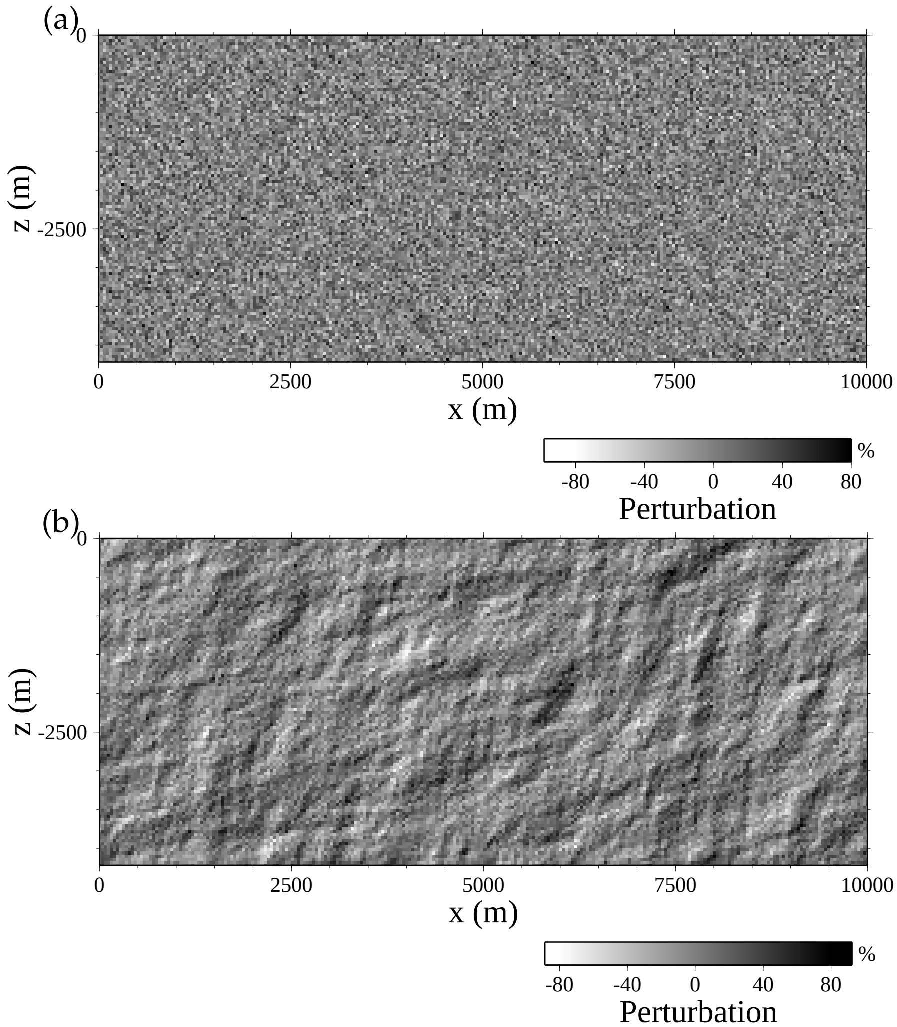

Fig. 7.2. Representation of (a) a pointwise random heterogeneous medium with a standard deviation of velocity perturbation of 20% and (b) a stochastic random heterogeneous medium generated by von Karman ACF with the Hurst number (ν) of 0.25, a correlation distance of 100 m and a standard deviation of velocity perturbation of 52%.

in separate spaces but at the same time), and therefore retains accuracy throughout the domain without accumulating numerical errors across the grid.

As a further demonstration of the efficacy of the WBM we consider the stability of the calculations for highly perturbed media. For this test, two kinds of models with high velocity perturbations are considered; a pointwise random medium (Fig. 7.2 (a)) where wave speeds vary randomly with the Gaussian probability distribution with a standard deviation of velocity perturbation of 20 % and a systematic random media generated by von Karman autocorrelation function (ACF) with a Hurst number (ν) of 0.25 (Fig. 7.2 (b)), a correlation distance of 100 m and a standard deviation of velocity perturbation of 52 %. The maximum value of the velocity perturbations reach 98 % for the pointwise

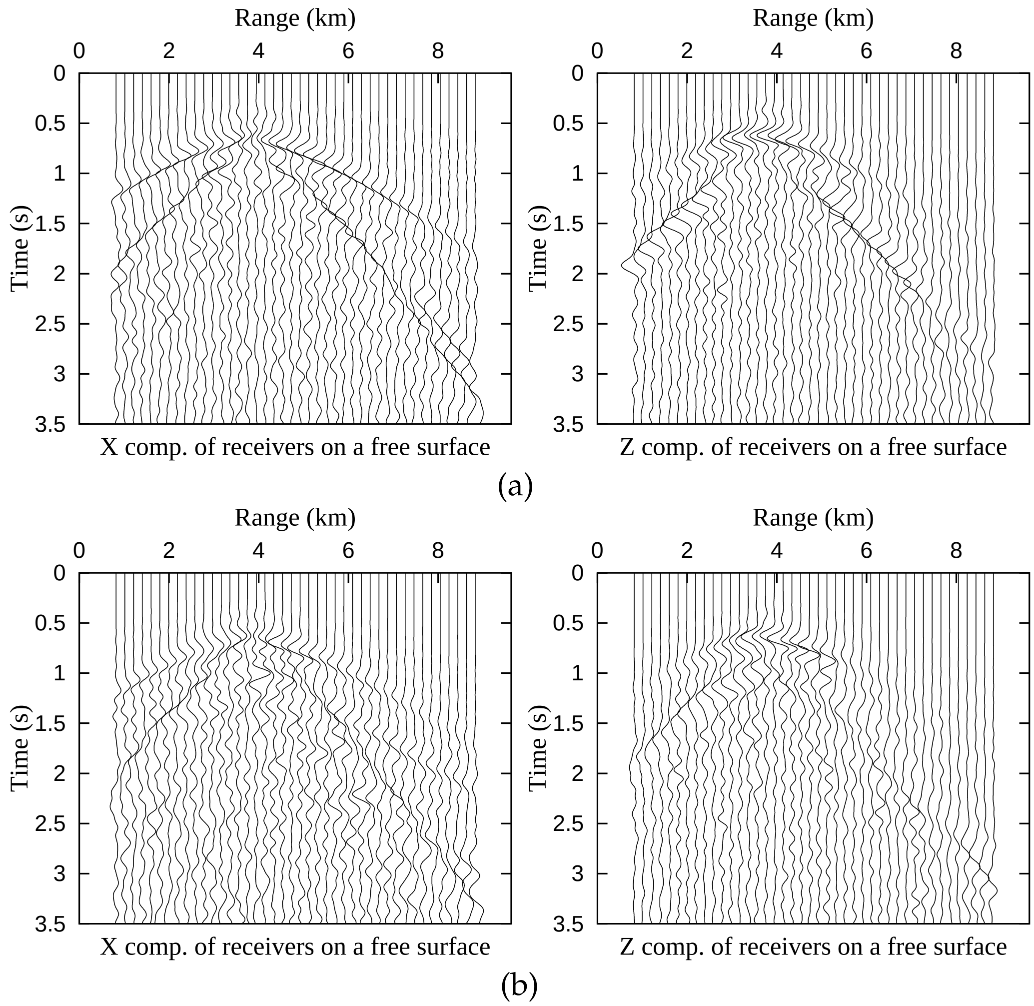

Fig. 7.3. Time responses of displacement at the free surface receivers for the highly perturbed models shown in Figure 7.2): (a) the pointwise random medium and (b) the stochastic random medium.

medium and 92 % for the von Karman medium. For such high levels of perturbation, the conventional FDM is subject to strong dispersion in the numerical results (Roth, 2001).

The reference P and S wave speeds for the WBM calculation are 3.5 and 2.0 km/s, and a vertically directed force is applied at depth 1500 m in a $10 \times 5\ \mathrm{km}^2$ domain. 42 receivers deployed at the free surface collect the time responses. Despite the large variations in the physical parameters, the WBM generates stable time responses with large coda waves following the main phases for both the pointwise and stochastic random heterogeneous media (Fig. 7.3). Since the scattering effects depend on both the frequency content of source time function and the scale of heterogeneities, the coda waves in pointwise random media are smaller than those in the stochastic random media.

These two experiments, demonstrate that the WBM can generate accurate and stable results in even strongly heterogeneous random media. We are therefore able to undertake the simulation of elastic wave propagation in different styles of random heterogeneous media and measure the scattering attenuation factors by assessing the scattered energy.

7.3 Theoretical scattering attenuation of elastic waves

7.3.1 P-wave incidence

We estimate the scattering attenuation factors (Q_P^{-1}) as a function of normalized wavenumber (ka) based on single scattering theory in 2-D random heterogeneous media, where k is the wavenumber of incident waves and a the correlation distance.

We represent the wavefield (u_j, $j = x, z$) as composed of primary waves (u_j^0, $j = x, z$) and scattered waves (u_j^s, $j = x, z$). The primary waves in 2-D elastic media satisfy the relationships

$$\rho_0 \frac{\partial^2 u_x^0}{\partial t^2} = \frac{\partial \sigma_{xx}^0}{\partial x} + \frac{\partial \sigma_{xz}^0}{\partial z}, \qquad \rho_0 \frac{\partial^2 u_z^0}{\partial t^2} = \frac{\partial \sigma_{xz}^0}{\partial x} + \frac{\partial \sigma_{zz}^0}{\partial z}, \tag{7.3}$$

where

$$\sigma_{xx}^0 = (\lambda_0 + 2\mu_0)\frac{\partial u_x^0}{\partial x} + \lambda_0 \frac{\partial u_z^0}{\partial z}, \qquad \sigma_{zz}^0 = \lambda_0 \frac{\partial u_x^0}{\partial x} + (\lambda_0 + 2\mu_0)\frac{\partial u_z^0}{\partial z},$$
$$\sigma_{xz}^0 = \mu_0 \left(\frac{\partial u_x^0}{\partial z} + \frac{\partial u_z^0}{\partial x} \right), \tag{7.4}$$

λ_0 and μ_0 are Lamé coefficients, and ρ_0 is the density in the background medium. When vertically incident (z-axis direction) plane *P* waves (Fig. 7.4) are considered as the primary waves, they are represented as

$$u_x^0 = 0, \qquad u_z^0 = e^{i(k_\alpha z - \omega t)}, \tag{7.5}$$

where ω is the angular frequency, k_α the wavenumber of incident *P* waves (ω/α_0), and α_0 the background *P* velocity. The scattered waves can be represented using body forces f_j^s ($j = x, z$ or 1,2) arising from the scattering effects of the variation of physical parameters,

$$\rho_0 \frac{\partial^2 u_x^s}{\partial t^2} - \frac{\partial \sigma_{xx}^s}{\partial x} - \frac{\partial \sigma_{xz}^s}{\partial z} = f_x^s, \qquad \rho_0 \frac{\partial^2 u_z^s}{\partial t^2} - \frac{\partial \sigma_{xz}^s}{\partial x} - \frac{\partial \sigma_{zz}^s}{\partial z} = f_z^s. \tag{7.6}$$

The body forces f_j^s in (7.6) can be found from the primary waves and the fluctuation of physical parameters as (cf. Sato & Fehler, 1998, eq. (4.35))

$$f_x^s = -ik_\alpha \frac{\partial}{\partial x}(\delta\lambda)\, u_z^0, \quad f_z^s = -\left\{ k_\alpha^2(\alpha_0^2\, \delta\rho - \delta\lambda - 2\delta\mu) + ik_\alpha \frac{\partial}{\partial z}(\delta\lambda + 2\delta\mu) \right\} u_z^0. \tag{7.7}$$

From empirical studies (e.g., Shiomi *et al.*, 1997; Birch, 1961) on the perturbations of elastic wave velocities and mass density in real media which display a linear relationship among the parameters, we can represent the perturbations concisely in general by

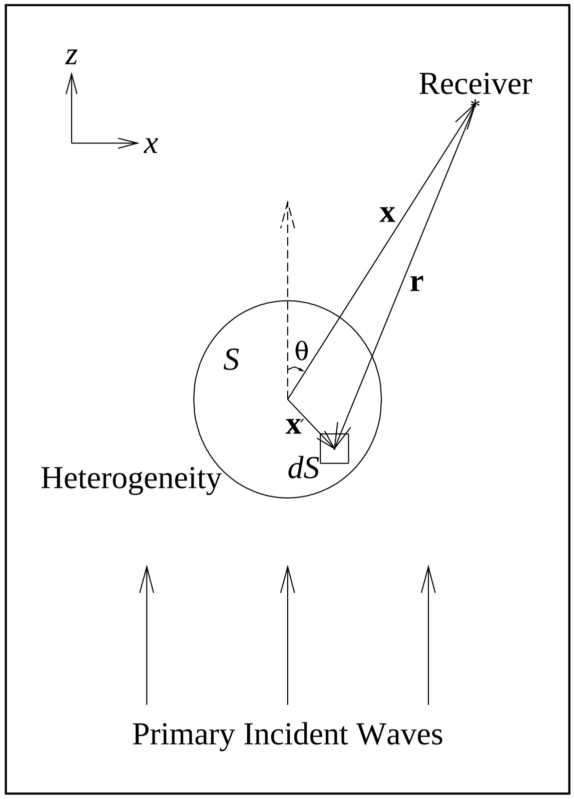

Fig. 7.4. The scattering of the primary incident waves at the scatterer dS, a part of the whole heterogeneous area S. θ is the scattering angle from the incident direction of primary waves along the z axis. $\mathbf{x}$, $\mathbf{x}'$ are the location vectors for the receiver and a scatterer. $\mathbf{r}$ links the scatterer to the receiver.

introducing a fractional-fluctuation term $\xi(x,z)$ as (e.g., Sato & Fehler, 1998, Section 4.2.2; Roth & Korn, 1993)

$$\xi(x,z) = \frac{\delta\alpha}{\alpha_0} = \frac{\delta\beta}{\beta_0} = \frac{1}{K}\frac{\delta\rho}{\rho_0}, \tag{7.8}$$

where α_0 is the P wave velocity in the background medium, β_0 the S wave velocity, and K is a constant which controls the magnitude of the density fluctuations. Hereafter we use symbols without the subscript 0 to represent the background medium to simplify the mathematical expressions. The equation (7.7) can be rewritten from (7.8) as

$$\begin{aligned} f_x^s &= -ik_\alpha\alpha^2\rho\, C_1^P\,\frac{\partial\xi}{\partial x}\,\exp\left[i(k_\alpha z-\omega t)\right], \\ f_z^s &= \left(2k_\alpha^2\alpha^2\rho\,\xi - ik_\alpha\alpha^2\rho\, C_2^P\,\frac{\partial\xi}{\partial z}\right)\exp\left[i(k_\alpha z-\omega t)\right], \end{aligned} \tag{7.9}$$

where C_1^P and C_2^P are constants given by

$$C_1^P = (K+2)\left(1-\frac{2\beta^2}{\alpha^2}\right), \quad C_2^P = K+2. \tag{7.10}$$

The solution of u_j^s ($j = x,z$ or 1,2) in (7.6) can be expressed using the Green's function in the frequency domain, $\overline{G}_{jk}(\mathbf{x}, \mathbf{x}')$ and body forces by an integral over the area of heterogeneity S as (e.g., Roth & Korn, 1993)

$$u_j^s(\mathbf{x}) = \sum_{k=1}^{2} \int_{\mathsf{S}} f_k^s(\mathbf{x}')\, \overline{G}_{jk}(\mathbf{x}, \mathbf{x}')\, d\mathsf{S}(\mathbf{x}'), \quad j = 1, 2. \tag{7.11}$$

The Green's function (G_{jk}, $j, k = 1, 2$) for 2-D elastic wave equations (7.3) for a vertically directed point force can be written as (Burridge, 1976, p115)

$$\begin{pmatrix} G_{12} \\ G_{22} \end{pmatrix} = \frac{1}{4\pi\rho r^2} \begin{pmatrix} (2t^2 - r^2/\alpha^2)\, \sin\theta\cos\theta \\ t^2\cos^2\theta - (t^2 - r^2/\alpha^2)\, \sin^2\theta \end{pmatrix} \frac{H(t - r/\alpha)}{\sqrt{t^2 - r^2/\alpha^2}}$$
$$+ \frac{1}{4\pi\rho r^2} \begin{pmatrix} (-2t^2 + r^2/\beta^2) \sin\theta\cos\theta \\ t^2\sin^2\theta - (t^2 - r^2/\beta^2)\cos^2\theta \end{pmatrix} \frac{H(t - r/\beta)}{\sqrt{t^2 - r^2/\beta^2}}, \tag{7.12}$$

where θ is the angle between vertical axis (z) and wave propagation direction and $H(t)$ is the Heaviside step function. In this case, the far-field *P* and *S* waves can be written simply as

$$\begin{pmatrix} G_{12}^P \\ G_{22}^P \end{pmatrix} = \frac{\cos\theta}{4\pi\alpha^2\rho} \begin{pmatrix} \sin\theta \\ \cos\theta \end{pmatrix} \frac{H(t - r/\alpha)}{\sqrt{t^2 - r^2/\alpha^2}}, \tag{7.13}$$

and

$$\begin{pmatrix} G_{12}^S \\ G_{22}^S \end{pmatrix} = \frac{\sin\theta}{4\pi\beta^2\rho} \begin{pmatrix} -\cos\theta \\ \sin\theta \end{pmatrix} \frac{H(t - r/\beta)}{\sqrt{t^2 - r^2/\beta^2}}. \tag{7.14}$$

We can replace $H(t - r/c)/\sqrt{t^2 - (r/c)^2}$ in (7.13) and (7.14) with the zeroth-order Hankel function of the first kind ($H_0^{(1)}$) by using the Fourier transform ($\mathcal{F}$) as (cf., Kennett, 1983, ch.7; Aki & Richards, 1980, ch.6)

$$\mathcal{F}\left[\frac{H(t - r/c)}{\sqrt{t^2 - (r/c)^2}}\right] = i\pi H_0^{(1)}(\omega r/c), \tag{7.15}$$

where $t > r/c$, ω is angular frequency and c is a wave velocity. We introduce the wavenumbers of *P* and *S* waves as k_α and k_β and write r for $|\mathbf{x} - \mathbf{x}'|$ (Fig. 7.4), to simplify (7.13) and (7.14) to the form

$$\begin{pmatrix} \overline{G}_{12}^P \\ \overline{G}_{22}^P \end{pmatrix} = \frac{i\cos\theta}{4\alpha^2\rho} H_0^{(1)}(k_\alpha|\mathbf{x} - \mathbf{x}'|) \begin{pmatrix} \sin\theta \\ \cos\theta \end{pmatrix}, \tag{7.16}$$

and

$$\begin{pmatrix} \overline{G}_{12}^S \\ \overline{G}_{22}^S \end{pmatrix} = \frac{i\sin\theta}{4\beta^2\rho} H_0^{(1)}(k_\beta|\mathbf{x} - \mathbf{x}'|) \begin{pmatrix} -\cos\theta \\ \sin\theta \end{pmatrix}. \tag{7.17}$$

We assume that the receiver is far away from the scatterers (i.e. $|\mathbf{x}| \gg |\mathbf{x}'|$; e.g., Roth & Korn, 1993), and then we can use the asymptotic expansion of Hankel function (Arfken, 1985, p618) and approximate $1/|\mathbf{x}-\mathbf{x}'|$ by $1/|\mathbf{x}|$ and $|\mathbf{x}-\mathbf{x}'|$ by $|\mathbf{x}|-\mathbf{n}\cdot\mathbf{x}'$ where $\mathbf{n}$ is the unit vector in x direction. The approximate Green's functions take the form

$$\begin{pmatrix} \overline{G}^P_{12} \\ \overline{G}^P_{22} \end{pmatrix} = \frac{i}{4\alpha^2\rho}\sqrt{\frac{2}{\pi k_\alpha|\mathbf{x}|}}\ \exp\left[i(k_\alpha|\mathbf{x}| - k_\alpha\mathbf{n}\cdot\mathbf{x}' - \frac{\pi}{4})\right]\begin{pmatrix} \sin\theta\cos\theta \\ \cos^2\theta \end{pmatrix}, \quad (7.18)$$

and

$$\begin{pmatrix} \overline{G}^S_{12} \\ \overline{G}^S_{22} \end{pmatrix} = \frac{i}{4\beta^2\rho}\sqrt{\frac{2}{\pi k_\beta|\mathbf{x}|}}\ \exp\left[i(k_\beta|\mathbf{x}| - k_\beta\mathbf{n}\cdot\mathbf{x}' - \frac{\pi}{4})\right]\begin{pmatrix} -\sin\theta\cos\theta \\ \sin^2\theta \end{pmatrix}. \quad (7.19)$$

The Green's functions for far-field P and S waves for a horizontally directed force can be obtained in the same way. We can therefore make a compact representation of the far-field Green's functions as

$$\begin{aligned}
\overline{G}^P_{jk} &= \frac{i}{4\alpha^2\rho}\sqrt{\frac{2}{\pi k_\alpha|\mathbf{x}|}}\ \exp\left[i(k_\alpha|\mathbf{x}| - k_\alpha\mathbf{n}\cdot\mathbf{x}' - \frac{\pi}{4})\right] A^P_{jk}(\theta), \\
\overline{G}^S_{jk} &= \frac{i}{4\beta^2\rho}\sqrt{\frac{2}{\pi k_\beta|\mathbf{x}|}}\ \exp\left[i(k_\beta|\mathbf{x}| - k_\beta\mathbf{n}\cdot\mathbf{x}' - \frac{\pi}{4})\right] A^S_{jk}(\theta), \quad (7.20)
\end{aligned}$$

where $A^P_{jk}(\theta)$ and $A^S_{jk}(\theta)$ are given by

$$\begin{aligned}
&A^P_{11}(\theta) = \sin^2\theta,\ \ A^P_{12}(\theta) = \sin\theta\cos\theta,\ \ A^P_{21}(\theta) = -\sin\theta\cos\theta,\ \ A^P_{22}(\theta) = \cos^2\theta, \\
&A^S_{11}(\theta) = \cos^2\theta,\ \ A^S_{12}(\theta) = -\sin\theta\cos\theta,\ \ A^S_{21}(\theta) = \sin\theta\cos\theta,\ \ A^S_{22}(\theta) = \sin^2\theta. \quad (7.21)
\end{aligned}$$

The primary waves (P waves in this study) generate both scattered P and scattered S waves at the boundaries of heterogeneities due to wavetype coupling, and therefore the total scattered wavefield u^s_j can be represented as a sum of scattered P and S waves (u^{PP}_j, u^{PS}_j where $j = x, z$ or 1,2). From (7.9), (7.11), (7.18) and (7.19), u^{PP}_j and u^{PS}_j are given by

$$\begin{aligned}
u^{PP}_j = &\sqrt{\frac{k_\alpha}{8\pi|\mathbf{x}|}}\exp\left[-i(\omega t - k_\alpha|\mathbf{x}| + \frac{\pi}{4})\right]\cdot\left\{C^P_1 A^P_{j1}(\theta)\int_{\mathsf{S}}\frac{\partial\xi}{\partial x}e^{ik_\alpha(z-\mathbf{n}\cdot\mathbf{x}')}\,d\mathsf{S}(\mathbf{x}')\right. \\
&\left.+2ik_\alpha A^P_{j2}(\theta)\int_{\mathsf{S}}\xi e^{ik_\alpha(z-\mathbf{n}\cdot\mathbf{x}')}\,d\mathsf{S}(\mathbf{x}') + C^P_2 A^P_{j2}(\theta)\int_{\mathsf{S}}\frac{\partial\xi}{\partial z}e^{ik_\alpha(z-\mathbf{n}\cdot\mathbf{x}')}\,d\mathsf{S}(\mathbf{x}')\right\}, \quad (7.22)
\end{aligned}$$

and

$$\begin{aligned}
u^{PS}_j = &\sqrt{\frac{k_\alpha\gamma^3}{8\pi|\mathbf{x}|}}\exp\left[-i(\omega t - k_\beta|\mathbf{x}| + \frac{\pi}{4})\right]\cdot\left\{C^P_1 A^S_{j1}(\theta)\int_{\mathsf{S}}\frac{\partial\xi}{\partial x}e^{ik_\alpha(z-\gamma\mathbf{n}\cdot\mathbf{x}')}\,d\mathsf{S}(\mathbf{x}')\right. \\
&\left.+2ik_\alpha A^S_{j2}(\theta)\int_{\mathsf{S}}\xi e^{ik_\alpha(z-\gamma\mathbf{n}\cdot\mathbf{x}')}\,d\mathsf{S}(\mathbf{x}') + C^P_2 A^S_{j2}(\theta)\int_{\mathsf{S}}\frac{\partial\xi}{\partial z}e^{ik_\alpha(z-\gamma\mathbf{n}\cdot\mathbf{x}')}\,d\mathsf{S}(\mathbf{x}')\right\}, \quad (7.23)
\end{aligned}$$

where we have written γ for α/β.

The integrals in (7.22) and (7.23) can be simplified by using integration by parts to yield

$$u^{PP}_j = i\sqrt{\frac{k^3_\alpha}{8\pi|\mathbf{x}|}}\left\{C^P_1 A^P_{j1}(\theta)\sin\theta + 2A^P_{j2}(\theta) + C^P_2 A^P_{j2}(\theta)(\cos\theta - 1)\right\}$$

$$\times \exp\left[-i(\omega t - k_\alpha|\mathbf{x}| + \frac{\pi}{4})\right] \int_{\mathsf{S}} \xi e^{ik_\alpha(z-\mathbf{n}\cdot\mathbf{x}')}\, d\mathsf{S}(\mathbf{x}'), \tag{7.24}$$

and

$$u_j^{PS} = i\sqrt{\frac{k_\alpha^3\gamma^3}{8\pi|\mathbf{x}|}} \left\{C_1^P A_{j1}^S(\theta)\gamma\sin\theta + 2A_{j2}^S(\theta) + C_2^P A_{j2}^S(\theta)(\gamma\cos\theta - 1)\right\}$$
$$\times \exp\left[-i(\omega t - k_\beta|\mathbf{x}| + \frac{\pi}{4})\right] \int_{\mathsf{S}} \xi e^{ik_\alpha(z-\gamma\mathbf{n}\cdot\mathbf{x}')}\, d\mathsf{S}(\mathbf{x}'). \tag{7.25}$$

In this far-field approximation, the scattered P and S waves can be isolated on a single component (radial or tangential) by rotation of the coordinate axes (e.g., Sato & Fehler, 1998):

$$\begin{aligned}
u_r^{PP} &= \sin\theta\, u_x^{PP} + \cos\theta\, u_z^{PP} \\
&= i\sqrt{\frac{k_\alpha^3}{8\pi|\mathbf{x}|}}\, C_r^P(\theta) \exp\left[-i\left(\omega t - k_\alpha|\mathbf{x}| + \frac{\pi}{4}\right)\right] \int_{\mathsf{S}} \xi\, e^{ik_\alpha(z-\mathbf{n}\cdot\mathbf{x}')}\, d\mathsf{S}(\mathbf{x}'), \\
u_t^{PS} &= \cos\theta\, u_x^{PS} - \sin\theta\, u_z^{PS} \\
&= i\sqrt{\frac{k_\alpha^3\gamma^3}{8\pi|\mathbf{x}|}}\, C_t^P!(\theta) \exp\left[-i\left(\omega t - k_\beta|\mathbf{x}| + \frac{\pi}{4}\right)\right] \int_{\mathsf{S}} \xi\, e^{ik_\alpha(z-\gamma\mathbf{n}\cdot\mathbf{x}')}\, d\mathsf{S}(\mathbf{x}'),
\end{aligned} \tag{7.26}$$

where $C_r^P(\theta)$ and $C_t^P(\theta)$ are

$$\begin{aligned}
C_r^P(\theta) &= \sin\theta\left\{C_1^P A_{11}^P(\theta)\sin\theta + 2A_{12}^P(\theta) + C_2^P A_{12}^P(\theta)(\cos\theta - 1)\right\} \\
&\quad + \cos\theta\left\{C_1^P A_{21}^P(\theta)\sin\theta + 2A_{22}^P(\theta) + C_2^P A_{22}^P(\theta)(\cos\theta - 1)\right\}, \\
C_t^P(\theta) &= \cos\theta\left\{C_1^P A_{11}^S(\theta)\gamma\sin\theta + 2A_{12}^S(\theta) + C_2^P A_{12}^S(\theta)(\gamma\cos\theta - 1)\right\} \\
&\quad - \sin\theta\left\{C_1^P A_{21}^S(\theta)\gamma\sin\theta + 2A_{22}^S(\theta) + C_2^P A_{22}^S(\theta)(\gamma\cos\theta - 1)\right\}.
\end{aligned} \tag{7.27}$$

To extract the average scattered energy, we consider an ensemble average over different realizations of the stochastic medium for the displacement terms:

$$\begin{aligned}
\langle|u_r^{PP}|^2\rangle &= \frac{k_\alpha^3}{8\pi|\mathbf{x}|}\,[C_r(\theta)]^2 \\
&\quad \times \int_{\mathsf{S}}\int_{\mathsf{S}} \langle\xi(\mathbf{x}')\xi(\mathbf{y}')\rangle \exp\left[ik_\alpha\left\{\mathbf{e}_z\cdot(\mathbf{x}'-\mathbf{y}') - \mathbf{n}\cdot(\mathbf{x}'-\mathbf{y}')\right\}\right]\, d\mathsf{S}(\mathbf{x}')\, d\mathsf{S}(\mathbf{y}'), \\
\langle|u_t^{PS}|^2\rangle &= \frac{k_\alpha^3\gamma^3}{8\pi|\mathbf{x}|}\,[C_t(\theta)]^2 \\
&\quad \times \int_{\mathsf{S}}\int_{\mathsf{S}} \langle\xi(\mathbf{x}')\xi(\mathbf{y}')\rangle \exp\left[ik_\alpha\left\{\mathbf{e}_z\cdot(\mathbf{x}'-\mathbf{y}') - \gamma\mathbf{n}\cdot(\mathbf{x}'-\mathbf{y}')\right\}\right]\, d\mathsf{S}(\mathbf{x}')\, d\mathsf{S}(\mathbf{y}'),
\end{aligned} \tag{7.28}$$

where $\mathbf{e}_z$ is the unit vector for the z axis direction. Following the procedure for scalar waves (e.g., Frankel & Clayton, 1986; Roth & Korn, 1993), we can rewrite (7.28) using the power spectral density function $\mathcal{P}(k)$ for the heterogeneity as

$$\langle|u_r^{PP}|^2\rangle = \frac{k_\alpha^3\,\mathsf{S}}{8\pi|\mathbf{x}|}[C_r(\theta)]^2\,\mathcal{P}\left[2k_\alpha\,\sin\frac{\theta}{2}\right],$$

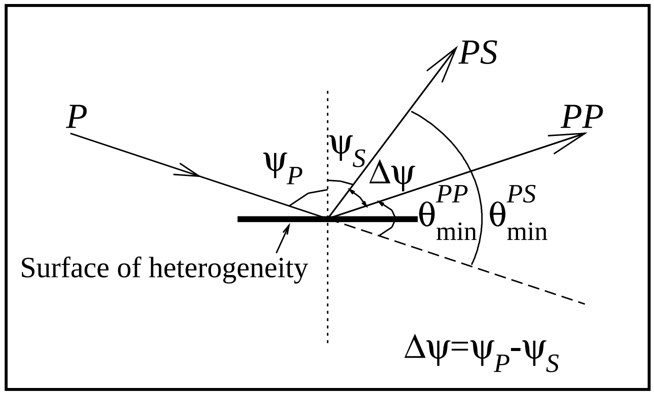

Fig. 7.5. The determination of the minimum scattering angle for *S* waves $\theta_{\min}^{PS}$ in terms of $\theta_{\min}^{PP}$ using Snell's law. *P* wave is incident with angle ψ_P to the normal to the surface of heterogeneity and the *PP* scattered wave is reflected at the surface with angle $\theta_{\min}^{PP}$ to the incident direction (z-axis direction in this study). The *PS* scattered wave is reflected on the surface with angle ψ_S to the normal and $\theta_{\min}^{PS}$ to the incident direction.

$$\langle |u_t^{PS}|^2 \rangle = \frac{k_\alpha^3 \gamma^3 \mathsf{S}}{8\pi|\mathbf{x}|}[C_t(\theta)]^2\, \mathcal{P}\left[k_\alpha \sqrt{1+\gamma^2-2\gamma\cos\theta}\right]. \tag{7.29}$$

The derivation of (7.29) from (7.28) is described in detail in Appendix B. The loss factor for scattering attenuation Q_P^{-1} corresponds to the energy loss per unit area divided by the solid angle (2π) and wavenumber, and so we can express Q_P^{-1} in terms of the standard deviation (ϵ) of velocity fluctuation in the 2-D media by

$$Q_P^{-1} = \frac{\epsilon^2}{2\pi \mathsf{S} k_\alpha}\int_\theta \left\{\langle |u_r^{PP}|^2\rangle + \langle |u_t^{PS}|^2\rangle\right\}\, d\mathsf{A}, \tag{7.30}$$

where A is the arc length through which scattered waves propagate, so that $d\mathsf{A}$ is given by $r\, d\theta$ (Frankel & Clayton, 1986).

An approximation for the scattering loss factor Q_P^{-1} can be made by restricting the angular range over which the single scattering theory is applied. For an angular span ($< \theta_{\min}$) about the forward direction we represent the true multiple scattering effects via a travel-time correction. Since the scattered angles of *PP* and *PS* waves from a heterogeneity are different, we introduce $\theta_{\min}^{PP}$ for the *P*-wave type scattering and $\theta_{\min}^{PS}$ for the *S*-wave type scattering. Then we can represent Q_P^{-1} with the approximate travel-time correction as

$$Q_P^{-1} = \frac{r\epsilon^2}{2\pi \mathsf{S} k_\alpha}\left\{\int_{\theta_{\min}^{PP}}^{2\pi-\theta_{\min}^{PP}} \langle |u_r^{PP}|^2\rangle\, d\theta + \int_{\theta_{\min}^{PS}}^{2\pi-\theta_{\min}^{PS}} \langle |u_t^{PS}|^2\rangle\, d\theta\right\}. \tag{7.31}$$

When $|\mathbf{x}|$ is large enough, we can assume $|\mathbf{x}| \approx r$. Also, $\theta_{\min}^{PS}$ can be represented in terms of $\theta_{\min}^{PP}$ by using the Snell's law; for *PP* scattered waves reflected with the minimum scattering angle $\theta_{\min}^{PP}$ from the boundary of heterogeneity, the corresponding reflection angle of PS scattered waves can be calculated for single scattering as (see, Fig. 7.5)

$$\theta_{\min}^{PS} = \theta_{\min}^{PP} + (\psi_P - \psi_S), \quad \text{where } \psi_P = \frac{\pi - \theta_{\min}^{PP}}{2}, \ \psi_S = \sin^{-1}\left(\frac{\sin\psi_P}{\gamma}\right). \tag{7.32}$$

Therefore, when we set $(\psi_P - \psi_S)$ to be $\Delta\psi$, the approximate relationship between Q_P^{-1} and $k_\alpha a$ for elastic waves is given with implicit dependence on a through $\mathcal{P}$ by

$$\begin{aligned}\frac{Q_P^{-1}}{\epsilon^2} &= \frac{k_\alpha^2}{(4\pi)^2}\int_{\theta_{\min}^{PP}}^{2\pi-\theta_{\min}^{PP}} [C_r^P(\theta)]^2\, \mathcal{P}\left[2k_\alpha \sin\frac{\theta}{2}\right] d\theta \\ &+ \frac{k_\alpha^2\gamma^2}{(4\pi)^2}\int_{\theta_{\min}^{PP}+\Delta\psi}^{2\pi-\theta_{\min}^{PP}-\Delta\psi} [C_t^P(\theta)]^2\, \mathcal{P}\left[k_\alpha\sqrt{1+\gamma^2-2\gamma\cos\theta}\right] d\theta.\end{aligned} \tag{7.33}$$

7.3.2 *S-wave incidence*

Following a similar procedure to that for the derivation of the theoretical *P*-wave scattering attenuation expressions in Section 7.3.1, the theoretical *S*-wave scattering attenuation forms can be derived as a function of $k_\beta a$:

$$\begin{aligned}\frac{Q_S^{-1}}{\epsilon^2} &= \frac{k_\beta^2}{8\pi\gamma^5}\int_{\theta_{\min}^{SP}}^{2\pi-\theta_{\min}^{SP}} [C_r^S(\theta)]^2\, \mathcal{P}\left[\frac{k_\beta}{\gamma}\sqrt{1+\gamma^2-2\gamma\cos\theta}\right] d\theta \\ &+ \frac{k_\beta^2}{8\pi}\int_{\theta_{\min}^{SS}}^{2\pi-\theta_{\min}^{SS}} [C_t^S(\theta)]^2\, \mathcal{P}\left[2k_\beta \sin\frac{\theta}{2}\right] d\theta,\end{aligned} \tag{7.34}$$

where k_β is the wavenumber of *S* waves, $\theta_{\min}^{SS}$ is the minimum scattering angle for in-phase scattered waves (*SS*), and the minimum scattering angle for the coupled phase ($\theta_{\min}^{SP}$) can be written by

$$\theta_{\min}^{SP} = \theta_{\min}^{SS} - (\phi_P - \phi_S), \quad \phi_S = \frac{\pi - \theta_{\min}^{SS}}{2}, \quad \phi_P = \sin^{-1}(\gamma\sin\phi_S). \tag{7.35}$$

Here, C_r^S and C_t^S are given by

$$\begin{aligned} C_r^S(\theta) &= \sin\theta\left\{-\gamma C_1^S A_{11}^P(\theta) + (\cos\theta-\gamma)C_2^S A_{11}^P(\theta) + \sin\theta\, C_2^S A_{12}^P(\theta)\right\} \\ &+ \cos\theta\left\{-\gamma C_1^S A_{21}^P(\theta) + (\cos\theta-\gamma)C_2^S A_{21}^P(\theta) + \sin\theta\, C_2^S A_{22}^P(\theta)\right\}, \\ C_t^S(\theta) &= \cos\theta\left\{-C_1^S A_{11}^S(\theta) + (\cos\theta-1)C_2^S A_{11}^S(\theta) + \sin\theta\, C_2^S A_{12}^S(\theta)\right\} \\ &- \sin\theta\left\{-C_1^S A_{21}^S(\theta) + (\cos\theta-1)C_2^S A_{21}^S(\theta) + \sin\theta\, C_2^S A_{22}^S(\theta)\right\}, \end{aligned} \tag{7.36}$$

where $C_1^S = -2$ and $C_2^S = K + 2$. Details in the derivation are given in Appendix C.

Note that we consider minimum scattering angles in terms of $\theta_{\min}^{PP}$ for a *P*-wave incident problem and $\theta_{\min}^{SS}$ for *S*-wave. The in-phase minimum scattering angles ($\theta_{\min}^{PP}$, $\theta_{\min}^{SS}$) are determined by constant angles regardless of the velocity ratio γ of the media, while those for coupled phases ($\theta_{\min}^{PS}$, $\theta_{\min}^{SP}$) vary with γ of the media (see, Figs. 7.5 and C.1).

7.4 Comparison with results with scalar approximation

We have derived the scattering attenuation formula for 2-D elastic waves in terms of normalized wavenumber (ka), for stochastic media where the physical parameters (Lamè coefficients and density) are varied randomly. There are significant differences in the characteristics of elastic waves and scalar waves, particularly in radiation patterns associated with scattering, the phase coupling on a boundary of heterogeneity and the differences in the frequency content of P and S waves. We therefore expect there to be noticeable differences in the scattering induced for scalar and elastic waves.

We therefore compare the scattering attenuation formula for elastic waves with that for scalar waves (e.g., Frankel & Clayton, 1986) and discuss possible problems when the theoretical attenuation curve for scalar waves is used instead of that for elastic waves. For convenience, we consider a case only with velocity perturbations, i.e., $K = 0$ in (7.8). The theoretical scattering attenuation formula as a function of ka for scalar waves is then given by (e.g., Frankel & Clayton, 1986; Frenje & Juhlin, 2000; cf. formula for *SH* waves, Appendix D)

$$Q_s^{-1} = \frac{k^2 \epsilon^2}{\pi} \int_{\theta_{\min}}^{\pi} \mathcal{P}\left[2k \sin\frac{\theta}{2}\right] d\theta, \tag{7.37}$$

where ϵ is the standard deviation of the velocity perturbation.

The theoretical expression for the scattering attenuation for elastic waves in (7.33) includes both the wavenumber for P waves and the ratio (γ) of P and S wave velocities, which means that the Poisson's ratio is an important factor in the scattering process of elastic waves. This is illustrated in Fig. 7.6 where we compare the theoretical scattering attenuation curves for elastic waves with different P/S velocity ratios (γ) for a random medium with a von Karman distribution with a Hurst number (ν) of 0.25. We consider a constant background P wave velocity of 6.74 km/s. In the figure the elastic scattering curves are plotted together with the curve for scalar waves for which $\theta_{\min}$ is $30°$. There is a significant dependence of the scattering attenuation behaviour as a function of the velocity ratio γ; as γ is increased, the normalized wavenumber for the peak attenuation is reduced and also the magnitude of the attenuation tends to increase. Although the attenuation curve for scalar waves displays a similar pattern to that for elastic waves with $\gamma = 1.75$, which is a plausible velocity ratio in the crust, the attenuation levels for elastic waves are smaller than that for scalar waves for large ka. It is therefore preferable to derive scattering attenuation relations directly for elastic waves rather than rely on the scalar wave results.

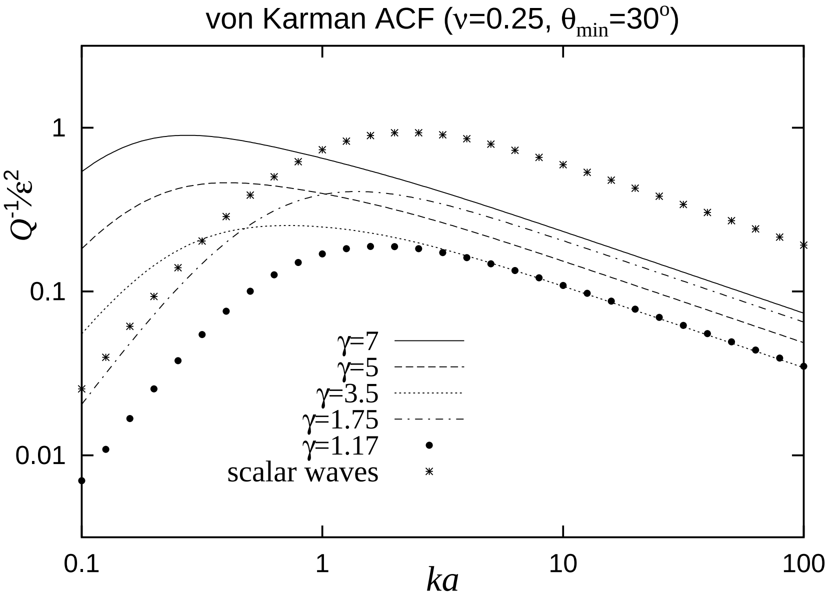

Fig. 7.6. Comparison of theoretical scattering attenuation (Q^{-1}) curves with the minimum scattering angle ($\theta_{\min}$) of 30° for scalar waves and elastic waves with various ratios (γ=1.17, 1.75, 3.5, 5, 7) of *P* and *S* wave velocities in von Karman random media with the Hurst number (ν) of 0.25. The reference *P* wave velocity is set at 6.74 km/s. The theoretical curves for elastic waves are highly dependent on the velocity ratio.

7.5 Construction of stochastic random media

A number of studies have been made of the theoretical conditions on media so that the scattering of elastic waves can be represented effectively with the first-order Born approximation, i.e., single scattering (Kennett, 1972; Aki & Richards, 1980; Hudson & Heritage, 1981; Wu & Aki, 1985). When comparisons are to be made with the results of numerical models, it is particularly important that an exact representation is made of a specific random medium. Recently, Frenje & Juhlin (2000) have presented theoretical conditions for implementation of a valid correlation distance in a discretized spatial medium. They have derived the conditions between the grid steps ($\delta x, \delta z$) and the correlation distance (a) on the basis that the minimum wavenumber ($k^j_{\rm min} = 2\pi/l_j$, $j = x, z$, l_j=length of domain in j direction) is smaller than the corner wavenumber ($k_c = 1/a$) and the Nyquist wavenumber ($k^j_{nyq} = \pi/\delta j$, $j = x, z$) is larger than the corner wavenumber. However, models based on an autocorrelation function (ACF) do not depend on the corner wavenumber (Mai & Beroza, 2002), and so it is necessary to check the suitability of a specific random medium by considering both the limits on the accuracy of the numerical differentiation and the representation of the medium with a given correlation distance. The accuracy requirement determines the smallest acceptable size of the heterogeneities in domain, and the physical limits of the model controls the maximum acceptable size.

The WBM will remain stable in a pointwise medium with large fluctuations for correlation distances down to $a = \max\{\delta x, \delta z\}/8$. The FDM needs a correlation distance which is sufficiently large compared to the grid steps (i.e., $\max\{\delta x, \delta z\} \ll a$, see Frenje & Juhlin, 2000). The physical limit comes from the confinement in size when using a limited number of grid points to represent the medium. When random heterogeneities with large correlation distance are placed in a relatively small medium, the heterogeneities behave as a 'virtual structure' and generate biased results (e.g., Frankel & Clayton, 1986). Therefore, it is necessary to check if the fractional fluctuation of physical parameters generated by a model is appropriate for the numerical representation of given random medium.

For this purpose, we introduce a measure of 'randomicity rate' (C_N) which is will be close to zero when the domain is sufficiently large compared with the heterogeneities. We define

$$C_N = \frac{|N_+ - N_-|}{N_t} \sim 0, \tag{7.38}$$

where N_+ and N_- are the number of grid points with positive and negative random values for the fractional fluctuation of physical parameters, and N_t is the total number of grid points. When the domain is large enough, the positive and negative random values are distributed homogeneously (i.e., $N_+ \simeq N_-$ in the domain) and C_N becomes close to zero.

In addition to these conditions, the distance from source to receiver is another important factor for the accurate measurement of scattering attenuation; since waves propagating through a random medium experience focusing and defocusing effects, the travel times and amplitudes of waves recorded at short distances from the source are very variable (e.g., Hoshiba, 2000). The time responses for short distances are thus not very suitable for a quantitative study. We therefore endeavour to set the receivers at a sufficient distance that the influence of the heterogeneity tends to minimize the variations in amplitudes between different receivers. For *P*-wave incidence problems, we introduce a domain which is composed of 512-by-512 grid points corresponding to 77×77 km^2 ($\delta x = \delta z$=150.3 m) in physical space (Fig. 7.7), and for *S*-wave scattering studies, a domain with 128-by-512 grid points (i.e., 19.3×77 km^2) is considered. The plane *P*- or *S*-wave sources are located at the 70th grid point from the bottom boundary Γ_B (i.e., $z = 10.5$ km), and the receivers are set at the 70th grid point from the top boundary Γ_T. The 128 receivers are deployed horizontally with uniform spacing, at every fourth grid point (i.e., x=0.6 km) for *P*-wave scattering problems and at every grid point (x=0.15 km) for *S*-wave problems. The reference compressional wave velocity (α_0) is 6.74 km/s, the

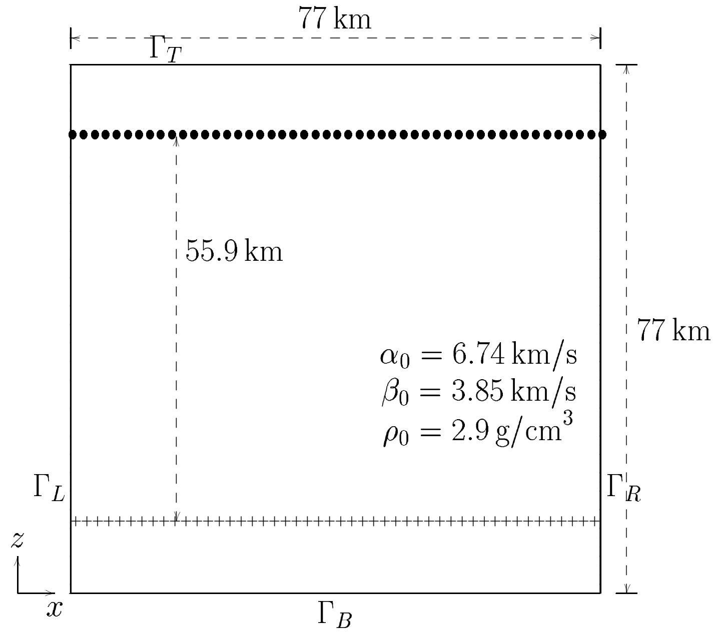

Fig. 7.7. Configuration of 2-D unbounded medium for the P-wave scattering studies. 128 receivers (•) are placed with uniform interval (602 m) at 10.5 km from the top boundary (Γ_T). A plane P wave source ($+$) is located at 10.5 km from the bottom boundary (Γ_B). The reference compressional (α_0) and shear (β_0) wave velocities are 6.74 and 3.85 km/s, and the reference density (ρ_0) is 2.9 g/cm^3. The top and bottom artificial boundaries (Γ_T, Γ_B) are treated by absorbing boundary conditions and the left and right boundaries (Γ_L, Γ_R) are considered with periodic boundary conditions.

shear wave velocity (β_0) is 3.85 km/s and the density (ρ_0) is 2.9 g/cm^3 which are typical crustal values (cf., Kennett *et al.*, 1995). The source time function is a Ricker wavelet with dominant frequency (f_c) 4.5 Hz. The top and bottom artificial boundaries (Γ_T, Γ_B in Fig. 7.7) are treated with absorbing boundary conditions, and the other boundaries (Γ_R, Γ_L) by periodic boundary conditions to imitate a domain with the unlimited horizontal length.

We construct stochastic random media using von Karman, exponential and Gaussian autocorrelation functions (ACF, $N(r)$) and their power spectral density functions (PSDF, $\mathcal{P}(k)$). The von Karman ACF and PSDF in 2-D media are (e.g., Sato & Fehler, 1998)

$$N(r) = \frac{1}{2^{\nu-1}\Gamma(\nu)} \left(\frac{r}{a}\right)^{\nu} K_{\nu}\left(\frac{r}{a}\right), \qquad \mathcal{P}(k) = \frac{4\pi\nu a^2}{(1+k^2a^2)^{\nu+1}}, \tag{7.39}$$

where r is a spatial lag, a the correlation distance, ν the Hurst number, Γ the Gamma function, k a wavenumber and K_ν is the modified Bessel function of order ν. The exponential ACF and PSDF are

$$N(r) = e^{-r/a}, \qquad \mathcal{P}(k) = \frac{2\pi a^2}{(1+k^2a^2)^{3/2}}, \tag{7.40}$$

and the Gaussian ACF and PSDF are given by

$$N(r) = e^{-r^2/a^2}, \qquad \mathcal{P}(k) = \pi a^2 e^{-k^2 a^2/4}. \tag{7.41}$$

We note that the exponential ACF corresponds to the von Karman ACF with Hurst number 0.5.

To generate the stochastic random models, we use the PSDF, the spectrum of the ACF, in the wavenumber domain (e.g., Roth & Korn, 1993) and assign random numbers distributed evenly between $-\pi$ and π to the phase $\Phi(k_x, k_z)$ at each point (k_x, k_z). The fractional fluctuation of velocities in the wavenumber domain $\bar{\xi}(k_x, k_z)$ is then expressed as

$$\bar{\xi}(k_x, k_z) = \sqrt{l_x l_z}\sqrt{P(k_r)}e^{i\Phi(k_x,k_z)}, \tag{7.42}$$

where k_r is the root mean square of k_x and k_z, and l_j ($j = x, z$) is the extent of the medium in the j direction. The resultant fractional fluctuation of the velocities in spatial domain $\xi(x, z)$ in (7.8) is obtained by 2-D Fourier transforms. We consider 10 % standard deviation ϵ for the wave-speed perturbation, and following Sato (1984) set $K = 0.8$ in (7.8) to controls the perturbation level for the density.

7.6 *P*-wave scattering patterns and process

We undertake numerical modelling of elastic waves in stochastic heterogeneous media with three different styles: (a) generated by von Karman ACFs with ν=0.05 and 0.25, (b) exponential ACF (corresponding to von Karman ACF with ν=0.5) and (c) a Gaussian ACF. Each type of random media is considered for six different values of the correlation distances (a=34, 85.4, 214.5, 538.7, 1353.2, 3399 m). In this situation, the normalized wavenumbers ($k_\alpha^d a$) for the dominant frequency (4.5 Hz in this study) of incident waves are 0.14, 0.36, 0.90, 2.26, 5.68 and 14.26. The scattering attenuation for each case is measured from a band of normalized wavenumbers including $k_\alpha^d a$. The smallest correlation distance implemented in this study, a=34 m, satisfies the required condition, $a \geq \max\{\delta x, \delta z\}/8$, for the application of the WBM. In Table 7.1, we present the randomicity rate (C_N) for each of the simulations. The C_N values increase with the size of correlation distances in von Karman and exponential media, but for the simulation of Gaussian media show a complicated pattern (see, C_N values for Gaussian media at a=538.7 m).

Fig. 7.8 displays the representative textures of stochastic random media resulting from velocity perturbation, which are constructed following the scheme in Section 7.5. In von Karman type models, with increase of the Hurst number (ν) high-frequency

Table 7.1. *Numbers of grid points with positive and negative values (N_+, N_-) for the random variation for the reference physical parameters of the stochastic random media and the randomicity rate C_N as a function of the correlation distance (a).*

a (m)	34	85.4	214.5	538.7	1353.2	3399
• von Karman ($\nu = 0.05$)						
N_+	131550	131545	131659	132080	132893	135024
N_-	130594	130599	130485	130064	129251	127120
C_N	0.0036	0.0036	0.0045	0.0077	0.0139	0.0302
• von Karman ($\nu = 0.25$)						
N_+	131522	131551	131796	132395	133365	136339
N_-	130622	130593	130348	129749	128779	125805
C_N	0.0034	0.0037	0.0055	0.0101	0.0175	0.0402
• von Karman ($\nu = 0.5$, exponential)						
N_+	131422	131542	132002	132548	133591	137422
N_-	130722	130602	130142	129596	128553	124722
C_N	0.0027	0.0036	0.0071	0.0113	0.0192	0.0484
• Gaussian						
N_+	131383	131389	131637	132164	131641	132593
N_-	130761	130755	130507	129980	130503	129551
C_N	0.0024	0.0024	0.0043	0.0083	0.0043	0.0116

textures reduce and transition of the velocity perturbation becomes smooth. The texture of Gaussian media is composed of extremely low-frequency structures with smooth transitions.

In order to obtain a good assessment of the scattering attenuation we need to take into account the nature of the scattered signal. For vertically incident plane P waves on media with small-scale heterogeneities, the primary waves are mostly recorded on the z component and the x component contains mostly scattered waves (see, Fig. 7.9). In this case the scattering attenuation can be measured by considering the energy loss of the incident waves on the z-component records. However, in a medium with large-scale heterogeneity, there can be significant deviations in the directions of the primary waves. Thus, e.g., in the synthetic seismograms for the Gaussian random medium with a=1353.2, 3399 m (Fig. 7.10), the primary waves recorded on z component display a systematic change of amplitudes and arrival times, which is also mirrored on the x-component seismograms. A similar phenomenon is found in seismograms from von Karman (also exponential) random media with large scale of heterogeneities (see, Fig. 7.11), where waves with systematic deviations in direction develop ahead of the

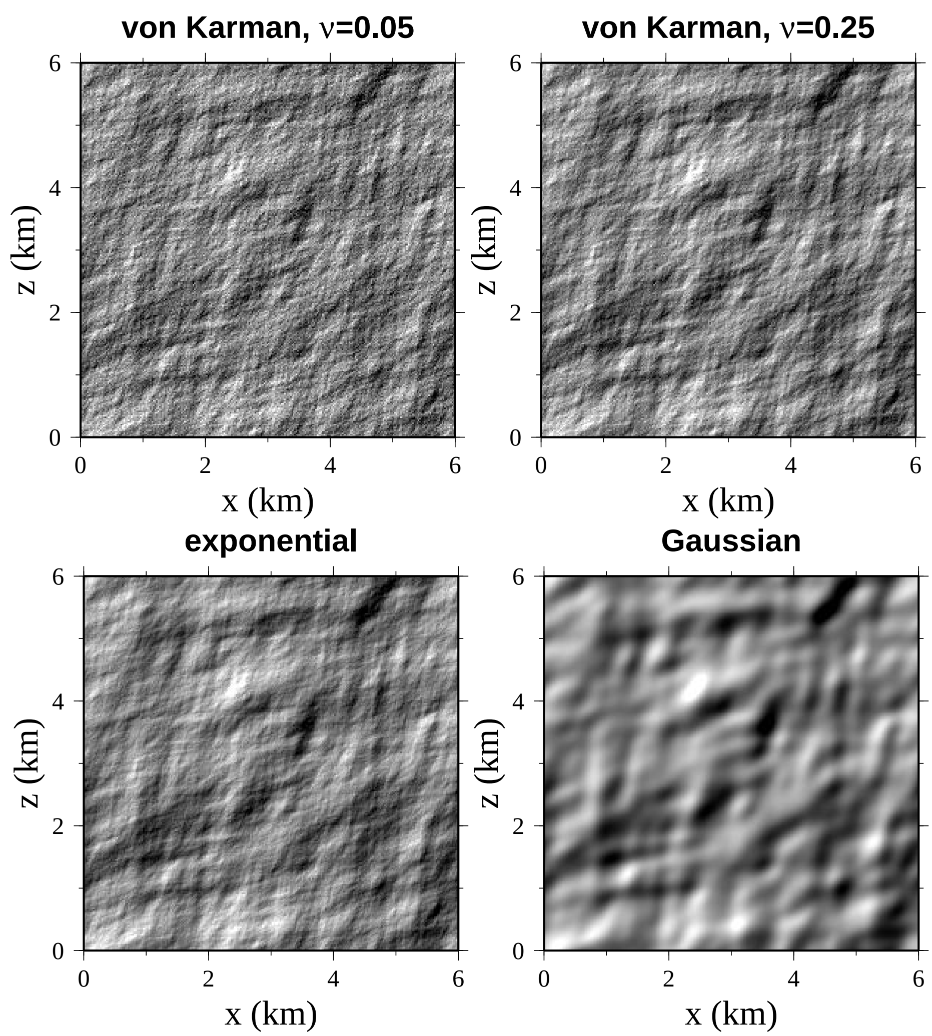

Fig. 7.8. Normalized velocity perturbation in stochastic random media (von Karman with ν=0.05, 0.25, exponential, Gaussian) with correlation distance 214.5 m. As the Hurst number increases, the perturbation changes smoothly in the von Karman type media; Textures of the von Karman medium with small Hurst number display relatively high-frequency variations, while those with large Hurst number show low-frequency variations. The Gaussian medium display extremely smooth variations of the perturbations.

scattered coda. However, the systematic variation becomes noticeably reduced for a von Karman medium with a small value of the Hurst number (see, Fig. 7.12). The level of scattered waves generated is related to the spectral filtering introduced by the particular autocorrelation function (Klimeš, 2002). For example, there are less scattered waves for a Gaussian media with a large correlation distance because the band of wavenumber coupling scales as $1/a$.

The scattering attenuation rate is measured from the seismograms calculated for the

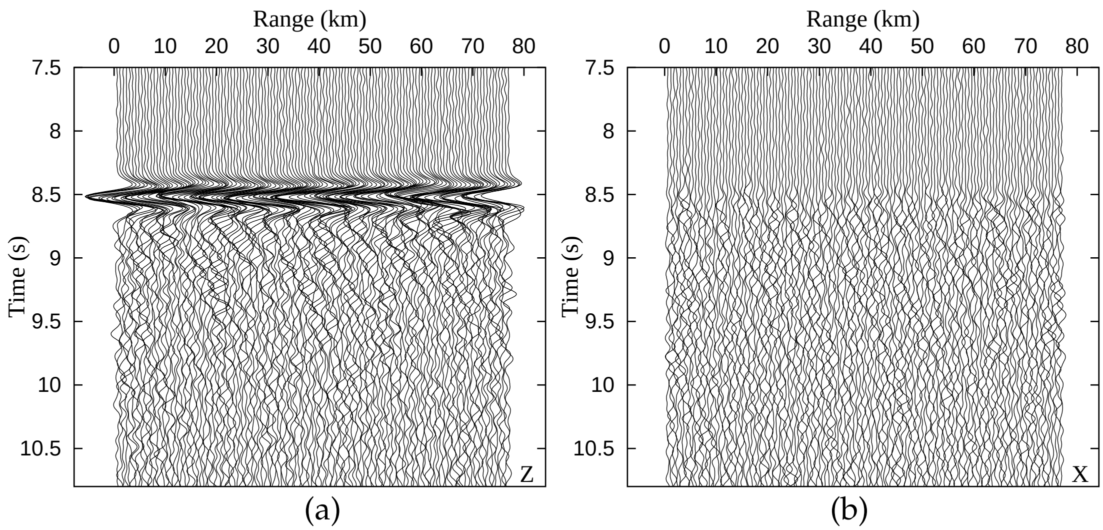

Fig. 7.9. Synthetic seismograms from the modelling in the von Karman random media with ν=0.25 and a=214.5 m. Random scattered waves are developed following the primary waves in z-component seismograms, and mainly scattered waves are recorded on the x component.

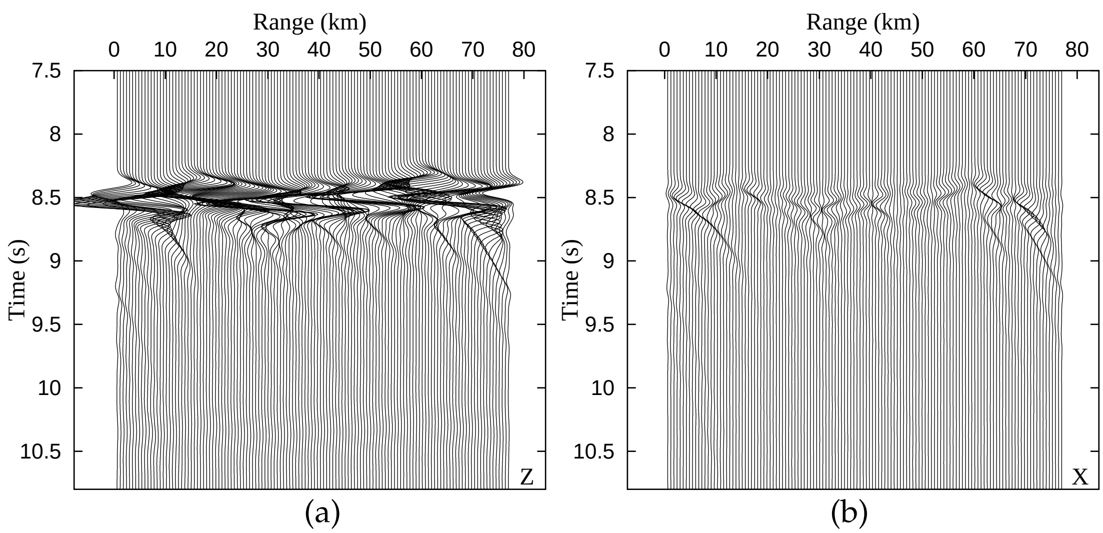

Fig. 7.10. Synthetic seismograms from the modelling in Gaussian random media with a=3399 m. The seismograms are composed of mainly primary waves without random scattered waves. The primary waves are recorded on both x and z components since the waves deviate from the incident direction due to the influence of the large scale of the heterogeneity.

random media using a spectral ratio approach (Aki & Richards, 1980):

$$Q^{-1}(\omega) = \frac{2c}{\omega r} \ln \left[\frac{A_0(\omega)}{A_r(\omega)} \right], \tag{7.43}$$

where c is the wave speed, r is the spatial lag, ω is the angular frequency, and $A_0(\omega)$ and $A_r(\omega)$ are the spectral amplitudes of waves for angular frequency ω at the origin and at the receiver. The spectral amplitudes of the primary waves are estimated by

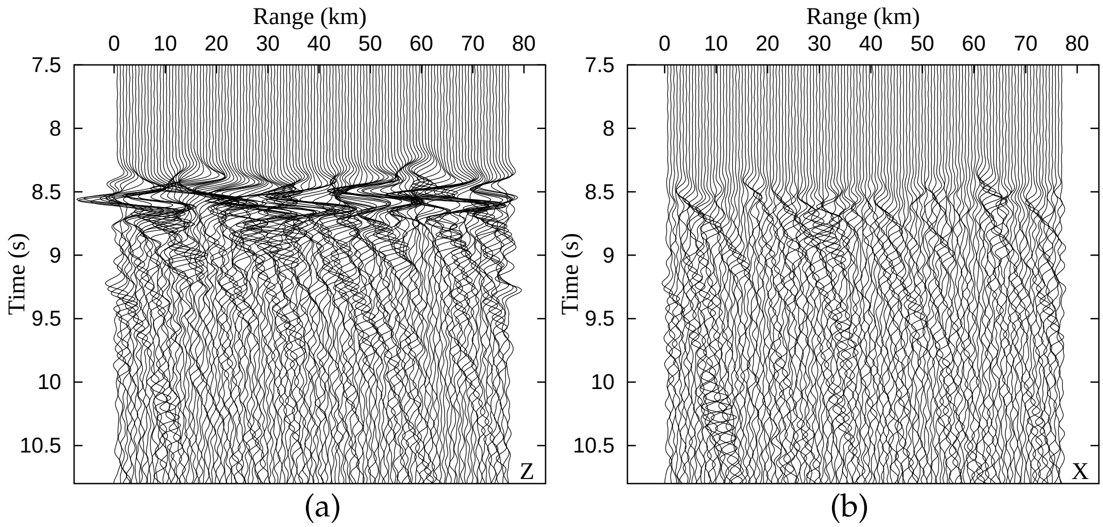

Fig. 7.11. Synthetic seismograms from the modelling in exponential random media with a=1353.2 m. The primary waves are recorded on both x and z components with background random scattered waves.

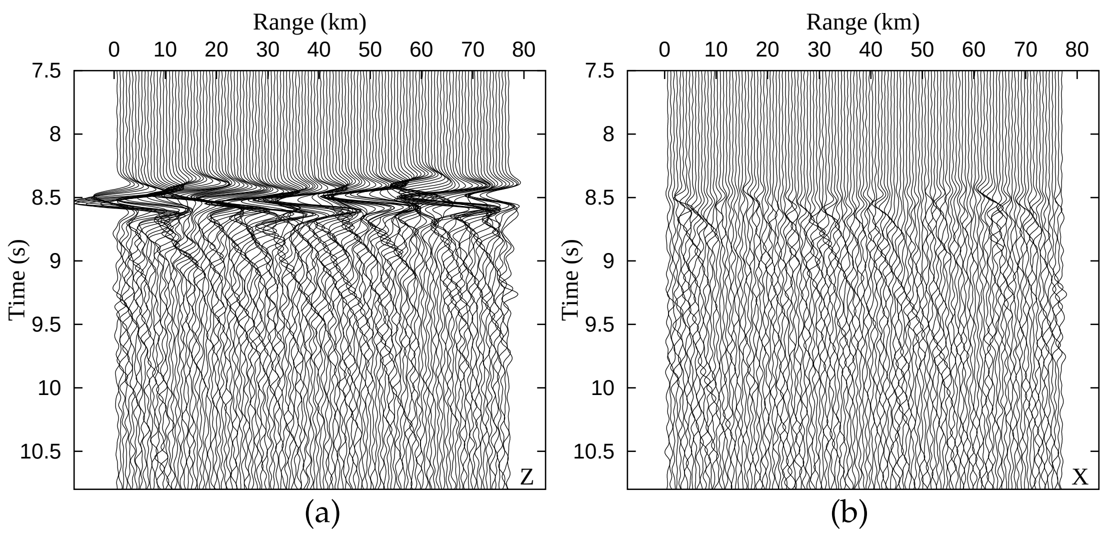

Fig. 7.12. Synthetic seismograms from the modelling in the von Karman random media with ν=0.05 and a=3399 m. The primary waves is not discernible and mainly random scattered waves are recorded on the x component even the heterogeneity (cf., Fig. 7.11).

stacking 128 seismograms in the frequency domain. These seismograms are tapered in the time domain using a 'cosine bell' (Kanasewich, 1981), as shown in Fig. 7.13, to isolate primary waves from scattered waves.. The time length L_1 and L_2 are measured from the maximum amplitude position ($P_{\max}$) and M controls the tapering rate at the edges of window.

The parameters of the tapering need to be adapted to the nature of the seismograms and so we use a constant size of cosine bell with L_1=0.22 s, L_2=0.18 s, for the calculations

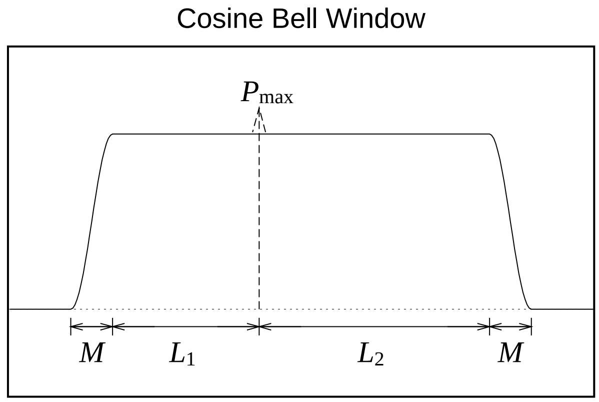

Fig. 7.13. The cosine bell window for tapering seismograms in time domain. $P_{\max}$ is the point where the amplitude of seismogram is largest, L_1 and L_2 determine the window size, and M controls the tapering rate at the ends of window.

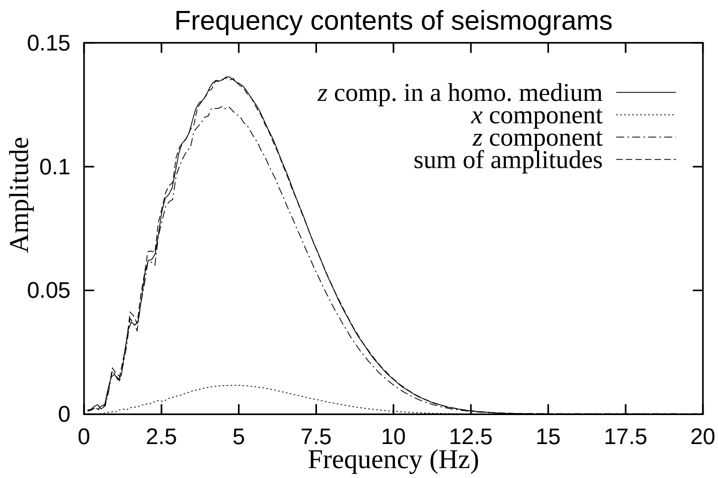

Fig. 7.14. Frequency content of seismograms obtained from modelling in the Gaussian random media with a=3399 m. Significant energy of primary waves is recorded in x component, and the sum of spectral amplitudes in x- and z-component data recover the spectral amplitudes expected in a homogeneous medium.

with $k_\alpha^d a$=0.14, 0.36, 0.90 and 2.26; for the other cases (i.e., $k_\alpha^d a$=5.68, 14.26) we employ L_1=0.22$\sim$0.5 s, L_2=0.18$\sim$0.5 s. M kept constant at 0.07 s. For cases with large-scale heterogeneity it is necessary to consider both the x- and z-component data. As indicated in Fig. 7.14 the amount of energy on the x component is too large to be ignored in estimates of scattering attenuation, since otherwise we would get an exaggerated loss by considering only the z component.

Therefore, in some case, such as Gaussian and exponential media with $k_\alpha^d a$=5.68, 14.26, and von Karman media with ν=0.25 and $k_\alpha^d a$=14.26, the scattering attenuation is measured by using dual component data and compared to single-component processing. The dual-component processing uses the sum of the spectral amplitudes of x- and

z-component seismograms (cf. Fig. 7.14). However, since the data on the x component are composed of both scattered and primary waves, appropriate tapering is required. For each case, the scattering attenuation is measured for a range of frequency from 2 to 9.5 Hz, and the results are displayed around the corresponding $k_\alpha^d a$ in the $Q_P^{-1} - k_\alpha a$ diagram.

7.7 Comparison between theory and numerical results: *P*-wave incidence

The scattering attenuation for the stochastic random media is measured from the synthetic seismograms for each case and compared with theoretical results in Fig. 7.15. Satisfactory results from a single realization of a stochastic medium can be obtained when $C_N \leq 0.05$. The cases with the different normalized wavenumbers are indicated by different symbols: an open triangle for $k_\alpha^d a$=0.14, a filled square for $k_\alpha^d a$=0.36, an open circle for $k_\alpha^d a$=0.90, a star for $k_\alpha^d a$=2.26, an open square for $k_\alpha^d a$=5.68, and a filled circle for a medium with $k_\alpha^d a$=14.26. The scattering attenuation rates measured just from z component data are shown by solid lines, and the symbols represent the results from the dual-component processing. The discrepancy between the single- and dual-component estimates of attenuation increases with the scale of the heterogeneity, and is also dependent on the style of random media. The Gaussian media displays significant discrepancy between the two styles of estimates and the discrepancy also increases with the value of the Hurst number implemented in von Karman media (including exponential media). This reflects the increasing deviation of the P wave from the incident direction with increasing a and ν. Measurements of single-component data may therefore give an overestimate of the scattering attenuation (especially for a Gaussian random media with large-scale heterogeneity).

The measured scattering attenuation rates from each set of data agree well with the trend of the theoretical curves from single scattering theory. The scattering attenuation values lie within the band for minimum scattering angles ($\theta_{\min}$) between 60-90° for all the random media tested. The results from modelling for random media with short correlation distances (e.g., $k_\alpha^d a$=0.14, 0.36, 0.90) show a parabolic variation as a function of normalized wavenumber.

Clearly the minimum scattering angle ($\theta_{\min}$) depends on the particular nature of the stochastic medium but is not less than 60°. This fully elastic result needs to be compared to previous studies which have often used scalar approximations. Sato (1982) predicted $\theta_{\min}$ to be $29°$ for scalar waves based on a cutoff wavelength for decomposition of the fractional fluctuation into long and short wavelengths at twice of the dominant wavelength. Recently, Kawahara (2002) gave a theoretical estimate of $\theta_{\min}$ as $65°$ in 2-D

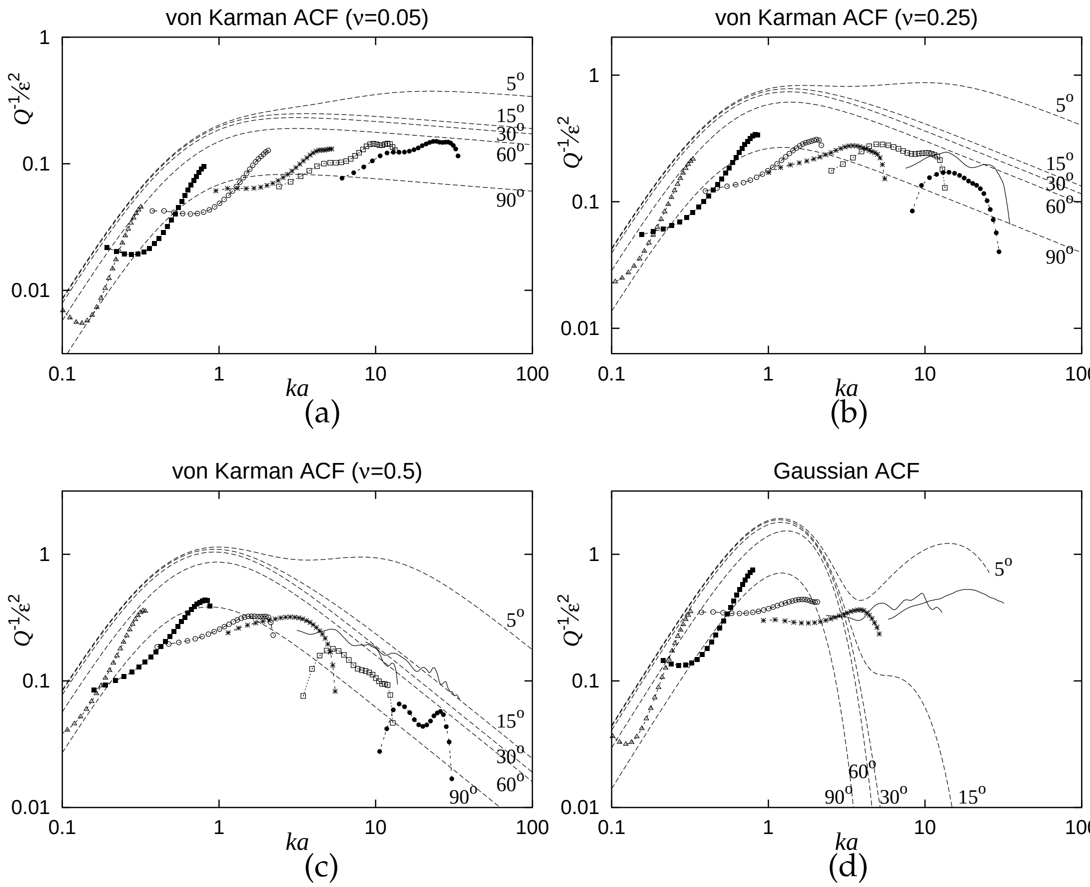

Fig. 7.15. Scattering attenuation factor Q^{-1} normalized for the variance ϵ^2 as a function of normalized wavenumber ka in the von Karman random media with the Hurst number (a) $\nu = 0.05$, (b) 0.25 (c) 0.5 (corresponding to the exponential random media) and (d) in the Gaussian random media. The symbols represent the data sets used for calculation of the scattering attenuation. The scattering attenuation measured by using single-component data is provided by solid lines for comparison with that measured by using dual component data. The minimum scattering angle is determined as lying in the range 60-90°.

acoustic media by considering the phase velocity of travel time corrected mean waves in high frequency limit. With a help of numerical modelling based on FDM, Frankel & Clayton (1986) measured $\theta_{\min}$ as 30-45° in 2-D elastic media (von Karman, exponential, Gaussian media), Jannaud *et al.* (1991) estimated 90° in 2-D acoustic Gaussian media with weak perturbation (4%) on velocity, Roth & Korn (1993) suggested 20-40° in 2-D anisotropic acoustic media, and recently Frenje & Juhlin (2000) computed the $\theta_{\min}$ for 2-D and 3-D acoustic media (von Karman, exponential, Gaussian media) as 10-20°.

The results of this study are similar to theoretical results of Kawahara (2002) and also close to the numerical study based on FDM in weakly perturbed acoustic media (Jannaud *et al.*, 1991).

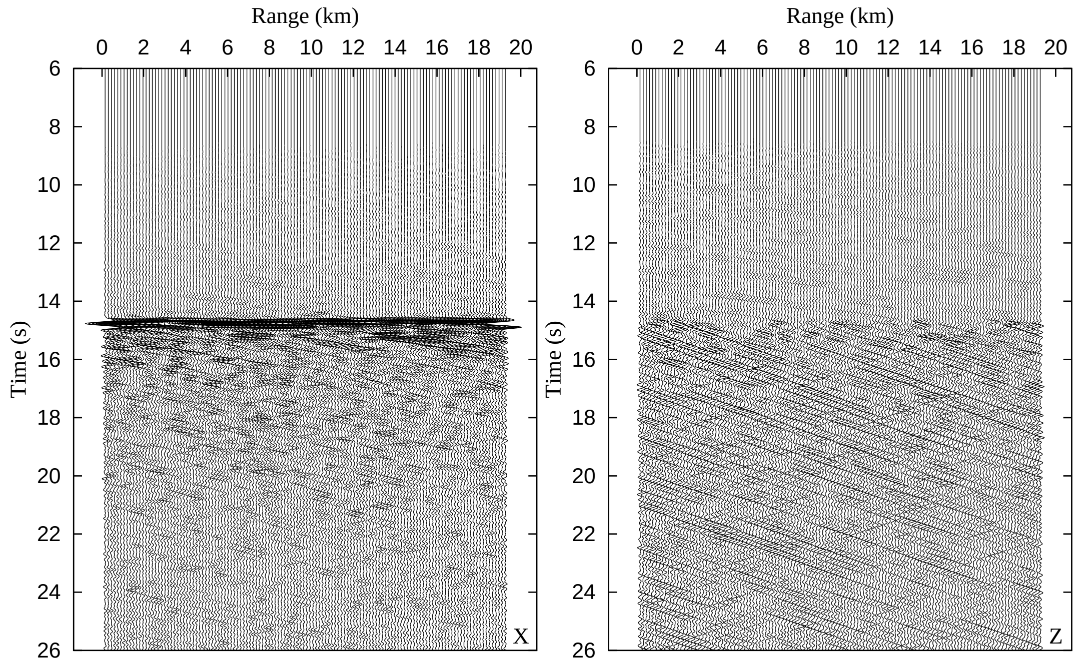

Fig. 7.16. Synthetic seismograms from numerical modelling in the von Karman random medium with ν=0.25 and a=214.5 m. Scattered *P* waves (*SP*) propagate faster before the primary *S* waves. Strong *S* coda waves develop after the primary waves.

7.8 *S*-wave scattering patterns and comparisons with theoretical curves

In order to check if numerical models behave as 'homogeneous' random media and constant scattering effects develop regardless of incidence direction, we set up simple problems where the positions of receivers and plane-wave sources are interchanged in the same models (case A: propagating upward (forward), case B: downward (reverse)). For case A, horizontal plane shear waves, propagating in the z direction and polarized in the x direction, are generated at line d=10.5 km above the bottom artificial boundary (Γ_B) and are collected at 128 receivers d=10.5 km below the upper artificial boundary (Γ_T). The receivers are deployed with constant spatial interval 150 m. Case B employs the reciprocal geometry between receivers and the source.

When plane shear waves are incident to random heterogeneous media, phase-coupled scattered P waves are generated at the boundaries of heterogeneities and are recorded before the primary waves in time responses (see, Figs. 7.16). Strong S coda waves follow after primary waves in x components, and multi-scattering effect enables a long temporal duration of coda. The multi-scattered waves are recorded dominantly on the z components. Fig. 7.17 shows a comparison of the spectral amplitudes for both forward and reverse propagation in von Karman media with Hurst number (ν) 0.25. A constant size of time window, sufficient to give an adequate description of the primary waves, is

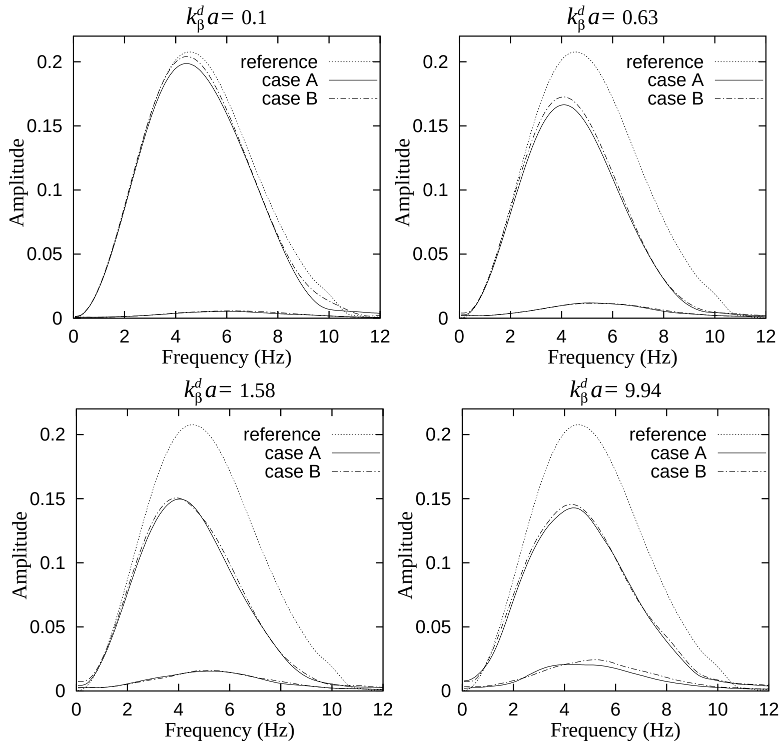

Fig. 7.17. Comparisons of spectral amplitudes of the primary waves between cases A (upward propagation) and B (downward propagation) as a function of frequency. Large amplitude sets are for x-component time responses and small ones for z-components. Considering average scattering energy loss, low-frequency waves with small normalized wavenumbers ($k_\beta^d a$=0.1, 0.63) exhibit relatively large discrepancy in spectral amplitudes. On the other hand, as $k_\beta^d a$ increases, measured energies of cases A and B lead to be equivalent.

used to resolve differences in energy loss due to scattering. The processing follows the scheme for P-wave data described in Section 7.6.

At low k_β^d (k_β^d=0.1, 0.63), there is a systematic difference in spectral amplitudes of x components; considering the overall energy loss, a significant difference between forward and reverse propagation develops around the dominant frequency. On the other hand, at large k_β^d, although there are some differences in the amplitudes, the differences are not significant compared to the overall energy loss and both cases A and B display equivalent energy losses. The variation of the spectral amplitudes of the z components (i.e., small amplitudes) is generally independent of those as the x components, but the amplitude differences on the z components increase with the overall energy losses (see, the case with k_β^d=9.94). The consistent amplitude differences between the x components at low k_β^d implies that low-frequency waves can be quite sensitive to the nature of the random media especially with small scale of heterogeneities. On the contrary, the energy loss at high-frequency range is consistent in modelling with low $k_\beta^d a$ and can be used for the analysis.

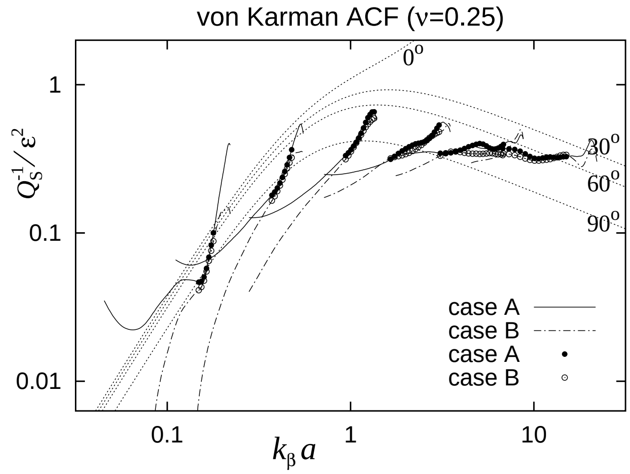

Fig. 7.18. Comparisons of scattering attenuation rates of shear waves between cases A (up-going) and B (down-going). Reasonable frequency ranges (see, Table 7.2) are marked with points, and the attenuation rates are equivalent in both cases.

Table 7.2. *Reliable frequency ranges for the measurement of scattering attenuation rates in von Karman media with ν=0.25.*

$k_\beta^d a$	0.1	0.25	0.63	1.58	3.96	9.94
Frequency (Hz)	6.7-8.3	6.7-8.7	6.7-9.7	4.7-8.7	3.5-8.0	3.0-7.0

Fig. 7.18 displays the measured attenuation rates (drawn as lines) of both cases A and B in the frequency range 2 to 10 Hz. Here the values in the most reliable ranges (see, Table 7.2) of each experiment are marked with points. The reliable ranges of other types of random media are determined to lie close to those for von Karman media with ν=0.25.

Along with the estimation in von Karman media with ν=0.25, we additionally consider von Karman media with ν=0.05 and 0.5 (corresponding to the exponential media) and Gaussian media. The modelling is undertaken in the case A geometry (e.g., Figs. 7.19 and 7.20). The randomicity rates (C_N) in (7.38) of stochastic random models for the S-wave scattering modellings are given in Table 7.3. The C_N values increase with the size of correlation distance (a), but are close to zero in every stochastic model. The maximum C_N is 0.047 (von Karman with ν=0.05 and a=1353.2 m) and is smaller than the maximum value (C_N=0.048) of the models for P-wave scattering studies. Also, parameters of tapering windows (cosine bell, Fig. 7.13) for seismograms with $k_\beta^d a$=0.1, 0.25, 0.63, 1.58 are L_1=0.25 s, L_2=0.25 s and M=0.05 s, and those for seismograms with $k_\beta^d a$=3.96, 9.94 are L_1=0.28-0.30 s, L_2=0.28-0.33 s and M=0.05 s. The dual-component analysis (see,

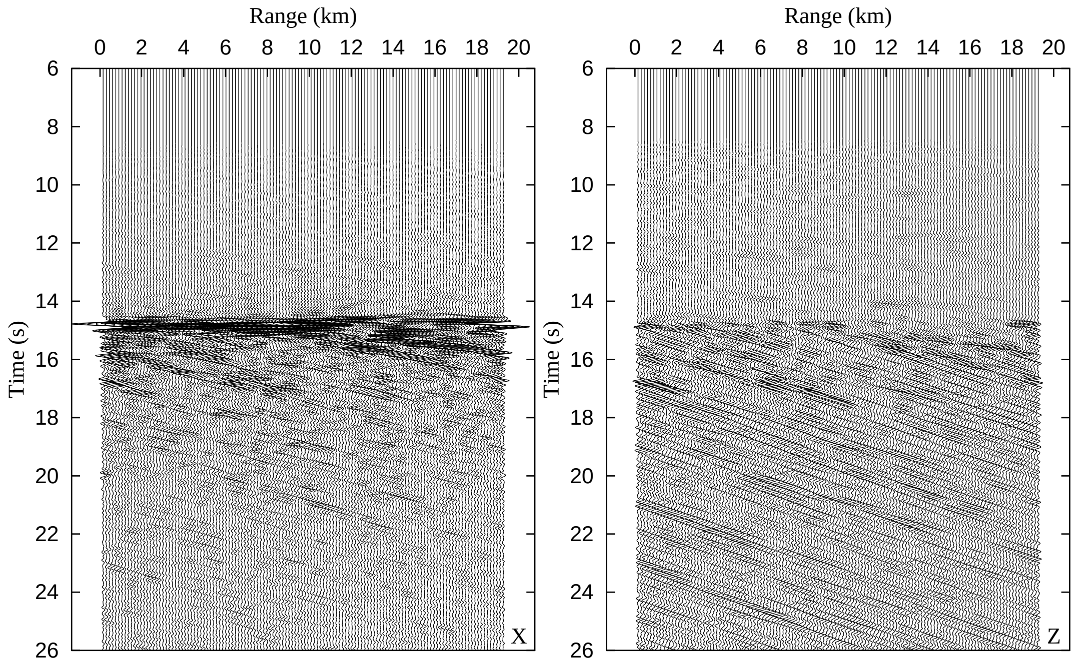

Fig. 7.19. Synthetic seismograms from numerical modelling in the von Karman random medium with ν=0.5 and a=538.7 m.

Table 7.3. *Randomicity rates C_N (=$|N_+ - N_-|/N_t$) of stochastic random heterogeneous media for S-wave scattering studies.*

a (m)	34	85.4	214.5	538.7	1353.2
• von Karman ($\nu = 0.05$)					
C_N	0.0043	0.0048	0.0068	0.0151	0.0273
• von Karman ($\nu = 0.25$)					
C_N	0.0034	0.0040	0.0102	0.0201	0.0403
• von Karman ($\nu = 0.5$, exponential)					
C_N	0.0039	0.0051	0.0119	0.0268	0.0471
• Gaussian					
C_N	0.0048	0.0013	0.0056	0.0185	0.0308

Section 7.6) is implemented for the correct estimation of scattering attenuation rates from seismograms in the exponential and the Gaussian media with k_β^d=9.96.

The estimated *S*-wave scattering attenuation rates from synthetic seismograms are well represented by the theoretical curves with minimum scattering angles ($\theta_{\rm min}^{SS}$) in the range 60° to 90° in all stochastic models (Fig. 7.21). Such result is identical to that of the *P*-wave scattering study in Section 7.7.

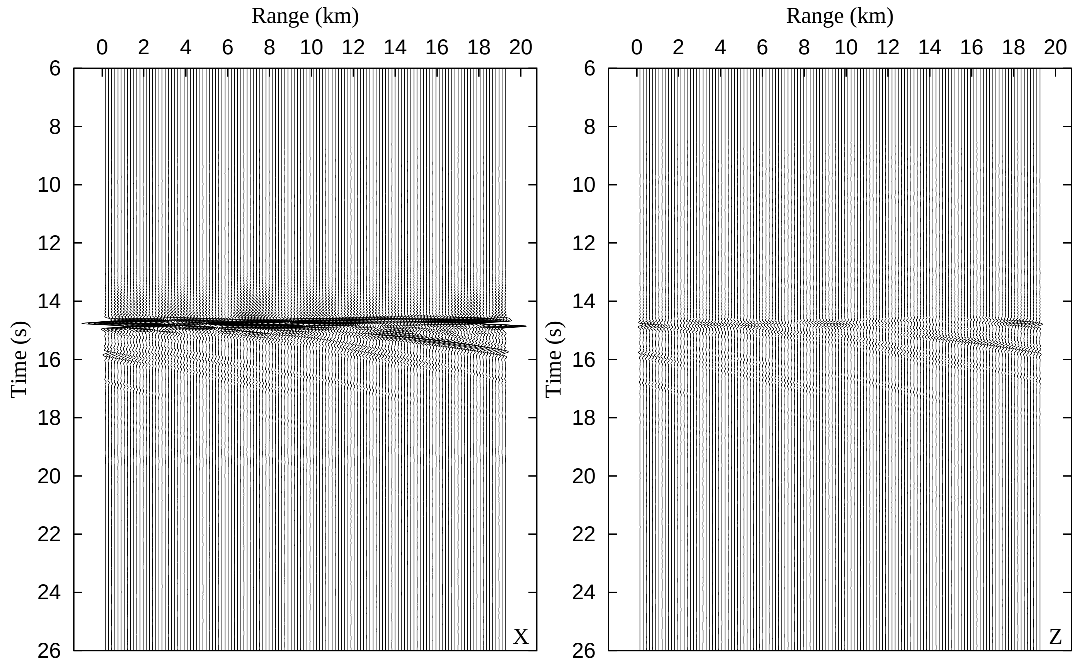

Fig. 7.20. Synthetic seismograms from numerical modelling in the Gaussian random medium with a=1353.2 m.

7.9 Scattering attenuation ratios of *P* and *S* waves

7.9.1 For wavenumber

We use the theoretical scattering attenuation expressions for *P* and *S* waves in (7.33) and (7.34), which have been shown to be compatible with the results of numerical modelling, for the investigation of scattering properties of elastic waves in random media. The use of theoretical expressions allows various case studies to be undertaken without massive numerical modelling.

The scattering attenuation rates depend on the velocity ratio (γ) of medium, and we consider representative crustal velocities: α_0=6.738 km/s, β_0=3.85 km/s, and γ=1.75 (Kennett *et al.*, 1995).

Fig. 7.22 displays comparisons between scattering attenuation rates of *P* and *S* waves as function of normalized wavenumber (ka), where k represents the wavenumber of incident waves, i.e., k_α for the *P*-wave incident case and k_β for the *S*-wave. In general, the attenuation-rate variation for ka is such that *P* waves lose slightly more energy due to scattering than *S* waves at $ka \ll 1$ and the attenuation rates are comparable at large normalized wavenumber ($ka \gg 1$). However, the Gaussian random models have different gradients of the scattering attenuation curves for *P* and *S* waves at $ka \gg 1$.

The characteristic attenuation patterns of *P* and *S* waves give rise to a relatively simple attenuation ratio (Q_P^{-1}/Q_S^{-1}) pattern in von Karman and exponential random models

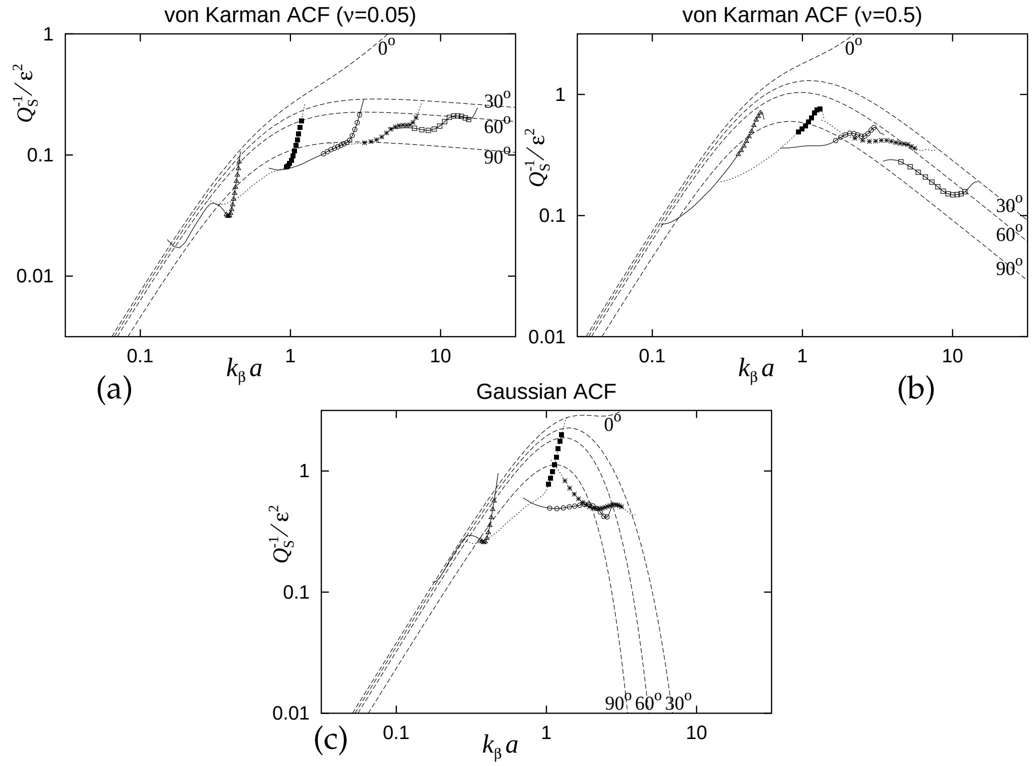

Fig. 7.21. Comparisons of theoretical and numerically estimated scattering attenuation rates of shear waves (Q_S^{-1}) as a function of normalized wavenumber $k_\beta a$ in the von Karman random media with the Hurst number (a) $\nu = 0.05$, (b) 0.5 (corresponding to the exponential random media) and (c) in the Gaussian random media, under case A geometry. The attenuation rates in the reliable ranges are marked with points and those in neighbour are drawn in lines. The scattering attenuation rates are well represented by the theoretical curves for 60-90° minimum scattering angle.

Table 7.4. *Maximum attenuation ratios ($R_Q = Q_P^{-1}/Q_S^{-1}$) for ka and fa in von Karman type media with different Hurst number (ν) when α_0=6.74 km/s and β_0=3.85 km/s (γ=1.75). The ratios are measured at ka=100 and fa=100 km/s.*

ν	0.05		0.25		0.5	
$\theta_{\min}$	60°	90°	60°	90°	60°	90°
$R_Q\|_{(ka=100)}$	1.03	0.94	0.99	0.91	0.96	0.89
$R_Q\|_{(fa=100)}$	1.09	0.99	1.31	1.21	1.67	1.56

(Fig. 7.23). At low ($ka \ll$0.1) and large ($ka \gg$10) normalized wavenumber, the magnitudes of the attenuation ratios depend on the minimum scattering angle but are nearly constant regardless of models. The maximum ratios at $ka \ll$0.1 are 1.36 at 60° and 1.19 at 90°. The minimum ratios at $ka \gg$10 vary with both the type of random model and the minimum scattering angle, but all are close to 1 (see, Table 7.4). For normalized wavenumber

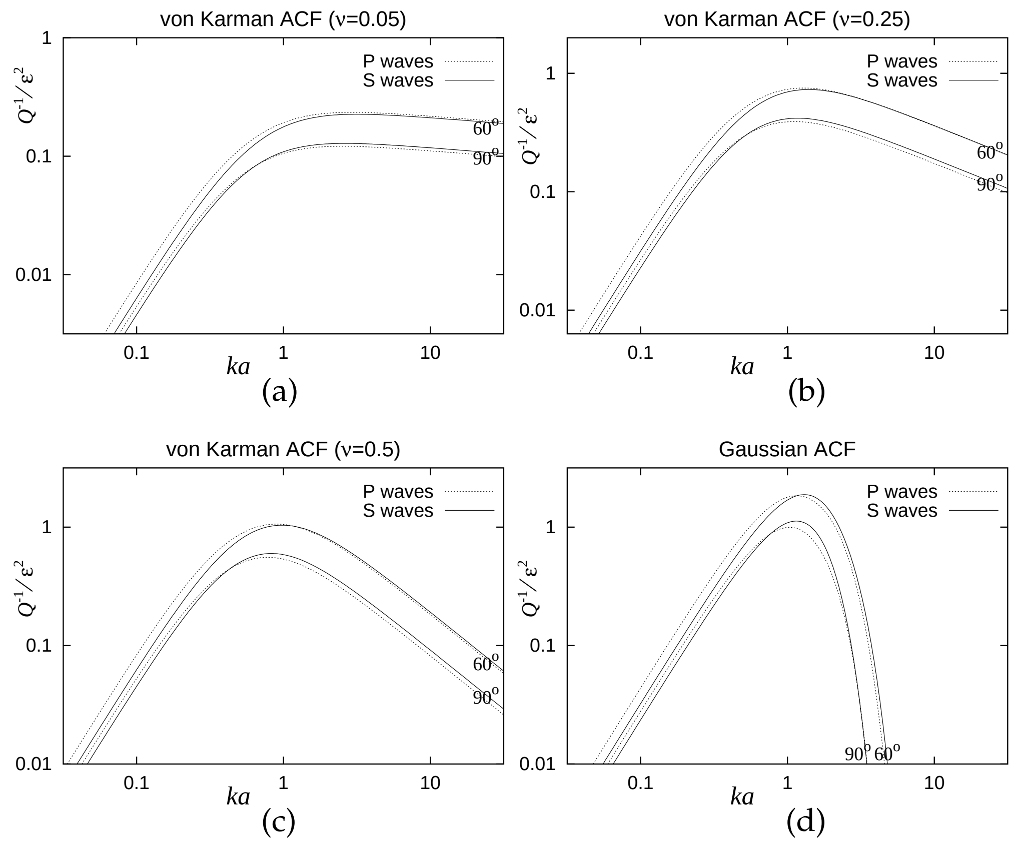

Fig. 7.22. Comparisons of *P* and *S* wave scattering attenuation rates as a function of normalized wavenumber (ka) in the von Karman type random media with the Hurst number (a) $\nu = 0.05$, (b) 0.25 (c) 0.5 and (d) in the Gaussian random media, when α_0=6.74 km/s and β_0=3.85 km/s (γ=1.75). k represents the wavenumber of the incident waves, i.e., k_α for *P* waves and k_{beta} for *S* waves.

0.1<ka<10, the attenuation ratios decrease with ka with gradients which depend on the models. The Gaussian random media do not exhibit a coherence between the two minimum scattering angles at large ka (ka>1), and show steep variation of ratio with ka.

In von Karman models (including exponential random models), *P* waves lose more energy at low wavenumber by scattering than *S* waves. The difference reduces with increase of wavenumber and the magnitude of the energy loss for *P* and *S* waves become equivalent at high wavenumber. This characteristic pattern can be found also in field-data analysis (e.g., Yoshimoto *et al.*, 1993).

7.9.2 For frequency

The consideration of attenuation ratios as a function of frequency (f) allows a direct comparison with those based on field-data analysis. Using the simple relationship $f = k_\beta \beta/(2\pi) = k_\alpha \alpha/(2\pi)$, we obtain expression for the attenuation rate as a function of

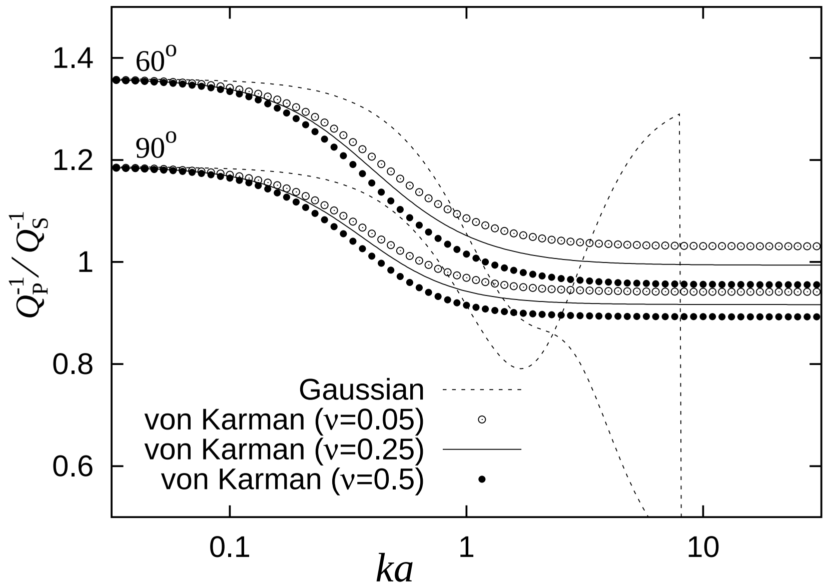

Fig. 7.23. Scattering attenuation ratios of *P* and *S* waves as a function of normalized wavenumber (ka) in the von Karman type random media with the Hurst number $\nu = 0.05$, 0.25, 0.5 and in the Gaussian random media, when α_0=6.74 km/s and β_0=3.85 km/s (γ=1.75).

normalized frequency (fa). Note that the implementation of a different set of velocities with γ=1.75 needs only a relative change of fa values (e.g., α_0=6.738 km/s, β_0=3.85 km/s $\rightarrow$ α_0=4.0 km/s, β_0=2.286 km/s).

In Fig. 7.24, we find that shear wave attenuation is more significant at low fa (<1 km/s) in all random models, while compressional wave attenuation is more dominant at large fa (>1 km/s). However, the dominancy of *P*-wave scattering in the high frequency region (fa>1 km/s) reduces with decrease of Hurst number in von Karman media. The frequency dependence of elastic-wave attenuation at high frequencies (fa>1) matches the behavior found in regional seismic data analysis (e.g., Castro *et al.*, 1997).

Attenuation ratios increase with fa in von Karman type models (Fig. 7.25), but Gaussian models exhibit a steep variation at fa>1. At low fa (<0.1 km/s), all models exhibit constant attenuation ratios depending on the minimum scattering angle; 0.444 for 60°, 0.388 for 90°. Also, the ratios are constant at large fa (>10 km/s), but the magnitudes vary with both the nature of the model and the minimum scattering angle. In particular, the maximum attenuation ratios increase with Hurst number in the von Karman models (Table 7.4).

The pattern of attenuation ratios in Fig. 7.25 agrees well with the reported results based on field-data analysis, which vary from 0.4 to 2.9 (see, Fig. 5.3 in Sato & Fehler (1998)). At low frequencies (f<0.05 Hz), Anderson *et al.* (1965) and Tsai & Aki (1969) present constant attenuation ratios around 0.4. Taylor *et al.* (1986) reported attenuation

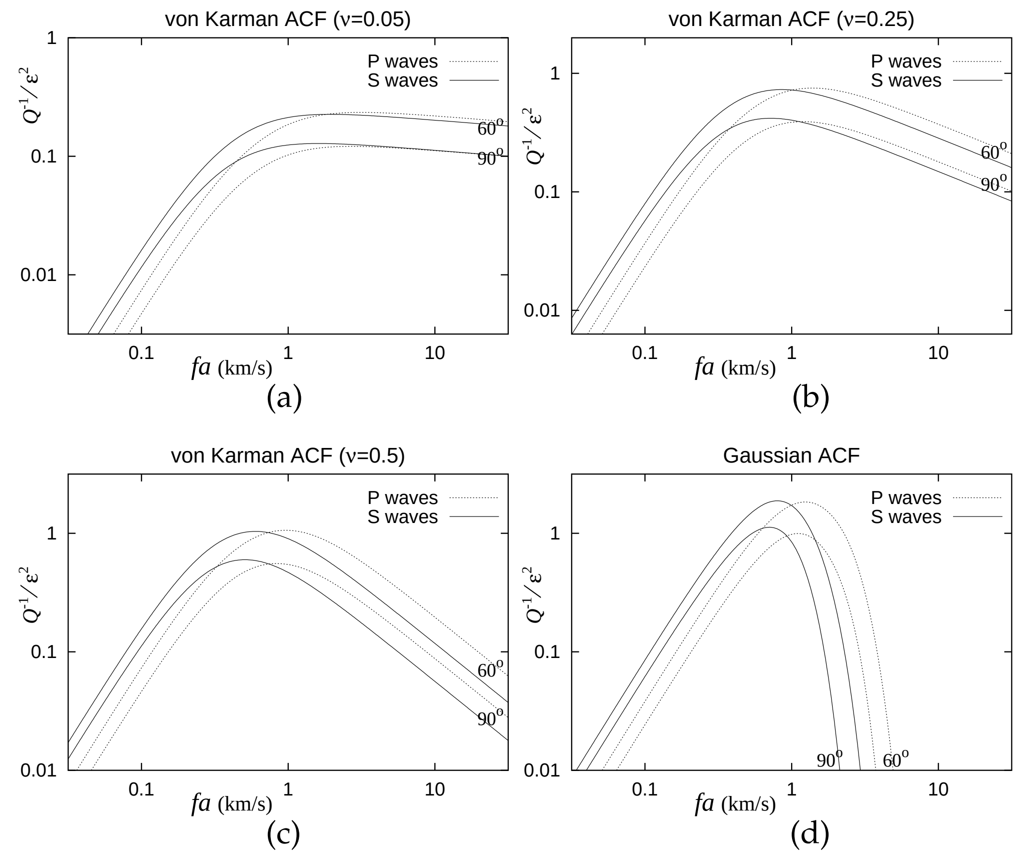

Fig. 7.24. Comparisons of P and S wave scattering attenuation rates as a function of normalized frequency (fa) in the von Karman type random media with the Hurst number (a) $\nu = 0.05$, (b) 0.25 (c) 0.5 and (d) in the Gaussian random media, when α_0=6.74 km/s and β_0=3.85 km/s (γ=1.75).

ratios increasing from about 0.5 to 2 with frequency in North America in the range 0.05 - 3 Hz. The attenuation ratios at high frequencies (f>10 Hz) have been reported to vary from 1.12 to 2.94 between different regions (e.g., Castro *et al.*, 1997; Yoshimoto *et al.*, 1993; Chung & Sato, 2001; Carpenter & Sanford, 1985; Modiano & Hatzfeld, 1982). Note that the reported attenuation ratios can be obtained using von Karman random models with appropriate Hurst number and correlation distance.

However, some studies (e.g., Yoshimoto *et al.*, 1993, 1998) present attenuation ratios which do not conform to the theoretical pattern (i.e., ratio increasing with frequency) at high frequencies due to the dominance of intrinsic attenuation. For example, the intrinsic attenuation rates in the Kanto area (see, Yoshimoto *et al.*, 1993) are about twice the scattering attenuation rates and vary independently of the scattering attenuation rates (Fehler *et al.*, 1992). The dominance of intrinsic attenuation at high frequency may result from a difference between the frequency dependences of scattering and intrinsic attenuation rates, which results in the decrease of the seismic albedo at high frequencies

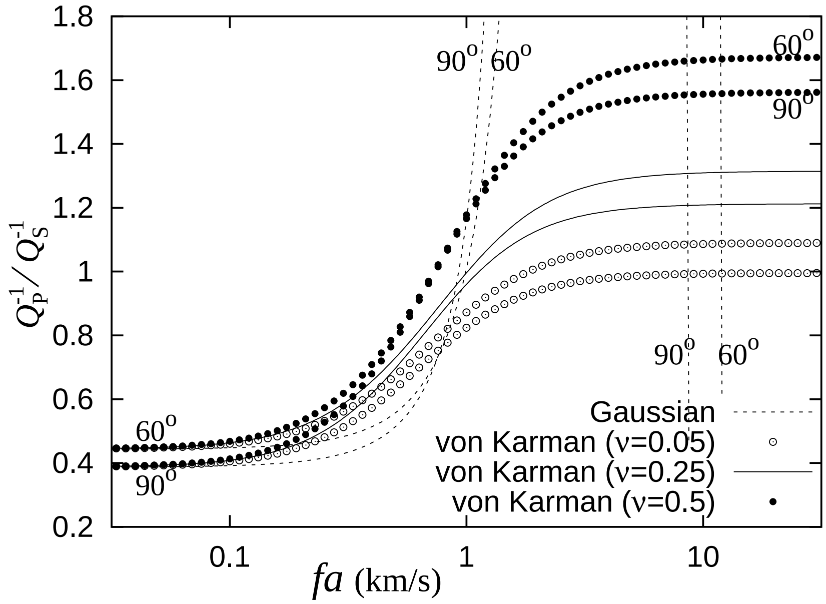

Fig. 7.25. Scattering attenuation ratios of P and S waves as a function of normalized frequency (fa) in the von Karman type random media with the Hurst number $\nu = 0.05$, 0.25, 0.5 and in the Gaussian random media, when α_0=6.74 km/s and β_0=3.85 km/s (γ=1.75).

(e.g., Akinci & Eyidoğan, 2000), as shown in northern Greece (Hatzidimitriou, 1994) where the scattering attenuation has $f^{-0.72}$ frequency dependence while the intrinsic attenuation has $f^{-0.45}$. In addition, complexity of media resulting from inhomogeneous (space and depth dependent) distribution of heterogeneities (e.g., Campillo & Plantet, 1991; Menke *et al.*, 1995; Tselentis, 1993) can lead to attenuation variation at high frequency with increasing hypocentral distance.

7.10 Discussion and conclusions

We have been able to establish a consistent approach to the estimation of scattering attenuation for elastic waves, using multi-component information and fully elastic analytic results. We formulated the scattering attenuation variation (Q_s^{-1}) for 2-D elastic waves in terms of the normalized wavenumber (ka) for stochastic random media. The theoretical scattering attenuation rates of elastic waves are highly dependent on the ratio of P and S wave velocities; so it is necessary to use a full elastic treatment rather than employ scalar results as a reference.

Accurate numerical modelling is critical for quantitative assessment of stochastic media. Through an example of numerical differentiation, we have shown that there is a possibility of excessive attenuation in rapidly varying media when the smoothness assumptions built into FDM methods are violated. We have shown that the wavelet-based method (WBM) can achieve high accuracy in numerical differentiation and stability in highly perturbed media, and so is very suitable for work on scattering attenuation.

Synthetic seismograms have been computed for 4 types of random media (Gaussian, exponential and von Karman media with ν=0.05, 0.25) with 6 different correlation distances. With large-scale heterogeneity energy in the primary waves gets transferred to the perpendicular to the incident direction; this means that dual-component seismograms are needed for correct measurement of scattering attenuation. For the broad range of stochastic models the minimum scattering angle for elastic waves, derived from comparison of the WBM with theoretical curves, lies in a band from as 60-90°. This range of values is similar to those presented by Kawahara (2002) and Jannaud *et al.* (1991) for 2-D acoustic media.

The discrepancies in previous results, $\theta_{\min}$=90° in mildly perturbed media (4%) and 20-30° in more highly perturbed media, may well arise from limitations in previous numerical modelling. The limitations of the FDM can give rise to overestimates of attenuation in media with strong variations.

Also, the nature of scattering attenuation ratios (Q_P^{-1}/Q_S^{-1}) of elastic waves has been investigated as a function of wavenumber and frequency in stochastic random models by using theoretical attenuation expressions based on the first-order Born approximation. The theoretical attenuation expressions were compared with results from numerical modelling. The theoretical curves with minimum scattering angle 60-90° fitted well to the results.

In general, the scattering attenuation rates of *P* and *S* waves display almost equivalent magnitudes for normalized wavenumbers (ka). However, *P* waves lose more energy by scattering for $ka < 1$, and the attenuation rates of both waves become comparable for $ka > 1$. Thus, elastic waves have maximum attenuation ratios at ka<0.06 and the minimum at ka>10. The maximum ratios are measured to be constant regardless of the form of stochastic model, but depend on the minimum scattering angle: 1.36 for 60° and 1.19 for 90°. On the other hand, the minimum ratios depend on the models but lie close to 1. Thus, the difference in energy loss of *P* and *S* waves due to scattering reduce with wavenumber and becomes indistinguishable at high wavenumbers in random media.

The relative variations of the scattering attenuation rates of *P* and *S* waves change with frequency; *S* waves lose more energy than *P* waves at low frequencies (fa≤1.0 km/s), while *P* waves decay more at large frequencies. This characteristic feature leads to a frequency-dependent pattern of attenuation ratio: the ratios increase with normalized frequency from 0.1 to 2 km/s and are measured to be constant at low (fa<0.1 km/s) and high (fa>2 km/s) normalized frequencies. The minimum ratios for low frequencies are 0.4 regardless of the nature of the stochastic model, and the maximum ratios at high frequencies depend on both the model and the minimum scattering angle. The maximum ratios increase with the Hurst number (ν) in von Karman type random models (including the exponential random model). However, Gaussian models show sharp variations in ratios with fa. Reported attenuation ratios based on field-data analysis are consistent with the theoretical attenuation ratios. Thus, it appears that random heterogeneities in the crust may be modelled by a set of von Karman models with appropriate Hurst numbers (see also, Tripathi & Ram, 1997).

Intrinsic attenuation plays as a dominant factor in apparent attenuation of seismic waves at high frequencies in some regions, and thus numerical studies including both intrinsic and scattering attenuation effects may be required in order to understand the attenuation patterns of high-frequency seismic waves in the crust. The Q^{-1}-fa diagram allows straightforward comparison to the attenuation factors measured in nature, and is useful in both assessing scattering effects for frequencies and characterizing the media in terms of average scale (correlation distance) of random heterogeneities.

8

Comparison of scattering patterns between acoustic and *SH* waves

8.1 Introduction

In Chapter 7, we have investigated scattering patterns and scattering attenuation rates for elastic waves. With comparisons with previous studies on acoustic (scalar) waves, we concluded that the scattering attenuation rates in *P-SV* waves are different from those for acoustic waves.

This discrepancy may be related in part to the differences in the characteristics between elastic and acoustic waves, for example, the presence of wavetype coupling on a boundary. However, it is not certain if the scattering pattern will be identical between acoustic waves and *SH* waves which have a similar form of equation and share Green's function for homogeneous media. Although the equation systems of acoustic and *SH* waves are similar to each other, the placement of the density term and the incompressibility term is reversed in acoustic-wave equations compared to elastic-wave equations. Thus, we may find the dependence of the scattering on the parameter perturbations by comparing the scattering patterns of acoustic and *SH* waves.

We compare the scattering patterns and attenuation rates under the same conditions (magnitude of velocity perturbation, propagation distance, dominant frequency of incident waves etc.), with the inclusion of the additional perturbation in the density for *SH* problems. Also, we formulate the theoretical scattering attenuation expression for *SH* waves as a reference in comparison with numerical results, and this result is compared with those of scalar waves (Frankel & Clayton, 1986; Frenje & Juhlin, 2000). The effect of the density on the *SH* scattering is discussed using the theoretical attenuation variation.

8.2 Theoretical scattering attenuation variations

The 2-D acoustic wave equation is given by

$$\frac{\partial^2 P}{\partial t^2} = \mathcal{K}\frac{\partial}{\partial x}\left(\frac{1}{\rho}\frac{\partial P}{\partial x}\right) + \mathcal{K}\frac{\partial}{\partial z}\left(\frac{1}{\rho}\frac{\partial P}{\partial z}\right), \tag{8.1}$$

where P is the pressure in the fluid, $\mathcal{K}$ the incompressibility and ρ is the density. Here, the wave velocity (c) is given by $\sqrt{\mathcal{K}/\rho}$. When ρ is assumed to be invariant in the spatial domain, equation (8.1) can be simply rewritten in the form of a scalar wave equation:

$$\frac{\partial^2 P}{\partial t^2} = c^2\left(\frac{\partial^2}{\partial x^2} + \frac{\partial^2}{\partial z^2}\right)P. \tag{8.2}$$

When the velocity perturbation in (7.8) is considered, the theoretical scattering attenuation variations of the scalar waves are given by (Frankel & Clayton, 1986; Frenje & Juhlin, 2000)

$$Q_s^{-1} = \frac{k_s^2\epsilon^2}{\pi}\int_{\theta_{\min}}^{\pi}\mathcal{P}\left[2k_s\sin\frac{\theta}{2}\right]d\theta, \tag{8.3}$$

where k_s is the wavenumber of the incident scalar waves, ϵ is the standard deviation of the velocity perturbation, $\theta_{\min}$ is the minimum scattering angle, and $\mathcal{P}$ is the power spectral density function.

The 2-D *SH* wave equation has a similar form to the acoustic wave equation but positions of the density (ρ) and the shear modulus (μ) are different:

$$\frac{\partial u_y^2}{\partial t^2} = \frac{1}{\rho}\frac{\partial}{\partial x}\left(\mu\frac{\partial u_y}{\partial x}\right) + \frac{1}{\rho}\frac{\partial}{\partial z}\left(\mu\frac{\partial u_y}{\partial z}\right), \tag{8.4}$$

where u_y is the *SH*-wave displacement. Theoretical scattering attenuation variations can be derived following the scheme in Section 7.3.1 and are given by

$$\frac{Q_H^{-1}}{\epsilon^2} = \frac{k_\beta^2}{8\pi^2}\int_{\theta_{\min}}^{2\pi-\theta_{\min}}\left[C_1^H + C_2^H(1-\cos\theta)\right]^2\mathcal{P}\left(2k_\beta\sin\frac{\theta}{2}\right)d\theta, \tag{8.5}$$

where C_1^H=-2, C_2^H=K+2 and k_β is the wavenumber of the incident *S* waves. Details of the derivation are described in Appendix D.

8.3 Modelling and scattering patterns

For modelling in acoustic wave propagation, we implement only velocity perturbation (10%) without consideration of density perturbation, which is often considered in acoustic layers in the earth. Thus, the resultant wave propagation pattern is similar to scalar wave propagation. On the other hand, we consider both velocity (10%) and density perturbations (8%) in modelling for *SH* waves, and compare the scattering patterns between acoustic and *SH* waves. We employ the same background wave-velocity

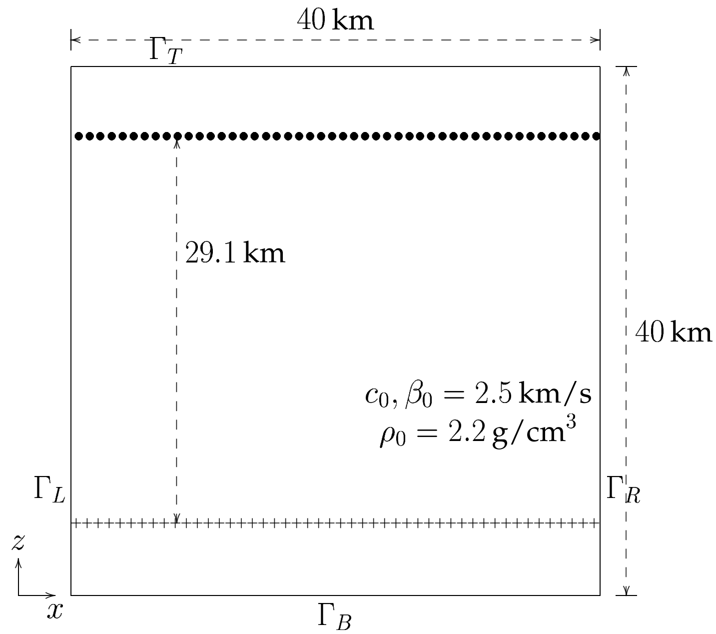

Fig. 8.1. Description of 2-D unbounded medium for the acoustic and *SH* wave scattering. 128 receivers (•) are placed with uniform interval (312.5 m) at 29.1 km from the source (+). The wave velocity in the background medium is 2.5 km/s and the density is 2.2 g/cm^3. The top and bottom artificial boundaries (Γ_T, Γ_B) are treated by absorbing boundary conditions and the left and right boundaries (Γ_L, Γ_R) are considered with periodic boundary conditions.

(c_0, β_0=2.5 km/s) and the same magnitude of external force for the source. The domain is represented by 512-by-512 grid points corresponding to a 40 km-by-40 km in physical space (Fig. 8.1). The media are considered to be unbounded by considering the top and the bottom boundaries (Γ_T, Γ_B) with absorbing boundary conditions and the left and the right boundaries (Γ_L, Γ_R) with periodic boundary conditions. Plane waves are generated at the source positions (+) and 128 receivers (•) with a uniform interval (312.5 m) are placed at 29.1 km from the source.

Five different values of correlation distances (a= 17.6, 44.3, 111.4, 279.8, 702.9 m) are implemented for the representation of stochastic random heterogeneities. As in the *P* and *S* wave scattering problems in Chapter 7, we implement four different types of stochastic random media (exponential, Gaussian, von Karman with ν=0.05, 0.25). The construction of the appropriate random media is described in detail in Section 7.5.

Figs. 8.2, 8.3, 8.4 and 8.5 show the time responses of acoustic pressure and *SH* displacement recorded for the stochastic random media. Although the same order of velocity perturbation has been introduced in both experiments, different scattering patterns in time responses are observed; the coda in acoustic-wave problems display random waveforms, while those in *SH*-wave problems show more consistency in coda

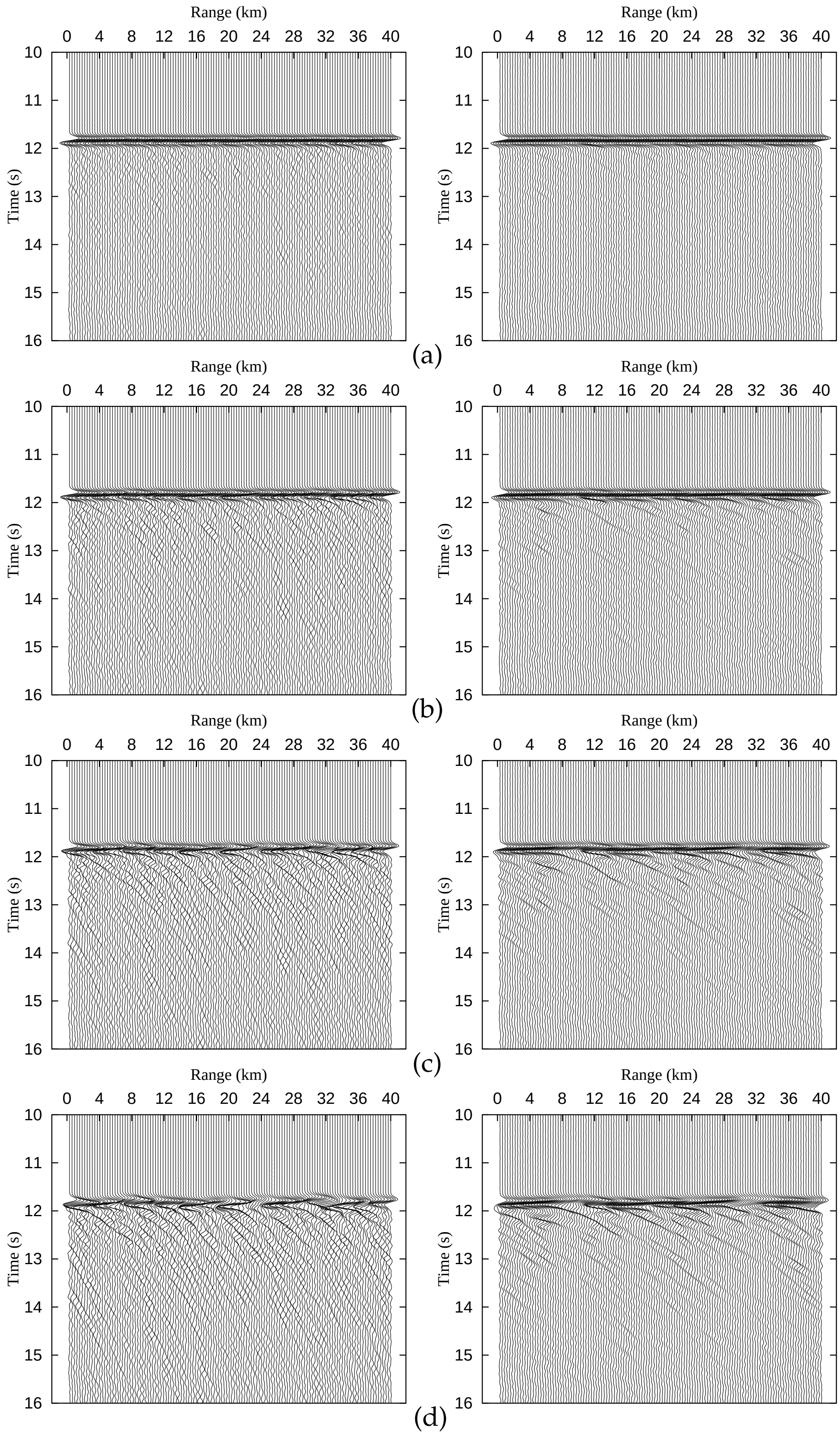

Fig. 8.2. Time responses in von Karman media with Hurst number (ν) 0.05 and correlation distance (a) for stochastic heterogeneities (a) 44.3 m, (b) 114.3 m, (c) 279.8 m, and (d) 702.9 m.

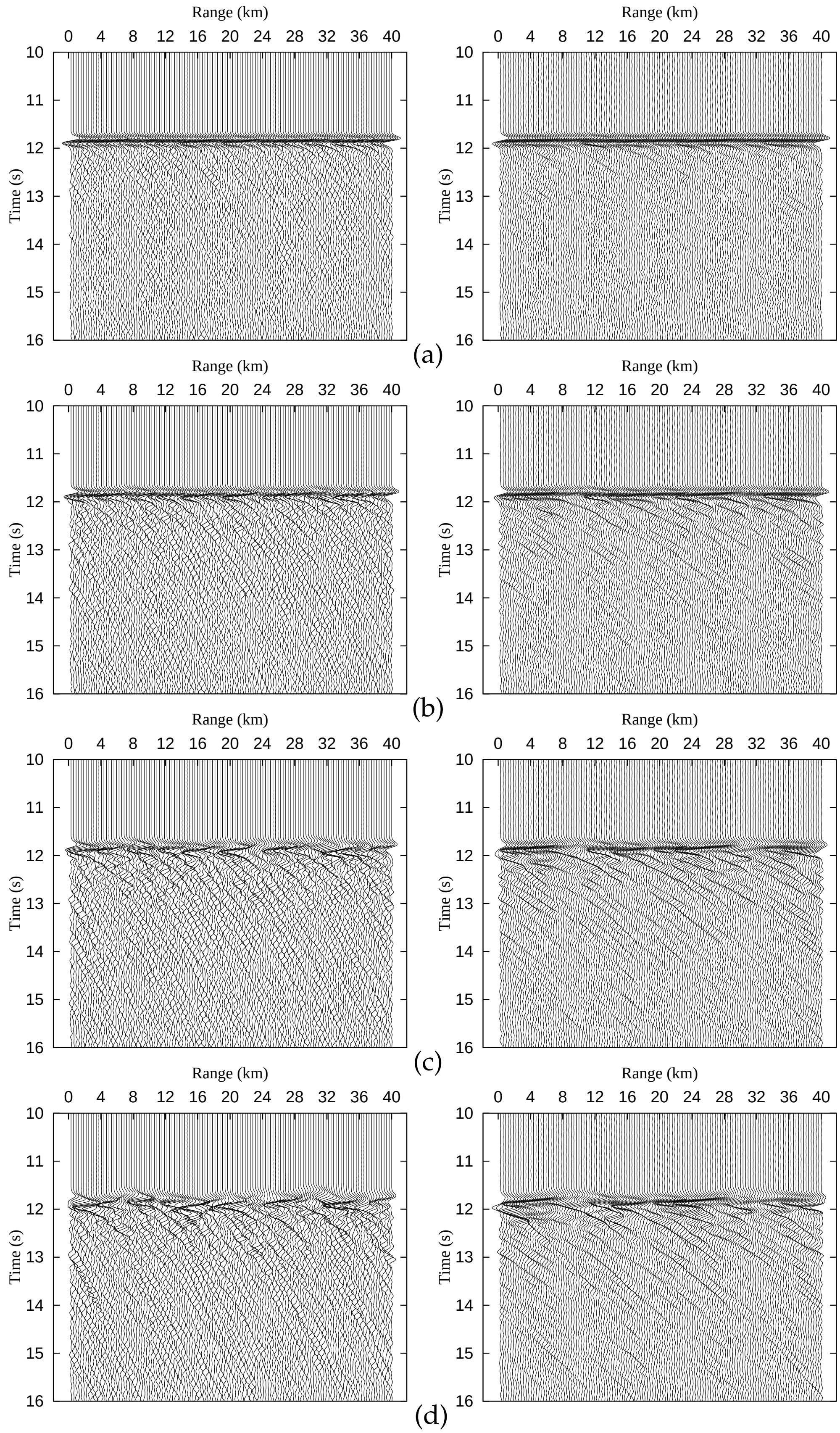

Fig. 8.3. Time responses in von Karman media with Hurst number (ν) 0.25 and correlation distance (a) for stochastic heterogeneities (a) 44.3 m, (b) 114.3 m, (c) 279.8 m, and (d) 702.9 m.

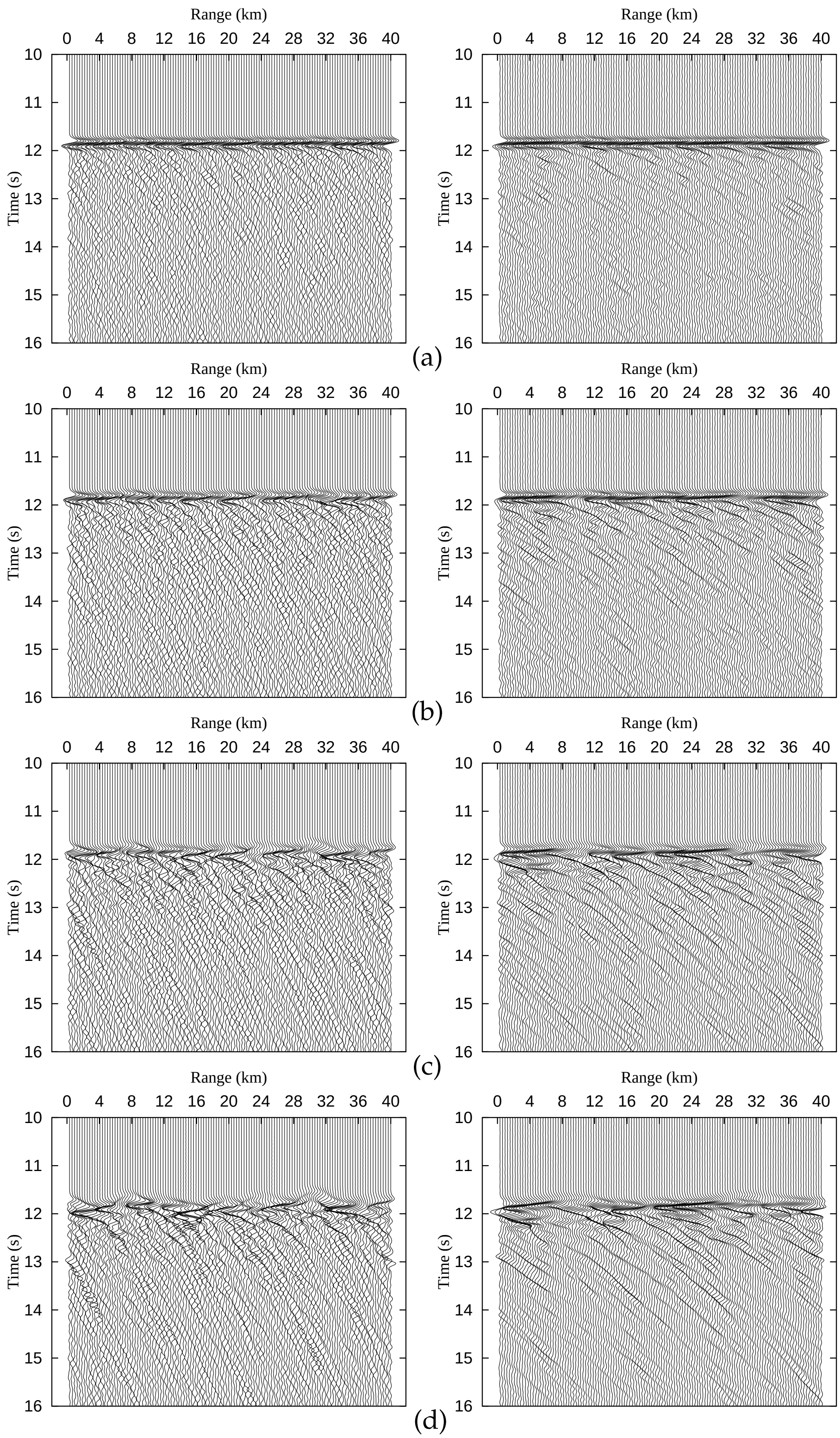

Fig. 8.4. Time responses in the exponential media with correlation distance (a) for stochastic heterogeneities (a) 44.3 m, (b) 114.3 m, (c) 279.8 m, and (d) 702.9 m.

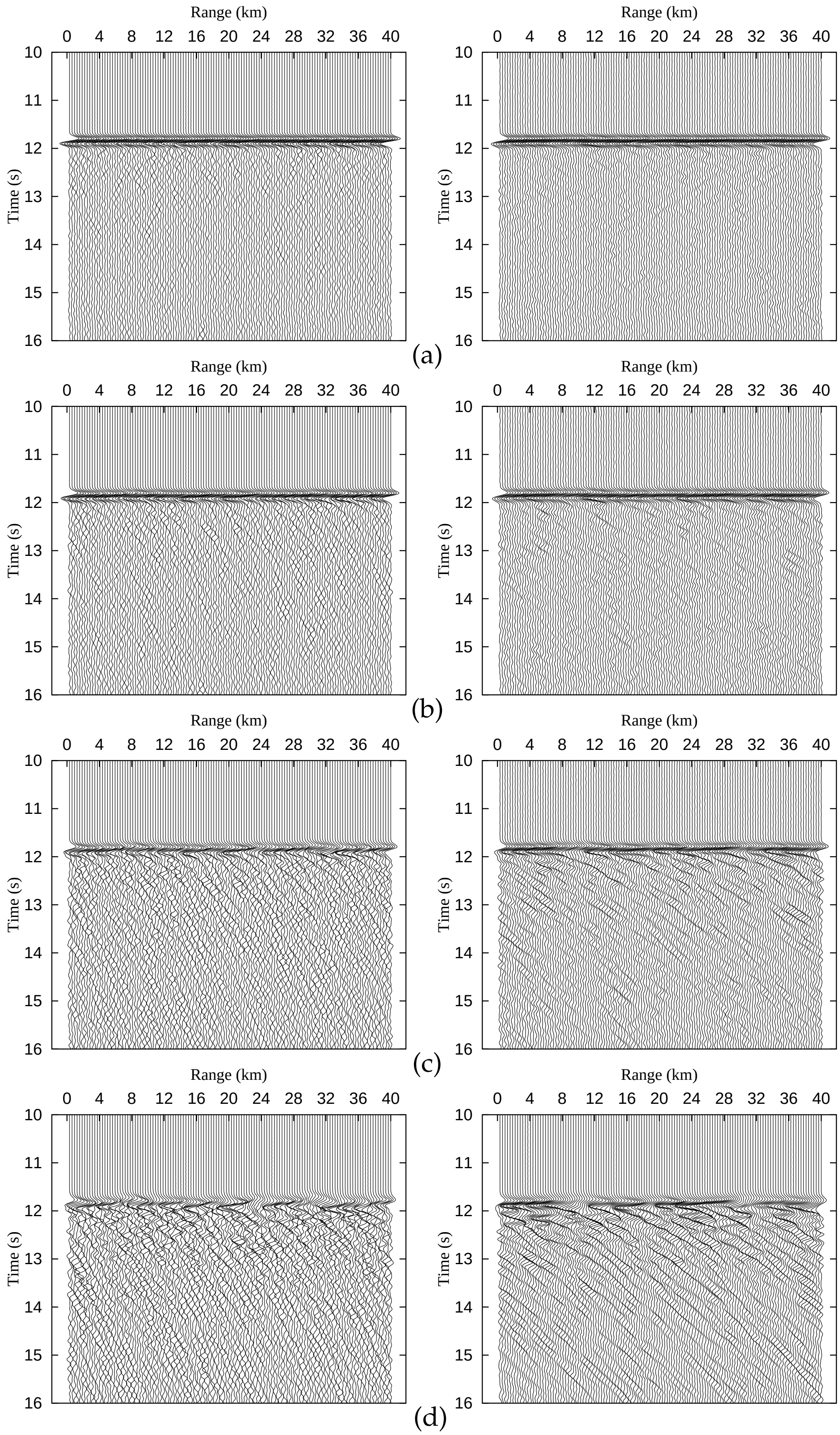

Fig. 8.5. Time responses in Gaussian media with correlation distance (a) for stochastic heterogeneities (a) 17.6 m, (b) 44.3 m, (c) 114.3 m and (d) 279.8 m.

wavetrains. The coda waves in the acoustic problem are similar to those in the P wave scattering problem (Section 7.6), and the coda waves in the *SH* problem to the S-wave problem (Section 7.8).

In order to investigate the difference in scattering patterns between acoustic and *SH* waves, we first resolve the effect of the density perturbation on scattering. From (7.8), μ can be expressed in terms of β as μ=$\beta^2\rho$=$\beta_0^2\rho_0(1+\xi)^2(1+K\xi)$. That is, when given magnitudes of velocity and density perturbation are considered, μ has a magnitude multiplication by $(1+\xi)^2(1+K\xi)$ and this enhances the fractional perturbation by relatively reducing small perturbations and increasing large perturbations. The terms in the *SH* wave equations require multiplication of the displacement by the enhanced physical parameter and a spatial differentiation (e.g., $\partial_x(\mu\partial_x u_y)$). The differentiated scattered wavefield is modulated by the density with a scaling by $(1+K\xi)$. However, the implementation of the density perturbation does not look to cause the systematic pattern. Time responses in random media with no density perturbation (K=0) still display the systematic pattern (see, Fig. 8.6) and, moreover, the waveforms in coda are close to those with the density perturbation (see, Fig. 8.7). But, primary waves for media without density perturbation display larger amplitudes than those for media with density perturbation. That is, the implementation of the density perturbation enhances physical perturbation and, as a result, introduces additional energy loss during scattering. But the scattering paths and patterns appear to be conserved regardless of the density perturbation rate.

On the other hand, the acoustic waves have only a velocity perturbation like the *SH* waves without density perturbation. The velocity term has an magnitude multiplication of $(1+\xi)^2$, and this relative enhancement of the fractional perturbation is identical to *SH* waves without density perturbation. However, a direct multiplication is made to the differentiated wavefield in the acoustic wave equation (e.g., $c^2\partial_x^2 P$), and therefore time responses do not include the effects of the physical parameter gradients in spatial domain. So, comparisons between the time responses of acoustic and *SH* waves do not display any distinctly correlated features (see, Fig. 8.8).

The origin of the systematic patterns in the *SH* coda can be explained by the shear-wave radiation pattern. Acoustic waves have isotropic radiation pattern at a point heterogeneity, but *SH* waves, polarized in the tangential direction, have polarized radiation pattern relative to the incident direction. Therefore, scattered waves from heterogeneities laid parallel (or close to parallel) to the *SH* incident direction are enhanced, and scattered waves from heterogeneities laid perpendicular to the incident direction are suppressed. The preferential scattering direction is reinforced

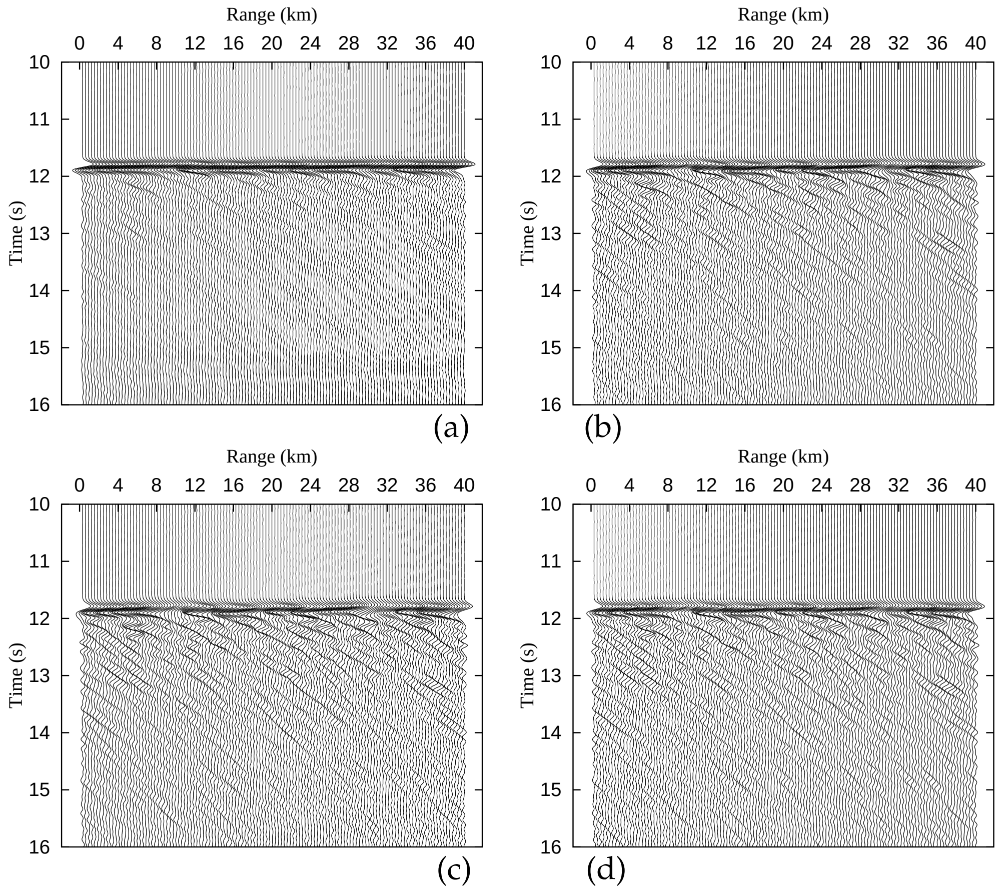

Fig. 8.6. Time responses in stochastic random media with correlation distance (a) 114.3 m when the density perturbation is suppressed (i.e., K=0): (a) von Karman medium with ν=0.05, (b) von Karman medium with ν=0.25, (c) exponential medium and (d) Gaussian medium. Wavefields in the time responses are so close to those in random media with density perturbation (see, Figs. 8.2, 8.3, 8.4, 8.5).

as the primary wavefront moves in the medium, and becomes more pronounced with increasing distance (see, Figs. 8.2, 8.3, 8.4, 8.5). In contrast, acoustic scattering waves develop in all directions homogeneously and thus are shown to be distributed homogeneously in time responses.

The appearance of the P and S coda in Sections 7.6 and 7.8 can be explained similarly. The primary P waves which are vertically incident on the stochastic random media satisfy $u_x^0 = 0$ and $u_z^0 = e^{i(k_\alpha z - \omega t)}$ (see, (7.5)) and first-order scattered waves are developed from the terms $\lambda \partial_z u_z^0$ and $(\lambda + 2\mu)\partial_z u_z^0$ in σ_{xx} and σ_{zz}. Therefore, the combination of the two sources of scattered waves allows development of extensively random coda. Also, the P waves convey most energy in the radial direction and the energy is gradually reduced by transfer to the tangential direction. Thus, scattering waves from heterogeneities are distributed homogeneously as shown in the acoustic case. On the other hand, the

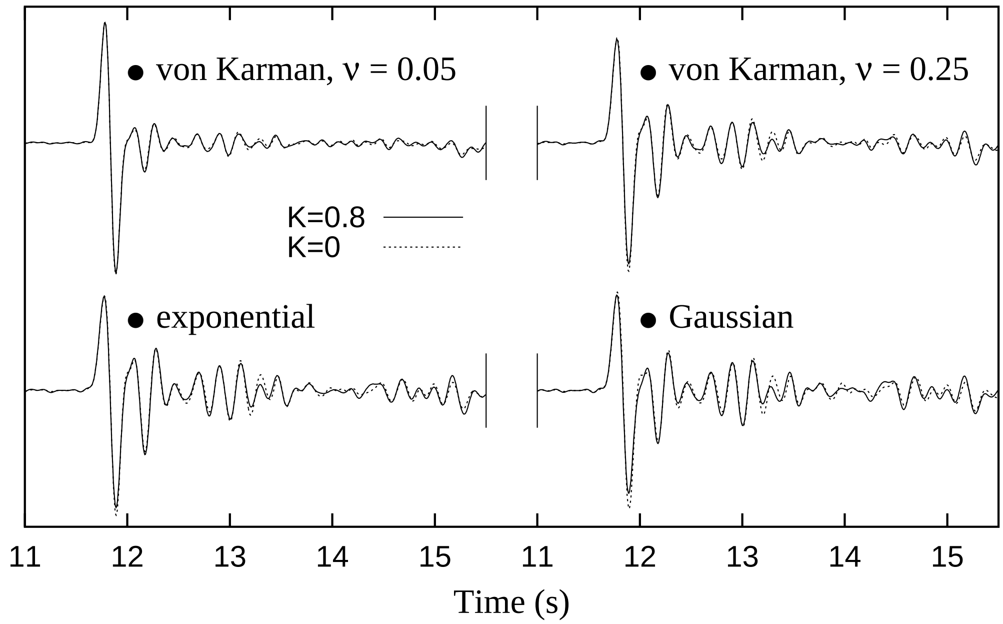

Fig. 8.7. Comparisons between *SH* time responses for stochastic random media with density perturbation K=0.8 and those without density perturbation (K=0) at the 20th receiver in Fig. 8.1. Waveforms of time responses are very close, but primary waves for the media without density perturbation display larger amplitudes than those with density perturbation.

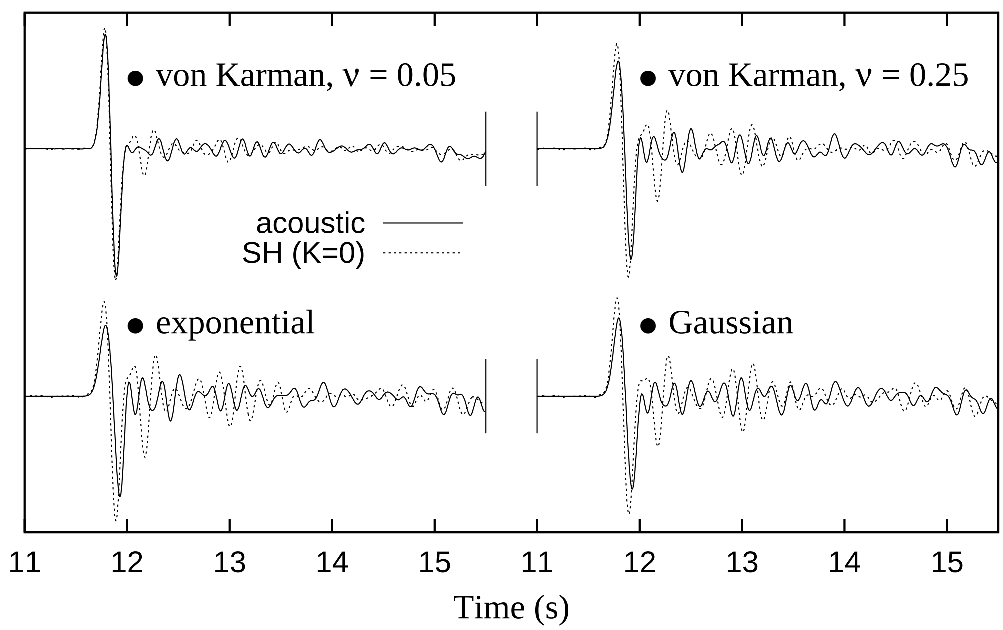

Fig. 8.8. Comparisons between acoustic and *SH* waveforms for stochastic random media with no density perturbation at the 20th receiver in Fig. 8.1. Although the reproduced random heterogeneities are same between the both media, the coda waves do not show any correlated features each other.

primary waves in the *S*-wave problem are written as $u_x^0 = e^{i(k_\beta z - \omega t)}$ and $u_z^0 = 0$ (see, (C.1)), and the first-order scattered waves develop from the term $\mu \partial_z u_x^0$ of σ_{xz}. In this case, the scattered waves develop from just one term and the spatial variation of the perturbation is involved. Moreover, *SV* waves share the radiation pattern with *SH* waves. So, we can expect a coherent scattering wavetrain in the stochastic random media like the *SH*-wave case.

In general, coda waves increase with the correlation distance (a) of heterogeneities in media, but decrease after about $k_c a > 1$ where k_c is the wavenumber for the dominant frequency of incident waves. Also, the phase shift of primary waves increases with the correlation distance, but acoustic waves display a much stronger variation compared to *SH* waves.

8.4 Scattering attenuation

For comparisons of the scattering attenuation rates between acoustic and *SH* waves, we apply constant time windows for processing and the spectral amplitudes of the primary waves recorded in the stochastic random media are shown in Figs. 8.9, 8.10, 8.11 and 8.12. In general, acoustic waves display more energy dissipation by scattering than *SH* waves. Also, the discrepancy between the spectral amplitudes of acoustic and *SH* waves increases with the Hurst number (ν) in the von Karman type media.

The theoretical scattering attenuation curves for acoustic (8.3) and *SH* waves (8.5) display a similar trend for ka but some magnitude differences are expected in the attenuation rates between acoustic and *SH* waves for specific minimum scattering angle (see, Fig. 8.13). Also, the *SH* theoretical curves with minimum scattering angle ($\theta_{\min}$) 60° and 90° have nearly equivalent values unlike the acoustic ones and those of elastic waves in Chapter 7. This means that *SH* scattering waves propagate dominantly to around the incidence direction.

Fig. 8.13 exhibits comparisons between reference attenuation curves and numerical attenuation rates estimated from the time responses. The reference curves for acoustic waves are drawn in solid lines and those for *SH* waves in broken lines. The numerical attenuation rates of acoustic waves are represented by open circles and squares, and those of *SH* by filled ones. As expected in the comparisons of spectral amplitudes, the measured attenuation rates of both problems are comparable at low ka (<1) but those of acoustic waves display more energy loss than *SH* waves at high normalized wavenumber ($ka > 1$). The appearance of a large difference between the numerical attenuation rates at low ka (<1) in von Karman media with ν=0.05 looks to be related to numerical errors induced during the evaluation of the attenuation rates (e.g., the interpolation process

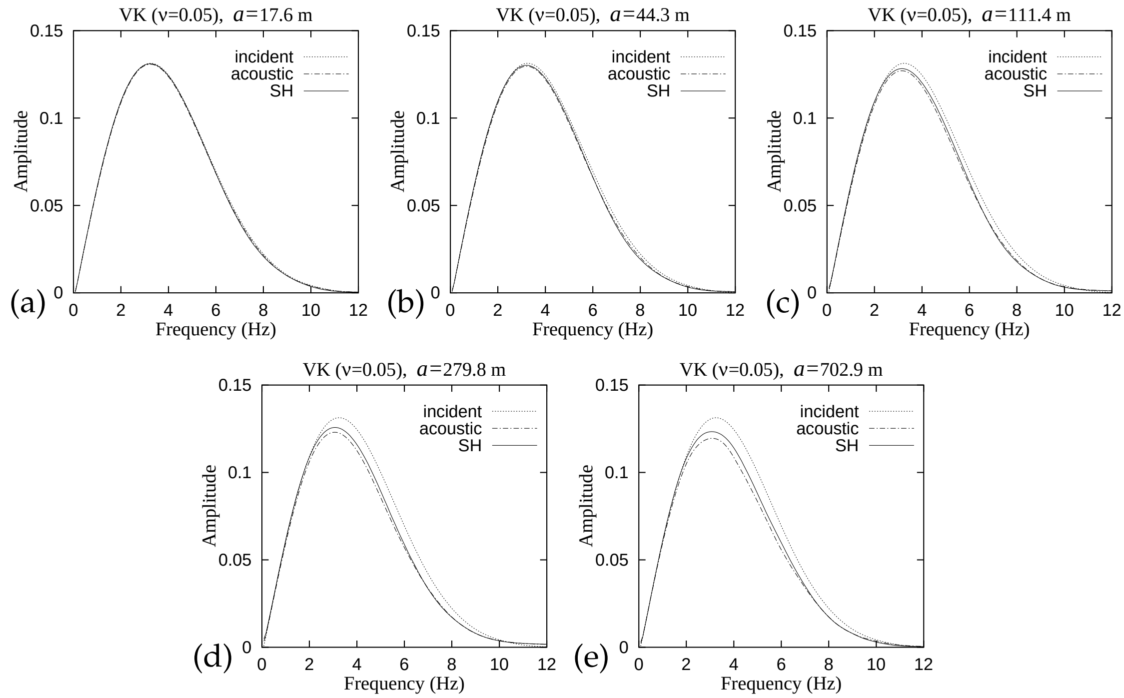

Fig. 8.9. Comparisons of spectral amplitudes of acoustic and *SH* waves in von Karman media with Hurst number (ν) 0.05 and correlation distance (a) for stochastic heterogeneities (a) 17.6 m, (b) 44.3 m, (c) 114.3 m, (d) 279.8 m, and (e) 702.9 m. Spectral amplitudes of the incident waves are provided for a reference.

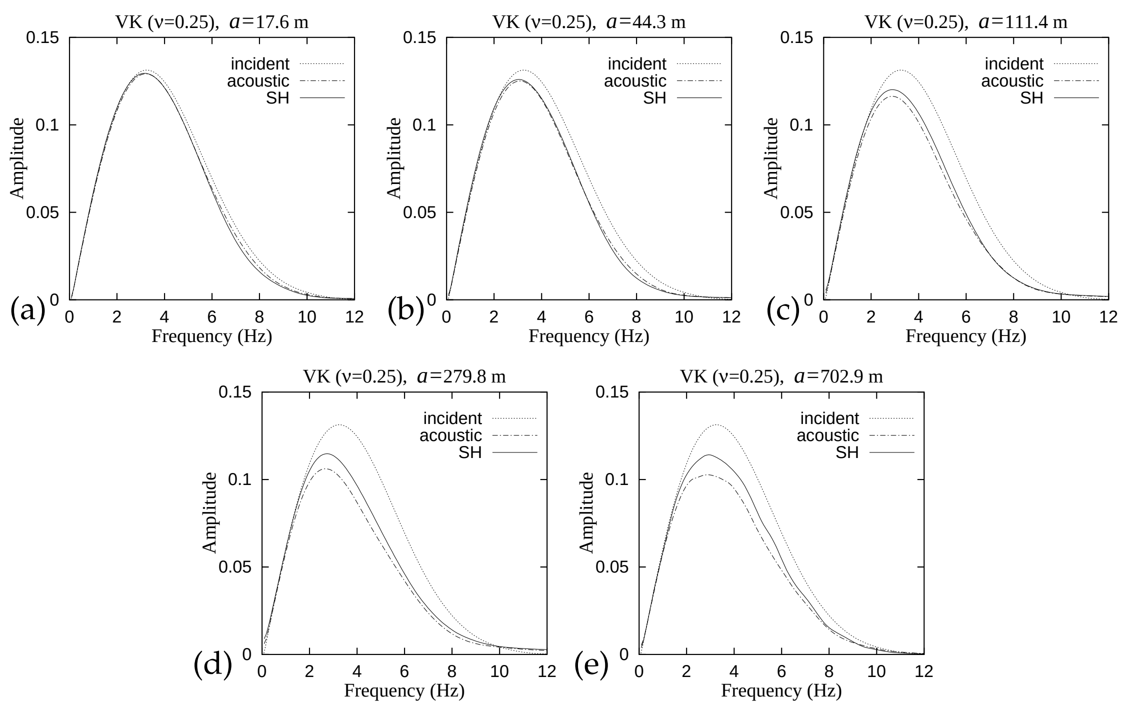

Fig. 8.10. Comparisons of spectral amplitudes of acoustic and *SH* waves in von Karman media with Hurst number (ν) 0.25 and correlation distance (a) for stochastic heterogeneities (a) 17.6 m, (b) 44.3 m, (c) 114.3 m, (d) 279.8 m, and (e) 702.9 m.

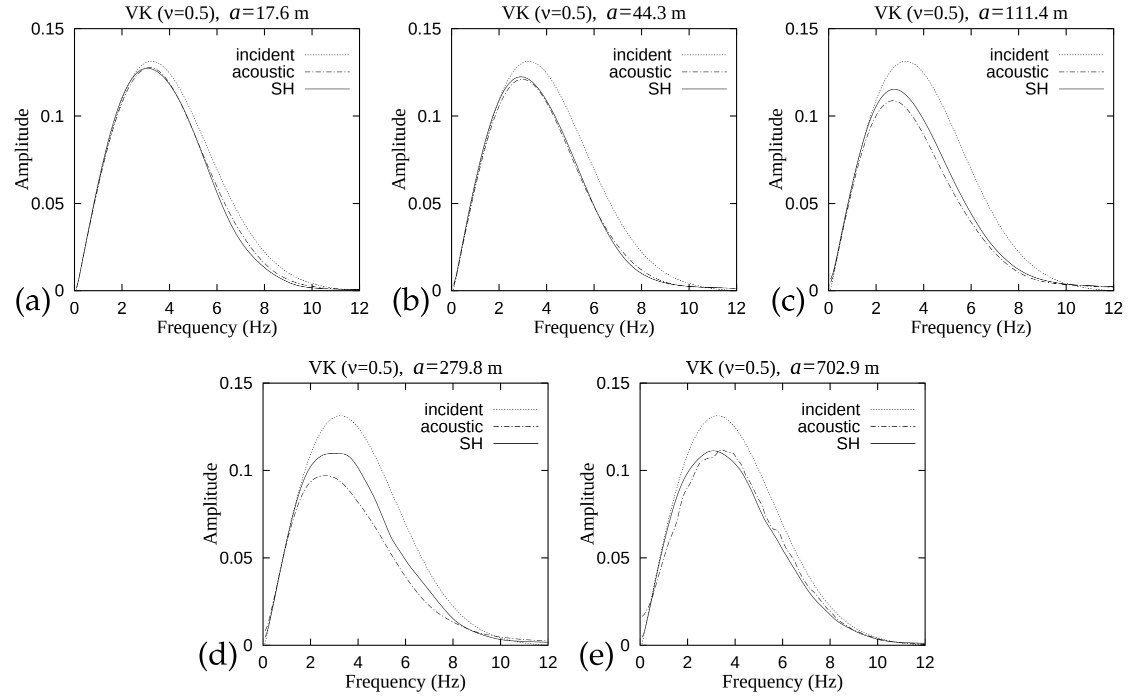

Fig. 8.11. Comparisons of spectral amplitudes of acoustic and *SH* waves in the exponential media with correlation distance (a) for stochastic heterogeneities (a) 17.6 m, (b) 44.3 m, (c) 114.3 m, (d) 279.8 m, and (e) 702.9 m.

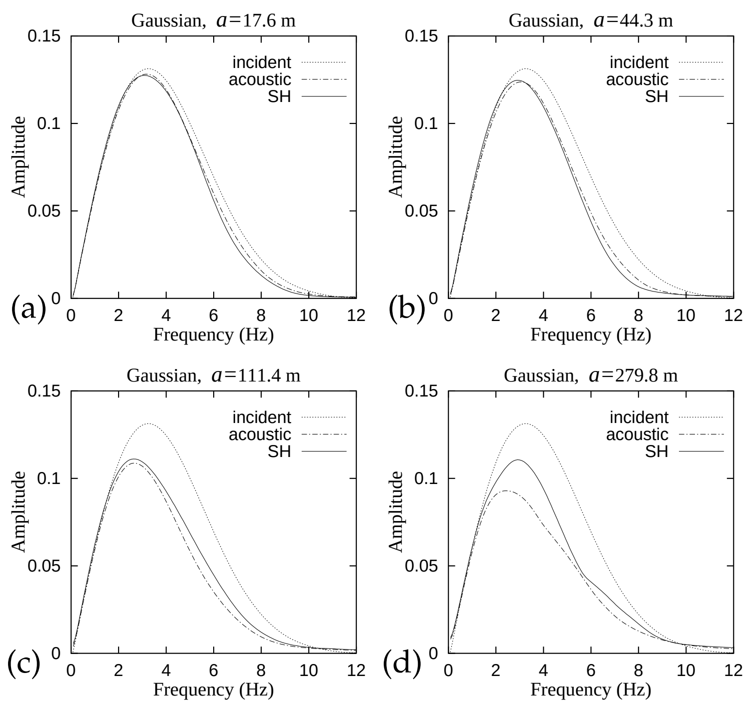

Fig. 8.12. Comparisons of spectral amplitudes of acoustic and *SH* waves in Gaussian media with correlation distance (a) for stochastic heterogeneities (a) 17.6 m, (b) 44.3 m, (c) 114.3 m, (d) 279.8 m, and (e) 702.9 m.

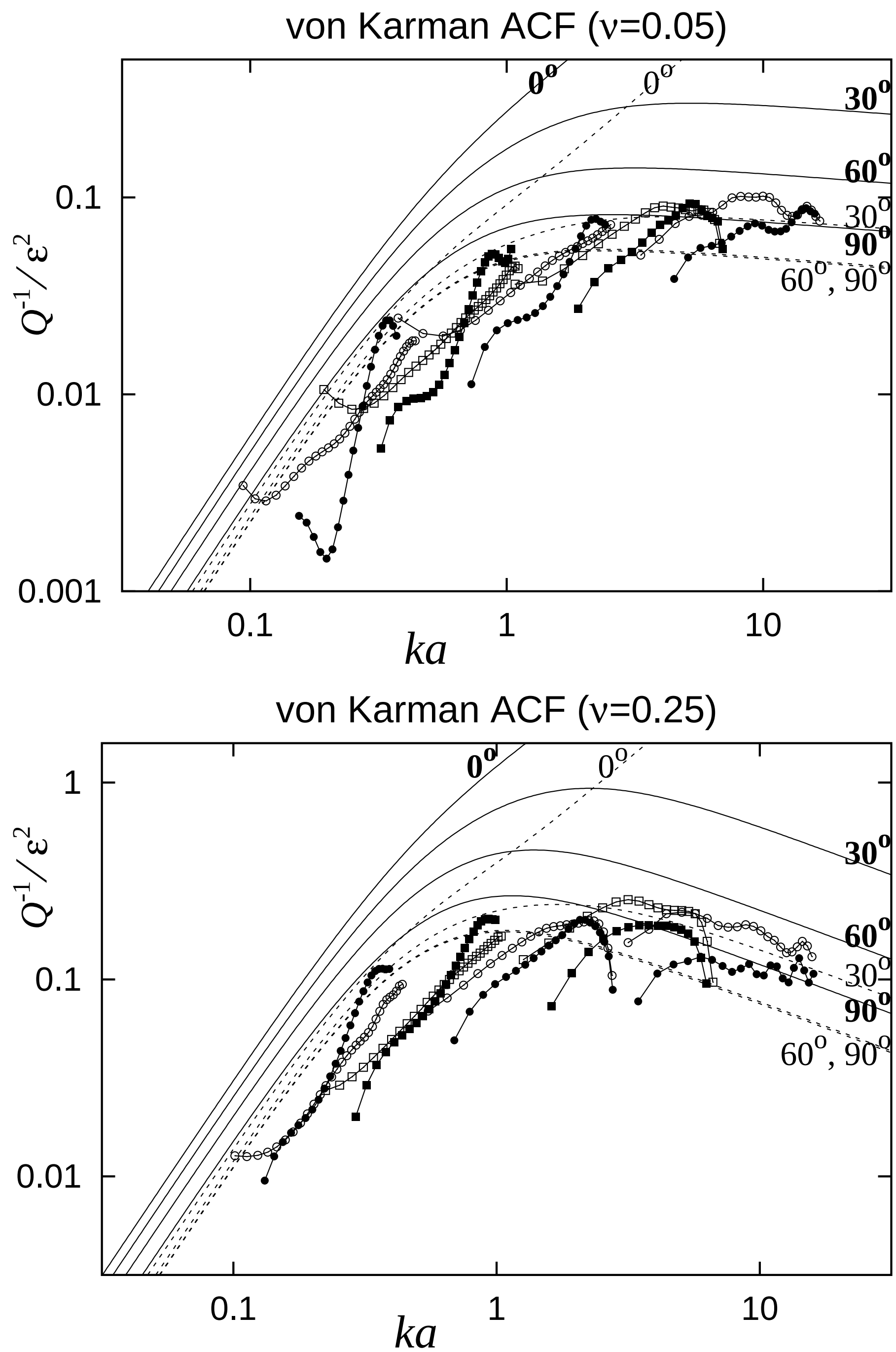

Fig. 8.13. Comparisons between numerical attenuation rates and theoretical variation for stochastic random media. The numerical results from *SH* modelling are represented with open circles and squares and those from acoustic modelling with filled ones. The solid lines and the bold labels represent for theoretical curves for the acoustic waves, and the broken lines and the normal labels for the *SH* waves. Attenuation rates of acoustic and *SH* waves are comparable each other, but acoustic waves have more energy loss at large normalized wavenumber (ka) than *SH* waves. This figure continues at the following page.

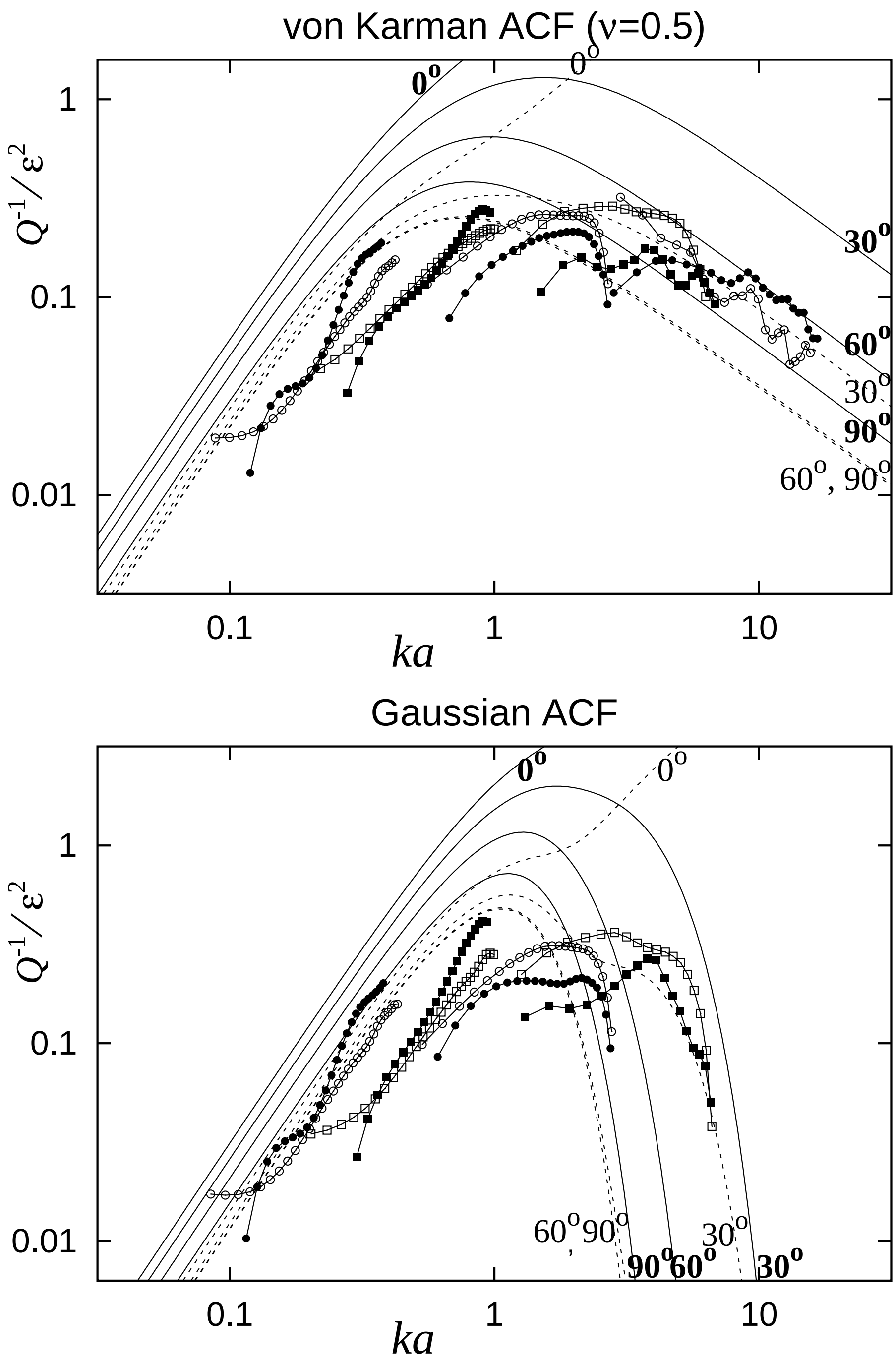

Fig. 8.13. *continued.*

to match the frequency interval of time responses). Note that the magnitudes of the numerical attenuation rates are rather small compared to the others and the difference in spectral amplitudes between acoustic and *SH* waves is not noticeable (see, Fig. 8.9(a)).

The numerical attenuation rates of acoustic waves lie in a range between reference curves with $\theta_{\min}$=60 and 90° at high ka (>1), but lie below the 90° reference curve at low

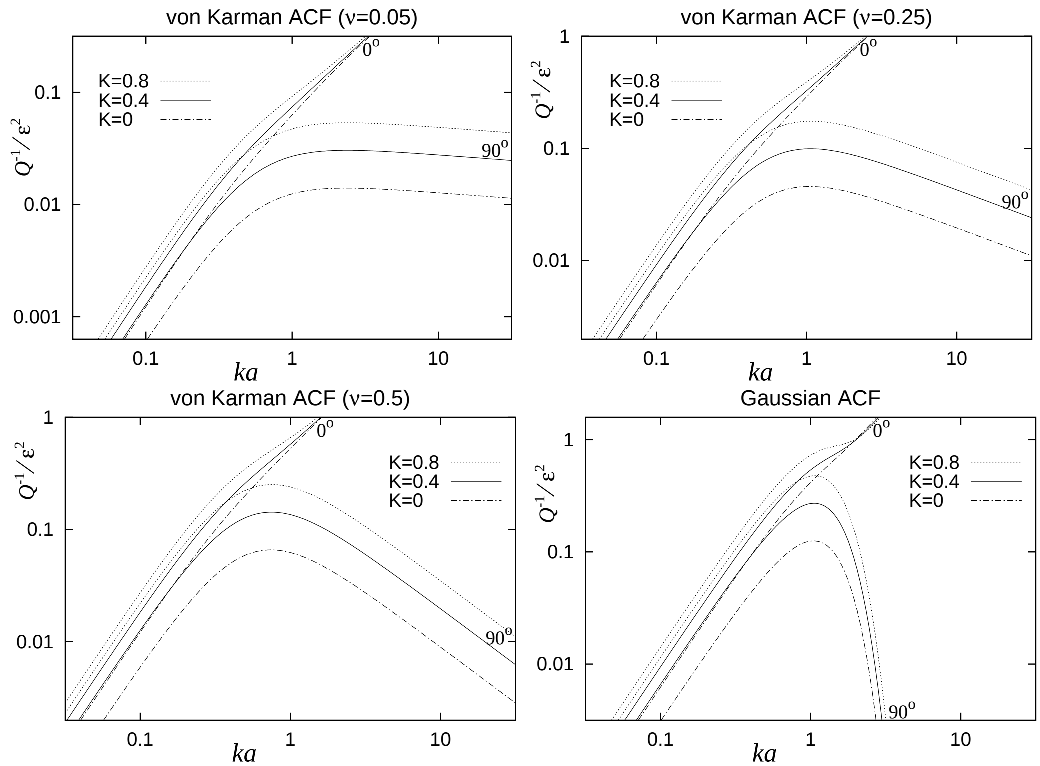

Fig. 8.14. Comparisons of the theoretical *SH* scattering attenuation variations with three different magnitudes of the density perturbation, 0, 4 and 8 % (i.e., K=0, 0.4, 0.8), for minimum scattering angles ($\theta_{\min}$) 0° and 90°. The attenuation rates are proportional to the density perturbation, but the trend in curves is conserved.

ka (<1). Similar patterns have been shown in the *P*-wave attenuation (see, Fig. 7.15). Also, the scattering attenuation rates of *SH* waves lie in the region of the reference curves with $\theta_{\min}$=30-60°.

Using the theoretical attenuation expression for *SH* waves, the effects of the density perturbation on the scattering attenuation can be deduced. We compute theoretical attenuation curves for two additional cases with 0 and 4 % density perturbation (i.e., K=0, 0.4). Fig. 8.14 shows comparisons between the attenuation curves with K=0, 0.4, 0.8 when $\theta_{\min}$=0, 90°. Also, the detailed variation of attenuation rates with $\theta_{\min}$ is shown in Fig. 8.15 for K=0 and 0.4. As expected in Fig. 8.7, the introduction of the density perturbation raises additional energy dissipation and the energy loss is proportional to the density perturbation rate. The trends of the attenuation variation for K=0 and 0.4 are similar to that for K=0.8. However, Gaussian random media have different curve slopes for the density perturbation rate at large ka (see, Fig. 8.15). This indicates that forward scattering waves become stronger with the density perturbation (K) in Gaussian media

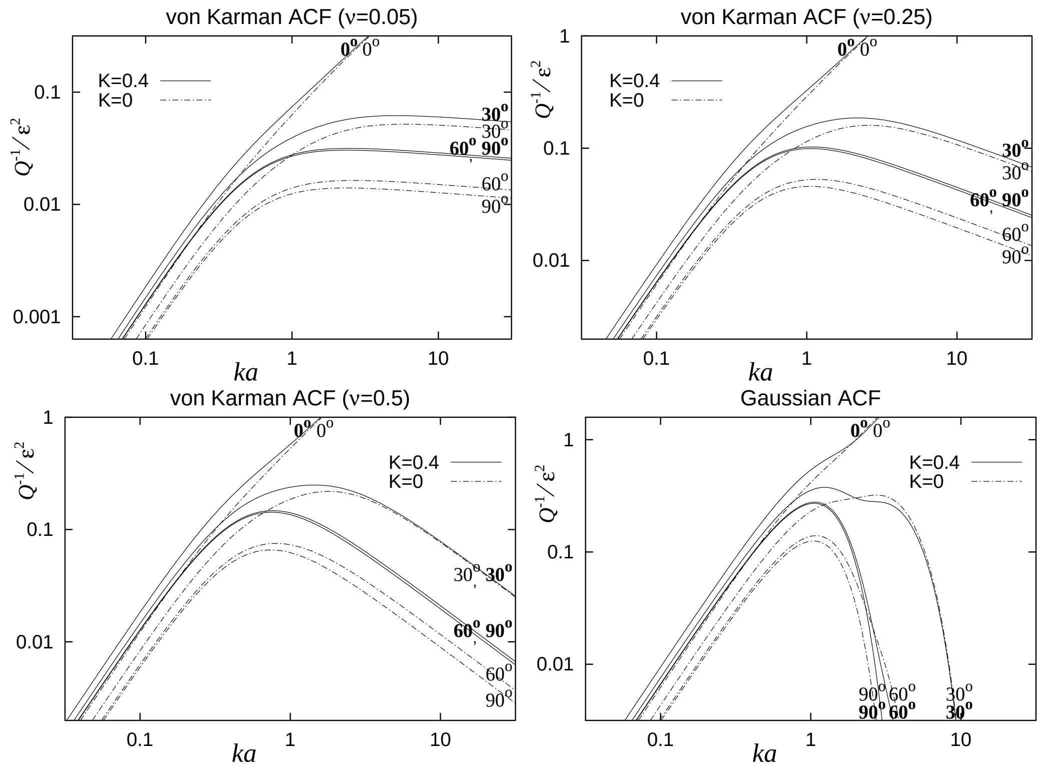

Fig. 8.15. Theoretical *SH* attenuation variations for K=0 and 0.4. The bold labels represent for the case K=0.4 and the normal labels for the case K=0.

and also energy loss by scattering at large ka (>1) increases with the reduction of the density perturbation.

The attenuation rates increase with K and the density perturbation controls the magnitude of scattering and the entire energy dissipation. Further, as K decreases, the variation of attenuation rates for a change of $\theta_{\min}$ gets larger (see, Fig. 8.15). As a result, when K=0, differences between the attenuation curves with θ_{min}=60° and 90° become noticeable. That is, the perturbation without density variation (i.e., K=0) allows much random directional scattering.

8.5 Discussion and conclusions

We have compared scattering patterns and attenuation rates of acoustic and *SH* waves in stochastic random media. Although the same magnitude of velocity perturbation is considered in both acoustic- and *SH*-wave modelling, the resultant scattering patterns and attenuation rates have somewhat different behaviour. The differences becomes much larger when large-scale heterogeneities are implemented. The coda waves in the *SH* time responses show a characteristic scattering coherency in the wavetrains. On the contrary, the coda waves in acoustic time responses display a relatively homogeneous distribution of scattered waves.

The coherency texture in *SH* coda is developed by the radiation pattern of shear waves and increases with the scale of heterogeneities. A similar pattern is also observed in *SV* time responses. The implementation of the density perturbation introduces additional energy loss, but waveforms are likely conserved regardless of the density perturbation. The density perturbation also raises the concentration of perturbation in specific physical parameters and, resultantly, enhances forward scattering.

The energy losses by scattering at small normalized wavenumber (ka) are nearly identical between acoustic and *SH* waves. But, the energy loss in acoustic waves increases rapidly relative to that of *SH* waves at large normalized wavenumber. The minimum scattering angles determined for acoustic waves are similar to those for elastic waves (θ_{min}=60-90°), but *SH* waves have smaller angles (θ_{min}=30-60°). That is, forward scattering is dominant in *SH* waves and especially the scattered waves with large wavelengths are concentrated inside a small cone of angles from the incident direction.

9

Scattering in media with a random distribution of fluid-filled cavities

9.1 Introduction

Since Chernov (1960) introduced a stochastic representation technique employing smooth variation in perturbation for random heterogeneities in the earth, many studies have implemented stochastic random media for the investigation of scattering of elastic or acoustic waves (e.g. Frankel & Clayton, 1987; Roth & Korn, 1993; Sato & Fehler, 1998). We also have studied scattering attenuation variation of acoustic and elastic waves in previous chapters (Chapters 7 and 8). However, some studies (e.g., Yomogida & Benites, 1995; Kawahara & Yamashita, 1992) suggested an alternative way to represent a random medium via a set of randomly distributed homogeneous heterogeneities with sharp physical impedance to the background, for examples, crack or cavities.

Theoretical scattering attenuation rates for fracture zones with randomly distributed cracks (fluid filled or unfilled) have been formulated by Kawahara & Yamashita (1992) by using the representation theorem for displacement discontinuity across the crack and the mean wave formalism (e.g., Hudson, 1980) considering the average wavefield over the random media. The cracks are considered to be thin compared to both the length of the cracks and the wavelength of incident waves. Murai *et al.* (1995) have compared the theoretical variations with numerical results for 2-D *SH* waves, and found that attenuation rates depend on the state of the crack surfaces (e.g., viscous, dry) and are inversely proportional to wavenumber at large wavenumbers.

However, only numerical studies have been made for scattering and attenuation in media with a random distribution of cavities (Benites *et al.*, 1992; Yomogida & Benites, 1995), and thus the numerical results are compared with the theoretical attenuation variations for scalar waves in stochastic random media (e.g., Wu, 1982). However, it is not certain if the scattering pattern in the stochastic random media is identical or even comparable to that for media with randomly distributed cavities. Also, it is unclear which term or parameter corresponds to the standard deviation of the perturbations of the physical parameters in the theoretical attenuation expression for stochastic random media. Therefore, it is necessary to derive a theoretical attenuation expression for media with a random distribution of cavities for a correct investigation.

For numerical simulation in random media, many numerical techniques have been implemented. For stochastic random media, finite difference methods (FDM) have been widely used due to the simplicity in designing numerical models and codes (Frankel & Clayton, 1987; Roth & Korn, 1993). But, the accuracy limitation in numerical differentiation prevent the FDM from treating small heterogeneities without the introduction of a dense grid system. On the other hand, Nagano (1998) applied the Haskell's matrix method (Haskell, 1953) to analyze the crack waves trapped inside a single fracture that is layered horizontally between low velocity layers. However, this class of method is limited to simplified layered-structure problems, and thus it is hard to consider micro-structures properly. Also, there has been an attempt to use an indirect boundary element method (IBEM) for modelling of elastic waves in single crack media (Pointer *et al.*, 1998), in which variations of diffraction and scattering have been studied with change of the crack length, the crack opening size and the internal materials. Carcione (1998) has implemented a pseudospectral Chebyshev method for modelling of elastic waves in a medium with a single crack. However, the technique inhibits incorporation of heterogeneities in various sizes and shapes without an interpolation procedure.

In order to overcome the limitations in representing complex shapes of cracks or cavities, several alternative numerical techniques have been introduced. For 2-D *SH*-wave modelling in fracture zones with identical cracks aligned parallel, Murai *et al.* (1995) have computed total wavefields using the representation theorem (Pao & Mow, 1973) as a function of wavenumber. Liu *et al.* (1997) have investigated diffraction and scattering of 3-D elastic waves in media with a single crack using the Kirchhoff approximation technique that requires a small computational cost compared to classical grid-based methods. Also, boundary integral methods (Coutant, 1989; Yomogida & Benites, 2002; Yomogida & Benites, 1995) have been implemented for modelling of wave propagation in media with random cracks (or cavities) and for the estimation of scattering attenuation.

These semi-analytic techniques allow accurate modelling in media with cavities of complex shape, but it is hard to expand the technique to problems with heterogeneous background media (random physical perturbation or layered structure) due to the difficulty in obtaining the Green's function for the media. Moreover, when the shapes of cracks or cavities are complicated, the computational cost increases significantly. Also, when the cracks (or cavities) are filled with elastic or fluid materials, additional computational efforts are required to include the effects of the internal crack (or cavity) waves properly.

We implement the wavelet-based method, which allows consideration of media composed of small heterogeneities with high impedance. We measure attenuation rates of elastic waves in random fluid-filled cavity media which are numerically challenging, and investigate effects of size of the cavity to the attenuation rates.

In order to derive theoretical attenuation expressions for random cavity media, we consider the analytic wavefields in the media (Pao & Mow, 1973). We compare the theoretical attenuation variations with numerical results estimated from time responses by the wavelet modelling. The autocorrelation function for the cavity distribution is determined empirically by a least square fitting. Differences in theoretical attenuation variations between stochastic random media and random cavity media are discussed, and characteristics of the both media are compared.

9.2 Waveform in a medium with a fluid-filled cavity

We have investigated the scattering of elastic waves in stochastic random media in Chapters 7 and 8. As an alternative representation of random media, media composed of randomly distributed homogeneous heterogeneities with high impedance to the backgrounds such as cracks and cavities, have been considered. We consider media with fluid-filled cavities and investigate differences in wavefields and scattering between stochastic random media and random cavity media.

We first simulate elastic wave propagation in medium with a fluid-filled circular cavity. The wave velocities in the background medium are 3.6 km/s for P waves and 2.06 km/s for S waves, and the density is 2.4 g/cm^3. The physical parameters of the material in the cavity are 1.8 km/s for P waves and 1.2 g/cm^3 for the density, but the shear wave velocity is zero. The radius of the cavity is 0.47 km. Plane P waves are incident in vertical direction from the bottom. Fig. 9.1 shows successive snapshots of the wavefield. The snapshot for t=2.0 s clearly displays the dimension of the cavity.

Diffracted coupled P and S waves are developed by the incident P waves at the boundary of the cavity, and only P waves are transmitted inside the cavity. The transmitted waves are multiply reflected inside the cavity and successive multi-order coupled reverse-transmitted waves follow the diffracted waves. The secondary phases are clearly displayed in the x-component snapshots where there is an absence of the

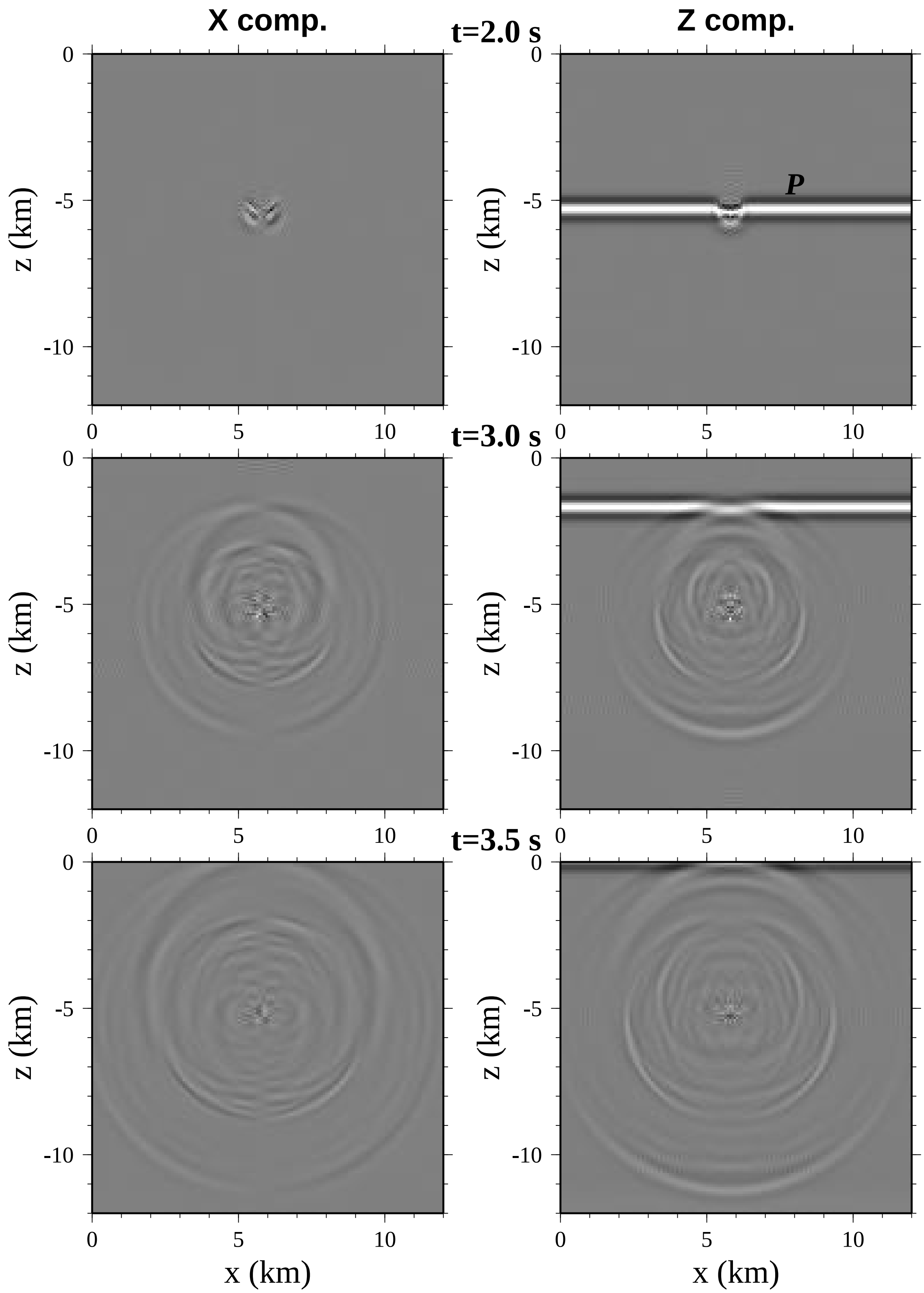

Fig. 9.1. Snapshots of displacement wavefield for a plane P wave incidence in a medium with a fluid-filled cavity at t=2.0, 3.0 and 3.5 s. Diffracted and reflected waves are successively generated.

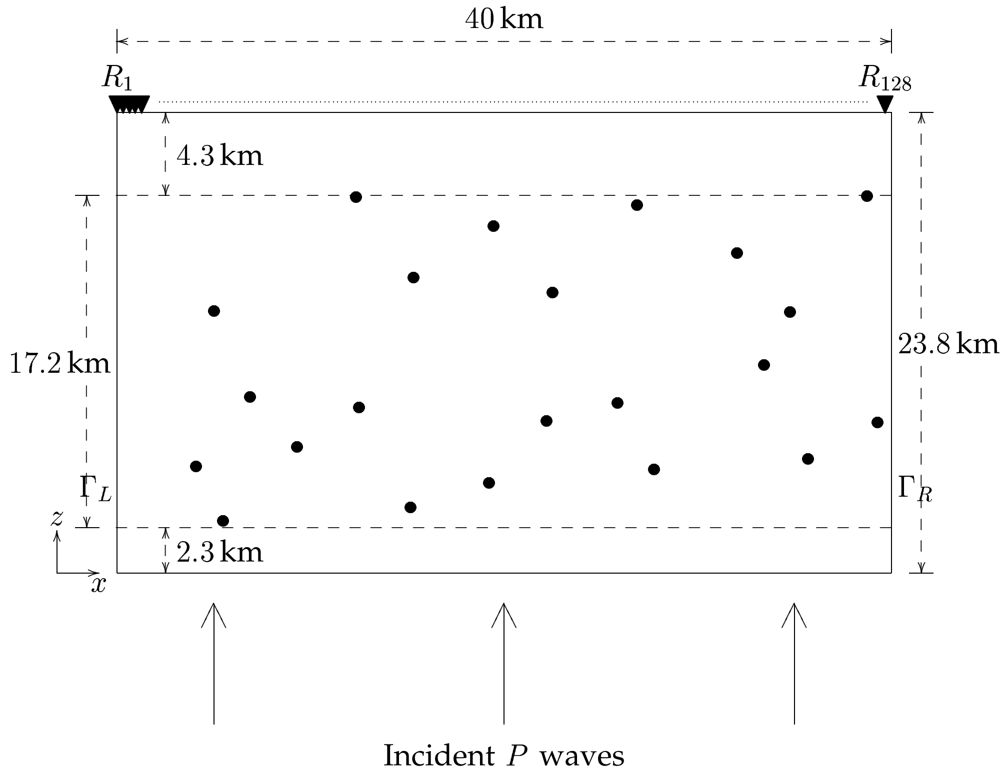

Fig. 9.2. Representation of a domain (40×23.8 km) with randomly distributed 22 fluid-filled cavities. The cavities are distributed in a confined region (40×17.2 km) and 128 receivers (R_j) are placed at the top boundary of the domain. For domains with 89 or 112 cavities, additional random positions are included to the given 22 cavity positions. Plane P waves are incident from the bottom of domain. Left and right boundaries are considered with periodic boundary conditions to satisfy with the condition for homogeneous distribution of cavity in a medium.

primary incident waves. Moreover, the plane waves undergo a phase healing as they propagate through the uniform medium, and we find that the amplitudes of the plane waves vary smoothly over a wide area (see, z-component snapshots for t=2.0 and 3.0 s). After a long time lapse, the internal interference of the fluid waves is still clearly shown (see, snapshot for t=3.5 s).

Scattering attenuation may be dependent on the number of the cavities inside a medium and also on the scale of cavities. In order to study the wavefield variation and the scattering attenuation, cavities are randomly distributed inside a specific cavity zone. The cavity positions are used consistently regardless of the change of cavity radius. Fig. 9.2 shows the distribution of 22 fluid-filled cavities in a homogeneous medium. Wave speeds in the medium are α_0=3.15 km/s and β_0=1.8 km/s, and the density is ρ_0=2.2 g/cm^3. Also, the P wave velocity (α_f) and the density (ρ_f) in the cavities are half of those in the back ground, and the shear wave velocity (β_f) is zero. When more

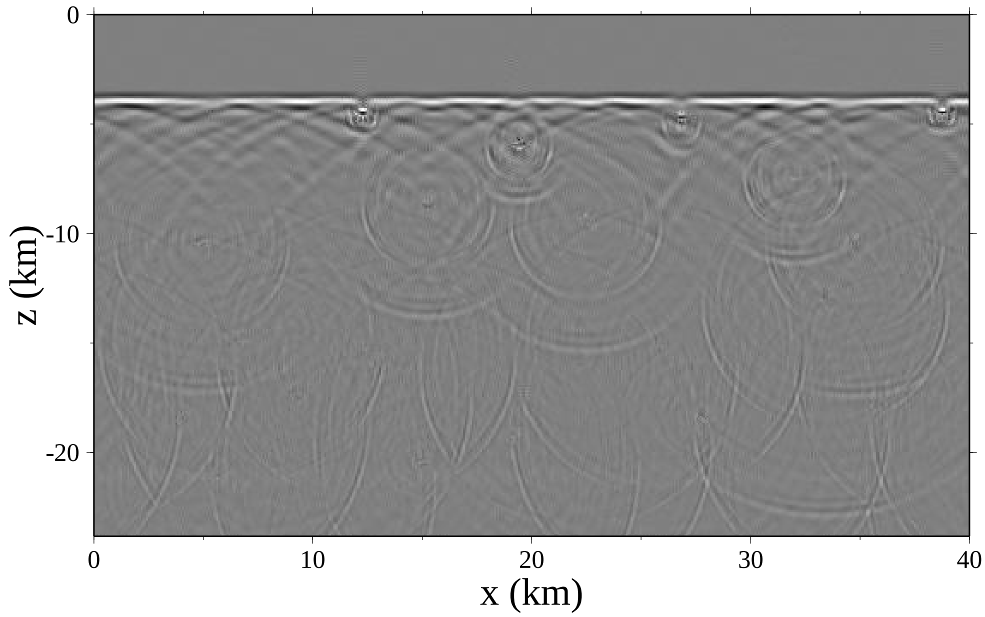

Fig. 9.3. Snapshot of displacement wavefield for a plane P wave incidence in a medium with 22 fluid-filled cavity at t=6.5 s. The radius of the cavities are 31.2 m.

cavities are considered in a medium, additional random positions are included. The cavity zone comprises 40 km-by-17.2 km in physical space. The size of the media is 40 km-by-23.8 km and the the grid step ($\delta x, \delta z$) is 78.1 m. 128 receivers are placed on the top of the media with constant interval 312.4 m. Two vertical artificial boundaries (Γ_R,Γ_L) are considered with periodic boundary conditions to satisfy with the condition for homogeneous distribution of cavities inside the medium and to include scattered waves from neighbours. Ricker wavelets with dominant frequency 4.5 Hz are used as the source time function of the incident plane P waves.

A snapshot of the displacement wavefield at t=6.5 s in a medium with 22 fluid-filled cavities with radius 31.2 m is shown in Fig. 9.3. Reflected or diffracted waves from the cavities follow after the primary plane P waves. Also, multi-order secondary waves develop continuously from the cavities.

The time responses show that the magnitudes of the scattered waves are dependent on the size and the number of cavities (see, Fig. 9.4). In general, with increase of the size and the number, the scattered waves become stronger. Also, as shown in Fig. 9.1, primary waves are recorded mainly on the z component regardless of the scale and the number of cavities. The wavefield pattern is different from that in stochastic random media with large scale of heterogeneities, where primary waves are recorded on both x and z components by the influence of refraction.

Also, the time responses for media with cavities show that the magnitude variations

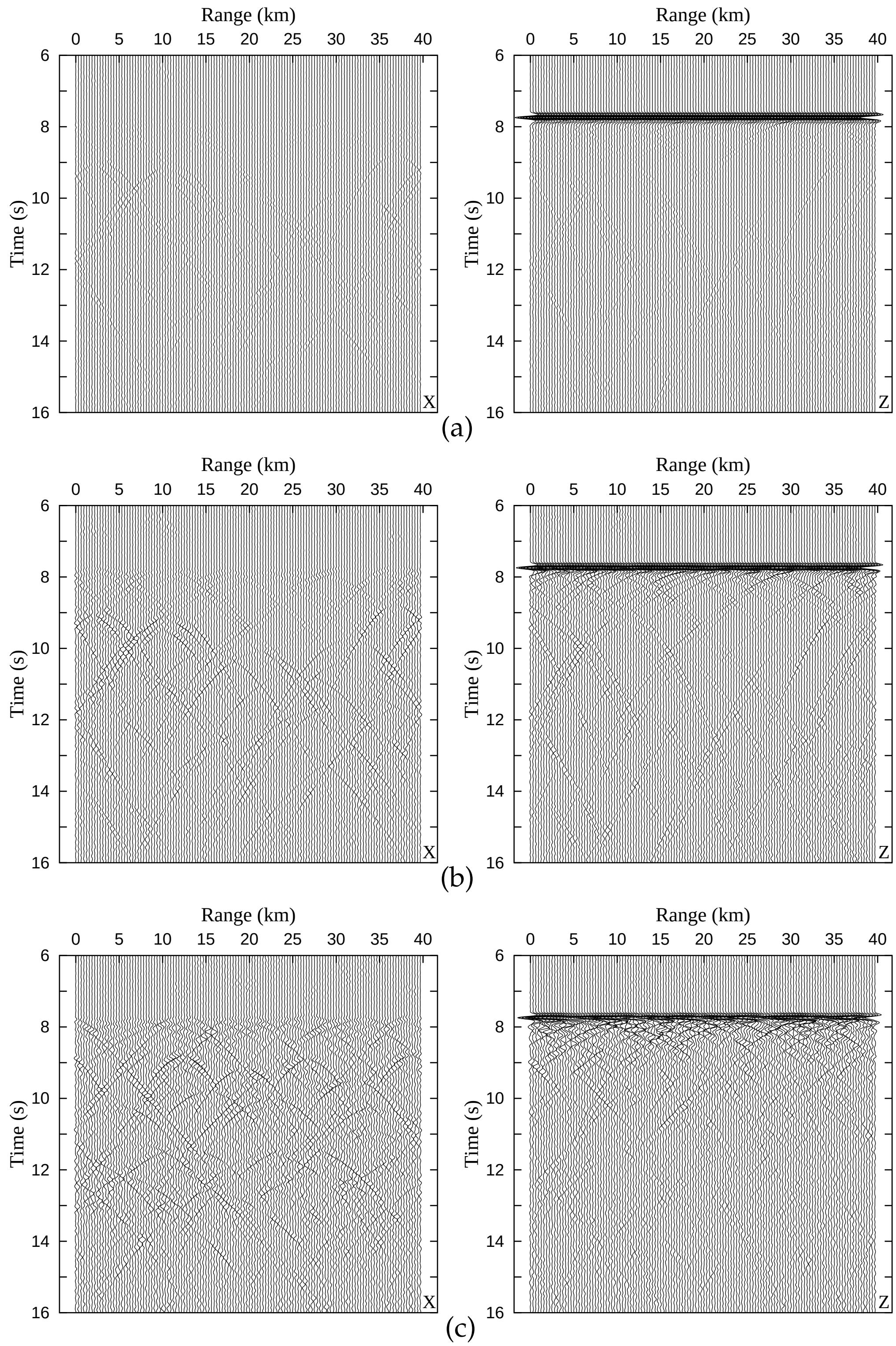

Fig. 9.4. Time responses recorded at the 112 receivers (R_j, j=1,2,. . .,128 in Fig. 9.2 in media composed of (a) 22 cavities with radius (a_c) 3.9 m, (b) 22 cavities with a_c=9.4 m and (c) 22 cavities with a_c=23.4 m. This figure continues at the following page.

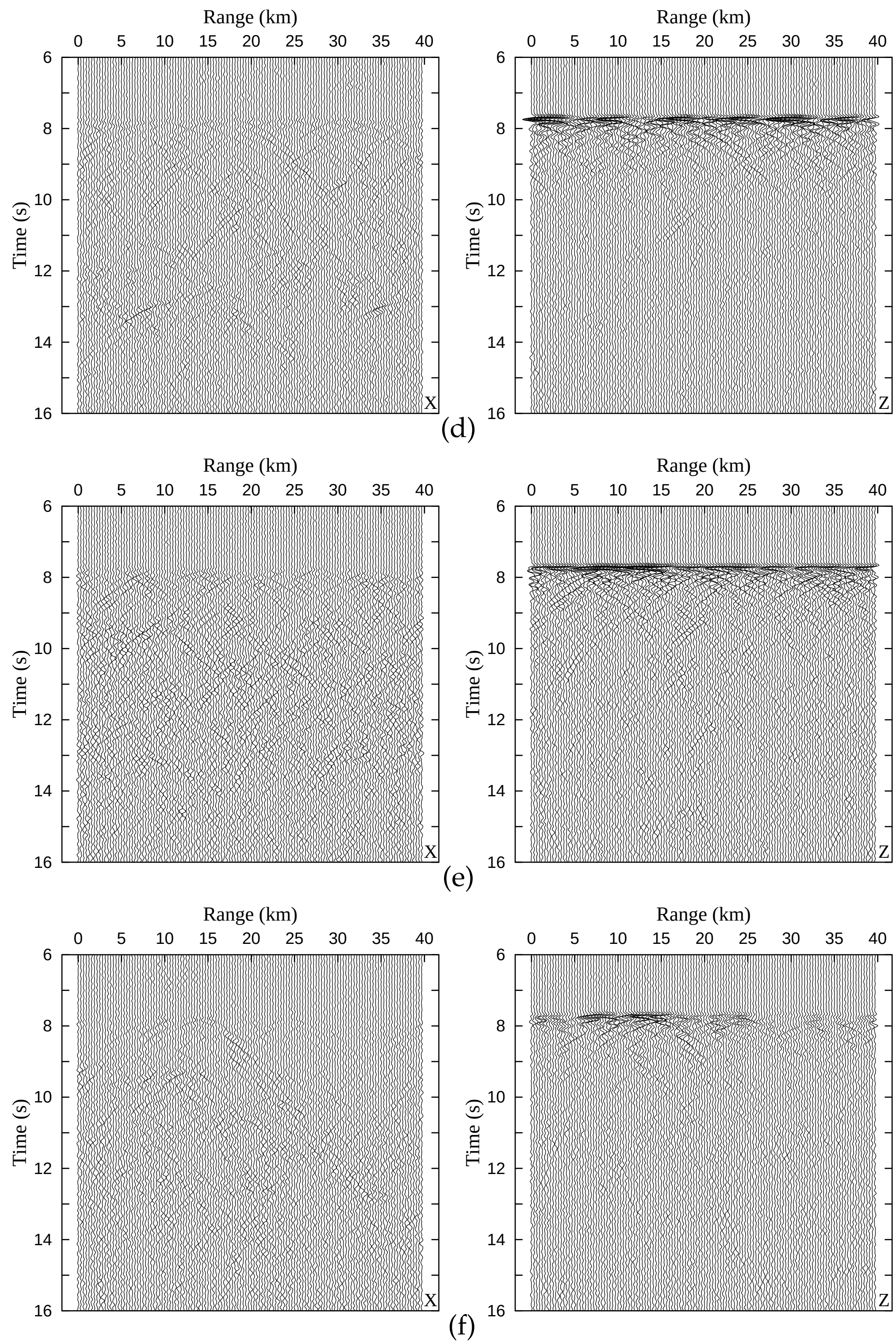

Fig. 9.4. (*continued*) Time responses recorded at the 112 receivers (R_j, j=1,2,. . .,128 in Fig. 9.2 in media composed of (d) 22 cavities with a_c=62.5 m, (e) 89 cavities with a_c=15.6 m, and (f) 112 cavities with a_c=31.2 m. With increase of the number and the radius of cavities, the energy loss of the incident waves increases. Also, scattered waves are distributed homogeneously at the receivers regardless of the scale and the number of the cavities.

in the primary waves do not directly affect the magnitude of the scattered waves (see, Fig. 9.4(f)), unlike the situation for stochastic random media. Such a pattern is related to the characteristics of the random cavity distribution. That is, a significant part of the incident waves are blocked by cavities which have a large physical impedance relative to the background media, and are reflected back (propagation backward). Back-scattered waves thus become stronger and multiply-scattered waves are distributed homogeneously in the domain. The travel time anomaly is not significant in the time responses even for media with a large size and number of cavities. Therefore, it appears that a travel time correction is not required for the determination of scattering attenuation for media with random cavities, unlike stochastic random media.

9.3 Theoretical scattering attenuation rate

We formulate an analytical expression for the scattering attenuation of P waves (Q^{-1}) in media with randomly distributed cavities. We consider a medium with a cavity with radius a_c and the medium is divided by two domains, Ω_0 (medium except the inclusion) and Ω_1 (inside the cavity). The P and S wave velocities in Ω_0 are α_0 and β_0, and those in Ω_1 are α_1 and β_1. When the center of cavity is located at the origin ($\mathbf{0}$) of a coordinate system, the displacement potential at x for vertically incident unit P waves (Φ^{i}) is given by (Pao & Mow, 1973; Liu *et al.*, 2000)

$$\Phi^{\mathrm{i}}(\mathbf{x};\mathbf{0}) = \exp\left[i(k_\alpha z - \omega t)\right] = \sum_{m=0}^{\infty} i^m \epsilon_m J_m(k_\alpha r)\cos(m\phi)\, e^{-i\omega t}, \tag{9.1}$$

where k_α is the wavenumber of the incident P waves with velocity α_0, J_m is a Bessel function of the first kind of order m and ϵ_m is a Neumann factor given by ϵ_0=1 and ϵ_j=2 for $j \geq 1$. The angle ϕ is measured from z axis and therefore x is given by ($r\sin\phi$, $r\cos\phi$).

The displacement potentials for scattering waves (Φ^{s}, Ψ^{s}) outside the inclusion region are given by

$$\begin{aligned}
\Phi^{\mathrm{s}}(\mathbf{x};\mathbf{0}) &= \sum_{m=0}^{\infty} i^m \epsilon_m\, A_m\, H_m^{(1)}(k_\alpha r)\cos(m\phi)\, e^{-i\omega t},\\
\Psi^{\mathrm{s}}(\mathbf{x};\mathbf{0}) &= \sum_{m=0}^{\infty} i^{m+1} \epsilon_m\, B_m\, H_m^{(1)}(k_\beta r)\sin(m\phi)\, e^{-i\omega t},
\end{aligned} \tag{9.2}$$

and the transmitted waves (Φ^{f}, Ψ^{f}) inside the inclusion are

$$\begin{aligned}
\Phi^{\mathrm{f}}(\mathbf{x};\mathbf{0}) &= \sum_{m=0}^{\infty} i^{m+1} \epsilon_m\, C_m\, J_m^{(1)}(k_{\alpha_2} r)\cos(m\phi)\, e^{-i\omega t},\\
\Psi^{\mathrm{f}}(\mathbf{x};\mathbf{0}) &= \sum_{m=0}^{\infty} i^{m+1} \epsilon_m\, D_m\, J_m^{(1)}(k_{\beta_2} r)\sin(m\phi)\, e^{-i\omega t},
\end{aligned} \tag{9.3}$$

where k_β is the wavenumber of S waves, $H_m^{(1)}$ is a Hankel function of the first kind of order m, and A_m, B_m, C_m and D_m are unknown complex-value constants given by

$$A_m = -\frac{K_1(m)}{K_0(m)}, \quad B_m = -\frac{2}{\pi}\frac{K_2(m)}{K_0(m)}, \quad C_m = -\frac{2}{\pi}\frac{K_3(m)}{K_0(m)}, \quad D_m = -\frac{2}{\pi}\frac{K_4(m)}{K_0(m)}, \tag{9.4}$$

and the K_j (j=0,1,2,3,4) are determined by the boundary conditions of the inclusion. The boundary conditions (continuity of displacement, continuity of stress at the boundary) are varied following the material of the inclusion.

The displacement and the stress components can be represented in terms of potentials by

$$\begin{aligned}
u_r^j &= \frac{\partial \Phi^j}{\partial r} + \frac{1}{r}\frac{\partial \Psi^j}{\partial \theta}, \qquad u_\theta^j = \frac{1}{r}\frac{\partial \Phi^j}{\partial \theta} - \frac{\partial \Psi^j}{\partial r},\\
\sigma_{rr}^j &= (\lambda+2\mu)\frac{\partial^2 \Phi^j}{\partial r^2} + \frac{\lambda}{r}\frac{\partial \Phi^j}{\partial r} + \frac{\lambda}{r^2}\frac{\partial^2 \Phi^j}{\partial \theta^2} - \frac{2\mu}{r^2}\frac{\partial \Psi^j}{\partial \theta} + \frac{2\mu}{r}\frac{\partial^2 \Psi^j}{\partial r \partial \theta},\\
\sigma_{\theta\theta}^j &= \frac{\lambda+2\mu}{r^2}\frac{\partial^2 \Phi^j}{\partial \theta^2} + \lambda\frac{\partial^2 \Phi^j}{\partial r^2} + \frac{\lambda+2\mu}{r}\frac{\partial \Phi^j}{\partial r} - \frac{2\mu}{r}\frac{\partial^2 \Psi^j}{\partial r \partial \theta} + \frac{2\mu}{r^2}\frac{\partial \Psi^j}{\partial \theta},\\
\sigma_{r\theta}^j &= \frac{2\mu}{r}\frac{\partial^2 \Phi^j}{\partial r \partial \theta} - \frac{2\mu}{r^2}\frac{\partial \Phi^j}{\partial \theta} + \frac{\mu}{r^2}\frac{\partial^2 \Psi^j}{\partial \theta^2} - \mu\frac{\partial^2 \Psi^j}{\partial r^2} + \frac{\mu}{r}\frac{\partial \Psi^j}{\partial r},
\end{aligned} \tag{9.5}$$

where j=0,1 which denotes the domain (i.e., Ω_0, Ω_1). Therefore, the potential wavefield in domain Ω_0 (Φ^0) can be expressed by the sum of the incident wave potential and scattered (or refracted) wave potential ($\Phi^{\mathrm{i}} + \Phi^{\mathrm{s}}$).

Using the relationships $i^{-m}J_{-m}(x) = i^m J_m(x)$ and $i^{-m}H_{-m}(x) = i^m H_m(x)$ (cf., Arfken, 1985), equations (9.1) and (9.2) can be rewritten as

$$\Phi^{\mathrm{i}}(\mathbf{x};\mathbf{0}) = \sum_{m=-\infty}^{\infty} i^m J_m(k_\alpha r)\cos(m\phi)\, e^{-i\omega t}, \tag{9.6}$$

and

$$\begin{aligned}
\Phi^{\mathrm{s}}(\mathbf{x};\mathbf{0}) &= \sum_{m=-\infty}^{\infty} i^m\, \mathcal{A}_m\, H_m^{(1)}(k_\alpha r)\cos(m\phi)\, e^{-i\omega t},\\
\Psi^{\mathrm{s}}(\mathbf{x};\mathbf{0}) &= \sum_{m=-\infty}^{\infty} i^{m+1}\, \mathcal{B}_m\, H_m^{(1)}(k_\beta r)\sin(m\phi)\, e^{-i\omega t},
\end{aligned} \tag{9.7}$$

where $\mathcal{A}_m$ and $\mathcal{B}_m$ are

$$\begin{aligned}
\mathcal{A}_m &= A_p, \quad p = |m|,\\
\mathcal{B}_m &= \begin{cases} B_p, & m \ge 0 \\ -B_p, & m < 0. \end{cases}
\end{aligned} \tag{9.8}$$

Since $\mathcal{A}_{-m}\sin(-m\phi) = -\mathcal{A}_m \sin(m\phi)$ and $\mathcal{B}_{-m}\cos(-m\phi) = -\mathcal{B}_m\cos(m\phi)$, we can

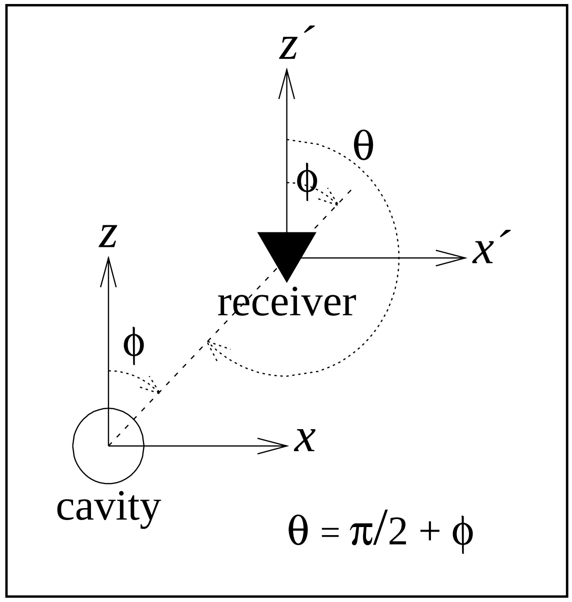

Fig. 9.5. Change of reference axis centering from cavity to receiver and a related angle change from ϕ to θ.

include $\sin(m\phi)$ and $\cos(m\phi)$ in (9.7) for convenience in treatment as

$$
\begin{aligned}
\Phi^{s}(\mathbf{x};\mathbf{0}) &= \sum_{m=-\infty}^{\infty} i^m \mathcal{A}_m H_m^{(1)}(k_\alpha r)\{\cos(m\phi) + i\sin(m\phi)\}\, e^{-i\omega t} \\
&= \sum_{m=-\infty}^{\infty} i^m \mathcal{A}_m H_m^{(1)}(k_\alpha r)\, e^{i(m\phi-\omega t)}, \\
\Psi^{s}(\mathbf{x};\mathbf{0}) &= \sum_{m=-\infty}^{\infty} i^m \mathcal{B}_m H_m^{(1)}(k_\beta r)\{\cos(m\phi) + i\sin(m\phi)\}\, e^{-i\omega t} \\
&= \sum_{m=-\infty}^{\infty} i^m \mathcal{B}_m H_m^{(1)}(k_\beta r)\, e^{i(m\phi-\omega t)}.
\end{aligned}
\tag{9.9}
$$

In order to consider the scattering of elastic waves in media with randomly distributed cavities with a given radius, we account for the whole set of scattered waves propagating to a given receiver in a sense of single scattering theory. We consider a sufficiently large medium bearing N_c cavities with radius a_c. The cavities are assumed to be distributed homogeneously and take a tiny area compared to the whole medium (S), i.e., $N_c a_c^2 \ll$ S. So, multiple scattered waves are not strong between the cavities. For simplicity of the treatment, we set the reference axis through a receiver away from a cavity center and make an angular transformation using θ ($\theta = \pi/2 + \phi$, see Fig. 9.5).

The total scattered P waves (Φ^{t}) arriving at a receiver can be computed by integrating the scattering waves from all heterogeneities. We introduce 'location map' $R(\mathbf{x})$ indicating locations of cavities inside a medium; $R(\mathbf{x})$ is set to have the value of 1 at locations of cavity centers ($\mathbf{x}_j^c$, j=1,2,...,N_c) and zero elsewhere:

$$R(\mathbf{x}) = \sum_{j=1}^{N_c} \delta(\mathbf{x} - \mathbf{x}_j^c), \tag{9.10}$$

where N_c is the number of cavities implemented in medium. When we consider the whole cavities using the location map, the relative position for the location of cavity center ($\mathbf{x}'$) can be implemented for the representation of potentials and therefore $\Phi(\mathbf{y};\mathbf{0})$ can be written by $\Phi(\mathbf{y}+\mathbf{y}_c;\mathbf{y}_c)$ for example. Therefore, the total wavefields from cavities can be written as

$$\begin{aligned}\Phi_a^{\mathrm{s}}(\mathbf{x}) &= \sum_{j=1}^{N_c} \Phi_j^{\mathrm{s}}(\mathbf{x}) = \sum_{j=1}^{N_c} \int_{\mathsf{S}} \Phi^{\mathrm{s}}(\mathbf{x};\mathbf{x}_j^c)\, d\mathsf{S}(\mathbf{x}_j^c),\\ \Psi_a^{\mathrm{s}}(\mathbf{x}) &= \sum_{j=1}^{N_c} \Psi_j^{\mathrm{s}}(\mathbf{x}) = \sum_{j=1}^{N_c} \int_{\mathsf{S}} \Psi^{\mathrm{s}}(\mathbf{x})(\mathbf{x};\mathbf{x}_j^c)\, d\mathsf{S}(\mathbf{x}_j^c).\end{aligned} \tag{9.11}$$

Using an asymptotic expression for the Hankel function (Arfken, 1985), we rewrite the Hankel function, $H_m^{(1)}$ as

$$H_m^{(1)}(x) \approx \sqrt{\frac{2}{\pi x}} \exp\left[i\left(x - \frac{\pi}{4} - \frac{m\pi}{2}\right)\right]. \tag{9.12}$$

Since the receiver is placed at large distance from scatters (i.e., $|\mathbf{x}| \gg |\mathbf{x}_j^c|$), r_j (=$|\mathbf{x} - \mathbf{x}_j^c|$) in Fig. 7.4 can be given by $|\mathbf{x}| - \mathbf{n}\cdot\mathbf{x}_j^c$ where $\mathbf{n}$ is the unit vector in $\mathbf{x}$ direction, and $1/r_j$ can be approximated by $|\mathbf{x}|$ (e.g., Frankel & Clayton, 1986). With (9.9) and (9.12), $\Phi_j^{\mathrm{s}}(\mathbf{x})$ and $\Psi_j^{\mathrm{s}}(\mathbf{x})$ in (9.11) can be written as

$$\begin{aligned}\Phi_j^{\mathrm{s}}(\mathbf{x}) &= \int_{\mathsf{S}} \left\{ \sum_{m=-\infty}^{\infty} i^m \mathcal{A}_m \sqrt{\frac{2}{\pi k_\alpha |\mathbf{x}|}} \right.\\ &\quad \left. \times \exp\left[i\left(k_\alpha|\mathbf{x}| - k_\alpha \mathbf{n}\cdot\mathbf{x}_j^c - \frac{\pi}{4} - \frac{m\pi}{2} + m\phi - \omega t\right)\right] \right\} d\mathsf{S}(\mathbf{x}_j^c),\\ \Psi_j^{\mathrm{s}}(\mathbf{x}) &= \int_{\mathsf{S}} \left\{ \sum_{m=-\infty}^{\infty} i^m \mathcal{B}_m \sqrt{\frac{2}{\pi k_\beta |\mathbf{x}|}} \right.\\ &\quad \left. \times \exp\left[i\left(k_\beta|\mathbf{x}| - k_\beta \mathbf{n}\cdot\mathbf{x}_j^c - \frac{\pi}{4} - \frac{m\pi}{2} + m\phi - \omega t\right)\right] \right\} d\mathsf{S}(\mathbf{x}_j^c).\end{aligned} \tag{9.13}$$

The expression in (9.13) can be simplified using $\exp(-im\pi/2)$=$(-i)^m$ to give

$$\begin{aligned}\Phi_j^{\mathrm{s}}(\mathbf{x}) &= \sum_{m=-\infty}^{\infty} \mathcal{A}_m \sqrt{\frac{2}{\pi k_\alpha |\mathbf{x}|}} \exp\left[i\left(k_\alpha|\mathbf{x}| - \omega t - \frac{\pi}{4}\right)\right]\\ &\quad \times \int_{\mathsf{S}} \exp[i(m\phi - k_\alpha \mathbf{n}\cdot\mathbf{x}_j^c)]\, d\mathsf{S}(\mathbf{x}_j^c)\end{aligned}$$

$$\Psi_j^s(\mathbf{x}) = \sum_{m=-\infty}^{\infty} \mathcal{B}_m \sqrt{\frac{2}{\pi k_\beta |\mathbf{x}|}} \exp\left[i\left(k_\beta|\mathbf{x}| - \omega t - \frac{\pi}{4}\right)\right] \times \int_{\mathsf{S}} \exp[i(m\phi - k_\beta \mathbf{n}\cdot\mathbf{x}_j^c)]\, d\mathsf{S}(\mathbf{x}_j^c), \tag{9.14}$$

where ϕ is the angular distance from the reference position ($\mathbf{x}$) to a scatterer's position ($\mathbf{x}_j^c$).

In order to compute average energy dissipation by scattering, we consider an ensemble average of Φ_a^s and Ψ_a^s:

$$< |\Phi_a^s|^2 >= \frac{2N_c}{\pi k_\alpha |\mathbf{x}|} \sum_{m=-\infty}^{\infty} (\mathcal{A}_m)^2 \times \int_{\mathsf{S}}\int_{\mathsf{S}} < R(\mathbf{x})R(\mathbf{y}) > \exp\left[i\left\{m(\phi_{\mathbf{x}} - \phi_{\mathbf{y}}) - k_{\alpha_1}\mathbf{n}\cdot(\mathbf{x}_j^c - \mathbf{y}_j^c)\right\}\right] d\mathsf{S}(\mathbf{x}_j^c)\, d\mathsf{S}(\mathbf{y}_j^c),$$

$$< |\Psi_a^s|^2 >= \frac{2N_c}{\pi k_\beta |\mathbf{x}|} \sum_{m=-\infty}^{\infty} (\mathcal{B}_m)^2 \times \int_{\mathsf{S}}\int_{\mathsf{S}} < R(\mathbf{x})R(\mathbf{y}) > \exp\left[i\left\{m(\phi_{\mathbf{x}} - \phi_{\mathbf{y}}) - k_{\beta_1}\mathbf{n}\cdot(\mathbf{x}_j^c - \mathbf{y}_j^c)\right\}\right] d\mathsf{S}(\mathbf{x}_j^c)\, d\mathsf{S}(\mathbf{y}_j^c). \tag{9.15}$$

We introduce new variables $\mathbf{p}$ for the center-of-mass coordinate variable and $\mathbf{q}$ for the relative coordinate variable (e.g., Frankel & Clayton, 1986):

$$\mathbf{p} = (\mathbf{x}_j^c + \mathbf{y}_j^c)/2, \qquad \mathbf{q} = \mathbf{x}_j^c - \mathbf{y}_j^c. \tag{9.16}$$

When we consider the integrals in (9.15) with the new variables ($\mathbf{p}$, $\mathbf{q}$), the integration for $\mathbf{p}$ yields the area S and the integration for $\mathbf{q}$ can be considered simply in a polar coordinate system (r',ϕ') using the relationship

$$r' = |\mathbf{q}|, \qquad \phi' = \phi_{\mathbf{x}} - \phi_{\mathbf{y}}, \qquad d\mathsf{S}(\mathbf{q}) = r'dr'd\phi'. \tag{9.17}$$

The ensemble averages, therefore, can be simplified with additional introduction of an autocorrelation function $N(r')$ for the ensemble of the location maps:

$$< |\Phi_a^s|^2 >= \frac{2N_c\mathsf{S}}{\pi k_\alpha |\mathbf{x}|} \sum_{m=-\infty}^{\infty} (\mathcal{A}_m)^2 \times \int_{r'=0}^{r'=\infty}\int_{\phi'=0}^{\phi'=2\pi} N(r') \exp\left[i(m\phi' - k_{\alpha_1} r' \cos\phi')\right] r'dr'd\phi',$$

$$< |\Psi_a^s|^2 >= \frac{2N_c\mathsf{S}}{\pi k_\beta |\mathbf{x}|} \sum_{m=-\infty}^{\infty} (\mathcal{B}_m)^2 \times \int_{r'=0}^{r'=\infty}\int_{\phi'=0}^{\phi'=2\pi} N(r') \exp\left[i(m\phi' - k_{\beta_1} r' \cos\phi')\right] r'dr'd\phi', \tag{9.18}$$

where we note that the limit of the integral in r' is extended to $r' = \infty$ since we consider the distribution of heterogeneities to be sparse and homogeneous in the media, and therefore, the value of $N(r')$ is small at large offsets (e.g., Frankel & Clayton, 1986).

The integral of the exponential function in (9.18) can be rewritten in terms of Bessel functions and the integral of a function with a Bessel function can be expressed by a Hankel transform $\mathcal{H}$ (Arfken, 1985, p587, p795):

$$\int_0^{2\pi} \exp\left[i(x\cos\phi' + m\phi')\right] d\phi' = i^m\, 2\pi J_m(x),$$
$$\mathcal{H}_m(k) = \mathcal{H}\left[m, N(r'); k\right] = \int_0^{\infty} N(r')r' J_m(kr')\, dr', \tag{9.19}$$

where $J_m(x)$ is the mth order of Bessel function and $\mathcal{H}_m(k)$ is the Hankel-transformed autocorrelation function $N(r')$. We note that when m=0, the Hankel transform is equivalent to a two-dimensional Fourier transform and $\mathcal{H}_0(k_j)$ is a power spectral density function, the spectrum of $N(r')$. Therefore, $< |\Phi_a^{\mathrm{s}}|^2 >$ and $< |\Psi_a^{\mathrm{s}}|^2 >$ in (9.18) are given by

$$< |\Phi_a^{\mathrm{s}}|^2 >= \frac{4N_c\mathsf{S}}{k_\alpha|\mathbf{x}|} \sum_{m=-\infty}^{\infty} (\mathcal{A}_m)^2\, \mathcal{H}_m(-k_\alpha),$$
$$< |\Psi_a^{\mathrm{s}}|^2 >= \frac{4N_c\mathsf{S}}{k_\beta|\mathbf{x}|} \sum_{m=-\infty}^{\infty} (\mathcal{B}_m)^2\, \mathcal{H}_m(-k_\beta). \tag{9.20}$$

The attenuation rate (Q^{-1}) corresponds to the energy loss per unit area divided by the solid angle (2π) and the wavenumber of incident waves, and therefore the attenuation rate Q^{-1} over a spatial lag r is given by

$$Q^{-1} = \frac{N_c r}{2\pi\mathsf{S}k_\alpha}\Big\{ < |\Phi_a^{\mathrm{s}}|^2 > + < |\Psi_a^{\mathrm{s}}|^2 > \Big\}. \tag{9.21}$$

Here, N_c can also be expressed as the multiplication of the area of the random cavity region (A_c) and the number density (η), i.e., $N_c = \eta\mathsf{A}_c$. Therefore, the theoretical scattering attenuation variation for media bearing randomly distributed cavities with number density η is given by

$$\frac{Q^{-1}}{\eta} = \frac{2\mathsf{A}_c}{\pi k_\alpha^2}\Big\{ \sum_{m=-\infty}^{\infty} (\mathcal{A}_m)^2\, \mathcal{H}_m(-k_\alpha) \Big\} + \frac{2\mathsf{A}_c}{\pi k_\alpha k_\beta}\Big\{ \sum_{m=-\infty}^{\infty} (\mathcal{B}_m)^2\, \mathcal{H}_m(-k_\beta) \Big\}. \tag{9.22}$$

Note that the theoretical scattering attenuation expression (9.22) is not only for media with fluid-filled cavities but also for any style of cavities. One can estimate the scattering attenuation variation for different style of cavities by implementing the appropriate A_m and B_m in (9.4) for the material inside the cavities.

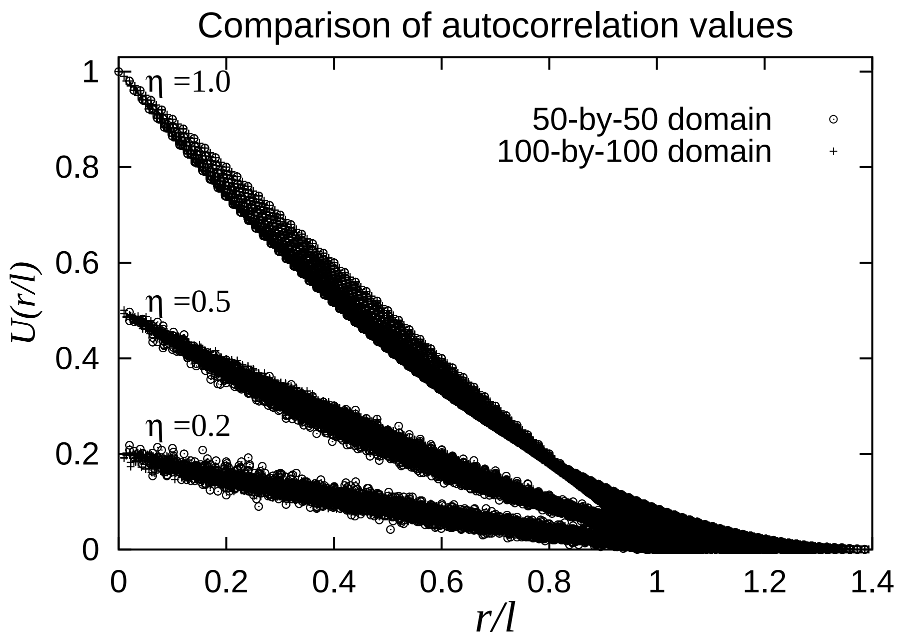

Fig. 9.6. Estimated autocorrelation values of $R(\mathbf{x})$ for three number densities (η=0.2, 0.5, 1.0) in 50-by-50 and 100-by-100 grid point domains. The estimated values of the two domains are very close.

9.4 Determination of the autocorrelation function

In order to compute the theoretical attenuation variations for the media with random cavities in (9.22), it is necessary to determine the autocorrelation function (ACF) $N(r)$ in the spatial domain. We determine $N(r)$ empirically with numerical experiments in media with various number densities (η=0.05, 0.2, 0.5, 0.8, 1.0). The $R(\mathbf{x})$ in (9.10) corresponds to the locations of cavity centers and is given as a polynomial composed of delta functions. Therefore, the autocorrelation values can be determined numerically (e.g., Roth & Korn, 1993) by

$$U(r) =< R(\mathbf{x})R(\mathbf{y}) >= \frac{1}{r_{\max}} \int_0^{r_{\max}} R(r')R(r+r')\, dr', \tag{9.23}$$

where $r_{\max}$ is the maximum spatial lag in the medium. Here $U(r)$ represents unnormalized autocorrelation values dependent on the number density (η) of the medium, and the normalized autocorrelation values $N(r)$ can be expressed using $U(r)$ as

$$U(r) = \eta\, N(r). \tag{9.24}$$

The representative autocorrelation function can be implemented for any number density problems.

The autocorrelation values should be determined to be constant regardless of the number of grid points implemented for the representation of the domain if the number density is constant. We therefore compare the numerical autocorrelation values in two different sizes of domains; 50-by-50 and 100-by-100 grid points (Figure 9.6). For the normalization in distance, we introduce a relative distance r/l where l is the reference distance (e.g., vertical or horizontal length of the medium). The estimated autocorrelation values are very close between the two experiments, but the 100-by-100 grid point domain which has a smaller grid step shows more confined trend. Fig. 9.6 displays that the autocorrelation values are proportional to the number density as indicated in (9.24).

For the numerical determination of ACF, one may implement polynomials or single functions. However, it is usually difficult to obtain the Hankel transform ($\mathcal{H}_m$, m=integer) for arbitrary functions (Sneddon, 1972). The numerical evaluation technique for Hankel transform is used popularly in electromagnetic modelling (Anderson, 1984) but is restricted to lower orders (i.e., m=0,1, see, Anderson, 1989). Only a few functions are known to have analytic forms for any order m. Gaussian (e^{-pr^2}) and exponential functions (e^{-pr}) may be appropriate for the basis function, and the Hankel-transformed outputs are given by

$$\mathcal{H}\left(m, e^{-pr}; k\right) = k^m \left(p^2 + k^2\right)^{-\frac{3}{2}} \left(p + m\sqrt{p^2 + k^2}\right) \left(p + \sqrt{p^2 + k^2}\right)^{-m}, \tag{9.25}$$

and

$$\mathcal{H}\left(m, e^{-pr^2}; k\right) = \frac{k^m \Gamma(\frac{1}{2}m + 1)}{2^{m+1} p^{\frac{1}{2}m+1} \Gamma(m+1)} \times {}_1F_1\left(\frac{1}{2}m + 1; m + 1; -\frac{k^2}{4p}\right), \tag{9.26}$$

where p is a constant, Γ is the Gamma function, and ${}_1F_1$ is the confluent hypergeometric function defined as

$${}_1F_1(g; h; x) = \sum_{n=0}^{\infty} \frac{(g)_n}{n!(h)_n} x^n, \tag{9.27}$$

and $(g)_n = g(g+1)\cdots(g+n-1)$.

We implement a polynomial composed of exponential functions for the basis function:

$$N(r) = \sum_{n=1}^{N_p} a_n \exp\left(-b_n r\right), \quad (b_n > 0), \tag{9.28}$$

where r/l is the normalized distance and a_n and b_n are constants to be determined in a least-squares sense. It is evident that the more functions are considered, the better the least square fitting for a given data set. However, we find empirically that when many functions are introduced for the fitting, ACF at certain long distances outside of the data set has unreasonable values (negative autocorrelation values). That is, when the number of functions implemented increases, the coefficients a_n are determined to be mixtures of positive and negative values. Thus, for certain distances out of the data set, negative values are determined for the ACF. Therefore, the coefficient a_n should be required to be positive to satisfy the expected trend. For the purpose, we find that two functions are

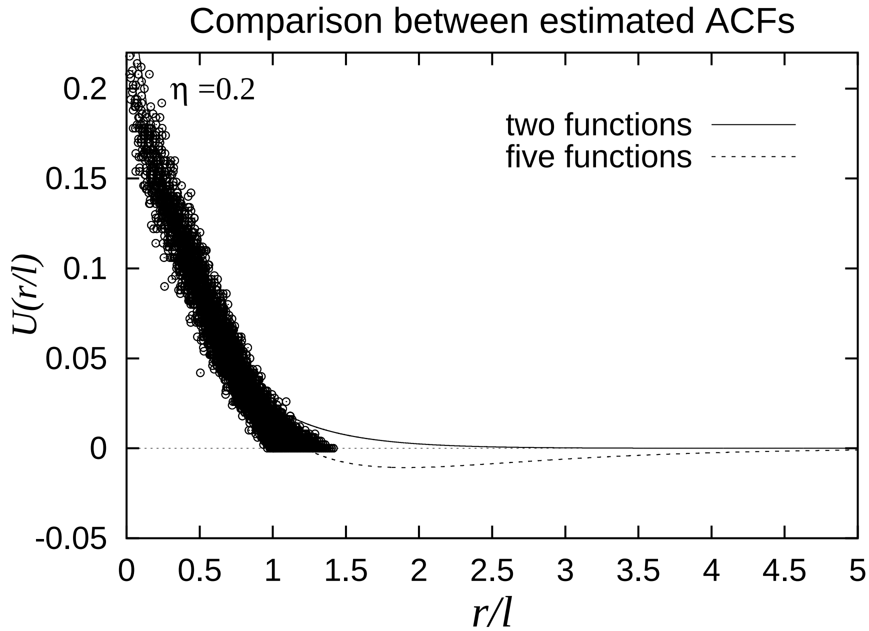

Fig. 9.7. Comparison of ACFs composed of two and five exponential functions for data set with η=0.2. Both ACFs satisfy the data set well, but the ACF with five basis functions display unreasonable negative values at r/l >1.5.

sufficient for the fitting. Fig. 9.7 shows comparison between the numerically estimated ACFs based on two and five exponential functions. The ACF based on five exponential function displays negative values at large distance outside the data set, while the other ACF exhibits a reasonable pattern.

When two exponential functions are considered for the basis functions of ACF (i.e., N_p=2), the constants a_n and b_n in (9.28) are determined as

$$a_1 = 0.982, \quad a_2 = 0.397, \quad b_1 = 2.2, \quad b_2 = 4. \tag{9.29}$$

Comparisons between numerical values and the estimated ACF ($U(r/l)$) in Fig. 9.8 display a good fitting for data set with small number densities (η=0.05, 0.2), but poor agreement for those with large density numbers (η=0.5, 0.8, 1.0). However, since the area of random cavity region (A$_c$) should be much larger than the area of cavities ($N_c \pi a_c^2$, refer to the assumption in the previous section), N_c is normally small (N_c <0.001 in this study) and thus the estimated ACF is sufficient for the representation of the data set. Therefore, from (9.25) and (9.28) the Hankel transform of the estimated ACF in (9.22) can be written in the form

$$\begin{aligned}\mathcal{H}_m(k) &= \mathcal{H}\left[m, N(r); k\right] \\ &= k^m \sum_{n=1}^{N_p} a_n \left(b_n^2 + k^2\right)^{-\frac{3}{2}} \left(b_n + m\sqrt{b_n^2 + k^2}\right) \left(b_n + \sqrt{b_n^2 + k^2}\right)^{-m}.\end{aligned} \tag{9.30}$$

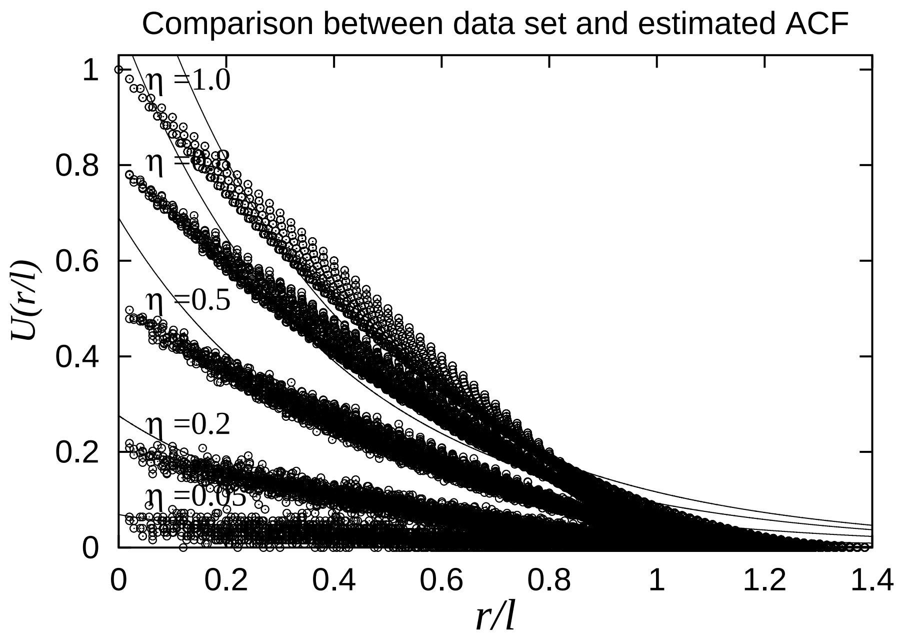

Fig. 9.8. Comparisons between data sets and ACF based on two-exponential functions when η=0.05, 0.2, 0.5, 0.8 and 1.0. The ACF satisfies with the data sets for η=0.05, 0.2 well, but become worse for the data sets with large η.

We may implement an alternative polynomial composed of Gaussian-type exponential functions. However, although the Gaussian-type exponential function has its own analytic expression for the Hankel transform, it is often difficult to compute the Hankel transform due to the hypergeometric function ($_1F_1$) which converse slowly to the accurate value.

9.5 Scattering attenuation

The spectral amplitudes of primary waves are measured from time responses recorded for several different models with random cavities (Fig. 9.9). The spectral amplitudes of the primary wave transmitted through the media with cavities decrease with increase of the number of cavities (N_c) and the radius of the cavities (a_c). The spectral amplitudes of the x components are invariant for changes in the z components even when N_c and a_c become large. That is, primary waves are recorded mainly at z components. Therefore, scattering attenuation rates can be estimated correctly using only z-component time responses.

In general, the theoretical attenuation rates are expected to be proportional to normalized wavenumber $k_\alpha a_c$ where k_α is the wavenumber of the incident waves (Fig. 9.10). However, the slope of the curve is not constant in whole range but can be divided into several segments. In particular, the slope at $k_\alpha a_c > 10^{1.3}$ is nearly zero

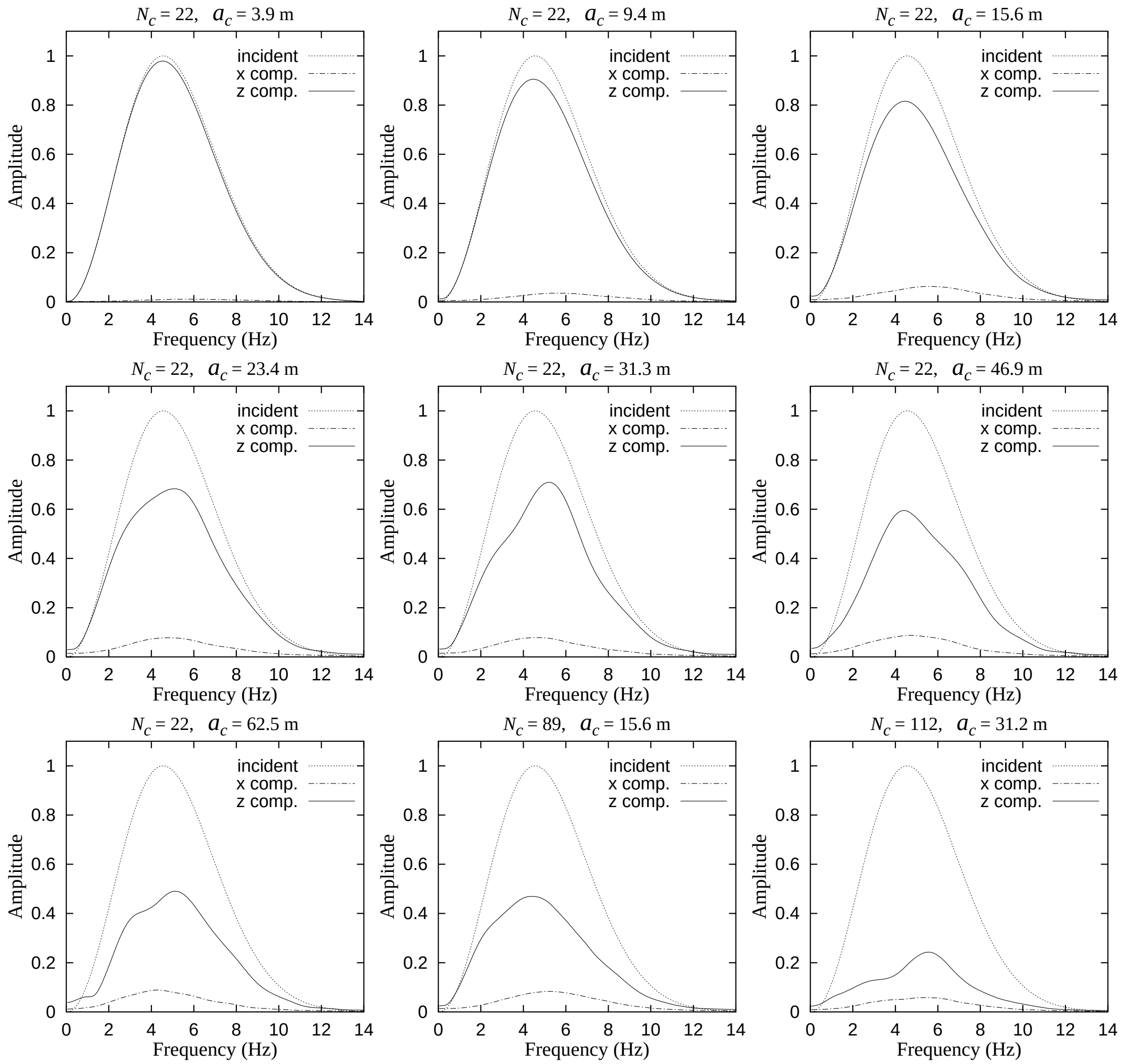

Fig. 9.9. Spectral amplitudes of time responses in x and z components. For the reference, the spectral amplitudes of incident waves are provided. Energy dissipation is proportional to the number of cavities and the size of radius. Spectral amplitudes in x components are nearly invariant for the change of spectral amplitudes in z components.

and primary waves are expected to dissipate almost completely under single scattering theory. Scattering energy loss is made during interaction (e.g., refraction, reflection) between incident waves and cavity surfaces. Therefore, the energy loss increases with the scale of cavities (a_c) or with decrease of incident wavelength (k_α). So, the scattering energy loss is proportional to normalized wavenumber ($k_\alpha a_c$). As we have discussed in Section 9.2, the energy loss at a specific cavity is compensated (i.e., homogeneous energy loss in the entire primary wavefront) through the phase healing process during

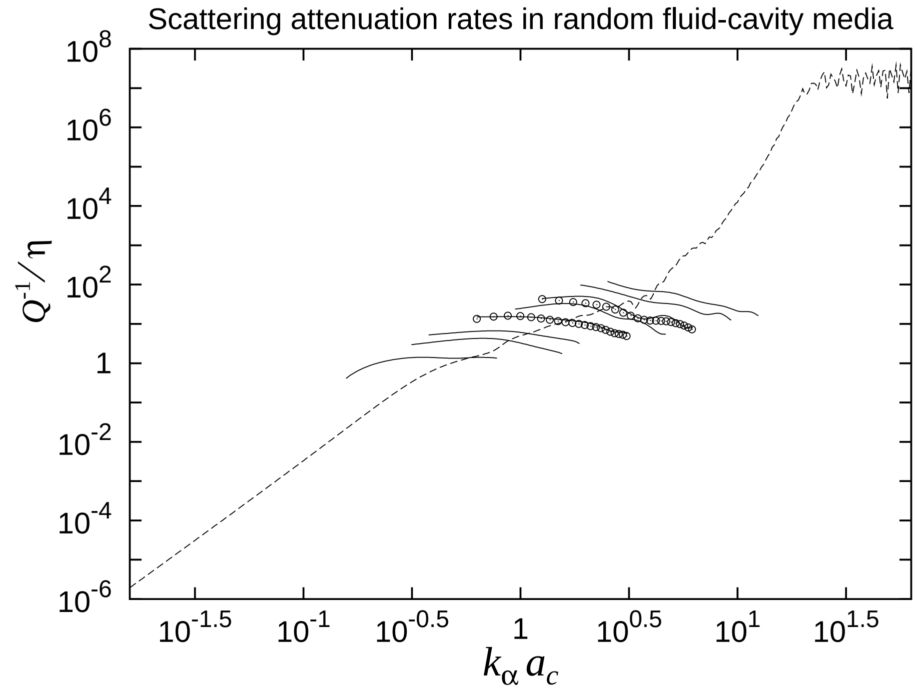

Fig. 9.10. Comparison between estimated scattering attenuation rates and theoretical variation. Scattering attenuation rate is expected to increase with normalized wavenumber ($k_\alpha a_c$). The estimated rates agree with the theoretical trend well.

propagation. Finally the primary waves are exhausted completely by scattering when sufficiently large scales of cavities are introduced.

The numerical results are compared with the theoretical rates. Solid lines in the figure represent the data set from media with 22 cavities and the open circles the data from media with 89 or 112 cavities. The numerical results agree well with the theoretical variation. In particular, the attenuation rates measured from data in media with 89 and 112 cavities are coincident with those from data in media with 22 cavities with the same radius (i.e., a_c=15.6, 31.2 m). That is, the scattering attenuation rates are proportional to the number density (η) and the energy dissipation is mainly affected by the first-order scattered waves. Also, the attenuation rates at given media can be inferred efficiently by the single scattering theory.

The trend of attenuation variation with a random set of fluid-filled cavities is quite different from that in stochastic random media; the attenuation rates are mainly proportional to the normalized wavenumber in the random fluid-cavity media, while the attenuation rates in the stochastic random media increase and then decrease with normalized wavenumber (see, Chap. 7). Thus, when large scales of cavities are implemented in a medium, significant energy loss is expected, but the energy loss in a medium with large stochastic heterogeneities is expected to be small. The scattering patterns in the time responses are also different between the two random media, and therefore, the random heterogeneities with high impedance contrast to the background medium are not well represented by stochastic random heterogeneities.

9.6 Discussion and conclusions

Random heterogeneities with high physical impedance have been implemented as an alternative representation of random heterogeneities in the crust, and the scattering pattern has been investigated. The heterogeneities are introduced using fluid-filled cavities. Scattered waves are distributed homogeneously in media with random cavities compared to those in random stochastic media. Primary waves rarely deviate from the incidence direction. Thus, the primary P waves are recorded mainly on the z components unlike the case for random stochastic media, where a significant travel time anomaly is introduced and a dual-component process is essential for estimation of the scattering attenuation rates at large normalized wavenumbers (see, Sections 7.7 and 7.8). Moreover, energy loss in the primary waves is not transferred directly to scattering waves, but rather the energy in scattering waves is kept nearly constant.

The numerical estimates of scattering attenuation rates have been compared with a new formulation of the theoretical variation of attenuation. In order to compute the theoretical attenuation rates, the autocorrelation function (ACF) for randomly distributed cavities is required to be determined empirically. With a polynomial composed of two exponential functions, the ACF can be well represented. The theoretical attenuation expression can be applied not only to media with fluid-filled cavities but also to media with cylindrical cavities filled with any materials by implementing suitable reflection or transmission coefficients for the materials in the cavities.

The numerical attenuation rates agree well with the theoretical attenuation variation. The attenuation rates are proportional to the number density (η) as expected from the theory, and the normalized attenuation rates (Q^{-1}/η) are constant regardless of the number density. The scattering pattern and attenuation rates in media with random cavities are rather different form those in random stochastic media. Therefore, it may be better to use the both representation techniques for a full description of random heterogeneities in the crust.

Finally, the wavelet-based method provides accurate and stable time responses in media composed of random heterogeneities with high physical impedance and allows a quantitative seismic study in numerically challenging problems.

10

Summary and future studies

10.1 Summary and characteristics of the wavelet-based method

The thesis is concerned with the development of a new technique based on a wavelet transform for the modelling of acoustic and elastic wave propagation, and shows its capacity as a wave simulator by applying to challenging problems such as topography problems, modelling in tectonic regions and investigation of scattering of elastic waves.

A wavelet-based method is developed based on the idea that the consideration of wave action (e.g., differentiation of wavefield in spatial domain) using wavelets, which are confined in both physical and wavelet spaces, will allow a more concise and correct representation of the behaviour of the waves which are also confined in physical space. In order to implement the technique, the governing equation system is recast using a displacement-velocity formulation, and this allows a representation of the equation system in an explicit discrete time form where linear operators for spatial derivatives are considered by the operator projection technique in wavelet bases.

The wavelet-based method retains high accuracy in numerical differentiation and allows high stability even in complex and perturbed media. Due to the accuracy and stability, most natural physical boundary conditions which occur at the contact boundary of different materials are satisfied automatically through the governing equation system during modelling without requiring additional consideration of the conditions, even in media with high impedance contrast. But, the traction-free condition at a free surface, which occurs between elastic (or acoustic) and vacuum layers, requires an additional treatment due to the stability condition which needs to be imposed between wave velocity and grid step (see, Section 3.9). The traction-free conditions are considered by implementing equivalent forces to the equation system. This sort of approach can be extended for the consideration of other physical conditions that can not be included in the governing equation system such as azimuthal anisotropy. The technique implementing equivalent forces for boundary conditions works correctly, and numerical results show good agreement with analytic solutions in various models including media with topography.

The implementation of the equivalent forces, however, requires additional computational work, and the high stability of the wavelet-based method can be weakened due to the departure from its inherently periodic characteristic. Therefore, a careful treatment is required in code development to link the equivalent forces to the main equation system.

Artificial boundaries of numerical domains are treated by including attenuation terms in the governing equation system, which are active around the boundaries and attenuate waves incident to the boundaries. The attenuation terms are designed to be both continuous and differentiable in space in order to be stable under the multi-order differentiations which are required in the discrete time form of the wave equation system. However, since the attenuation zones around the boundaries are set to be consistent during modelling, and the absorption rates in the region can be varied with the wave type and the wave speed, low-frequency waves in media with a large Poisson ratio can not be absorbed well relative to the high-frequency waves. The difference in absorption can be cured by implementing larger attenuation zones with smoother variation or by composite use of existing other techniques (e.g., a one-dimensional analysis scheme, Carcione, 1994).

The wavelet-based method can be extended to media with topography using a suitable grid mapping technique. The wavelet-based method displays stability in treatment of media with high variation of topography. However, due to the inherent periodic characteristic, the topography needs to be implemented at the bottom of the domain and to be continuous at the left and right boundaries, like Fourier methods. The wavelet method was also implemented for modelling in tectonic zones with an extension of the technique for the source region, which allows the implementation of both complex source media and complicated source activation. The technique will provide a chance to investigate short-period seismic waves in realistic tectonic models at local distances.

The high stability and accuracy of the wavelet-based method is especially useful for quantitative studies of the scattering of seismic waves in random heterogeneous media. The measured attenuation rates from the numerical results are smaller than those of previous studies based on finite difference techniques, and the wavelet-based method conserves seismic energy during modelling better than other grid-based techniques. Moreover, the wavelet-based method demonstrates that high-frequency scattering waves causing the travel time anomaly in P, SV and acoustic wave studies are not confined at a region inside a narrow region to the incident direction (e.g., $\theta_{\min}$=30-45°), but are distributed to a rather large area (60-90°). So, high-frequency waves are expected to be scattered rather randomly in all directions. However, in the study of *SH* wave scattering, we found that directional (polarized) scattering by the radiation pattern is rather more effective than for acoustic and P waves, and so the high-frequency scattering is also confined at a narrower area (30-60°). Although SV scattering waves display a directional scattering pattern, scattered P waves showing a less polarized pattern are also developed by the wavetype coupling on boundaries of heterogeneities. Thus, it appears that this composite effect determines the minimum scattering of SV waves to be comparable to those of P and acoustic waves.

S waves lose more energy by scattering at low frequency ranges than P waves, and the phenomenon is reversed for higher frequencies. The scattering attenuation ratios of P and S waves are proportional to the normalized frequency (fa) in the range 0.1$<fa<$2 km/s, but are nearly constant outside that range.

The wavelet-based method also allows modelling in media with randomly distributed fluid-filled cavities which display high physical impedance to the background. Scattering waveforms in the media are similar to those in stochastic random media, but high-frequency scattering waves are developed less in the media with random cavities, and so the travel-time anomaly is not noticeable in the time responses. Further, the energy dissipation of incident waves by scattering increases with the scale of cavities since the portion of scattering waves reflected backward from the cavity boundaries with high impedance is also increased. Under a single scattering theory, the energy of incident waves is expected to be dissipated completely at media with sufficiently large scales of cavities.

The scattering attenuation pattern in media with random cavities is different from that in stochastic random media where the energy loss is expected to increase and then decrease with the scale of heterogeneities. Such stochastic random media are composed of smoothly varying heterogeneities, and thus incident waves are rather easily transmitted with less energy loss by backward scattering into the heterogeneities. Also, the variation rate of the heterogeneities become much smoother with the scale of heterogeneities; therefore, the scattering effect becomes strong in stochastic random media when the wavelength of incident waves is comparable to the scale of heterogeneities. The coda in media with random cavities displays rather more homogeneous distribution of scattering waves than for stochastic random media. It seems that a combined use of media with random cavities and the stochastic random representation may allow a more realistic description of heterogeneities in the earth.

10.2 Future studies

In this thesis, we have confined our scope to 2-D problems. However, it is essential to consider 3-D problems for the modelling of realistic physical situation. The formulation of the wave equations as a set of first-order differential equations for the evolution of the displacement and velocity fields in time can readily be extended to 3-D media problems. Using the separability of the differential operators we expect to be able to make a comparable extension to the 3-D case. In order to make the expansion of the wavelet-based method feasible in current computers, we need to modify the Beylkin's original scheme (Beylkin, 1992) for numerical differentiation in the wavelet domain, which consumes most computational time, in order to achieve a fast operation of spatial differentiations.

In Chapter 6, we have applied the wavelet-based method to the modelling of elastic wave propagation in fault zones. As shown in this chapter, the wavelet-based method can incorporate complex source time functions in complicated media. The wavelet-based method can be extended to problems with dynamic rupture depending on the frictional law, initial stress fields (dynamic and static) and fault geometry. Note that such problems have been investigated theoretically (e.g., Ionescu & Campillo, 1999) and numerically (e.g., Voisin, 2002; Aagaard *et al.*, 2001) in various studies. However, interactions with transient seismic waves in the system are often neglected (e.g., Voisin, 2002) and random heterogeneities (Mai & Beroza, 2002; Beroza & Mikumo, 1996) in the fault region can not be considered due to the limitation of the numerical technique implemented. In particular, the wavelet-based method may allow investigation of the slip pulse present along an interface between dissimilar materials (e.g., Andrew & Ben-Zion, 1997; Ben-Zion & Huang, 2002) in realistic environments (i.e., complex media, inhomogeneous initial stress field, pore pressures).

For such modelling, it is expected to include the effects of the time-dependent static stress change in the elastic wave equation system, and also the coupling between heat (friction) and strain needs to be considered. Through the modelling including dynamic rupture system, seismic waves at short distances can be well understood in terms of fault geometry, dynamic and static stress drops and rupture properties.

We approximate the air layer as a vacuum layer for numerical modelling and a traction-free condition is implemented at the boundary between the air and elastic (or acoustic) media. However, the air layer over the earth surface has some density and a finite sound wave velocity although they are so small compared to those in elastic and acoustic layers. The treatment of the real air/earth boundary will require a very fine grid system due to the stability condition. However, if we are concerned with atmosphere coupling by the seismic waves, the direct implementation of the air layer may be the best way to describe the phenomenon. The wavelet-based method is stable in media with high physical impedance contrast, and the method can be extended to the study by implementing high-order wavelets.

Appendix A

NS-forms of wavelet expansions

A.1 Formulation of matrix operators via wavelets in *NS*-form

As we have discussed in Section 2.2, a physical $\mathbf{L}^2(\mathbf{R})$ can be decomposed into a scaling subspace ($\mathbf{V}_j$) and a wavelet subspace ($\mathbf{W}_j$) The scaling and wavelet subspaces are orthogonal each other and so the direct sum of the both spaces reconstruct the $\mathbf{L}^2(\mathbf{R})$. The scaling subspace $\mathbf{V}_j$ can also be decomposed into the higher scaling and wavelet spaces ($\mathbf{V}_{j+1}$,$\mathbf{W}_{j+1}$), and the sequential decomposition can be made until the scaling subspace reach to the null space ($\{0\}$). This process is called 'multiresolution analysis'. Therefore, any physical space can be represented with direct sum of wavelet subspaces by the multiresolution analysis, and action of an operator T in physical space can be represented with a matrix operator in the wavelet space. However, the matrix operator has a form requiring large computational resources (memory, time), and the matrix operator is recast in the non-standard form (*NS*-form, Belykin, 1992).

The construction of a matrix operator in *NS*-form based on the work of Beylkin (1992) is described briefly. The operator T on $\mathbf{L}^2(\mathbb{R})$ in *NS*-form is obtained by through the use of operators (A_j, B_j, Γ_j), for each level j ($j \in \mathbb{Z}$), in subspaces which project the subspaces produced by the action of T onto the subspaces ($\mathbf{W}_j, \mathbf{V}_j$):

$$T = \{A_j, B_j, \Gamma_j\}_{j \in \mathbb{Z}}, \tag{A.1}$$

where each operator is specified by

$$\begin{aligned} A_j &= Q_j T Q_j : \quad \mathbf{W}_j \to \mathbf{W}_j, \\ B_j &= Q_j T P_j : \quad \mathbf{V}_j \to \mathbf{W}_j, \\ \Gamma_j &= P_j T Q_j : \quad \mathbf{W}_j \to \mathbf{V}_j. \end{aligned} \tag{A.2}$$

Here, P_j is a projector onto the scaling subspace $\mathbf{V}_j$ and Q_j onto the wavelet subspace

$\mathbf{W}_j$. The expression (A.2) means that the distorted space due to an operation of T on $\mathbf{L}^2(\mathbb{R})$ space, can be reorganized into subspaces $\mathbf{V}_j$ and $\mathbf{W}_j$.

Following the discussion in Section 2.2, the physical space where data are collected is identified as $\mathbf{V}_0$, and the operator T implemented on the space $\mathbf{V}_0$ as T_0. Therefore, considering (A.1) T_0 can be expressed with a set of operators in subspaces $(A_j, B_j, \Gamma_j,$ $j > 0)$ up to a scale N where T_N becomes a null space as

$$T_0 = \{A_j, B_j, \Gamma_j\}_{j=1}^{N}. \tag{A.3}$$

Therefore, when T_0 is decomposed up to a certain scale J which is less than N, we can express T_0 generally as

$$T_0 = \{\{A_j, B_j, \mathit{\Gamma}_j\}_{j=1}^{J}, T_J\}, \tag{A.4}$$

where T_J is the operator on the scaling subspace of coarsest scale ($\mathbf{V}_J$), which corresponds to

$$T_J = P_J T P_J : \quad \mathbf{V}_J \to \mathbf{V}_J. \tag{A.5}$$

Thus, considering (A.3), T_J can be represented through the operator projections on to subspaces of higher scales up to the scale N, (i.e., $T_J = \{A_j, B_j, \mathit{\Gamma}_j\}_{j=J+1}^{N}\}$). Therefore, considering (A.2) and (A.5), the operator T_0 in (A.4) can be rewritten by

$$T_0 = \sum_{j=1}^{J}(Q_j T Q_j + Q_j T P_j + P_j T Q_j) + P_J T P_J. \tag{A.6}$$

Since the one-dimensional operator (e.g., d/dx in 1-D) is applied for the multi-dimensional operator (e.g., $\partial_x \partial_y$ in 2-D) via separation into operators acting on the different directions (see, Section 2.2), we focus on the construction of a homogeneous differential operator with degree p (d^p/dx^p). When $\mathcal{A}_{il}^j$, $\mathcal{B}_{il}^j$, $\mathcal{C}_{il}^j$, $\mathcal{T}_{il}^j$ are considered as components of matrices A_j, B_j, $\mathit{\Gamma}_j$, T_j $(i, l, j \in \mathbb{Z})$, the matrix components can be determined using those for the scale $j = 0$ through the relationships (see, Beylkin, 1992)

$$\begin{aligned}
\mathcal{A}_{il}^j &= 2^{-pj}\int_{-\infty}^{\infty}\psi(2^{-j}x - i)\psi^{(p)}(2^{-j}x - l)2^{-j}\,dx = 2^{-pj}\mathcal{A}_{il}^0,\\
\mathcal{B}_{il}^j &= 2^{-pj}\int_{-\infty}^{\infty}\psi(2^{-j}x - i)\varphi^{(p)}(2^{-j}x - l)2^{-j}\,dx = 2^{-pj}\mathcal{B}_{il}^0,\\
\mathcal{C}_{il}^j &= 2^{-pj}\int_{-\infty}^{\infty}\varphi(2^{-j}x - i)\psi^{(p)}(2^{-j}x - l)2^{-j}\,dx = 2^{-pj}\mathcal{C}_{il}^0,\\
\mathcal{T}_{il}^j &= 2^{-pj}\int_{-\infty}^{\infty}\varphi(2^{-j}x - i)\varphi^{(p)}(2^{-j}x - l)2^{-j}\,dx = 2^{-pj}\mathcal{T}_{il}^0.
\end{aligned} \tag{A.7}$$

When we set $\alpha_{i-l}^p = \mathcal{A}_{il}^0$, $\beta_{i-l}^p = \mathcal{B}_{il}^0$, $\gamma_{i-l}^p = \mathcal{C}_{il}^0$ and $\tau_{i-l}^p = \mathcal{T}_{il}^0$, the components ($\alpha_{i-l}^p$, β_{i-l}^p,

γ_{i-l}^p, τ_{i-l}^p) can be expressed through the wavelet projection theory as

$$\begin{aligned}
\alpha_l^p &= \int_{-\infty}^{\infty} \psi(x-l)\frac{d^p}{dx^p}\psi(x)\,dx,\\
\beta_l^p &= \int_{-\infty}^{\infty} \psi(x-l)\frac{d^p}{dx^p}\varphi(x)\,dx,\\
\gamma_l^p &= \int_{-\infty}^{\infty} \varphi(x-l)\frac{d^p}{dx^p}\psi(x)\,dx,\\
\tau_l^p &= \int_{-\infty}^{\infty} \varphi(x-l)\frac{d^p}{dx^p}\varphi(x)\,dx.
\end{aligned} \tag{A.8}$$

Here, with use of the two-scale difference equations (Beylkin, 1992; Daubechies, 1992), we are led to

$$\begin{aligned}
\alpha_l^p &= 2^p \sum_{k=0}^{L-1}\sum_{k'=0}^{L-1} (g_k g_{k'} \tau_{2l+k-k'}^p),\\
\beta_l^p &= 2^p \sum_{k=0}^{L-1}\sum_{k'=0}^{L-1} (g_k h_{k'} \tau_{2l+k-k'}^p),\\
\gamma_l^p &= 2^p \sum_{k=0}^{L-1}\sum_{k'=0}^{L-1} (h_k g_{k'} \tau_{2l+k-k'}^p),
\end{aligned} \tag{A.9}$$

where the coefficients h_k, g_k are the quadrature mirror filters of length L which is determined by wavelets used in the analysis. For Daubechies wavelets with M vanishing moments, $L = 2M$.

Since α_l^p, β_l^p, and γ_l^p can be expressed in terms of $\tau_{2l+k-k'}^p$ as in (A.9), the differential operator d^p/dx^p can be completely determined by using τ_l^p. The coefficients τ_l^p ($-L+2 \leq l \leq L-2$) are given by (Beylkin, 1992)

$$\tau_l^p = 2^p \left\{ \tau_{2l}^p + \frac{1}{2}\sum_{k=1}^{L/2} a_{2k-1}\left(\tau_{2l-2k+1}^p + \tau_{2l+2k-1}^p\right) \right\}, \tag{A.10}$$

and

$$\sum_{l=-L+2}^{L-2} l^p \tau_l^p = (-1)^p p!, \tag{A.11}$$

where a_{2k-1} is an autocorrelation of h_i defined by

$$a_n = 2\sum_{i=0}^{L-n-1} h_i h_{i+n}, \quad n = 1, 2, \ldots, L-1. \tag{A.12}$$

Thus, the autocorrelation coefficients a_n with even indices are

$$a_0 = \sqrt{2}, \quad a_{2k} = 0, \quad k = 1, 2, \ldots, L/2-1, \tag{A.13}$$

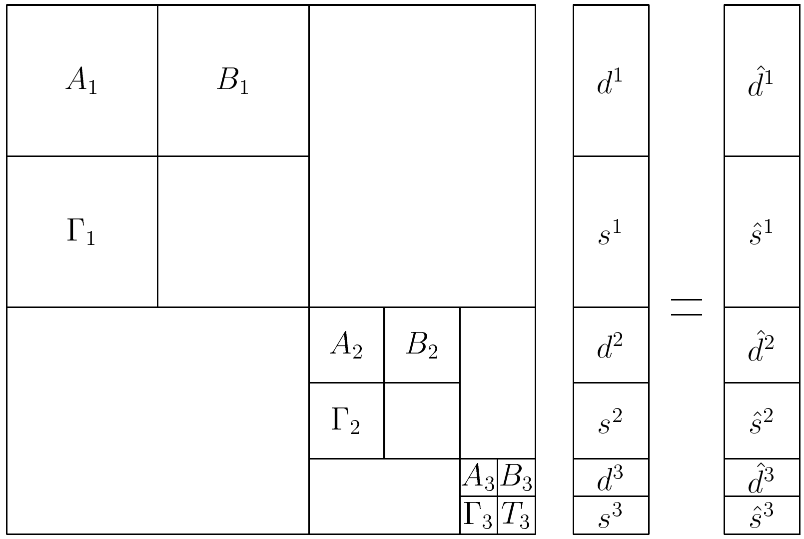

Fig. A.1. Illustration of the application of a matrix operator in non-standard form to a vector when J=3.

and the autocorrelation coefficients with odd indices are given by

$$a_{2k-1} = \frac{(-1)^{k-1} C_M}{(M-k)!\,(M+k-1)!\,(2k-1)}, \quad k = 1, 2, \ldots, M, \tag{A.14}$$

where C_M is

$$C_M = \left[\frac{(2M-1)!}{(M-1)!\,4^{M-1}} \right]^2 . \tag{A.15}$$

The coefficients τ_l^p for d^p/dx^p (p = integer) using Daubechies-6 and Daubechies-20 wavelets are given in Appendix A.3.

A.2 Application of a matrix operator to a vector and reconstruction to physical space

In this section, we describe the way to apply a matrix operator in NS-form (see, Appendix A.2) to a vector (e.g., wavefield) in wavelet space following Beylkin (1992).

Using (A.6) and applying a matrix operator in *NS* wavelet form to a vector $f(x)$ (e.g., horizontal (or, vertical) row in a displacement field, pth (or, qth) row in Fig. 2.3), a vector $(T_0 f)(x)$ can be represented in the wavelet basis by (Beylkin, 1992, see Fig. A.1)

$$(T_0 f)(x) = \sum_{j=1}^{J} \left(\sum_{k \in \mathbb{F}_{2^{N-j}}} \hat{d}_k^j \psi_{j,k}(x) + \sum_{l \in \mathbb{F}_{2^{N-j}}} \hat{s}_l^j \varphi_{j,l}(x) \right), \tag{A.16}$$

where N is a maximum number of scale level which can be achievable with a given data set (i.e., $\mathbf{V}_N$ is a null space) in the wavelet expansion, and thereby $J \leq N$. The set $\mathbb{F}_{2^{N-j}}$ is composed of positive integers which are less than 2^{N-j}, namely $\mathbb{F}_{2^{N-j}} = \{0, 1, 2, \ldots, 2^{N-j} - 1\}$.

$$\begin{tikzcd}[column sep=small]
\{\hat{s}^1\} \arrow[r] \arrow[dr] & \{\hat{s}^2+\tilde{s}^2\}=\{s^2\} \arrow[r] \arrow[dr] & \cdots \arrow[r] \arrow[dr] & \{\hat{s}^J+\tilde{s}^J\}=\{s^J\} \\
 & \{\hat{d}^2+\tilde{d}^2\}=\{d^2\} & \cdots & \{\hat{d}^J+\tilde{d}^J\}=\{d^J\}
\end{tikzcd}$$

Fig. A.2. Projection of the product of the matrix operator in *NS*-form and a vector into a wavelet basis.

$$\begin{tikzcd}
\{s^0\} & \{s^1\} \arrow[l] & \cdots \arrow[l] & \{s^{J-1}\} \arrow[l] & \{s^J\} \arrow[l] \\
 & \{d^1\} \arrow[ul] & \cdots \arrow[ul] & \{d^{J-1}\} \arrow[ul] & \{d^J\} \arrow[ul]
\end{tikzcd}$$

Fig. A.3. Reconstruction of the product of the matrix operator in *NS*-form and a vector to the physical space $\mathbf{V}_0$.

As shown in Fig. A.1, the output wavelet coefficients ($\hat{d}^j, \hat{s}^j$) contain both the wavelet and scaling components, and thus a complex projection procedure (A.16) is required for the reconstruction of the output vector ($T_0 f$) in physical space. Therefore, it is desirable to reorganize the output coefficients ($\hat{d}^j, \hat{s}^j$) in the regular form of wavelet coefficients (i.e., d^j, s^j), which reflect the effects of only wavelet or scaling functions.

Additional multiresolution analysis is applied to the coefficient for the scaling functions ($\hat{s}_l^j \varphi_{j,l}(x)$), and these are decomposed into wavelet and scaling coefficients. First, the $\hat{s}_l^1 \varphi_{1,l}(x)$ are decomposed into $\tilde{d}_k^2 \psi_{2,k}(x)$ and $\tilde{s}_k^2 \varphi_{2,k}(x)$, and then $d_k^2 \psi_{2,k}(x)$ and $s_k^2 \varphi_{2,k}(x)$ are formulated from the composite sums $\left(\hat{d}_k^2 + \tilde{d}_k^2\right) \psi_{2,k}(x)$ and $\left(\hat{s}_k^2 + \tilde{s}_k^2\right) \varphi_{2,k}(x)$. Here, $s_k^2 \varphi_{2,k}(x)$ can also be decomposed recursively into $d_k^3 \psi_{3,k}(x)$ and $s_k^3 \varphi_{3,k}(x)$ in the wavelet bases (Fig. A.2). We iterate the procedure until $j = J-1$ and finally we obtain a simplified expression for $(T_0 f)(x)$ in wavelet bases:

$$(T_0 f)(x) = \sum_{j=1}^{J} \sum_{k \in \mathbb{F}_{2^{N-j}}} d_k^j \psi_{j,k}(x) + \sum_{l \in \mathbb{F}_{2^{N-J}}} s_l^J \varphi_{J,l}(x), \tag{A.17}$$

where d_k^0 corresponds to $\hat{d}_k^0$. Finally, the operation on the vector ($T_0 f$) in physical space ($\mathbf{V}_0$) can be constructed by the usual wavelet reconstruction scheme (see, Fig. A.3).

A.3 Coefficients of *NS*-form of derivative operators

The coefficients (τ_l^2) of the non-standard form (*NS*-form) of second order derivative operator (∂_x^2) for Daubechies-6 wavelets, can be obtained by solving simultaneous equations in (A.10) and (A.11) using mathematical software (e.g., Mathematica), and are given by

$$\tau_0^2 = \frac{-376411229271430529}{102117402777924000}, \qquad \tau_1^2 = \frac{391969578590190173888}{16954680029972194125},$$

$$
\begin{aligned}
\tau_2^2 &= \frac{-21387760637407692931}{33909360059944388250}, & \tau_3^2 &= \frac{3474106670623164416}{16954680029972194125},\\
\tau_4^2 &= \frac{-3347641256627152657}{67818720119888776500}, & \tau_5^2 &= \frac{109833452180703232}{16954680029972194125},\\
\tau_6^2 &= \frac{-4455438357648059}{67818720119888776500}, & \tau_7^2 &= \frac{-5266935414784}{96883885885555395},\\
\tau_8^2 &= \frac{-23360548516687}{673974858334298400 0}, & \tau_9^2 &= \frac{7077855232}{269121905237653875},\\
\tau_{10}^2 &= \frac{-1511993}{119609735661179500}, & \tau_{-l}^2 &= \tau_l^2 \qquad (l = 1, 2, \ldots, 10),
\end{aligned} \tag{A.18}
$$

where the coefficient τ_l^2 satisfies the relationship as

$$
\tau_l^2 = \int_{-\infty}^{\infty} \varphi(x-l) \frac{d^2}{dx^2} \varphi(x)\, dx, \qquad -10 \le l \le 10. \tag{A.19}
$$

where $\varphi(x)$ is a scaling function. In the same way, we can obtain the coefficients (τ_l^3, τ_l^4) for third and fourth order of derivative operators:

$$
\begin{aligned}
\tau_0^3 &= 0, & \tau_1^3 &= \frac{22116565010234368}{9492080172157275},\\
\tau_2^3 &= \frac{-420791418307754477}{242997252407226240}, & \tau_3^3 &= \frac{7841073309070336}{17085744309883095},\\
\tau_4^3 &= \frac{-11397730655490923}{202497710339355200}, & \tau_5^3 &= \frac{-5044095026176}{632805344810485},\\
\tau_6^3 &= \frac{91367818221882449}{21869752716650361600}, & \tau_7^3 &= \frac{-136220198656}{271202290633065},\\
\tau_8^3 &= \frac{7847540783}{6942778640206464}, & \tau_9^3 &= \frac{44221184}{90400763544355},\\
\tau_{10}^3 &= \frac{-10882557}{23142595467354880}, & \tau_{-j}^3 &= -\tau_j^3 \qquad (j = 1, 2, \ldots, 10),
\end{aligned} \tag{A.20}
$$

and

$$
\begin{aligned}
\tau_0^4 &= \frac{5453233167428123}{141090751716480}, & \tau_1^4 &= \frac{-23559695353083136}{763874147965005},\\
\tau_2^4 &= \frac{382370390316173657}{24443972734880160}, & \tau_3^4 &= \frac{-1244004587271296}{254624715988335},\\
\tau_4^4 &= \frac{33138229116685523}{48887945469760320}, & \tau_5^4 &= \frac{118758284987008}{763874147965005},\\
\tau_6^4 &= \frac{-1381122434602789}{16295981823253440}, & \tau_7^4 &= \frac{1253534094848}{109124878280715},\\
\tau_8^4 &= \frac{49919995963}{27935968839863040}, & \tau_9^4 &= \frac{-274889216}{12124986475635},\\
\tau_{10}^4 &= \frac{3758251}{86222126048960}, & \tau_{-j}^4 &= \tau_j^4 \qquad (j = 1, 2, \ldots, 10).
\end{aligned} \tag{A.21}
$$

Also, we provide the coefficients of the *NS*-form of derivative operator (∂) based on the Daubechies-20 wavelets. The coefficients $(\tau_j^1, -38 \le j \le 38)$ of the first order derivative operator are given by

$$
\tau_0^1 = 0
$$

$$
\begin{aligned}
\tau^1_1 &= -0.95122025816280881689532916709533637411 58\\
\tau^1_2 &= 0.40924669691064934226928544889776754033222\\
\tau^1_3 &= -0.21220235235817125241138778371057557905874\\
\tau^1_4 &= 0.11174482984917235280645039046569709415 7023\\
\tau^1_5 &= -0.05655635346747988268541634561994005024 1633\\
\tau^1_6 &= 0.02679936774693490724310382908409417889 84621\\
\tau^1_7 &= -0.01170202807403020480638436325828414863 89714\\
\tau^1_8 &= 0.00465417919502178093224881196618884141 49408\\
\tau^1_9 &= -0.00166934220231212180073645966992405276 065193\\
\tau^1_{10} &= 0.00053477115388658414862943774657691290 096661\\
\tau^1_{11} &= -0.00015143564780404289970142715147157287 9414476\\
\tau^1_{12} &= 0.00003746201279105294193528178559819939 6928948\\
\tau^1_{13} &= -7.9806261237317771745141187865142359860246 \times 10^{-6}\\
\tau^1_{14} &= 1.4376253289349348427079331116912536645 0063 \times 10^{-6}\\
\tau^1_{15} &= -2.1370459395084275467483780041305514413 8844 \times 10^{-7}\\
\tau^1_{16} &= 2.5326833334713243907070627205738380219 4626 \times 10^{-8}\\
\tau^1_{17} &= -2.2748054429921684433037580597932746002 0808 \times 10^{-9}\\
\tau^1_{18} &= 1.4442654182777885772836587076502784274 7995 \times 10^{-10}\\
\tau^1_{19} &= -6.4418054540880497376102707094163608532 222 \times 10^{-12} \qquad \text{(A.22)}\\
\tau^1_{20} &= 3.4456490556165440527824686262774597822 3022 \times 10^{-13}\\
\tau^1_{21} &= -1.7081086228900746331253004073390880320 6041 \times 10^{-14}\\
\tau^1_{22} &= -5.0669011245078448936245959607994213867 125 \times 10^{-15}\\
\tau^1_{23} &= 1.0772873705307011407388357431834535765 5184 \times 10^{-15}\\
\tau^1_{24} &= -2.0600341789131776438736304011948414029 5314 \times 10^{-17}\\
\tau^1_{25} &= -1.1274367960599394298930221752299728083 6838 \times 10^{-17}\\
\tau^1_{26} &= 4.7106029731183941435312561199964695630 19 \times 10^{-19}\\
\tau^1_{27} &= 5.8570005057404587722549701560290047426 849 \times 10^{-19}\\
\tau^1_{28} &= 9.5286432963244412815358765268948885542 051 \times 10^{-22}\\
\tau^1_{29} &= 2.2090498689721172202922390870195049631 9178 \times 10^{-24}\\
\tau^1_{30} &= 3.3357114583507211377450705602138920359 5443 \times 10^{-26}\\
\tau^1_{31} &= -7.4336231434888703297882185230485225497 906 \times 10^{-28}
\end{aligned}
$$

$$\tau^1_{32} = 6.3994877436235609991592269588157459338184 \times 10^{-30}$$
$$\tau^1_{33} = -2.73557349984210029408405391458398409911042 \times 10^{-32}$$
$$\tau^1_{34} = -1.04765720469823213817922778531469877580904 \times 10^{-36}$$
$$\tau^1_{35} = 3.4721190547343456809901262124187162033694 \times 10^{-40}$$
$$\tau^1_{36} = 1.27967643177469868693835368282035919724671 \times 10^{-44}$$
$$\tau^1_{37} = -1.62422490373905792231749611455567746048172 \times 10^{-52}$$
$$\tau^1_{38} = 7.5979725818395493818388650700711955570933 \times 10^{-65}$$
$$\tau_{-j} = -\tau_j, \qquad 1 \leq j \leq 38.$$

The coefficients of the second order derivative operator can also be computed in the same way.

Appendix B

Procedure for ensemble average for wavefields

Stochastic random media are constructed by adding fractional fluctuation of physical parameters to background media. The fractional fluctuation ($\xi(\mathbf{x}')$) is regarded as stationary and isotropic, and distributed homogeneously in a medium. However, the stochastic random heterogeneities appear to have locally inhomogeneous distribution and biased effects are locally enhanced. Moreover, in a single scattering theory, the scattering energy loss is determined by the sum of energy of first-order scattered waves, which reflect the physical behaviour of specific heterogeneity. It is therefore convenient to determine the energy loss in a statistically averaging scheme, and Sato (1984) and Wu (1982) have introduced an ensemble averaging technique.

In this section, we derive ensemble-averaged wavefields to determine scattered energy. First, we consider the ensemble average of the velocity fluctuations in (7.28):

$$\begin{aligned}
\langle |u_r^{PP}|^2 \rangle &= \frac{k^3}{8\pi|\mathbf{x}|}\,[C_r(\theta)]^2 \\
&\quad\times \int_S \int_S \langle \xi(\mathbf{x}')\xi(\mathbf{y}')\rangle \exp\left[ik\left\{\mathbf{e}_z\cdot(\mathbf{x}'-\mathbf{y}') - \mathbf{n}\cdot(\mathbf{x}'-\mathbf{y}')\right\}\right]\, dS(\mathbf{x}')\, dS(\mathbf{y}'), \\
\langle |u_t^{PS}|^2 \rangle &= \frac{k^3\gamma^3}{8\pi|\mathbf{x}|}\,[C_t(\theta)]^2 \\
&\quad\times \int_S \int_S \langle \xi(\mathbf{x}')\xi(\mathbf{y}')\rangle \exp\left[ik\left\{\mathbf{e}_z\cdot(\mathbf{x}'-\mathbf{y}') - \gamma\mathbf{n}\cdot(\mathbf{x}'-\mathbf{y}')\right\}\right]\, dS(\mathbf{x}')\, dS(\mathbf{y}'),
\end{aligned} \tag{B.1}$$

where $\mathbf{e}_z$ is the unit vector for the z axis direction and $\mathbf{n}$ is the unit vector for $\mathbf{x}$ direction in (7.18) and (7.19). We make a change of variables from $\mathbf{x}'$ and $\mathbf{y}'$ to $\mathbf{p}$ (center-of-mass coordinate variable) and $\mathbf{q}$ (relative coordinate variable) by

$$\mathbf{p} = (\mathbf{x}' + \mathbf{y}')/2, \qquad \mathbf{q} = \mathbf{x}' - \mathbf{y}'. \tag{B.2}$$

Also, we introduce difference vectors $\mathbf{E}_r$ and $\mathbf{E}_t$ to simplify the integrals for the radial and tangential ensemble average:

$$\mathbf{E}_r = \mathbf{e}_z - \mathbf{n} = (-\sin\theta, 1-\cos\theta), \qquad |\mathbf{E}_r| = 2\sin(\theta/2),$$
$$\mathbf{E}_t = \mathbf{e}_z - \gamma\mathbf{n} = (-\gamma\sin\theta, 1-\gamma\cos\theta), \qquad |\mathbf{E}_t| = \sqrt{1+\gamma^2-2\gamma\cos\theta}. \tag{B.3}$$

When we consider the integrals in (B.1) with variables $\mathbf{p}$ and $\mathbf{q}$, the integration over $\mathbf{p}$ yields the area S and we can simplify the resulting equations using $\mathbf{E}_r$ and $\mathbf{E}_t$ to the form

$$\langle |u_r^{PP}|^2\rangle = \frac{Sk^3}{8\pi|\mathbf{x}|}\,[C_r(\theta)]^2 \int_S \langle \xi(\mathbf{x}')\xi(\mathbf{y}')\rangle \exp\left[ik\mathbf{E}_r\cdot\mathbf{q}\right]\, dS(\mathbf{q}),$$
$$\langle |u_t^{PS}|^2\rangle = \frac{Sk^3\gamma^3}{8\pi|\mathbf{x}|}\,[C_t(\theta)]^2 \int_S \langle \xi(\mathbf{x}')\xi(\mathbf{y}')\rangle \exp\left[ik\mathbf{E}_t\cdot\mathbf{q}\right]\, dS(\mathbf{q}). \tag{B.4}$$

The integration over $\mathbf{q}$ is simple in a polar coordinate system (r', ϕ'):

$$r' = |\mathbf{q}|, \qquad dS(\mathbf{q}) = r'dr'd\phi', \tag{B.5}$$

and the ensemble of fluctuation $\langle \xi(\mathbf{x}')\xi(\mathbf{y}')\rangle$ can be represented by the autocorrelation function (ACF) $N(r')$ for the stochastic media. Therefore, (B.4) can be written using (B.3) and (B.5) as

$$\langle |u_r^{PP}|^2\rangle = \frac{Sk^3}{8\pi|\mathbf{x}|}\,[C_r(\theta)]^2 \int_{r=0}^{r=\infty}\int_{\phi'=-\pi}^{\phi'=\pi} N(r')\exp\left[i2kr'\sin\left(\frac{\theta}{2}\right)\cos\phi'\right] r'dr'd\phi', \tag{B.6}$$
$$\langle |u_t^{PS}|^2\rangle = \frac{Sk^3\gamma^3}{8\pi|\mathbf{x}|}\,[C_t(\theta)]^2 \int_{r=0}^{r=\infty}\int_{\phi'=-\pi}^{\phi'=\pi} N(r')\exp\left[ikr'\sqrt{1+\gamma^2-2\gamma\cos\theta}\,\cos\phi'\right] r'dr'd\phi'.$$

We can express the power spectral density $\mathcal{P}$ for the stochastic medium in terms of $N(\mathbf{r})$ through a two-dimensional Fourier transform, which can be recast as a Hankel transform using the the representation of the zeroth order Bessel function ($J_0(x)$) as angular integral over the exponential function (cf., Frankel & Clayton, 1986)

$$\int_{-\pi}^{\pi} \exp[ix\cos\phi']\, d\phi' = 2\pi J_0(x), \tag{B.7}$$
$$\mathcal{P}(k) = 2\pi\int_0^\infty N(r')r'J_0(kr')\, dr'. \tag{B.8}$$

With these relations we can rewrite (B.6) as

$$\langle |u_r^{PP}|^2\rangle = \frac{k^3\, S}{8\pi|\mathbf{x}|}[C_r(\theta)]^2\, \mathcal{P}\left[2k\,\sin\frac{\theta}{2}\right].$$
$$\langle |u_t^{PS}|^2\rangle = \frac{k^3\gamma^3\, S}{8\pi|\mathbf{x}|}[C_t(\theta)]^2\, \mathcal{P}\left[k\sqrt{1+\gamma^2-2\gamma\cos\theta}\right], \tag{B.9}$$

where $P(k)$ is the power spectral density function (PSDF), the spectrum of the ACF $N(r)$.

Appendix C

Derivation of theoretical attenuation variation for 2-D SV-wave scattering

Following the procedure for the derivation of P-wave scattering attenuation in Section 7.3.1, we formulate the scattering attenuation rates of S waves (Q_S^{-1}) as a function of normalized wavenumber ($k_\beta a$) in 2-D random heterogeneous media.

When vertically incident (z-axis direction) and horizontally polarized (x-axis direction) plane S waves (Fig. 7.4) are considered as the primary waves, they can be represented as

$$u_x^0 = e^{i(k_\beta z - \omega t)}, \qquad u_z^0 = 0, \tag{C.1}$$

where ω is an angular frequency, k_β the wavenumber of incident S waves (ω/β_0), and β_0 the background S wave velocity. The scattered waves can be represented using body forces f_j^s ($j = x, z$ or 1,2) for the scattering effects from the variation of physical parameters, as shown in (7.6). Thus, the body forces f_j^s can be computed by using (7.3) and (C.1), and they are written in terms of the primary waves and the fluctuation of physical parameters as

$$f_x^s = -\left\{ k_\beta^2(\delta\rho\beta_0^2 - \delta\mu) + ik_\beta \frac{\partial}{\partial z}(\delta\mu) \right\} u_x^0, \qquad f_z^s = -ik_\beta \frac{\partial}{\partial x}(\delta\mu) u_x^0. \tag{C.2}$$

Using the empirical relationship (7.8) among physical parameters, equation (C.2) can be rewritten in terms of the fractional-fluctuation term $\xi(x, z)$ as

$$\begin{aligned} f_x^s &= -k_\beta\beta_0^2\rho_0 \left(k_\beta C_1^S \xi + iC_2^S \frac{\partial \xi}{\partial z} \right) \exp\left[i(k_\beta z - \omega t)\right], \\ f_z^s &= -ik_\beta\beta_0^2\rho_0\, C_2 \frac{\partial \xi}{\partial x} \exp\left[i(k_\beta z - \omega t)\right], \end{aligned} \tag{C.3}$$

where C_1^S and C_2^S are constants given by

$$C_1^S = -2, \quad C_2^S = K + 2. \tag{C.4}$$

Hereafter we use symbols without the subscript 0 representing the background medium for simplicity in the mathematical expressions.

Displacement fields, generated by body forces (f_k^s, k=x, z or 1,2) which are induced by perturbation of physical properties, can be expressed using the Green tensor $\overline{G}_{jk}(\mathbf{x}, \mathbf{x}')$:

$$u_j^s(\mathbf{x}) = \sum_{k=1}^{2} \int_{\mathsf{S}} f_k^s(\mathbf{x}')\, \overline{G}_{jk}(\mathbf{x}, \mathbf{x}')\, d\mathsf{S}(\mathbf{x}'), \quad j = 1, 2, \tag{C.5}$$

where S is the inhomogeneity area. With the far-field Green's functions (7.20), we can obtain scattered *P* (u_j^{SP}) and *S* (u_j^{SS}) waves at sufficiently large distances where near- and intermediate-field waves are not effective. The far-field scattered wavefields are given by

$$\begin{aligned} u_j^{SP} &= \sqrt{\frac{k_\alpha}{\gamma^2 8\pi|\mathbf{x}|}} \exp\left[-i(\omega t - k_\alpha|\mathbf{x}| + \frac{\pi}{4})\right] \cdot \left\{ -ik_\beta C_1^S A_{j1}^P(\theta) \int_{\mathsf{S}} \xi e^{ik_\alpha(\gamma z - \mathbf{n}\cdot\mathbf{x}')}\, d\mathsf{S}(\mathbf{x}') \right. \\ &\left. + C_2^S A_{j1}^P(\theta) \int_{\mathsf{S}} \frac{\partial \xi}{\partial z} e^{ik_\alpha(\gamma z - \mathbf{n}\cdot\mathbf{x}')}\, d\mathsf{S}(\mathbf{x}') + C_2^S A_{j2}^P(\theta) \int_{\mathsf{S}} \frac{\partial \xi}{\partial x} e^{ik_\alpha(\gamma z - \mathbf{n}\cdot\mathbf{x}')}\, d\mathsf{S}(\mathbf{x}') \right\}, \end{aligned} \tag{C.6}$$

and

$$\begin{aligned} u_j^{SS} &= \sqrt{\frac{k_\beta}{8\pi|\mathbf{x}|}} \exp\left[-i(\omega t - k_\beta|\mathbf{x}| + \frac{\pi}{4})\right] \cdot \left\{ -ik_\beta C_1^S A_{j1}^S(\theta) \int_{\mathsf{S}} \xi e^{ik_\beta(z - \mathbf{n}\cdot\mathbf{x}')}\, d\mathsf{S}(\mathbf{x}') \right. \\ &\left. + C_2^S A_{j1}^S(\theta) \int_{\mathsf{S}} \frac{\partial \xi}{\partial z} e^{ik_\beta(z - \mathbf{n}\cdot\mathbf{x}')}\, d\mathsf{S}(\mathbf{x}') + C_2^S A_{j2}^S(\theta) \int_{\mathsf{S}} \frac{\partial \xi}{\partial x} e^{ik_\beta(z - \mathbf{n}\cdot\mathbf{x}')}\, d\mathsf{S}(\mathbf{x}') \right\}, \end{aligned} \tag{C.7}$$

where γ is α/β and θ is the angle between the direction of incident waves and scattered wave propagation direction. Also, A_{ij}^k (i, j=1,2, k=*P*,*S*) is given in (7.21).

The integrations for the partial differentials of ξ in (C.6) and (C.7) can be simplified using partial integration. The resultant equations are given by

$$\begin{aligned} u_j^{SP} &= i\sqrt{\frac{k_\alpha^3}{\gamma^2 8\pi|\mathbf{x}|}} \left\{ -\gamma C_1^S A_{j1}^P(\theta) + (\cos\theta - \gamma) C_2^S A_{j1}^P(\theta) + \sin\theta\, C_2^S A_{j2}^P(\theta) \right\} \\ &\times \exp\left[-i(\omega t - k_\alpha|\mathbf{x}| + \frac{\pi}{4})\right] \int_{\mathsf{S}} \xi e^{ik_\alpha(\gamma z - \mathbf{n}\cdot\mathbf{x}')}\, d\mathsf{S}(\mathbf{x}'), \end{aligned} \tag{C.8}$$

and

$$\begin{aligned} u_j^{SS} &= i\sqrt{\frac{k_\beta^3}{8\pi|\mathbf{x}|}} \left\{ -C_1^S A_{j1}^S(\theta) + (\cos\theta - 1) C_2^S A_{j1}^S(\theta) + \sin\theta\, C_2^S A_{j2}^S(\theta) \right\} \\ &\times \exp\left[-i(\omega t - k_\beta|\mathbf{x}| + \frac{\pi}{4})\right] \int_{\mathsf{S}} \xi e^{ik_\beta(z - \mathbf{n}\cdot\mathbf{x}')}\, d\mathsf{S}(\mathbf{x}'). \end{aligned} \tag{C.9}$$

The scattered *P* and *S* waves can be considered on a single component (radial or tangential) by rotation of the coordinate axes (e.g., Sato & Fehler, 1998):

$$\begin{aligned} u_r^{SP} &= \sin\theta\, u_x^{SP} + \cos\theta\, u_z^{SP} \\ &= i\sqrt{\frac{k_\alpha^3}{\gamma^2 8\pi|\mathbf{x}|}}\, C_r^S(\theta) \exp\left[-i\left(\omega t - k_\alpha|\mathbf{x}| + \frac{\pi}{4}\right)\right] \int_{\mathsf{S}} \xi\, e^{ik_\alpha(\gamma z - \mathbf{n}\cdot\mathbf{x}')}\, d\mathsf{S}(\mathbf{x}'), \\ u_t^{SS} &= \cos\theta\, u_x^{SS} - \sin\theta\, u_z^{SS} \end{aligned} \tag{C.10}$$

$$= i\sqrt{\frac{k_\beta^3}{8\pi|\mathbf{x}|}}\, C_t^S(\theta) \exp\left[-i\left(\omega t - k_\beta|\mathbf{x}| + \frac{\pi}{4}\right)\right] \int_{\mathsf{S}} \xi\, e^{ik_\beta(z-\mathbf{n}\cdot\mathbf{x}')}\, d\mathsf{S}(\mathbf{x}'),$$

where $C_r^S(\theta)$ and $C_t^S(\theta)$ are

$$\begin{aligned} C_r^S(\theta) &= \sin\theta\left\{-\gamma C_1^S A_{11}^P(\theta) + (\cos\theta-\gamma)C_2^S A_{11}^P(\theta) + \sin\theta\, C_2^S A_{12}^P(\theta)\right\} \\ &\quad + \cos\theta\left\{-\gamma C_1 A_{21}^P(\theta) + (\cos\theta-\gamma)C_2^S A_{21}^P(\theta) + \sin\theta\, C_2^S A_{22}^P(\theta)\right\}, \\ C_t^S(\theta) &= \cos\theta\left\{-C_1^S A_{11}^S(\theta) + (\cos\theta-1)C_2^S A_{11}^S(\theta) + \sin\theta\, C_2^S A_{12}^S(\theta)\right\} \\ &\quad - \sin\theta\left\{-C_1^S A_{21}^S(\theta) + (\cos\theta-1)C_2^S A_{21}^S(\theta) + \sin\theta\, C_2^S A_{22}^S(\theta)\right\}. \end{aligned} \tag{C.11}$$

To get an average scattered energy, we consider the ensemble average for the displacement terms:

$$\begin{aligned} <|u_r^{SP}|^2> &= \frac{k_\alpha^3}{\gamma^2 8\pi|\mathbf{x}|}\,[C_r^S(\theta)]^2 \\ &\quad \times \int_{\mathsf{S}}\int_{\mathsf{S}} <\xi(\mathbf{x}')\xi(\mathbf{y}')> \exp\left[ik_\alpha\left\{\gamma\mathbf{e}_z\cdot(\mathbf{x}'-\mathbf{y}') - \mathbf{n}\cdot(\mathbf{x}'-\mathbf{y}')\right\}\right]\, d\mathsf{S}(\mathbf{x}')\, d\mathsf{S}(\mathbf{y}'), \\ <|u_t^{SS}|^2> &= \frac{k_\beta^3}{8\pi|\mathbf{x}|}\,[C_t^S(\theta)]^2 \\ &\quad \times \int_{\mathsf{S}}\int_{\mathsf{S}} <\xi(\mathbf{x}')\xi(\mathbf{y}')> \exp\left[ik_\beta\left\{\mathbf{e}_z\cdot(\mathbf{x}'-\mathbf{y}') - \mathbf{n}\cdot(\mathbf{x}'-\mathbf{y}')\right\}\right]\, d\mathsf{S}(\mathbf{x}')\, d\mathsf{S}(\mathbf{y}'), \end{aligned} \tag{C.12}$$

where $\mathbf{e}_z$ is the unit vector for the z axis direction. Following the procedure described in the Appendix B, we can rewrite (C.12) using the power spectral density function $\mathcal{P}(k)$ as

$$\begin{aligned} <|u_r^{SP}|^2> &= \frac{k_\alpha^3\,\mathsf{S}}{\gamma^2 8\pi|\mathbf{x}|}[C_r^S(\theta)]^2\,\mathcal{P}\left[k_\alpha\sqrt{1+\gamma^2-2\gamma\cos\theta}\right], \\ <|u_t^{SS}|^2> &= \frac{k_\beta^3\,\mathsf{S}}{8\pi|\mathbf{x}|}[C_t^S(\theta)]^2\,\mathcal{P}\left[2k_\beta\sin\frac{\theta}{2}\right]. \end{aligned} \tag{C.13}$$

The derivation of (C.13) from (C.12) is described in detail in the Appendix . Since Q_S^{-1} corresponds to the energy loss per unit area divided by wavenumber, we can express Q_S^{-1} in terms of the standard deviation (ϵ) of velocity fluctuation in the 2-D media by

$$\frac{Q_S^{-1}}{\epsilon^2} = \frac{1}{\mathsf{S}k_\beta}\int_\theta \left\{<|u_r^{SP}|^2> + <|u_t^{SS}|^2>\right\}\, d\mathsf{A}, \tag{C.14}$$

where A is the arc length through which scattered waves propagate and therefore $d\mathsf{A}$ is given by $r\, d\theta$ (Frankel & Clayton, 1986).

In order to determine a reasonable approximation for Q_S^{-1}, we consider the travel-time correction proposed by Sato (1984), which excludes the forward scattering energy inside the minimum scattering angle, with an idea that the travel time fluctuations are caused by longer wavelengths than the incident wavelength in a perturbed medium and cause scattering energy increase in the forward direction. Since the scattered angles of *SP*

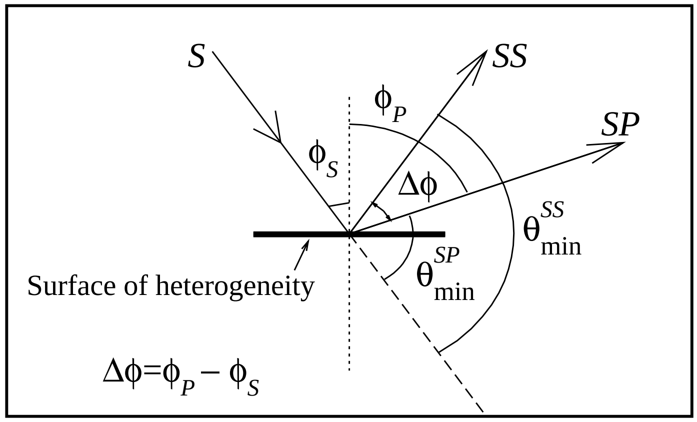

Fig. C.1. Diagram for determining the minimum scattering angle for *S* waves using the Snell's law. A specific situation is considered for the determination of $\theta_{\min}^{SP}$ in terms of $\theta_{\min}^{SS}$; *S* wave is incident with angle ϕ_S on the surface of heterogeneity for the perpendicular axis to the surface and *SS* scattered waves is reflected on the surface with angle $\theta_{\min}^{SS}$ for the incident direction (z-axis direction in this study). The *SP* scattered wave is reflected on the surface with angle ϕ_P for the perpendicular axis and $\theta_{\min}^{SP}$ for the incident direction.

and *SS* waves from a heterogeneity are different, we introduce $\theta_{\min}^{SP}$ for the P-wave type scattering and $\theta_{\min}^{SS}$ for the *S*-wave type scattering. Therefore we can represent the theoretical Q_S^{-1} with the travel-time correction as

$$\frac{Q_S^{-1}}{\epsilon^2} = \frac{r}{\mathsf{S}k_\beta}\left\{\int_{\theta_{\min}^{SP}}^{2\pi-\theta_{\min}^{SP}} < |u_r^{SP}|^2 > \,d\theta + \int_{\theta_{\min}^{SS}}^{2\pi-\theta_{\min}^{SS}} < |u_t^{SS}|^2 > \,d\theta\right\}. \tag{C.15}$$

When $|\mathbf{x}|$ is large enough, we can assume $|\mathbf{x}| \approx r$. Also, $\theta_{\min}^{SP}$ can be represented in terms of $\theta_{\min}^{SS}$ by using the Snell's law. When we consider the *SS* scattered waves which are reflected with the minimum scattering angle $\theta_{\min}^{SS}$ from the boundary of heterogeneity, the corresponding reflection angle of *SP* scattered waves can be calculated with consideration of the single scattering idea as (see, Fig. C.1)

$$\theta_{\min}^{SP} = \theta_{\min}^{SS} - \Delta\phi, \tag{C.16}$$

where $\Delta\phi = \phi_P - \phi_S$ and ϕ_j ($j = P, S$) is

$$\phi_S = \frac{\pi - \theta_{\min}^{SS}}{2}, \qquad \phi_P = \sin^{-1}(\gamma \sin\phi_S)\,. \tag{C.17}$$

Thus, the theoretical scattering variation is given by

$$\frac{Q_S^{-1}}{\epsilon^2} = \frac{k_\beta^2}{8\pi\gamma^5}\int_{\theta_{\min}^{SP}}^{2\pi-\theta_{\min}^{SP}} [C_r^S(\theta)]^2\,\mathcal{P}\left[\frac{k_\beta}{\gamma}\sqrt{1+\gamma^2-2\gamma\cos\theta}\right]\,d\theta$$
$$+\frac{k_\beta^2}{8\pi}\int_{\theta_{\min}^{SS}}^{2\pi-\theta_{\min}^{SS}} [C_t^S(\theta)]^2\,\mathcal{P}\left[2k_\beta\,\sin\frac{\theta}{2}\right]\,d\theta. \tag{C.18}$$

Appendix D

Derivation of theoretical attenuation variation for 2-D *SH*-wave scattering

Theoretical scattering attenuation expressions of 2-D *SH* waves are derived following the scheme in Section 7.3.1. The 2-D *SH* wave equation is given by

$$\rho \frac{\partial^2 u_y}{\partial t^2} - \frac{\partial}{\partial x}\left(\mu \frac{\partial u_y}{\partial x}\right) - \frac{\partial}{\partial z}\left(\mu \frac{\partial u_y}{\partial z}\right) = f_y, \tag{D.1}$$

where u_y is the *SH* displacement, μ the shear modulus, and f_y is the body force which is zero in steady state. *SH* waves (u_y^0) polarized in the y direction are incident in the z vertical direction,

$$u_y^0 = e^{i(k_\beta z - \omega t)}, \tag{D.2}$$

where k_β is the wavenumber of *SH* waves, ω the angular frequency, and ω can be expressed as $k_\beta \beta$ where $\beta = \sqrt{\mu/\rho}$. The perturbation of the wave velocity and the density is governed by

$$\xi(x, z) = \frac{\delta\beta}{\beta_0} = \frac{1}{K}\frac{\delta\rho}{\rho_0}, \tag{D.3}$$

where K is a constant controlling the density perturbation rate. Thus, from (D.3), $\delta\mu$ and $\delta\rho$ can be represented by

$$\delta\mu = \beta_0^2 \rho_0 (2 + K)\xi, \qquad \delta\rho = K\rho_0\xi. \tag{D.4}$$

The induced force (f_y^s) by the perturbation of wave velocity and the density is

$$f_y^s = (\rho_0 + \delta\rho)\frac{\partial^2 u_y^0}{\partial t^2} - \frac{\partial}{\partial x}\left[(\mu_0 + \delta\mu)\frac{\partial u_y^0}{\partial x}\right] - \frac{\partial}{\partial z}\left[(\mu_0 + \delta\mu)\frac{\partial u_y^0}{\partial z}\right], \tag{D.5}$$

and (D.5) can be simplified as

$$f_y^s = -\beta_0^2 \rho_0 \left(C_1^H k_\beta^2 \xi + i C_2^H k_\beta \frac{\partial \xi}{\partial z}\right) e^{i(k_\beta z - \omega t)}, \tag{D.6}$$

where $C_1^H = -2$ and $C_2^H = K + 2$.

The Green's function for the 2-D *SH* wave equation is given by (Arfken, 1986, p912)

$$G(\mathbf{x}, \mathbf{x}') = \frac{i}{4\beta_0^2 \rho_0} H_0^{(1)}(k_\beta |\mathbf{x} - \mathbf{x}'|), \tag{D.7}$$

where $\mathbf{x}$ is the receiver location, $\mathbf{x}'$ the source location, and $H_0^{(1)}$ is the zeroth-order Hankel function of the first kind. The $H_0^{(1)}(k_\beta|\mathbf{x} - \mathbf{x}'|)$ can be expressed in the asymptotic form as

$$H_0^{(1)}(k_\beta |\mathbf{x} - \mathbf{x}'|) = \sqrt{\frac{2}{\pi k_\beta |\mathbf{x}|}} \exp\left[i\left(k_\beta |\mathbf{x}| - k_\beta \mathbf{n} \cdot \mathbf{x}' - \frac{\pi}{4}\right)\right], \tag{D.8}$$

where $\mathbf{n}$ is the unit vector in $\mathbf{x}$ direction.

The scattered waves (u_y^s) developed by the perturbation can be expressed using both the Green's function and the induced force:

$$u_y^s(\mathbf{x}) = \int_{\mathsf{S}} f_y^s(\mathbf{x}') G(\mathbf{x}, \mathbf{x}')\, d\mathsf{S}(\mathbf{x}'). \tag{D.9}$$

Thus the scattered waves are given by

$$\begin{aligned} u_y^s = -i\sqrt{\frac{k_\beta^3}{8\pi|\mathbf{x}|}} &\exp\left[-\left(\omega t - k_\beta|\mathbf{x}| + \frac{\pi}{4}\right)\right] \\ &\times [C_1^H + C_2^H(1 - \cos\theta)] \int_{\mathsf{S}} \xi(\mathbf{x}') \exp[ik_\beta(z - \mathbf{n}\cdot\mathbf{x}')]\, d\mathsf{S}(\mathbf{x}'), \end{aligned} \tag{D.10}$$

where θ is the angle between vertical axis (incident direction) and wave propagation direction.

In order to estimate the energy of scattered waves, we measure the ensemble average of the waves:

$$\begin{aligned} \langle |u_y^s|^2 \rangle = &\frac{k_\beta^3}{8\pi|\mathbf{x}|}[C_1^H + C_2^H(1 - \cos\theta)]^2 \\ &\times \int_{\mathsf{S}}\int_{\mathsf{S}} \langle \xi(\mathbf{x}')\xi(\mathbf{y}')\rangle \exp[ik_\beta\{\mathbf{e}_z\cdot(\mathbf{x}' - \mathbf{y}') - \mathbf{n}\cdot(\mathbf{x}' - \mathbf{y}')\}]\, d\mathsf{S}(\mathbf{x}')\, d\mathsf{S}(\mathbf{y}'), \end{aligned} \tag{D.11}$$

where $\mathbf{e}_z$ is the unit vector for the z axis direction. Here (D.11) can be expressed in terms of power spectral density function $\mathcal{P}(k)$:

$$\langle |u_y^s|^2 \rangle = \frac{k_\beta^3 \mathsf{S}}{8\pi|\mathbf{x}|}[C_1^H + C_2^H(1 - \cos\theta)]^2\, \mathcal{P}\left(2k_\beta \sin\frac{\theta}{2}\right). \tag{D.12}$$

The scattering attenuation rate Q_{SH}^{-1} is estimated by the energy loss per unit area divided by wavenumber and the solid angle (π):

$$Q_{SH}^{-1} = \frac{\epsilon^2}{\pi \mathsf{S} k_\beta} \int_\theta \langle |u_y^s|^2\rangle\, d\mathsf{A}, \tag{D.13}$$

where A is the arc length, $d\mathsf{A}$ corresponds to $r\, d\theta$ and ϵ is the standard deviation of velocity fluctuation (ξ). Here, since the receiver is considered to locate at a far distance compared to the scatterers (i.e., $|\mathbf{x}| \gg |\mathbf{x}'|$), r can be approximated by $|\mathbf{x}|$.

By considering the travel-time correction with introduction of the minimum scattering angle ($\theta_{\min}$), the scattering attenuation rate is given by

$$\frac{Q_H^{-1}}{\epsilon^2} = \frac{k_\beta^2}{8\pi^2} \int_{\theta_{\min}}^{2\pi-\theta_{\min}} [C_1^H + C_2^H(1 - \cos\theta)]^2 \, \mathcal{P}\left(2k_\beta \sin\frac{\theta}{2}\right) \, d\theta. \tag{D.14}$$

References

Aagaard, B.T., Heaton, T.H. & Hall, J.F., 2001. Dynamic earthquake ruptures in the presence of lithostatic normal stresses: Implications for friction models and heat production, *Bull. seism. Soc. Am.*, **91**, 1765-1796.

Adams, D.A. & Abercrombie, R.E., 1998. Seismic attenuation above 10 Hz in southern California from coda wave recorded in the Cajon Pass borehole, *J. Geophys. Res.*, **103**, 24,257-24,270.

Aki, K., 1980. Attenuation of shear-waves in the lithosphere for frequencies from 0.05 to 25 Hz, *Phys. Earth Planet. Inter.*, **21**, 50-60.

Aki, K. & Richards, P.G., 1980. *Quantitative Seismology, Theory and Methods*, Volume 1, W.H. Freeman and Company, San Francisco.

Akinci, A. & Eyidoğan, H., 2000. Scattering and anelastic attenuation of seismic energy in the vicinity of north Anatolian fault zone, eastern Turkey, *Phys. Earth Planet. Inter.*, **122**, 229-239.

Alterman, Z. & Karal, Jr., F.C., 1968. Propagation of elastic waves in layered media by finite difference methods, *Bull. seism. Soc. Am.*, **58**, 367-398.

Alford, R.M., Kelly, K.R. & Boore, D.M., 1974. Accuracy of finite-difference modeling of the acoustic wave equation, *Geophysics*, **39**, 834-842.

Anant, K.S. & Dowla, F.U., 1997. Wavelet transform methods for phase identification in three-component seismograms, *Bull. seism. Soc. Am.*, **87**, 1598-1612.

Anderson, W.L., 1984. Computation of green's tensor integrals for three-dimensional electromagnetic problems using fast Hankel transforms, *Geophysics*, **49**, 1754-1759.

Anderson, W.L., 1989. A hybrid fast Hankel transform algorithm for electromagnetic modelling, *Geophysics*, **54**, 263-266.

Andrews, D.J. & Ben-Zion, Y., 1997. Wrinkle-like slip pulse on a fault between different materials, *J. Geophys. Res.*, **102**, 553-571.

Arfken, G., 1985. *Mathematical Methods for Physicists*, 3rd edition, Academic Press, New York.

Assefa, S., McCann, C., & Sothcott, J., 1999. Attenuation of *P*- and *S*-waves in limestones, *Geophys. Prospect.*, **47**, 359-392.

Augenbaum, J.M., 1992. The pseudospectral method for limited-area elastic wave calculations, in *Computational Methods in Geosciences* eds. W.E. Fitzgibbon & M.F. Wheeler, SIAM, Philadelphia.

Bayliss, A., Jordan, K.E., Lemesurier, B.J. & Turkel, E., 1986. A fourth-order accurate finite-difference scheme for the computation of elastic waves, *Bull. seism. Soc. Am.*, **76**, 1115-1132.

Bear, L.K. & Pavlis, G.L., 1997. Estimation of slowness vectors and their uncertainties using multi-wavelet seismic array processing, *Bull. seism. Soc. Am.*, **87**, 755-769.

Bear, L.K. & Pavlis, G.L., 1999. Multi-channel estimation of time residuals from broad band seismic data using multi-wavelets, *Bull. seism. Soc. Am.*, **89**, 681-692.

Belleni-Morante, A., 1979. *Applied Semigroups and Evolution Equations*, Oxford University Press, Great Britain.

Benites, R., Aki, K. & Yomogida, 1992. Multiple scattering of *SH* waves in 2-D media with many cavities, *Pure Appl. Geophys.*, **138**, 353-390.

Ben-Menahem, A. & Singh, S.J., 1981. *Seismic Waves and Sources*, Springer-Verlag, Berlin, Heidelberg, New York.

Ben-Zion, Y., 1998. Properties of seismic fault zone waves and their utility for imaging low-velocity structures, *J. geophys. Res.*, **103**, 12,567-12,585.

Ben-Zion, Y., 2001. Dynamic ruptures in recent models of earthquake faults, *J. Mech. Phys. Solids*, **49**, 2209-2244.

Ben-Zion, Y. & Aki, K., 1990. Seismic radiation from an *SH* line source in a laterally heterogeneous planar fault zone, *Bull. seism. Soc. Am.*, **80**, 971-994.

Ben-Zion, Y. & Andrews, D.J., 1998. Properties and implications of dynamic rupture along a material interface, *Bull. seism. Soc. Am.*, **88**, 1085-1094.

Ben-Zion, Y. & Huang, Y., 2002. Dynamic rupture on an interface between a compliant fault zone layer and a stiffer surrounding solid, *J. Geophys. Res.*, **107** (B2), 10.1029/2001JB000254.

Beroza, G.C & Mikumo, T., 1996. Short slip duration in dynamic rupture in the presence of heterogeneous fault properties, *J. Geophys. Res.*, **101**, 22.449-22.460.

Beylkin, G., 1992. On the representation of operators in bases of compactly supported wavelets, *SIAM J. Numer. Anal.*, **6**(6), 1716-1740.

Beylkin, G., 1993. Wavelets and fast numerical algorithms, *Proceedings of Symposia in Applied Mathematics*, **47**, 89-117.

Beylkin, G. & Keiser, J.M., 1997. On the adaptive numerical solution of nonlinear partial differential equations in wavelet bases, *J. Comput. Phys.*, **132**, 233-259.

Beylkin, G., Keiser, J.M. & Vozovoi, L., 1998. A new class of time discretization schemes for the solution of nonlinear PDEs, *J. Comput. Phys.*, **147**, 362-387.

Birch, F., 1961. The velocity of compressional waves in rocks to 10 kilobars, part 2, *J. Geophys. Res*, **66**, 2199-2224.

Boore, D.M., 1972. Finite difference methods for seismic wave propagation in heterogeneous materials, in *Methods in Computational Physics*, volume 11, Seismology: Surface Waves and Earth Oscillations, ed. Bolt, B.A., pp1-37, Academic Press, New York.

Bouchon, M., 1981. A simple method to calculate Green's functions for elastic layered media, *Bull. seism. Soc. Am.*, **71**, 959-971.

Bouchon, M., Schultz, C.A. & Toksöz, M.N., 1996. Effect of three-dimensional topography on seismic motion, *J. Geophys. Res.*, **101**, 5835-5846.

Burridge, R., 1976. *Some Mathematical Topics in Seismology*, Courant Institute of Mathematical Sciences, New York University.

Cai, W. & Wang, J., 1996. Adaptive multiresolution collocation methods for initial boundary value problems of nonlinear PDEs, *SIAM J. Numer. Anal.*, **33**, 937-970.

Campillo, M. & Plantet, J.L., 1991. Frequency dependence and spatial distribution of seismic attenuation in France: experimental results and possible interpretations, *Phys. Earth Planet. Inter.*, **67**, 48-64.

Carcione, J.M., 1994. The wave equation in generalized coordinates, *Geophysics*, **59**, 1911-1919.

Carcione, J.M., 1998. Scattering of elastic waves by a plane crack of finite width in a transversely isotropic medium, *Int. J. Num. Anal. Meth.*, **22**, 263-275.

Carcione, J.M., Kosloff, D. & Kosloff, R., 1988. Wave-propagation simulation in an elastic anisotropic (transversely isotropic) solid, *Quart. J. Mech. Appl. Math.*, **41** (3), 319-345.

Carpenter, P.J. & Sanford, A.R., 1985. Apparent *Q* for upper crustal rocks of the Central Rio Grande Rift, *J. Geophys. Res.*, **90**, 8661-8674.

Castro, R.R., Rebollar, C.J., Inzunza, L., Orozco, L., Sánchez, J., Gálvez, O., Farfán, F.J. & Méndez, I., 1997. Direct body-wave *Q* estimates in northern Baja California, Mexico, *Phys. Earth Planet. Inter.*, **103**, 33-38.

Cerjan, C., Kosloff, D., Kosloff, R. & Reshef, M., 1985. A nonreflecting boundary condition for discrete acoustic and elastic wave equations, *Geophysics*, **50**, 705-708.

Chaljub, E. & Tarantola, A., 1997. Sensitivity of *SS* precursors to topography on the upper-mantle 660-km discontinuity, *Gephys. Res. Lett.*, **24**, 2613-2616.

Chan, Y.T., 1995. *Wavelet Basics*, Kluwer Academic Publishers, Boston.

Chernov, L.A., 1960. *Wave Propagation in a Random Medium*, McGraw-Hill Book Company, Inc., New York.

Chung, T.-W. & Sato, H., 2001. Attenuation of high-frequency *P* and *S* waves in the crust of southeastern South Korea, *Bull. seism. Soc. Am.*, **91**, 1867-1874.

Clayton, R. & Engquist, B., 1977. Absorbing boundary conditions for acoustic and elastic wave equations, *Bull. seism. Soc. Am.*, **67**, 1529-1540.

Cormier, V.F., 1989. Slab diffraction of *S* waves, *J. Geophys. Res.*, **94**, 3006-3024.

Coutant, O., 1989. Numerical study of the diffraction of elastic waves by fluid-filled cracks, *J. Geophys. Res.*, **94**, 17805-17818.

Coutant, O., Virieux, J., & Zollo, A., 1995. Numerical source implementation in a 2D finite difference scheme, *Bull. seism. Soc. Am.*, **85**, 1507-1512.

Dahmen, W., 1997. Wavelet and multiscale methods for operator equations, *Acta Numerica*, **6**, 55-228.

Dai, N., Vafidis, A. & Kanasewich, E., 1994. Composite absorbing boundaries for the numerical simulation of seismic waves, *Bull. seism. Soc. Am.*, **84** (1), 185-191.

Daubechies, I., 1992. *Ten Lectures on Wavelets*, Society for Industrial and Applied Mathematics, Philadelphia, Pennsylvania.

Del Pezzo, E., Ibanez, J., Morales, J., Akinci, A. & Maresca, R., 1995. Measurement of intrinsic and scattering seismic attenuation in the crust, *Bull. seism. Soc. Am.*, **85**, 1373-1380.

Der, Z.A., 1998. High-frequency *P*- and *S*-wave attenuation in the Earth, *Pure Appl. Geophys.*, **153**, 273-310.

Deslauriers, G. & Dubuc, S., 1989. Symmetric iterative interpolation process, *Constr. Approx.*, **5**, 49-68.

Drijkoningen, G.G., 1991. Tunnelling and the generalized ray method in piecewise homogeneous media, *Geophys. Prospect.*, **39**, 757-781.

Dubuc, S., 1986. Interpolation through an iterative scheme, *J. Math. Anal. Appl.*, **114**, 185-204.

Faccioli, E., Maggio, F., Quarteroni, A. & Tagliani, A., 1996. Spectral-domain decomposition methods for the solution of acoustic and elastic wave equations, *Geophysics*, **61**, 1160-1174.

Falk, J., Tessmer, E., & Gajewski, D., 1998. Efficient finite-difference modelling of seismic waves using locally adjustable time steps, *Geophys. Prospect.*, **46**, 603-616.

Fang, Y. & Müller, G., 1996. Attenuation operators and complex wave velocities for scattering in random media, *Pure Appl. Geophys.*, **148**, 269-285.

Fehler, M., Hoshiba, M., Sato, H., & Obara, K., 1992. Separation of scattering and intrinsic attenuation for the Kanto-Tokai region, Japan, using measurements of *S*-wave energy versus hypocentral distance, *Geophys. J. Int.*, **108**, 787-800.

Fehler, M., Sato, H. & Huang, L.-J., 2000. Envelope broadening of outgoing waves in 2D random media: A comparison between the Markov approximation and numerical simulations, *Bull. seism. Soc. Am.*, **90**, 914-928.

Ferziger, J.H., 1981. *Numerical Methods for Engineering Application*, John Wiley & Sons, Inc., US, p.270.

Flanagan, M.P. & Wiens, D.A., 1998. Attenuation of broadband *P* and *S* waves in Tonga: observations of frequency dependent *Q*, *Pure Appl. Geophys.*, **153**, 345-375.

Frankel, A., 1989. A review of numerical experiments on seismic wave scattering, *Pure Appl. Geophys.*, **131**, 639-685.

Frankel, A. & Clayton, R., 1986. Finite difference simulation of seismic scattering: Implications for the propagation of short-period seismic waves in the crust and models in crustal heterogeneity, *J. Geophys. Res.*, **91**, 6465-6489.

Frankel, A., McGarr, A., Bicknell, J. Mori, J., Seeber, L., & Cranswick, E., 1990. Attenuation of high-frequency shear waves in the crust: measurements from New York State, South Africa, and southern California, *J. Geophys. Res.*, **95**, 17441-17457.

Frankel, A., 1993. Three-dimensional simulations of ground motions in the San Bernardino valley, California, for hypothetical earthquakes on the San Andreas fault, *Bull. seism. Soc. Am.*, **83**, 1020-1041.

Frenje, L. & Juhlin, C., 2000. Scattering attenuation: 2-D and 3-D finite difference simulations vs. theory, *J. Appl. Geophys.*, **44**, 33-46.

Fröhlich, J. & Schneider, K., 1997. An adaptive wavelet-Vaguelette algorithm for the solution of PDEs, *J. Comput. Phys.*, **130**, 174-190.

Fuchs, K. & Schulz, K., 1976. Tunneling of low-frequency waves through the subcrustal lithosphere, *J. Geophys.*, **42**, 175-190.

Furumura, M., Kennett, B.L.N. & Furumura, T., 1999. Seismic wavefield calculation for laterally heterogeneous earth models - II. the influence of upper mantle heterogeneity, *Geophys. J. Int.*, **139**, 623-644.

Furumura, T. & Kennett, B.L.N., 1998. On the nature of regional seismic phases- III. The influence of crustal heterogeneity on the wavefield for subduction earthquakes: The 1985 Michoacan and 1995 Copala, Guerrero, Mexico earthquakes, *Geophys. J. Int.*, **135**, 1060-1084.

Furumura, T., Kennett, B.L.N., & Furumura, M., 1998. Seismic wavefield calculation for laterally heterogeneous whole earth models using the pseudospectral method, *Geophys. J. Int.*, **135**, 845-860.

Garvin, W.W., 1956. Exact transient solution of the buried line source problem, *Proc. Royal Soc. London, Series A*, **234**, 528-541.

Givoli, D., 1991. Non-reflecting boundary conditions, *J. Comput. Phys.*, **94**, 1-29.

Gottlieb, D., Gunzburger, M. & Turkel, E., 1982. On numerical boundary treatment of hyperbolic systems for finite-difference and finite element methods, *SIAM J. Numer. Anal.*, **19**, 671-682.

Graves, R.W., 1996. Simulating seismic wave propagation in 3D elastic media using staggered-grid finite differences, *Bull. seism. Soc. Am.*, **86**, 1091-1106.

Haskell, N.A., 1953. The dispersion of surface waves on multilayered media, *Bull. seism. Soc. Am.*, **43**, 17-34.

Hatzidimitriou, P.M., 1994. Scattering and anelastic attenuation of seismic energy in northern Greece, *Pure Appl. Geophys.*, **143**, 587-601.

Hatzidimitriou, P.M., 1995. *S*-wave attenuation in the crust in northern Greece, *Bull. seism. Soc. Am.*, **85**, 1381-1387.

Hoffman, J.D., 1992. *Numerical Methods for Engineers and Scientists*, McGraw-Hill, Inc., US.

Holmström, M., 1999. Solving hyperbolic PDEs using interpolating wavelets, *SIAM J. Sci. Comput.*, **21** (2), 405-420.

Hong, T.-K., 2003. Scattering attenuation ratios of *P* and *S* waves in elastic media, *Geophys. J. Int.*, (submitted).

Hong, T.-K. & Kennett, B.L.N., 2002a. A wavelet-based method for simulation of two-dimensional elastic wave propagation, *Geophys. J. Int.*, **150**, 610-638.

Hong, T.-K. & Kennett, B.L.N., 2002b. On a wavelet-based method for the numerical simulation of wave propagation, *J. Comput. Phys.*, **183**, 577-622.

Hong, T.-K. & Kennett, B.L.N., 2003a. Scattering attenuation of 2D elastic waves: theory and numerical modeling using a wavelet-based method, *Bull. seism. Soc. Am.*, **93** (2), 922-938.

Hong, T.-K. & Kennett, B.L.N., 2003b. Modelling of seismic waves in heterogeneous media using a wavelet-based method: application to fault and subduction zones, *Geophys. J. Int.*, (in press).

Hong, T.-K. & Kennett, B.L.N., 2003c. Scattering of elastic waves in media with a random distribution of fluid-filled cavities: theory and numerical modelling, *Geophys. J. Int.*, (submitted).

Hoshiba, M., 2000. Large fluctuation of wave amplitude produced by small fluctuation of velocity structure, *Phys. Earth Planet. Inter.*, **120**, 201-217.

Hough, S.E., Ben-Zion, Y., & Leary, P., 1994. Fault-zone waves observed at the Southern Joshua Tree earthquake rupture zone, *Bull. seism. Soc. Am.*, **84**, 761-767.

Huang, B.-S., Teng, T.-L., & Yeh, Y.T., 1995. Numerical modeling of fault-zone trapped waves: Acoustic case, *Bull. seism. Soc. Am.*, **85**, 1711-1717.

Hudson, J.A., 1980. Overall properties of a cracked solid, *Math. Proc. Camb. Phil. Soc.*, **88**, 371-384.

Hudson, J.A., 1981. Wave speeds and attenuation of elastic waves in material containing cracks, *Geophys. J. R. astr. Soc.*, **64**, 133-150.

Hudson, J.A., 1991. Overall properties of heterogeneous material, *Geophys. J. Int.*, **107**, 505-511.

Hudson, J.A. & Heritage, J.R., 1981. The use of the Born approximation in seismic scattering problems, *Geophys. J. R. astr. Soc.*, **66**, 221-240.

Igel, H., Ben-Zion, Y., & Leary, P.C., 1997. Simulation of *SH*- and *P-SV*-wave propagation in fault zones, *Geophys. J. Int.*, **128**, 533-546.

Igel, H. & Gudmundsson, O., 1997. Frequency-dependent effects on travel times and waveforms of long-period *S* waves: Implications for the scale of mantle heterogeneity, *Phys. Earth Planet. Int.*, **104**, 229-246.

Igel, H., Jahnke, G., & Ben-Zion, Y., 2002. Numerical simulation of fault zone guided waves: Accuracy and 3-D effects, *Pure Appl. Geophys.*, **159**, 2067-2083.

Igel, H., Mora, P., & Riollet, B., 1995. Anisotropic wave propagation through finite-difference grids, *Geophysics*, **60**, 1203-1216.

Igel, H. & Weber, M., 1995. *SH* wave propagation in the whole mantle using high-order finite differences, *Geophys. Res. Lett.*, **22**, 731-734.

Igel, H. & Weber, M., 1996. *P-SV* wave propagation in the Earth's mantle using finite differences: Applications to heterogeneous lowermost mantle structure, *Geophys. Res. Lett.*, **23**, 415-418.

Jahnke, G., Igel, H., & Ben-Zion, Y., 2002. Three-dimensional calculations of fault-zone-guided waves in various irregular structures, *Geophys. J. Int.*, **151**, 416-426.

Jameson, L., 1995. On the spline-based wavelet differentiation matrix, *Appl. Numer. Math.*, **17**, 33-45.

Jannaud, L.R., Adler, P.M. & Jacquin, C.G., 1991. Frequency dependence of the *Q* factor in random media, *J. Geophys. Res.*, **96**, 18,233-18,243.

Jih, R.-S., McLaughlin, K.L. & Der, Z.A., 1988. Free-boundary conditions of arbitrary polygonal topography in a two-dimensional explicit elastic finite-difference scheme, *Geophysics*, **53**, 1045-1055.

Kanasewich, E.R., 1981. *Time Sequence Analysis in Geophysics*, 3rd edition, The University of Alberta Press.

Kasahara, K., 1981. *Earthquake Mechanics*, Cambridge University Press, Cambridge.

Käser, M. & Igel, H., 2001. Numerical simulation of 2D wave propagation on unstructured grids using explicit differential operators, *Geophys. Prospect.*, **49**, 607-619.

Kawahara, J., 2002. Cutoff scattering angles for random acoustic media, *J. Geophys. Res.*, **107** (B1), doi:10.1029/2001JB000429.

Kawahara, J. & Yamashita, T., 1992. Scattering of elastic waves by a fracture zone containing randomly distributed cracks, *Pure Appl. Geophys.*, **139**, 121-144.

Kelly, K.R., Ward, R.W., Treitel, S. & Alford, R.M., 1976. Synthetic seismograms: A finite-difference approach, *Geophysics*, **41**, 2-27.

Kennett, B.L.N., 1972. Seismic waves in laterally inhomogeneous media, *Geophys. J. R. astr. Soc.*, **27**, 301-336.

Kennett, B.L.N., 1983. *Seismic Wave Propagation in Stratified Media*, Cambridge University Press, Cambridge.

Kennett, B.L.N., 1988. Radiation from a moment-tensor source, in *Seismological Algorithm, Computational Methods and Computer Programs*, ed. Doornbos, D.J., Academic Press, Inc., San Diego.

Kennett, B.L.N., 2001. *The Seismic Wavefield*, volume I: Introduction and theoretical development, Cambridge University Press, New York, p.370.

Kennett, B.L.N., 2002. *The Seismic Wavefield*, volume II: Interpretation of seismograms on regional and global scales, Cambridge University Press, New York, p.534.

Kennett, B.L.N., Engdahl, E.R., & Buland, R., 1995. Constraints on seismic velocities in the Earth from travel times, *Geophys. J. Int.*, **122**, 108-124.

Kennett, B.L.N. & Furumura, T., 2002. The influence of 3-D structure on the propagation of seismic waves away from earthquakes, *Pure Appl. Geophys.*, **159**, 2113-2131.

Kilb, D., Gomberg, J. & Boldin, P., 2000. Triggering of earthquake aftershocks by dynamic stresses, *Nature*, **408**, 570-574.

Klimeš, L., 2002. Correlation functions of random media, *Pure Appl. Geophys.*, **159**, 1811-1831.

Komatitsch, D., Barnes, C. & Tromp, J., 2000. Wave propagation near a fluid-solid interface: A spectral-element approach, *Geophysics*, **66**, 623-631.

Komatitsch, D., Coutel, F. & Mora, P., 1996. Tensorial formulation of the wave equation for modelling curved interfaces, *Geophys. J. Int.*, **127**, 156-168.

Komatitsch, D. & Vilotte, J.-P., 1998. The spectral element method: An efficient tool to simulate the seismic response of 2D and 3D geological structures, *Bull. seism. Soc. Am.*, **88**, 368-392.

Komatitsch, D. & Tromp, J., 1999. Introduction to the spectral element method for three-dimensional seismic wave propagation, *Geophys. J. Int.*, **139**, 806-822.

Komatitsch, D. & Tromp, J., 2002. Spectral-element simulations of global seismic wave propagation- I. validation, *Geophys. J. Int.*, **149**, 390-412.

Korneev, V.A. & Johnson, L.R., 1993. Scattering of elastic waves by a spherical inclusion- I. Theory and numerical results, *Geophys. J. Int.*, **115**, 230-250.

Kosloff, D. & Baysal, E., 1982. Forward modeling by a Fourier method, *Geophysics*, **47**, 1402-1412.

Kosloff, D., Kessler, D., Filho, A.Q., Tessmer, E., Behle, A. & Strahilevitz, R., 1990. Solution of the equations of dynamic elasticity by a Chebychev spectral method, *Geophysics*, **55**, 734-748.

Kosloff, D., Reshef M. & Loewenthal, D., 1984. Elastic wave calculations by the Fourier method, *Bull. seism. Soc. Am.*, **74**, 875-891.

Kosloff, D. & Tal-Ezer, H., 1993. A modified Chebyshev pseudospectral method with an $O(N^{-1})$ time step restriction, *J. Comput. Phys.*, **104**, 457-469.

Kosloff, R. & Kosloff, D., 1986. Absorbing boundaries for wave propagation problems, *J. Comput. Phys.*, **63**, 363-376.

Kuhn, M.J., 1985. A numerical study of Lamb's problem, *Geophys. Prosp.*, **33**, 1103-1137.

Lamb, H., 1904. On the propagation of tremors over the surface of an elastic solid, *Phil. Trans, R. Soc. London, Ser. A*, **203**, 1-42.

Lay, T. & Wallace, T.C., 1995. *Modern Global Seismology*, Academic Press, Inc., San Diego.

Lay, T. & Young, C.J., 1989. Waveform complexity in teleseismic broadband *SH* displacements: Slab diffractions or deep mantle reflections? *Geophys. Res. Lett.*, **16**, 605-608.

Levander, A.R., 1988. Fourth-order finite-difference *P-SV* seismograms, *Geophysics*, **53**, 1425-1436.

Lewalle, J., 1998. Formal improvements in the solution of the wavelet-transformed Poisson and diffusion equations, *J. Math. Phys.*, **39**, 4119-4128.

Li, Y.-G., 1988. *Trapped Modes in a Transversely Isotropic Fault-Zone*, PhD Thesis, University of Southern California, pp168-189.

Li, Y.-G., Aki, K., Vidale, J.E. & Xu, F., 1999. Shallow structure of the Landers fault zone from explosion-generated trapped waves, *J. geophys. Res.*, **104**, 20,257-20,275.

Li, Y.-G. & Leary, P.C., 1990. Fault zone trapped seismic waves, *Bull. seism. Soc. Am.*, **80**, 1245-1271.

Li, Y.-G., Leary, P.C., Aki, K., & Malin, P.E., 1990. Seismic trapped modes in hte Oroville and San Andreas fault zones, *Science*, **249**, 763-766.

Li, Y.-G. & Vidale, J.E., 1996. Low-velocity fault-zone guided waves: numerical investigations of trapping efficiency, *Bull. seism. Soc. Am.*, **86**, 371-378.

Li, Y.-G., M., Vidale, J.E., Day, S.M., Oglesby, D.D., & the SCEC Field Working Team, 2002. Study of the 1999 M 7.1 Hector mine, California, earthquake fault plane by trapped waves, *Bull. seism. Soc. Am.*, **92**, 1318-1332.

Lilly, J.M. & Park, J., 1995. Multiwavelet spectral and polarization analysis of seismic records, *Gephys. J. Int.*, **122**, 1001-1021.

Lippert, R.A., Arias, T.A. & Edelman, A., 1998. Multiscale computation with interpolating wavelets *J. Comput. Phys.*, **140**, 278-310.

Liu, E., Crampin, S. & Hudson, J.A., 1997. Diffraction of seismic waves by cracks with application to hydraulic fracturing, *Geophysics*, **62**, 253-265.

Liu, Y., Wu, R.-S. & Ying, C.F., 2000. Scattering of elastic waves by an elastic or viscoelastic cylinder, *Geophys. J. Int.*, **142**, 439-460.

Mahrer, K.D., 1990. Numerical time step instability and Stacey's and Clayton-Engquist's absorbing boundary conditions, *Bull. seism. Soc. Am.*, **80**, 213-217.

Mai, P.M. & Beroza, G.C., 2002. A spatial random field model to characterize complexity in earthquake slip, *J. Geophys. Res.*, **107** (B11), 2308, doi:10.1029/2001JB000588.

Mayeda, K., Koyanagi, S., Hoshiba, M., Aki, K., & Zeng, Y., 1992. A comparative study of scattering, intrinsic, and coda Q^{-1} for Hawaii, Long Valley, and central California between 1.5 and 15.0 Hz, *J. Geophys. Res.*, **97**, 6643-6659.

Menke, W., Levin, V., & Sethi, R., 1995. Seismic attenuation in the crust at the mid-Atlantic plate boundary in south-west Iceland, *Geophys. J. Int.*, **122**, 175-182.

Moczo, P., 1998. *Introduction to Modeling Seismic Wave Propagation by the Finite-Difference Method*, Lecture Notes, Disaster Prevention Research Institute, Kyoto University.

Moczo, P., Bystricky, E., Kristek, J., Carcione, J.M. & Bouchon, M., 1997. Hybrid modeling of *P-SV* seismic motion at inhomogeneous viscoelastic topographic structures, *Bull. seism. Soc. Am.*, **87**, 1305-1323.

Moczo, P., Kristek, J. & Halada, L., 2000. 3D fourth-order staggered-grid finite-difference schemes: Stability and grid dispersion, *Bull. seism. Soc. Am.*, **90**, 587-603.

Modiano, T. & Hatzfeld, D., 1982. Experimental study of the spectral content for shallow earthquakes, *Bull. seism. Soc. Am.*, **72**, 1739-1758.

Morse, P.M. & Feshbach, H., 1953. *Methods of Theoretical Physics*, Part I, McGraw-Hill Book Company, Inc., New York.

Murai, Y., Kawahara, J. & Yamashita, T., 1995. Multiple scattering of *SH* waves in 2-D elastic media with distributed cracks, *Geophys. J. Int.*, **122**, 925-937.

Nagano, K., 1998. Crack-wave dispersion at a fluid-filled fracture with low-velocity layers, *Geophys. J. Int.*, **134**, 903-910.

Nolet, G., Grand, S.P. & Kennett, B.L.N., 1994. Seismic heterogeneity in the upper mantle, *J. Geophys. Res.*, **99**, 23,753-23,766.

Ohminato, T. & Chouet, B.A., 1997. A free-surface boundary condition for including 3D topography in the finite-difference method, *Bull. seism. Soc. Am.*, **87**, 494-515.

Oglesby, D.D., Archuleta, R.J. & Nielsen, S.B., 2000. Dynamics of dip-slip faulting: Explorations in two dimensions, *J. Geophys. Res.*, **105**, 13,643-13,653.

Pankow, K.L. & Lay, T., 2002. Modeling *S* wave amplitude patterns for events in the Kurile slab using three-dimensional Gaussian beams, *J. Geophys. Res.*, **107** (B8), 10.1029/2001JB000594.

Pao, Y.-H. & Mow, C.-C., 1973. *Diffraction of Elastic Waves and Dynamic Stress Concentrations*, Crane, Russak & Company Inc., New York.

Pilant, W.L., 1972. Complex roots of the Stoneley-wave equation in the finite-difference method, *Bull. seism. Soc. Am.*, **62**, 285-299.

Pilant, W.L., 1979. *Elastic Waves in the Earth*, Elsevier Scientific Publishing Company, New York.

Pointer, T., Liu, E. & Hudson, J.A., 1998. Numerical modelling of seismic waves scattered by hydrofractures: application of the indirect boundary element method, *Geophys. J. Int.*, **135**, 289-303.

Powers, D.L., 1972. *Boundary Value Problems*, Academic Press, New York.

Qian, S. & Weiss, J., 1993. Wavelets and the numerical solution of partial differential equations, *J. Comput. Phys.*, **106**, 155-175.

Queen, J.H. & Rizer, W., 1990. An integrated study of seismic anisotropy and the natural fracture system at the Conoco borehole test facility, Kay County, Oklahoma, *J. Geophys. Res.*, **95**, 11255-11273.

Rosa, J.W.C., Cardoso, F.A.C.M., Aki, K., Malvar, H.S., Artola, F.A.V. & Rosa, J.W.C., 2001. Modelling elastic media with the wavelet transform, *Geophys. J. Int.*, **146**, 454-488.

Roth, M., 2001. *Personal communications*.

Roth, E.G., Wiens, D.A. & Zhao, D., 2000. An empirical relationship between seismic attenuation and velocity anomalies in the upper mantle, *Geophys. Res. Lett.*, **27**, 601-604.

Roth, M. & Korn, M., 1993. Single scattering theory versus numerical modelling in 2-D random media, *Geophys. J. Int.*, **112**, 124-140.

Sarker, G. & Abers, G.A., 1998. Comparison of seismic body wave and coda wave measures of *Q*, *Pure Appl. Geophys.*, **153**, 665-683.

Sato, H., 1982. Amplitude attenuation of impulsive waves in random media based on travel time corrected mean wave formalism, *J. Acoust. Soc. Am.*, **71**, 559-564.

Sato, H., 1984. Attenuation and envelope formation of three-component seismograms of small local earthquakes in randomly inhomogeneous lithosphere, *J. Geophys. Res.*, **89**, 1221-1241.

Sato, H. & Fehler, M.C., 1998. *Seismic Wave Propagation and Scattering in the Heterogeneous Earth*, Springer-Verlag, New York.

Sekiguchi, S., 1992. Amplitude distribution of seismic waves for laterally heterogeneous structures including a subducting slab, *Geophys. J. Int.*, **111**, 448-464.

Shapiro, N.M., Olsen, K.B. & Singh, S.K., 2000. Wave-guide effects in subduction zones: Evidence from three-dimensional modeling, *Geophys. Res. Lett.*, **27**, 433-436.

Shapiro, S.A. & Kneib, G., 1993. Seismic attenuation by scattering: Theory and numerical results, *Geophys. J. Int.*, **114**, 373-391.

Shapiro, S.A., Schwarz, R. & Gold, N., 1996. The effect of random isotropic inhomogeneities on the phase velocity of seismic waves, *Geophys. J. Int.*, **127**, 783-794.

Shensa, M.J., 1992. The discrete wavelet transform: Wedding the À Trous and Mallat algorithms, *IEEE Trans. on Signal Processing*, **40** (10), 2464-2482.

Shiomi, K., Sato, H. & Ohtake, M., 1997. Broad-band power-law spectra of well-log data in Japan, *Geophys. J. Int.*, **130**, 57-64.

Sneddon, I.N., 1972. *The Use of Integral Transforms*, McGraw-Hill, Inc., New York.

Sochacki, J., Kubichek, R., George, J., Fletcher, W.R. & Smithson, S., 1987. Absorbing boundary conditions and surface waves, *Geophysics*, **52**, 60-71.

Spetzler, J. & Snieder, R., 2001. The effect of small-scale heterogeneity on the arrival time of waves, *Geophys. J. Int.*, **145**, 786-796.

Stacey, R., 1988. Improved transparent boundary formulations for the elastic-wave equation, *Bull. seism. Soc. Am.*, **78**, 2089-2097.

Stephen, R.A., Cardo-Casas, F. & Cheng, C.H., 1985. Finite-difference synthetic acoustic logs, *Geophysics*, **50**, 1588-1609.

Strang, G. & Nguyen, T., 1996. *Wavelets and Filter Banks*, Wellesley-Cambridge Press, Wellesley, USA.

Tal-Ezer, H., Kosloff, D. & Koren, Z., 1987. An accurate scheme for seismic forward modelling, *Geophys. Prospect.*, **35**, 479-490.

Taylor, S.R., Bonner, B.P. & Zandt, G., 1986. Attenuation and scattering of broadband *P* and *S* waves across North America, *J. Geophys. Res.*, **91**, 7309-7325.

Tessmer, E. & Kosloff, D., 1994. 3-D elastic modeling with surface topography by a Chebychev spectral method, *Geophysics*, **59**, 464-473.

Tessmer, E., Kosloff, D. & Behle, A., 1992. Elastic wave propagation simulation in the presence of surface topography, *Geophys. J. Int.*, **108**, 621-632.

Thompson, K.W., 1990. Time-dependent boundary conditions for hyperbolic systems, II, *J. Comput. Phys.*, **89**, 439-461.

Tibuleac, M. & Herrin, E.T., 1999. An automatic method for determination of *Lg* arrival times using wavelet transforms, *Seism. Res. Lett.*, **70**, 577-595.

Tripathi, J.N. & Ram, A., 1997. Elastic-wave scattering in a random medium characterized by the von Karman correlation function and small-scale inhomogeneities in the lithosphere, *Geophys. J. Int.*, **131**, 682-698.

Truell, R., Elbaum, C. & Chick, B.B., 1969. *Ultrasonic Methods in Solid State Physics*, Academic Press, Inc., New York.

Tsai, Y.-B. & Aki, K., 1969. Simultaneous determination of the seismic moment and attenuation of seismic surface waves, *Bull. seism. Soc. Am.*, **59**, 275-287.

Tselentis, G., 1993. Depth-dependent seismic attenuation in Western Greece, *Tectonophysics*, **225**, 523-528.

Tselentis, G., 1998. Intrinsic and scattering seismic attenuation in W. Greece, *Pure Appl. Geophys.*, **153**, 703-712.

Vasilyev, O.V., Podladchikov, Y.Y. & Yuen, D.A., 2001. Modelling of viscoelastic plume-lithosphere interaction using the adaptive multilevel wavelet collocation method, *Geophys. J. Int.*, **147**, 579-589.

Vidale, J.E., 1987. Waveform effects of a high-velocity, subducted slab, *Geophys. Res. Lett.*, **15** (5), 542-545.

Vidale, J., Helmberger, D.V., & Clayton, R.W., 1985. Finite-difference seismograms for *SH* waves, *Bull. seism. Soc. Am.*, **75**, 1765-1782.

Vidale, J.E. & Clayton, R.W., 1986. A stable free-surface boundary condition for two-dimensional elastic finite-difference wave simulation, *Geophysics*, **51**, 2247-2249.

Virieux, J., 1984. *SH*-wave propagation in heterogeneous media: Velocity-stress finite-difference method, *Geophysics*, **49**, 1933-1957.

Virieux, J., 1986. *P-SV* wave propagation in heterogeneous media: Velocity-stress finite-difference method, *Geophysics*, **51**, 889-901.

Widiyantoro, S., Kennett, B.L.N., & van der Hilst, R.D., 1999. Seismic tomography with *P* and *S* data reveals lateral variations in the rigidity of deep slabs, *Earth Planet. Sci. Lett.*, **173**, 91-100.

Wu, R.-S., 1982. Attenuation of short period seismic waves due to scattering, *Geophys. Res. Lett.*, **9**, 9-12.

Wu, R.-S., 1989. The perturbation method in elastic wave scattering, *Pure Appl. Geophys.*, **131**, 605-637.

Wu, R.S. & Aki, K., 1985. Elastic wave scattering by a random medium and the small-scale inhomogeneities in the lithosphere, *J. Geophys. Res.*, **90**, 10,261-10,273.

Wu, R.S., Jin, S. & Xie, X.-B., 2000. Seismic wave propagation and scattering in heterogeneous crustal waveguides using screen propagation: I. *SH* waves, *Bull. seism. Soc. Am.*, **90**, 401-413.

Wu, R.S., Xu, Z. & Li, X.-P., 1994. Heterogeneity spectrum and scale-anisotropy in the upper crust revealed by the German continental deep-drilling (KTB) holes, *Geophys. Res. Lett.*, **21**, 911-914.

Yomogida, K. & Benites, R., 1995. Relation between direct wave *Q* and coda *Q*: A numerical approach, *Geophys. J. Int.*, **123**, 471-483.

Yomogida, K. & Benites, R., 2002. Scattering of seismic waves by cracks with the boundary integral method, *Pure Appl. Geophys.*, **159**, 1771-1789.

Yomogida, K. & Etgen, J.T., 1993. 3-D wave propagation in the Los Angeles Basin for the Whittier-Narrows earthquake, *Bull. seism. Soc. Am.*, **83**, 1325-1344.

Yoshimoto, K., Sato, H., Iio, Y., Ito, H., Ohminato, T., & Ohtake, M., 1998. Frequency-dependent attenuation of high-frequency *P* and *S* waves in the upper crust in western Nagano, Japan, *Pure Appl. Geophys.*, **153**, 489-502.

Yoshimoto, K., Sato, H., & Ohtake, M., 1993. Frequency-dependent attenuation of *P* and *S* waves in the Kanto area, Japan, based on the coda-normalization method, *Geophys. J. Int.*, **114**, 165-174.

Zahradnik, J., 1995. Simple elastic finite-difference scheme, *Bull. seism. Soc. Am.*, **85**, 1879-1887.

Zhang, Y.-G. & Ballmann, J., 1997. Two techniques for the absorption of elastic waves using an artificial transition layer, *Wave Motion*, **25**, 15-33.